Nano-silica production at low temperatures from the dissolution of olivine : synthesis, tailoring and modelling

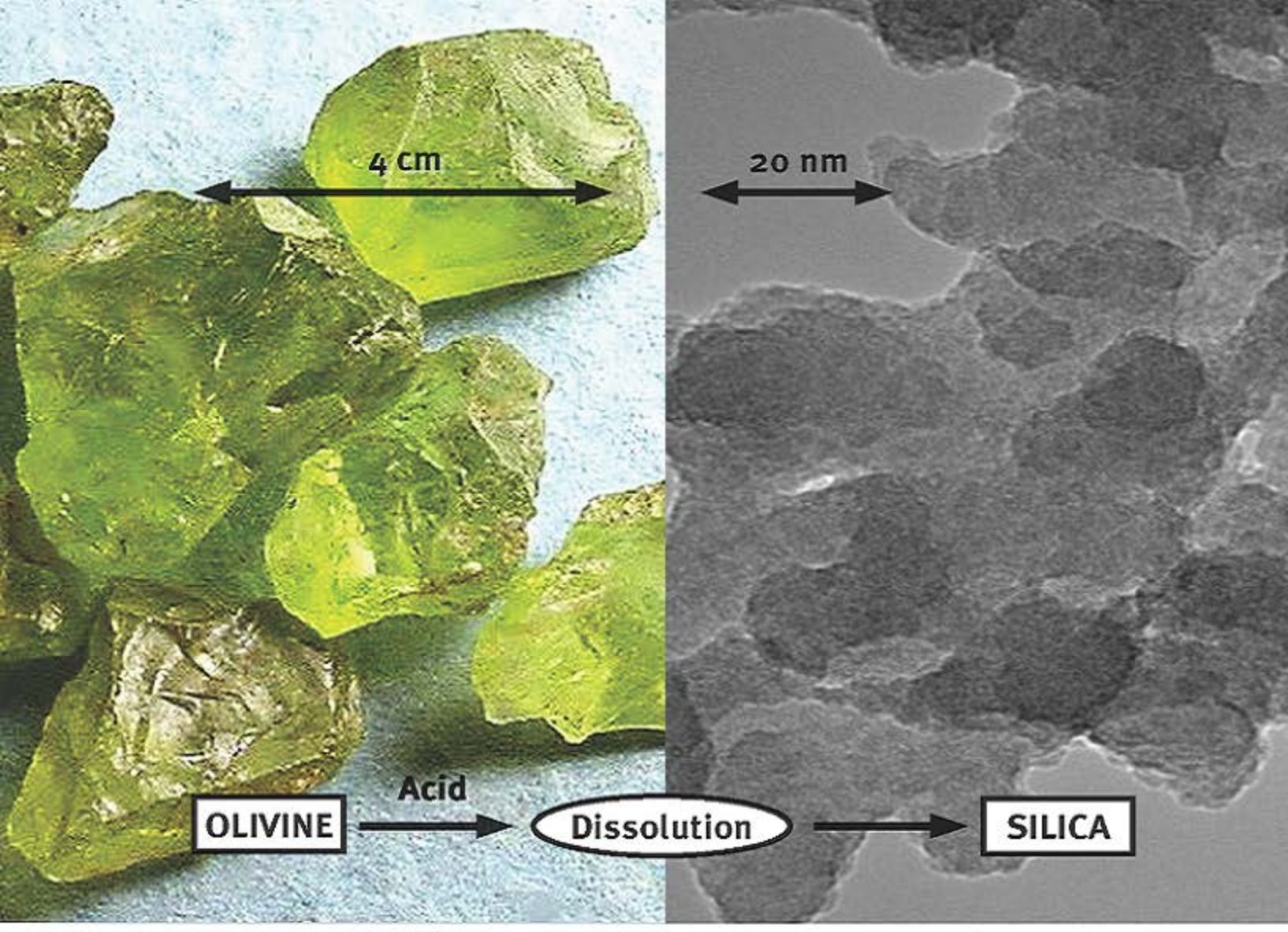

Nano-silica production at low temperatures from the dissolution of olivine

Synthesis, tailoring and modelling

Alberto Lázaro García

/ Department of the Built Environment

bouwstenen 195

Nano-silica production at low temperatures from the dissolution of olivine

Synthesis, tailoring and modelling

PROEFSCHRIFT

ter verkrijging van de graad van doctor
aan de Technische Universiteit Eindhoven,
op gezag van de rector magnificus prof.dr.ir. C.J. van Duijn,
voor een commissie aangewezen door het College voor Promoties,
in het openbaar te verdedigen
op dinsdag 24 juni 2014 om 16:00 uur

door

Alberto Lázaro García

geboren te Valencia, Spanje

Dit proefschrift is goedgekeurd door de promotoren en de samenstelling van de promotiecommissie is als volgt:

voorzitter:	prof.ir. E.S.M. Nelissen
1e promotor:	prof.dr.ir. H.J.H. Brouwers
copromotor:	prof.dr.ir. J.W. Geus (Utrecht University)
leden:	dr. K. Albertsen (Euro Support Advanced Materials)
	prof.dr. P.H.L. Notten
	prof.dr.dr. H. Pöllmann (Martin Luther Universität Halle-Wittenberg)
	prof.dr. J. Santamaria (Universidad de Zaragoza)
	prof.dr. R.A. van Santen

Nano-silica production at low temperatures from the dissolution of olivine

Synthesis, tailoring and modelling

A. Lázaro García

Technische Universiteit
Eindhoven
University of Technology

CIP-DATA LIBRARY TECHNISCHE UNIVERSITEIT EINDHOVEN

Nano-silica production at low temperatures from the dissolution of olivine – Synthesis, tailoring and modelling / by Alberto Lázaro García

ISBN 978-90-386-3640-5

Bouwstenen 195

NUR 955

PhD Thesis, Eindhoven University of Technology, the Netherlands

Cover design: A. Lazaro, A. J. Schmidt and A. Taher (a similar cover was published in the Chemical Engineering Journal, Volume 211-212, 2012); photographs provided by R. Weller and J.W. Geus.

Printed by: Ipskamp Drukkers, Enschede, The Netherlands

Dedicated to my family, especially to:
Anna Julia Schmidt
Carmen García Portillo
Vicente Lázaro Valero

Preface

When I started my PhD thesis in October 2009, I was not aware of what a PhD study would require, and I could not appreciate how exhausting the work and tremendous the personal achievements would be. At the beginning of this "journey", I faced many scientific challenges related to the chemistry of silica and the dissolution of silicates. In addition, the Building Materials group had recently moved from the University of Twente to the Technical University of Eindhoven, and, therefore, the members of the group had to arrange and prepare the research facilities. On the other hand, I have never experienced such a rewarding and motivating work; I have so many great memories of days in the lab or in the office, where I made small but important progress toward the completion of this thesis.

This thesis could not have been finished without the help and support of so many people that I have met and collaborated with, and for that I would like to express my most sincere gratitude. Thanks to all of you!

First of all, I would like to thank my supervisor and promotor Jos Brouwers for so many things, especially for providing me the opportunity to do my PhD in the group of Building Materials. His guidance, motivation and support, and all the scientific discussions during the course of this research period, particularly about the physical phenomena involved in the dissolution of olivine, were invaluable. Working with Jos has been an enriching experience that has taught me how to find within scientific investigations a useful application for industry and society. My most sincere gratitude also goes to my copromotor John Geus. Three years ago Jos and I decided to ask him to become involved in this research. I am deeply thankful that he decided to join us. Our scientific discussions about the chemistry of nano-silica are some of my more precious memories that I take with me. He has always been supportive and critically constructive with my work, and for that I thank him. In addition, John Geus has also performed the TEM photographs of the materials synthesized in this thesis.

I would also like to thank the members of my PhD defense committee – Dr. K. Albertsen, Prof. dr. P.H.L. Notten, Prof. dr. H. Poellmann, Prof. dr. J. Santamaria and Prof. dr. R.A. van Santen – for accepting and reviewing this PhD thesis:.

Furthermore, I want to express my gratitude to EU FP7 project ProMine: Nano-particle products from new mineral resources in Europe (grant agreement n° 228559). My sincere appreciation also goes to the companies Geochem and Selor, with which I have closely collaborated, especially to Dr. J.H. Baker, Ms. V. Heidweiller and Mr. R.J. van Enk.

During this PhD research, I had the opportunity to supervise daily the research projects of two master students, M.C. van de Griend and L.D. Barreto Torres. Their supervision has been a demanding task with many long discussions, but overall, it has been an enriching experience from which I have learned how to lead, guide and motive young scientists. In

addition, I have to thank them for their contributions to this thesis and the time we spent together.

I want to express my gratitude to all the scientists that have contributed to this thesis. Without their advice, suggestions and support this could not have been completed. To Dr. R.C.L. Jonckbloedt and Dr. D.J. Lieftink, your theses were the manuals that were always on my desk, and my thesis can only be understood as a continuation of your work; also, thanks for the discussions that we have had. To Prof. J. Bastida, for the advices and suggestions about the characterization of olivine, but also for your support. To Mr. L. Benac Vegas for aid with the PHREEQ model and hydrogen ion activity and for being a true friend. To Mr. R.J. van Enk for his fruitful discussions and practical comments about the geochemistry of olivine. To Dr. K. Sato for performing the Positronium annihilation lifetime spectroscopy analyses and for your time and collaboration without asking anything in return. To Mr. J. Nokes for his comments and suggestions. To Mr. P.H. Cappon for his help in the construction of the set-up and for finding brilliant solutions to practical problems. To Dr. A.J.J. van der Zanden for his comments and suggestions about transport phenomena. To Dr. P. Spiesz and Dr. Q. Yu for their fruitful discussions, useful comments and suggestions. To Mr. G. Quercia, who started his PhD research (about the application of nano-silica in concrete) almost at the same time as I did, for being a good colleague and friend, and for all the enriching discussions about the characterization of nanomaterials and application of nano-silica in concrete.

My most sincere appreciation goes to my colleagues and friends of the Building Materials group for their friendship, support and time together in the lab, in the sport center, in conferences, in de Zwarte Doos, etc. Ariën, Azee, Bo, Chris, George, Götz, Guillaume, Katrin, Milagros, Miruna, Qingliang, Pei, Pierre, Przemek, Rubina, Rui, Štěpán, Veronika and Xu. Also, I would like to thank the laboratory technicians and the secretaries for their help, support and (short and long) conversations; in particular to Geert-Jan, Harrie, Janet, Peter and Renée.

Finally, I have to thank my whole family for supporting, but especially to three persons. To my father for teaching me the passion for the engineering disciplines. To my mother –first I must apologize for not attending her PhD defense 15 years ago– now that I can understand all the effort and sacrifices that you made, I am deeply sorry. And second, thank you for everything, but especially for conveying to me a passion for chemistry. To my wife, Anna Julia, thanks for your unconditional support, for reading this thesis and for bringing our daughter into the world.

Alberto Lázaro García

June 2014

Contents

Chapter 1. Introduction

1.1 Synthetic amorphous silica

1.1.1 Description and classification of the existing silicas

Synthetic amorphous silica, abbreviated as SAS, is a highly pure, crystalline-free, silicon dioxide. SAS is mainly produced either from a wet route using sodium silicate or a thermal route. The main types of produced SAS are silica gel, precipitated silica and pyrogenic silica. The different polymorphs of silica and their CAS numbers are summarized in Figure 1.1 [1].

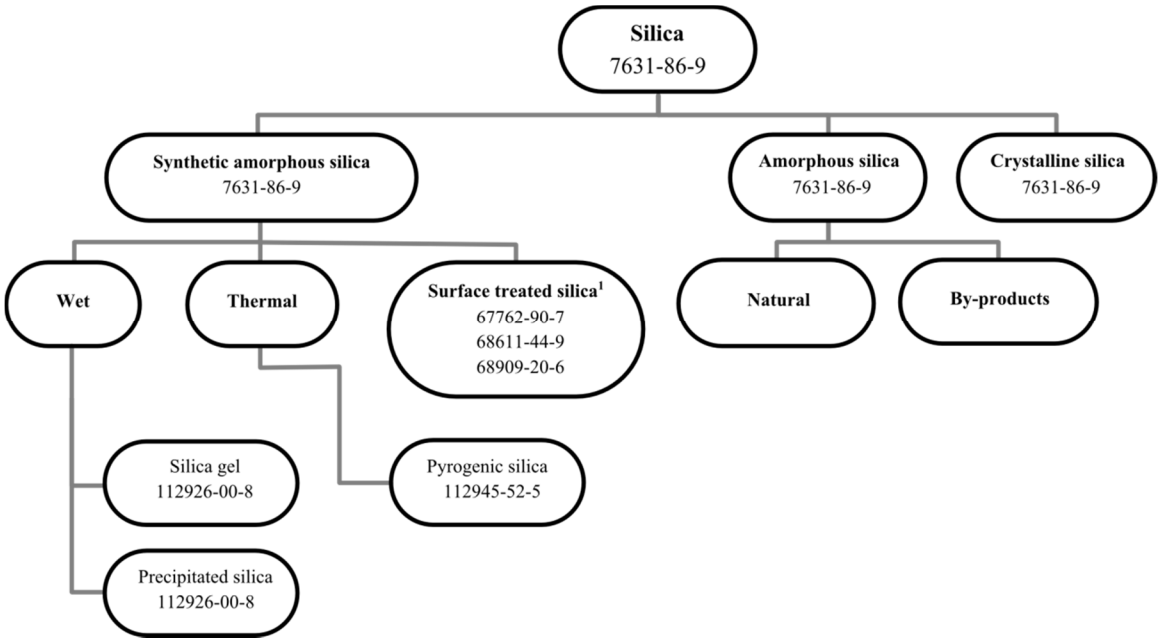

Figure 1.1. Different polymorphs of silica and their CAS numbers [1].

[1]All forms of SAS can be surface-treated physically or chemically.

Another type of commercial SAS is colloidal silica, which is usually produced using a sodium silicate solution as a precursor. Colloidal silica consists of discrete particles (typically between 3 and 100 nm) stabilized in a solution (normally water) [2]. The main properties of commercial amorphous silica are listed in Table 1.1 [1].

1.1.2 Consumption and uses of synthetic amorphous silica

At present a wide range of silica products are manufactured industrially for a diverse array of applications. Silicas are mainly used for reinforcing, thickening and flattening purposes; their main applications are in consumer use products (cosmetics,

pharmaceuticals and foods), animal feed, rubber and silicones, paints and coatings, plastics, and paper. Figures 1.2 - 1.4 present the consumption of synthetic amorphous silica (pyrogenic, precipitated and silica gel) in Western Europe [2]. World demand for specialty silicas, which include precipitated silica, pyrogenic silica, silica gel and silica sol, is rising 5.6% per year and is expected to reach 2.8 million metric tons in 2016 [3]. Likewise, the market is estimated to grow 7.5 per year reaching a total value of $6.4 billion in 2016, which results in an average value of 2300 $/tn [3].

Table 1.1. Properties of commercial amorphous silica [1].

Property		Pyrogenic	Precipitated	Gel	Sol a
Purity	(wt.%)	>99.8	>95 [b]	>95	15-50
Color		White	White	White	White, milky
Specific surface area	(m^2/g)	50 - 400	30 - 500	250 - 1000	50 - 400
Loss on drying	(wt.%)	< 2.5	5 - 7	2 - 6	50 - 85
pH [c]		3.6 - 4.5	5 - 9	3 - 7	3 - 5 8 - 11
Tapped (bulk) density	(g/L)	30 - 250	30 - 500	500 - 1000	NA [d]
Ignition loss	(wt.%)	< 2	3 -14	2 - 15	50 - 90
Primary particle size, d_1	(nm)	5 - 50 [e]	5 - 100 [e]	1 - 10	5 - 20
Aggregate size, d_2	(μm)	0.1 - 1	0.1 - 1	1 - 20	NA
Agglomerate size, d_3	(μm)	1 - 250	1 - 250	NA	NA
Mean pore size, d_p	(nm)	None	> 30	0.1 - 1000	NA
Pore size distribution		None	Very wide	Narrow	Wide
Specific gravity	(g/cm^3)	2.2	1.9 - 2.2	1.8 - 2.2	1.0 - 1.4

[a] After drying according to DIN 66131. [b] Dry product. [c] Hydrofilic grades. [d] Not applicable. [e] Primary particles do not normally exist as individual units. The definitions of aggregate and agglomerate are given in Appendix I.

1.1.3 Production routes of commercial silica

This section aims to describe briefly the two main routes for the production of synthetic amorphous nano-silicas, which are the thermal route and the wet route [1]. A more detailed description of the production of synthetic amorphous silica can be found in [1,2,4-6].

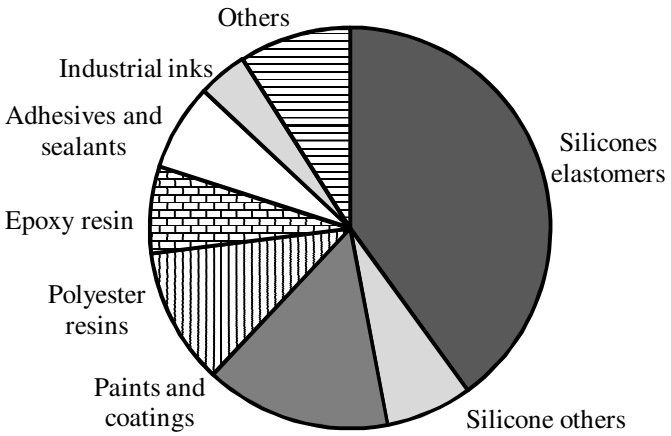

Figure 1.2. West European consumption of amorphous pyrogenic silica [2].

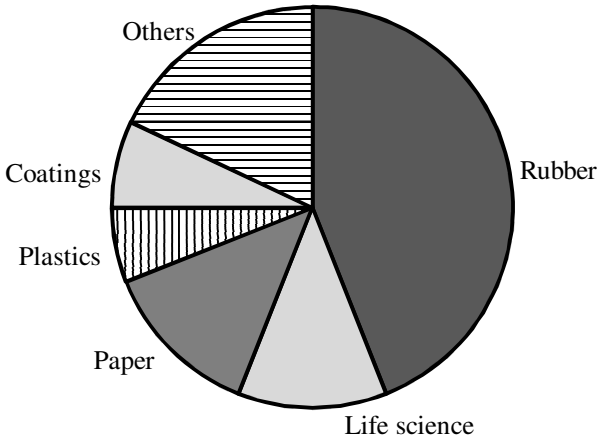

Figure 1.3. West European consumption of amorphous precipitated silica [2].

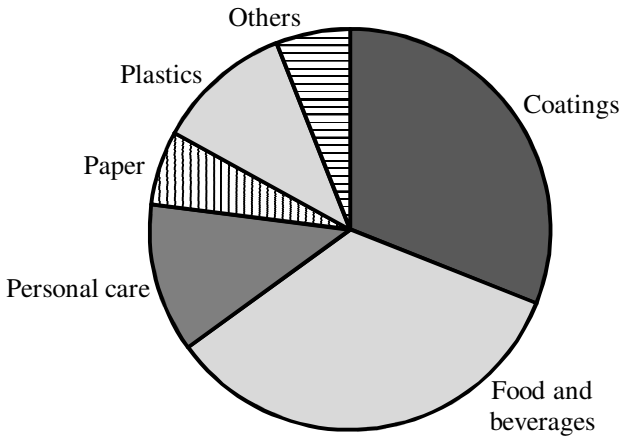

Figure 1.4. West European consumption of silica gel [2].

In the thermal production route of SAS, also called flame hydrolysis, highly dispersed silicas are formed from the gas phase at high temperatures. Chlorosilanes ($SiCl_4$ or $HSiCl_3$), which are the usual raw materials, are continuously vaporized, mixed with dry air, then with hydrogen and finally fed to a burner where they are hydrolyzed in an oxygen-hydrogen flame following Eqs. (1.1) and (1.2):

$$SiCl_4 + 2H_2 + O_2 \rightarrow SiO_2 + 4HCl\,, \qquad \textbf{(1.1)}$$

$$SiHCl_3 + H_2 + O_2 \rightarrow SiO_2 + 3HCl\,. \qquad \textbf{(1.2)}$$

Hydrolysis is followed first by the growth of silica (nucleation, condensation and coagulation) and then by aggregation as can be seen in Figure 1.5. The flame temperature is in the range of 1200-1600 °C [2], depending on the properties of the burner and the desired characteristics of nano-silica.

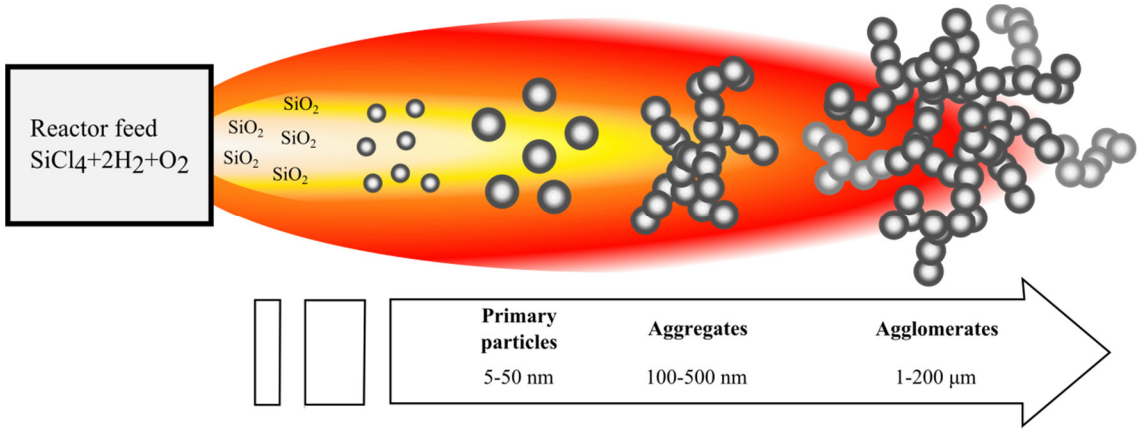

Figure 1.5. Particle formation of pyrogenic silica [1].

In the wet silica production route or sol-gel process, an aqueous alkali metal silicate solution is neutralized with acid (e.g. sulfuric acid) releasing the silica. The most commonly used aqueous alkali silicate is water glass ($Na_2O{\cdot}nSiO_2$; n = 2 – 4). Water glass is produced by melting quartz sand with soda at about 1300 °C [2]; subsequently, the resulting solid water glass is hydrothermally dissolved in water. Using sodium silicate solutions, precipitated silica, silica gel and colloidal silica can be produced:

$$Na_2O \cdot nSiO_2 + H_2SO_4 \rightarrow nSiO_2 + NaSO_4 + H_2O\,. \qquad \textbf{(1.3)}$$

Precipitated silica is produced under neutral or slightly alkaline media. The main operations consist of raw material storage, reaction and precipitation, filtration, drying, storage, packing and shipment [2]. A flow diagram of the production process of precipitated silica is presented in Figure 1.6 [2]. By changing the process conditions in the

precipitation reactor (i.e., temperature, pH, flows, residence time, etc.) a wide range of silica products can be obtained [1].

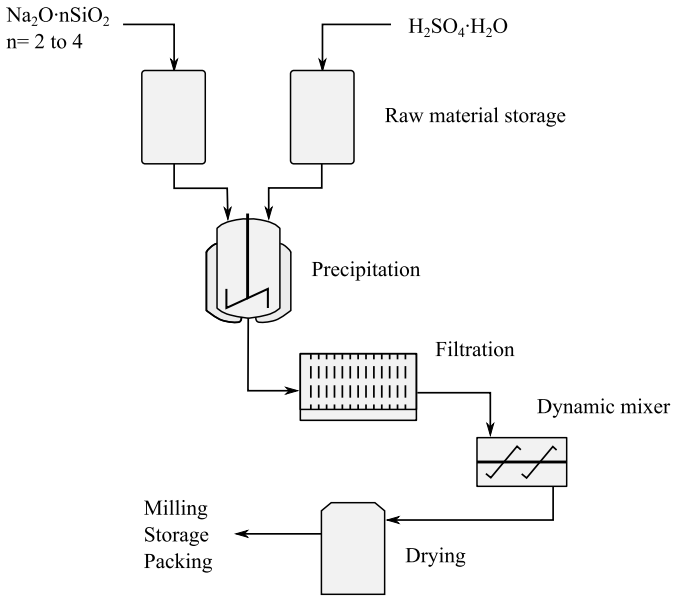

Figure 1.6. Flow diagram for the production process of precipitated silica [1].

Silica gels are also produced by the neutralization of water glass with acids but, in this case, under acidic conditions. The process comprises a raw material dilution (optional), sol formation and gelation, washing, filtering and drying [2]. The subsequent steps are similar to the production of precipitated silica. A flow diagram of the production process of silica gel is presented in Figure 1.7 [2].

The primary method to produce colloidal silica is the ion-exchange method. An aqueous water glass solution with a SiO_2 content of 30 wt.% and a molar ratio of SiO_2:Na_2O of 3 is normally used. The water glass is diluted and then passed through an ion exchange resin, where the sodium ions are removed leaving an unstable solution of active silicic acid with a molar ratio of SiO_2:Na_2O of about 20 to 500 and a pH between 2 and 4. The pH of the medium is increased in the range of 8 to 10.5 and the temperature is raised above 60 °C to allow the active silica to nucleate, polymerize and grow. The silica sol produced consists of dispersed spherical particles of 4 to 100 nm and a silica content between 2 and 6 wt.%. Subsequently, this silica sol is concentrated in the range of 15 to 60 wt.%. A flow chart of the production process of colloidal silica is presented in Figure 1.8 [6].

Apart from the amorphous silica previously described, SAS can also be obtained as a byproduct in other processes. An important amorphous silica byproduct is silica fume which is used commonly in cement for special applications. Silica fume is a byproduct of the reduction of quartz for the production of silicon and ferrosilicon. It is a very fine

powder consisting of non-crystalline silica spheres with an average diameter of circa 0.1 μm, and it is produced at temperatures of about 2000 °C [7,8].

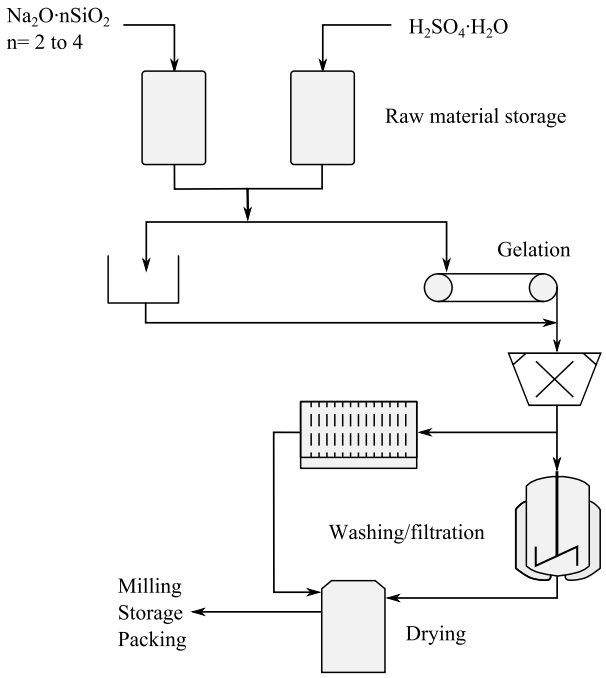

Figure 1.7. Flow diagram for the production process of silica gel [1].

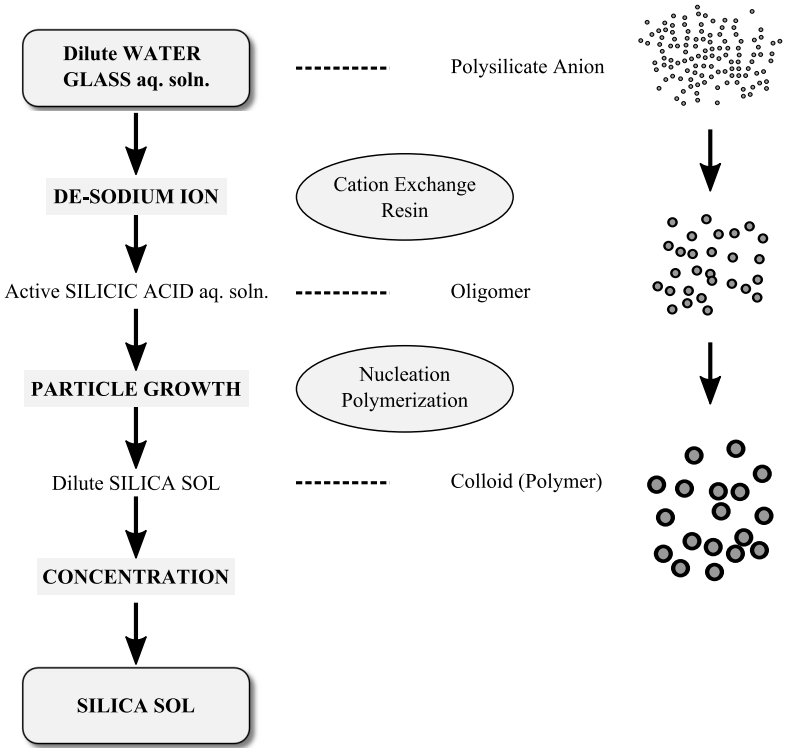

Figure 1.8. Flow chart for the production of colloidal silica [6].

In all the above-mentioned production methods, a high temperature process is involved either related to the raw materials (e.g. production of water glass) or the production process itself (e.g. flame pyrolysis). To reach these temperatures, huge amounts of fuel are consumed making these processes: a) non-sustainable because of the scarcity of fuels; b) environmentally unfriendly because of the huge amount of CO_2 emitted; and c) expensive because of the fuel price.

1.2 An alternative method: the olivine nano-silica process

1.2.1 Process description

An alternative synthesis route to the commercial production methods of amorphous nano-silica is the dissolution of silicate minerals in acid. The raw materials employed in this method are olivine ($(Mg,Fe)_2SiO_4$) and acid (in the present case sulfuric acid). Olivine is the fastest weathering silicate due to the absence of Si-O bonds in its structure. In addition, olivine is the most common mineral in the upper mantle and a common mineral in the earth's crust, which makes it a low-price commodity.

Olivine is a solid solution between forsterite (Mg_2SiO_4) and fayalite (Fe_2SiO_4). The crystalline structure of forsterite is represented in Figure 1.9. The rocks where 90% or more of the volume is made up of olivine are called dunites. The remaining 10% present in dunite ores can consist of pyroxenes, amphiboles, micas, carbonates, serpentines, etc. In many weathering and dissolution studies, pure olivines were used [9-11], but in this study dunite has been used because this research focuses on the commercial production of olivine nano-silica. More details about the material used to produce nano-silica in this study are presented in Chapter 2.

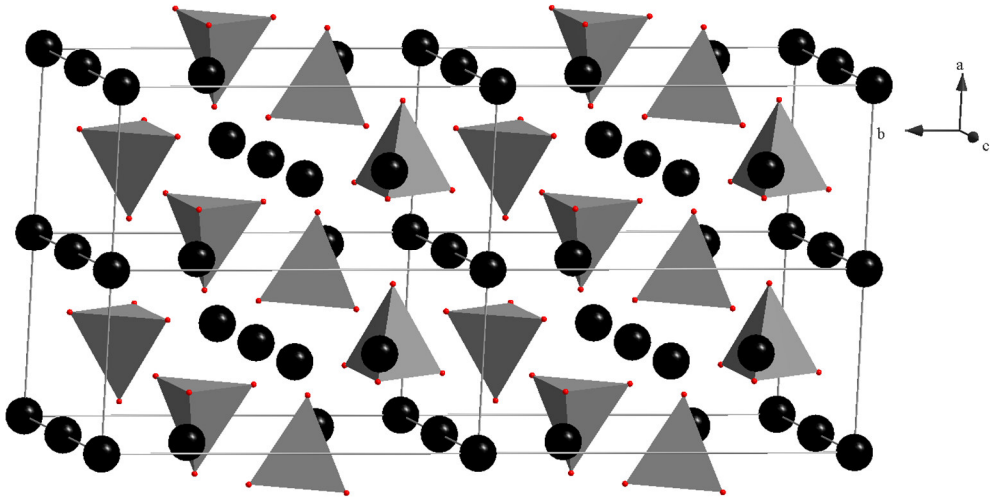

Figure 1.9. Crystalline structure of forsterite, Mg_2SiO_4.

Where the tetrahedrons are SiO_4 particles with four oxygen atoms at the vertex, and the spheres next to the SiO_4 tetrahedrons are magnesium ions.

The dissolution of olivine in acid at low temperatures (between 50 and 95 °C) produces amorphous silica:

$$(Mg,Fe)_2SiO_4 + 4H^+ \rightarrow Si(OH)_4 + 2(Mg,Fe)^{2+} . \quad \textbf{(1.4)}$$

The dissolution yields a slurry consisting of a mixture of magnesium/iron salts, amorphous silica, unreacted olivine and inert minerals. Once the reaction is complete, the unreacted olivine and inert minerals are removed from the final suspension by sedimentation. Subsequently, the silica can be cleaned from the resulting mixture by washing and filtering. After the filtration, a cake with around 20 wt.% solid content of nano-silica is obtained. A flow chart of this process is presented in Figure 1.10.

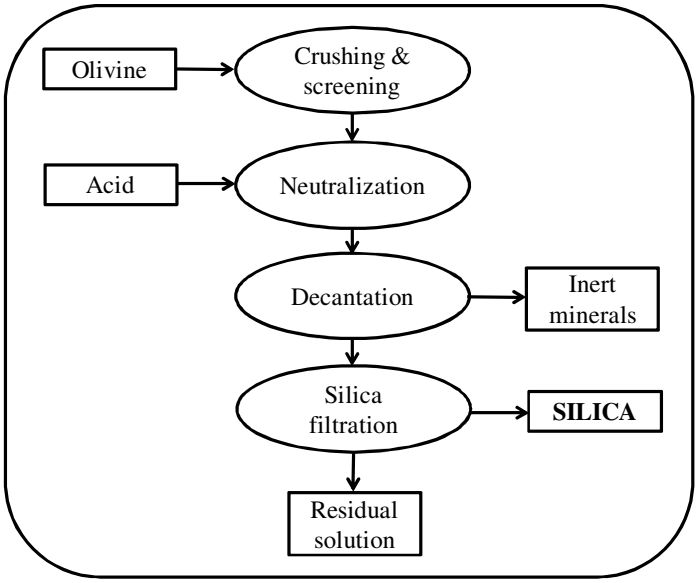

Figure 1.10. Flow chart of the production of nano-silica by the dissolution of olivine.

In addition to the low temperature of this procedure (below 95 °C), it is remarkable that the process is exothermic with a reaction heat of 223 kJ per mole of olivine [12]. The energy generation during the olivine nano-silica process for the hypothetical case of an adiabatic reactor is shown in Table 1.2. When 1.5 moles of olivine react with 1L solution of sulfuric acid 25%, the temperature of the mixture will increase 79 °C. Therefore, the reaction generates more than enough energy to keep the system at the desired temperature (between 50 and 90 °C) provided the reactor is sufficiently insulated. In addition, the dissolution of concentrated sulfuric acid also generates a considerable amount of heat.

Table 1.2. Energy generation during the olivine nano-silica process.

ΔH_r (kJ/mol)	$V_{H_2SO_4}$ (L)	$m_{H_2SO_4}$ (g)	n_{ol} (mol)	m_{du} (g)	X (%)	Q (kJ)	ΔT (°C)
223	1	1186	1.5	242	100	333.5	79.3

ΔH_r is the enthalpy of reaction, X the conversion degree of the reaction and Q is the heat generated. Heat capacities of 25% sulfuric acid and forsterite are 3.38 [13] and 0.83 [14] $J \cdot g^{-1} \cdot °C^{-1}$, respectively. The heat capacity of dunite has been approximated as the one of forsterite.

1.2.2 Literature review on olivine nano-silica

A few patents have been issued in the last years related to the production of nano-silica by the dissolution of olivine [15-17]. In 1986, Schuiling [15] patented the neutralization of waste sulfuric acid using olivine, where a silica gel was formed. However, this patent did not report the purity of nano-silica nor the BET specific surface area (SSA_{BET}).

In 1998, Olerud [16] patented a method for the production of nano-silica based on the dissolution of olivine in hydrochloric acid using a similar process to the one described in Section 1.2.1, but using HCl (instead of H_2SO_4) and centrifugation (instead of filtration) as a separation technique. He reported several experiments with different process conditions (i.e., reaction time, temperature, grain size of olivine and acid concentration), resulting in nano-silicas with a SSA_{BET} between 150 and 450 m^2/g, pore volumes between 0.74 and 1.4 mL/g and an impurity content below 1%. However, Olerud did not report the amount of olivine used, conversion degree or the purity of each single batch. Thus, even if the textural properties of the olivine nano-silica changed with the process conditions, a relationship between them and the process conditions could not be established. In addition, Olerud [16] claimed that after drying, spherical silica particles between 30 and 70 nm were obtained. However, no analyses concerning these results were presented.

Gunnarsson patented in 2012 [17] the production of precipitated silica from olivine in 18% HCl solution (~5.4M), reporting an average SSA_{BET} of 236 m^2/g. In this study, few details about the properties of silica were given, and little attention was paid to the influence of the process conditions on the textural properties of nano-silica. In addition, Gunnarsson [17] dispersed the filter cake of silica with the following steps: 1) mixing the cake with water; 2) addition of sodium aluminate to decrease the viscosity; and 3) ultrasonic treatment for 13 minutes. However, no data about the particle size distribution of the dispersion were presented.

The patents of Olerud [16] and Gunnarsson [17] provided some examples with useful information about the textural properties of olivine nano-silica at specific production conditions. However, they did not study the influence of the process conditions on the properties of olivine nano-silica.

A deeper study of the olivine nano-silica synthesis should comprise the dissolution of olivine in acid, and the particle growth of silica and its final textural properties. The

dissolution of olivine has been widely studied [9-12,18-25], but only Jonckbloedt [12,25] proposed a kinetic model under the conditions for the production of nano-silica. These conditions included a negative pH as well as a high solid content and dissolved fraction. Although Jonckbloedt's model was a considerable step forward, in order to have a more reliable and robust kinetic model, there are several points on which more effort could have been made: 1) Jonckbloedt did not follow the kinetic standard equation (i.e., Eq. (4.1)) for the dissolution of olivine; 2) the specific surface area and the mineralogical composition were not reported; 3) he obtained the kinetic parameters by fitting the plot of "log ($d[H^+]/dt$)" versus "$-$ m·log(mol $[H^+]$) $-$ n·log(act $[H^+]$)", which is a peculiar procedure. It would have been much simpler to obtain the kinetic parameters by fitting the data of the dissolution curve to Eq. (4.1); and 4) the reaction order is lower than that reported in most of the dissolution studies. In addition to these points, the mass transport mechanism should be more deeply investigated.

The texture of nano-silica is a complex topic addressed by several researchers (cited here are the most relevant studies for the particular case of olivine nano-silica [4,26-31]), but only Lieftink [30,32] thoroughly studied the properties of nano-silica produced from olivine. Although Lieftink [30] provided interesting results, in order to improve the properties of the nano-silica, and optimize the production process, more data about the following items are desired: 1) the effects of the process conditions (degree of conversion, impurities content and pressure of filtration) on the textural properties of the resulting nano-silica; 2) the influence of the mode of operation on the process, particularly on the process yield; 3) the chemical composition of nano-silica produced; 4) development of the silica particles; and 5) development of the pore structure.

1.3 Motivation and objective

The production of nano-silica by the dissolution of olivine is an interesting alternative to the existing commercial methods (the thermal and wet route processes) because of the low energy requirements and CO_2 emissions. However, after more than 25 years from the first patent [15], no commercial process for the production of olivine nano-silica is yet available. As was stated in the previous section, the main reason why this process is not yet industrialized is because the process has to be studied more thoroughly, especially regarding the process conditions and the final properties of the nano-silica.

The main objective of this research is to improve the technology of the olivine nano-silica production process to be able to tailor the properties of this material to meet the requirements of the possible applications. A secondary objective is to optimize the olivine nano-silica process. In addition to these objectives, this research contributes to understanding the three topics: the dissolution of olivine at negative pH, the silica particle growth below the isoelectric point, and the development of the pore structure at negative pH.

In this thesis, three main topics of the olivine nano-silica process are investigated (see the thesis outline in Figure 1.11): 1) the dissolution of olivine under the olivine nano-silica conditions; 2) the influence of the process conditions on the textural properties of olivine nano-silica; and 3) the technical aspects of the olivine nano-silica process. A concise description of these topics is summarized in what follows.

1.3.1 The dissolution of olivine in acid

The dissolution of olivine under the conditions of olivine nano-silica production is addressed in Chapters 3 and 4. Chapter 3 focuses on the experimental data and Chapter 4 proposes a kinetic model. The dissolution of olivine is essential to predict the conversion degree over time. Furthermore, the olivine dissolution kinetics influences the properties of olivine nano-silica.

Chapter 3 consists of three components: 1) the characterization of the olivine material focusing on the specific surface area and the mineralogical composition; 2) the surface characterization of olivine prior to and after dissolution; and 3) the experimental data of the olivine dissolution curves.

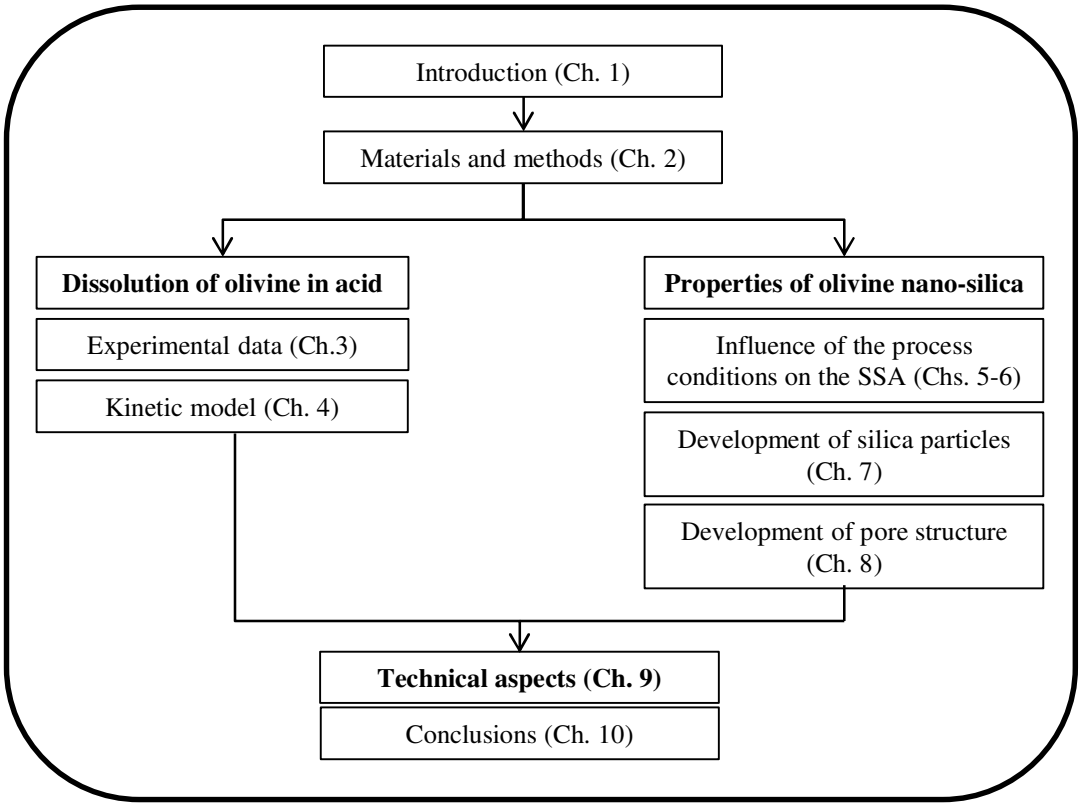

Figure 1.11. Outline of this thesis.

Chapter 4 is structured in two parts. In the first part, the mechanism of the dissolution of olivine is investigated focusing on the possible resistances to the ionic transport; in the second part, a kinetic model is developed. This kinetic model is successfully applied to the dissolution of other commercial dunites and for bigger reactor volumes. Therefore, this model can be considered to be robust, and it can be used in the industrial production of olivine nano-silica.

1.3.2 The properties of olivine nano-silica

Chapters 5 and 6 study the properties of olivine nano-silicas produced at different conditions. These chapters focus on the synthesis of amorphous nano-silica by the dissolution of olivine in acid, showing the influence of the process conditions on the properties of nano-silica. The main topics addressed are summarized below:

1. the influence of the reaction kinetics on the SSA_{BET} (specific surface area determined by the BET method);
2. the influence of the sulfate content on the SSA_{BET} and SSA_{MP} (specific surface area of the micropores);
3. the effect of the ripening treatment on the SSA_{BET} and SSA_{MP};
4. the development of the SSA_{BET} and SSA_{MP} with the conversion degree;
5. the process yield and the separation efficiency of the olivine nano-silica production process;
6. the development of the density and viscosity with the conversion degree;
7. the deagglomeration of the silica clusters using mechanical treatments.

The development of the olivine nano-silica particles is investigated in Chapter 7. This chapter consists of two main sections: 1) a literature review on the polymerization of silicic acid and particle growth of nano-silica, especially focusing on the investigations performed below the isoelectric point; and 2) the study of the particle growth of nano-silica when olivine is dissolved in acid. In addition to these, the zeta potential of an olivine nano-silica dispersion is studied in the pH range between 1 and 10.

In Chapter 8, additional textural properties of different olivine nano-silicas are presented. These properties are: 1) the pore size distribution (PoSD) determined using the BJH method; 2) the silanol content and SSA_{NMR} computed using ^{29}Si nuclear magnetic resonance (NMR); and 3) the pore sizes in the micropore range measured using annihilation spectroscopy. From these data and the results of the particle growth of olivine nano-silica, a model for the development of silica nanoparticles structure is proposed. Furthermore, the PoSD and SSA_{NMR} of precipitated and pyrogenic silicas are also studied in this chapter.

1.3.3 Technical aspects

Chapter 9 addresses different practical aspects of the olivine nano-silica process, focusing on the following points:

1. conditions chosen of the production process of olivine nano-silica;
2. possible problems that might be encountered during the production.
3. experiments performed in pilot plants;
4. cost analysis of olivine nano-silica and precipitated silica;
5. generation of waste solutions and byproducts;
6. application of olivine nano-silica in building materials.

Chapter 2. Materials and methods

2.1 Materials

Two types of dunite materials were used in this study for the production of olivine nano-silica, one from Norway and another one from Greece. The dunite from Norway was supplied by North Cape minerals (CRS) and by Eurogrit (GL50). Dunite CRS and GL50 are commercialized as slag conditioner and as abrasive material, respectively. The dunite from Greece (PROMGM) was a byproduct from the magnesite mining activities in Gerakini (Greece).

Figure 2.1 shows the original dunite materials from Greece: PROMGM-1, -2 and -3, which are classified based on the olivine content as high, medium and low grade, respectively. Even the high grade dunite has a lower content of olivine and considerably higher content of serpentine, carbonates, enstatite and talc (as was reported in [33]) than is advisable for the production of nano-silica as is mentioned in Chapter 9. These waste rocks were beneficiated by dense media separation in order to increase the olivine content, resulting in samples PROMGM-4, -8 and -10.

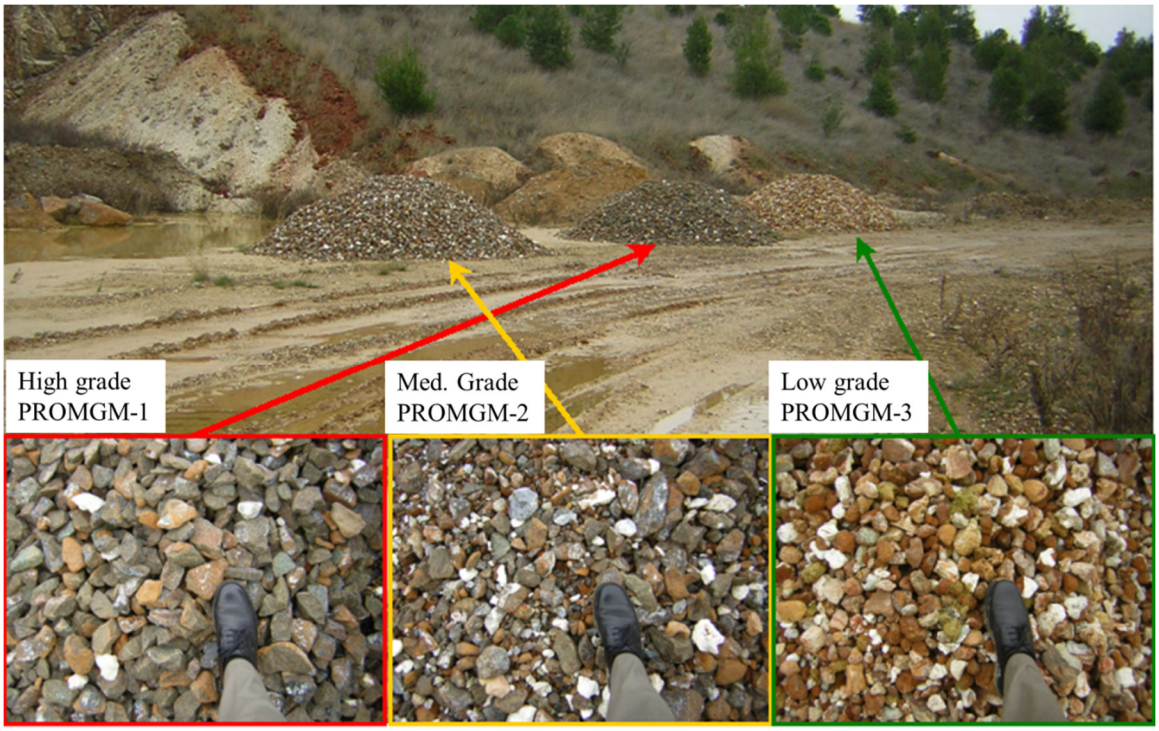

Figure 2.1. Waste dunite materials from the magnesite mine in Gerakini (by courtesy of Dr. Jonckbloedt).

Table 2.1 lists the chemical composition of the dunites determined by X-ray fluorescence (XRF), the loss on ignition (LOI), the carbon content measured by combustion infrared analysis and the olivine content. The olivine content of the Norwegian dunite was stoichiometrically estimated from the hydrogen ion consumption when olivine was put together with sulfuric acid (more details about this determination can be found in Chapter 3). In the case of the Greek dunite, the olivine content was determined by Grecian Magnesite [33] combining the results of X-Ray diffraction (XRD), XRF and thermogravimetric (TG) techniques. The low LOI and high magnesium content of the Norwegian dunite confirm the high olivine content. In contrast, the original Greek dunites feature a low content of magnesium, especially PROMGM-2, and a high LOI. After the beneficiation of the byproduct dunite, the loss on ignition decreases below 2.5%. The samples after beneficiation, PROMGM-4, -8 and -10, exhibit an olivine content twice that of the original dunite material.

Table 2.1. Chemical composition analyzed by XRF of Norwegian and Greek Dunites.

Dunite	MgO	Fe_2O_3	SiO_2	Cr_2O_3	Al_2O_3	NiO	MnO	CaO	Na_2O	LOI	Other Oxides	C	Olivine
CRS	47.41	7.84	41.42	0.31	0.75	0.33	0.12	0.34	0.06	1.29	0.13	0.05	88.4
GL50	49.32	7.32	41.44	0.31	0.46	0.32	0.09	0.15	0.02	0.59	0.00	0.03	88.9
PROMGM-1	41.62	8.63	41.46	0.5	0.52	0.3	0.15	0.69	0.09	5.92	0.12	-	44.0
PROMGM-2	18.9	6.33	41.09	0.36	0.84	0.19	0.00	9.84	0.16	22.03	0.26	-	>20
PROMGM-3	34.47	7.95	43.51	0.45	1.78	0.25	0.14	1.33	0.33	9.6	0.19	-	29.0
PROMGM-4	43.93	9.01	43.60	0.44	0.56	0.32	0.13	0.70	0.00	1.33	0.00	0.08	75.0
PROMGM-8	43.79	8.90	42.67	0.41	0.59	0.31	0.13	0.65	0.00	2.55	0.00	0.13	75.0
PROMGM-10	45.12	8.79	41.92	0.42	0.54	0.31	0.12	0.83	0.00	1.95	0.00	0.24	75.0

CRS and GL50 are dunite materials from Norway and PROMGM is a dunite material from Greece.
All values are expressed in wt.%.

2.2 Analytical and characterization methods

In this PhD thesis several characterization techniques were used to study the properties of the dunite materials and the nano-silica. The techniques used are XRF, X-ray diffraction (XRD), Inductively coupled plasma mass spectrometry (ICP-MS), combustion infrared analyses (carbon and sulfur), volumetric analysis or titration, thermogravimetric (TG) analysis, viscosity and density studies, laser light scattering (LLS), dynamic light scattering (DLS), gas physisorption, positron annihilation lifetime spectroscopy (PALS) and nuclear magnetic resonance (NMR).

The XRF and the infrared analyses were carried out in Canada by Actlab laboratories using routines 4C and 4F, respectively. The XRD equipment used was a Bruker D2

Phaser, where quartz was added to adjust the displacement of the diffractogram. The inductively coupled plasma analyses were carried out with an ICP-MS X2, after the samples were subjected to a "total" digestion. This digestion consists of a sequential exposure of the samples to hydrofluoric acid, perchloric acid and nitric acid. The density measurements were done with 50 ml glass picnometers, which were calibrated with water at 20 °C. An STA 449 F1 Jupiter (Netzsch Instruments) was used to perform the TG analysis. The buoyancy effect – meaning the forces affecting the balance due to the change of gas density – was corrected by means of performing the same temperature program to a blank. The concentration of hydrogen ions was determined by titration with a solution of 0.05 M $Na_2B_4O_7$; a 785 DMP Titrino with a pH probe was used.

2.2.1 Viscometer

The viscosity of the slurry was measured using a rotational rheometer with concentric cylinders (Haake Rotovisco RV 20). This equipment was used with a measuring system M10 (max. speed 1000 rpm) and a sensor system MV1. A diagram of the sensor MV1 is shown in Figure 2.2. The viscosity can be determined using:

$$\gamma(s^{-1}) = M \cdot \%\gamma, \quad \textbf{(2.1)}$$

$$\tau(Pa) = A \cdot \%\tau, \quad \textbf{(2.2)}$$

$$\mu(Pa \cdot s) = \frac{\tau}{\gamma}. \quad \textbf{(2.3)}$$

Where γ is the shear rate, $\%\gamma$ is the shear rate value displayed at the RV 20, τ is the shear stress, $\%\tau$ is the shear stress value of the display, μ is the viscosity, and M and A are factors depending on the sensor used. The factors A and M together with the geometrical parameters for sensor MV1 are listed in Table 2.2. This sensor can be used in the shear rate range between 0.1 and 1000 s^{-1}, and in the viscosity range between 2 and $2 \cdot 10^6$ mPa·s.

This viscometer with the sensor MV1 was validated using pure glycerol at 20 °C. The viscosity of glycerol at 20 °C is 1.41 Pa·s [34]. The viscosity measurement of glycerol was 7% lower than the expected value. Using the same equipment, Op de Hoek [35] found an error of 8% for the viscosity in the range of 0.002- 0.050 Pa·s.

Table 2.2. Geometrical parameters and factors A and M of sensor MV1.

R_i (mm)	L (mm)	R_a (mm)	A	M
20.4	60	21	6.44	23.4

R_i means radius of the inner cylinder, L length and R_a radius of the outer cylinder.

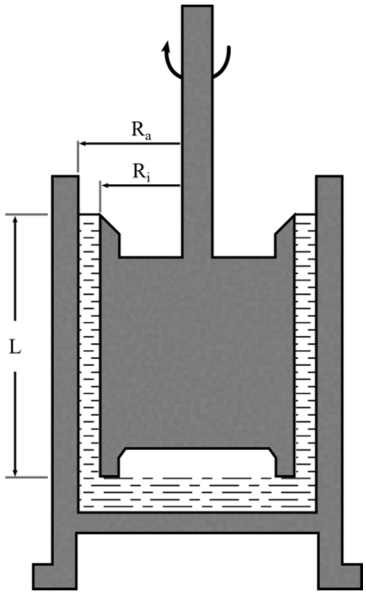

Figure 2.2. Diagram of the sensor MV1 (modified from the manual of Haake Rotovisco RV 20).

2.2.2 Laser light scattering and dynamic light scattering

The measurement of particle size distributions (PSD) is a major aspect of powder and nano-materials technology. In this thesis, the dimensional properties of olivine grains (in the range 0.01 to 0.6 mm) and olivine nano-silica agglomerates (approximately in the range 0.1 μm to 30 μm) have been studied. In the case of olivine, attention is paid to the specific surface area (SSA) of the granular material because it is one of the properties that influences the kinetics of the dissolution of olivine (see Chapter 4). The SSA of olivine can be measured using gas physisorption techniques. However, the determination of the SSA of olivine grains using gas physisorption presents some problems as is discussed more extensively in Chapter 3. The particle size of silica dispersions in liquids can be determined using laser light scattering (LLS) and dynamic light scattering (DLS) techniques. In addition, transmission electron microscopy (TEM) was also used in this study to determine the shape and size of the nano-silica particles. However, the microscopic analysis has two disadvantages. First, TEM analyzes the material properties locally and not globally as it is done by LLS and DLS. And second, the structure of nano-silica might be altered during this process since the samples are dried before performing the analysis and not measured dispersed in the liquid.

LLS has become the dominating method for the characterization of powders in research and industry [36]. The equipment used here is a Malvern Mastersizer 2000 together with a Hydro S unit to disperse the samples. The Mastersizer 2000 is equipped with a red and blue light source. This device measures the light scattered (an example of the light scattered can be seen in Figure 2.3) by the particles. From this data, using the Mie theory –which considers spherical particles–, the Mastersizer 2000 software calculates the

particle size distribution of the particles. According to the manual of this device, the measurement range is between 0.02 and 2000 µm [37]. However, in the case of olivine, the density is so high that when the sample had grains larger than 600 µm, which is the particle size limit used in this PhD thesis, the dispersion unit was not powerful enough, resulting in fast settling of the largest grains. The analyses of LLS have been performed following the recommendation of Malvern [37] and the ISO standard 13320 for particle analysis [38]. From the PSD measured by LLS, the geometric specific surface area is computed:

$$SSA_G = 6\sum_{i=1}^{n} m_i / (d_i \cdot \rho), \quad \textbf{(2.4)}$$

where m_i is the mass fraction i, d_i the grain diameter i and ρ the density of the material.

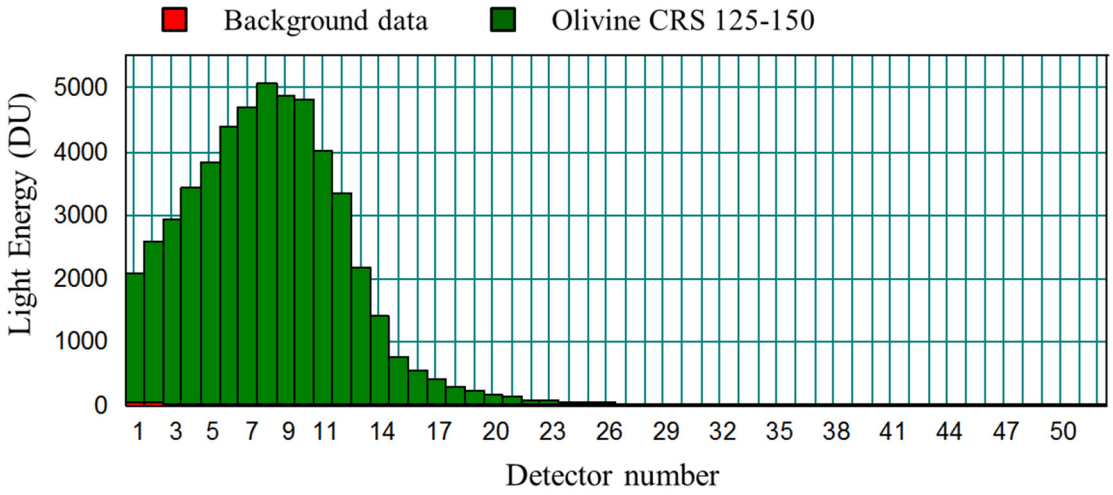

Figure 2.3. Light scattering pattern of dunite CRS.
The background data can barely be observed due to its low signal.

Dynamic light scattering (DLS) is a non-invasive, well-established technique for measuring the size of molecules and particles typically in the submicron region. The DLS equipment used here is Nano ZS. DLS measures the Brownian motion, which is defined as the random movement of particles suspended in a liquid due to collisions with the molecules that surround them [39]. The Nano ZS measures the scattered patterns of the particles at different time intervals. From these measurements, using a digital correlator, the Brownian motion of the particles can be calculated. The relationship between the particle size and the Brownian motion can be calculated with the Stokes-Einstein equation:

$$D_H = \frac{k \cdot T}{3 \cdot \pi \cdot \mu \cdot D} \quad , \qquad \textbf{(2.5)}$$

where k is the Boltzmann constant ($1.38065 \cdot 10^{-23}$ $J \cdot K^{-1}$), T the absolute temperature (K), μ the viscosity and D the diffusion coefficient. The size that is measured by DLS is called the hydrodynamic diameter (D_H) and is defined as "the size of hypothetical hard sphere that diffuses in the same fashion as that of the particle being measured" [39]. The D_H depends not only on the size of the particle "core", but also on the layer of tightly bound water molecules, the particle surface structure, the particle concentration, and the type of ions in the medium. This means that the D_H is larger than the size measured by electron microscopy [40].

The Nano ZS has one light source, i.e., a red helium-neon-laser, for detecting purposes. A conventional cell was used for particle size measurement (distribution in volume). The theoretical range in which this equipment can measure the particle size distribution is between 0.6 and 6000 nm [39].

2.2.3 Zeta potential

The zeta potential, also known as ζ-potential or electrokinetic potential, depends on the interfacial double layer around particles. The IUPAC defines the interfacial double layer as "the coulombic interaction of ions and the electrostatic interaction of interfacial molecules lead to particularly complex interfacial structures. The complex interfacial profiles can be approximated by two different layers with different physical properties, which are the Stern layer and the diffuse layer" [41]. Figure 2.4 represents the double layer around charged particles on the surface, where the distance to the surface of the particle, the different layers and the different potentials can be seen. In the Stern layer the ions are bound to the solid surface of the particle [42]. The diffuse layer consists of loosely ions. When a particle moves, a thin layer of liquid moves together with the particle. This layer is called the hydrodinamically stagnant layer and is located from the solid surface to the theoretical slipping plane. The slipping plane refers to the shear plane between the hydrodinamically mobile and immobile fluid [42].

From a theoretical point of view, the zeta potential is the difference in the electric potential between the slipping plane and a point in the bulk fluid (see Figure 2.4). The magnitude of the zeta potential (either positive or negative) gives an indication of the potential stability of the colloidal system. Usually, particles with magnitudes of zeta potential higher than 30 mV are considered to be stable [39].

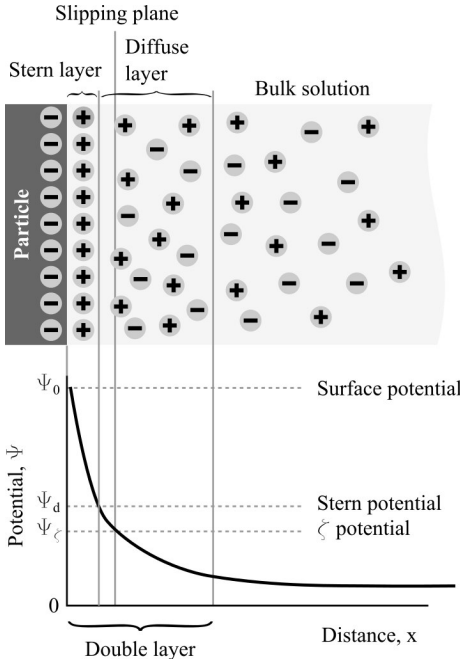

Figure 2.4. The interfacial double layer around charged surfaces.

The equipment used within this PhD thesis to measure zeta potential is a Nano ZS from Malvern. This equipment determines the electrophoretic mobility using laser doppler velocimetry. The electrophoretic mobility can be defined as the velocity of a particle in an electric field. With these data, the Henry equation can be applied to obtain the zeta potential:

$$U_E = \frac{2 \cdot \varepsilon \cdot z \cdot f\left(R \cdot L_{DL}^{-1}\right)}{3 \cdot \mu}, \qquad \textbf{(2.6)}$$

where U_E is the electrophoretic mobility, z the zeta potential, ε the dielectric constant, μ the viscosity, L_{DL} the length of the electrical double layer and R the particle radius. The term $f(R \cdot L_{DL}^{-1})$ is known as the Henry's function and usually takes values between 1 and 1.5 [39]. The term electrophoresis refers to the movement of charged particles (particles plus hydrodinamically stagnant layer) relative to the bulk fluid when an electric field is applied. The electrophoretic mobility is assessed using laser Doppler velocimetry to measure the velocity of the particles under an electric field. The zeta potential cell used in these analyses is presented in Figure 2.5 [39], where the two electrodes inducing the electric field are shown.

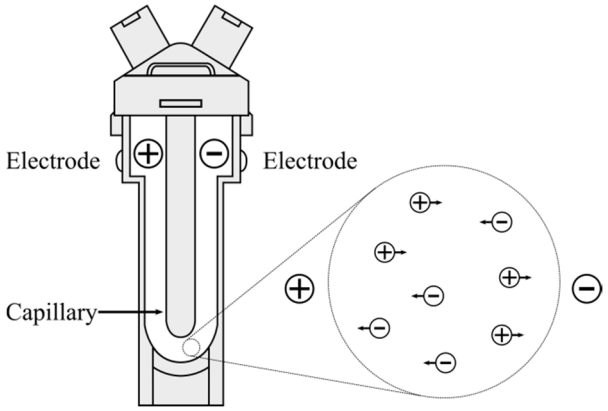

Figure 2.5. Folded capillary cell used in the zeta potential measurements [39].

2.2.4 Gas physisorption

Physical adsorption is described by the IUPAC as a phenomenon where the forces involved are intermolecular (van der Waals forces), which do not involve a significant change in the electronic orbital patterns of the species involved [41]. The extent of the adsorption of gases by solids rises with increasing pressure and decreasing temperature. The adsorption isotherms usually follow one of the curves depicted in Figure 2.6 [43]. Type I isotherm is typical for microporous materials with small external surface areas. Type II isotherm is representative of non-porous or macroporous materials. Types III and V are rarely found, and they are associated with weak adsorbent-adsorbate interactions. In the adsorption isotherm types IV and V, the adsorption and desorption curves are different. This phenomenon is known as hysteresis and is associated with capillary condensation in mesoporous structures. The point B in Figure 2.6 (types IV and V) indicates the stage at which an adsorbed monolayer is normally complete and multilayer adsorption begins. Type IV isotherm is characteristic of mesopores materials. Type VI isotherm is representative of stepwise multilayer adsorption on a uniform non-porous structure [43].

In gas physisorption, the isotherm curve can be subdivided into three regions: 1) gas molecules are adsorbed at the sites of the largest adsorption potentials (i.e., micropores are filled earlier than mesopores); 2) multilayer adsorption and 3) capillary condensation. The actual gas pressures where these three regions are exhibited depend on the solid material, temperature and type of adsorbate.

Pores are classified by the IUPAC as micropores (below 2 nm), mesopores (between 2 and 50 nm) and macropores (above 50 nm). The sorption behavior is different depending on the pore size [44]. Macropores are so wide that their walls can be considered as flat surfaces, while the sorption in micropores is ruled by the interaction between gas molecules and pore walls. In the case of mesopores, the behavior of the gas molecules is influenced by the gas-wall interplay as well as the interaction between the gas molecules. Condensation in mesopores can occur at a lower pressure than the saturation pressure of

the gas molecules (P_0). A representation of the adsorption potential in the three types of pores is shown in Figure 2.7 [44].

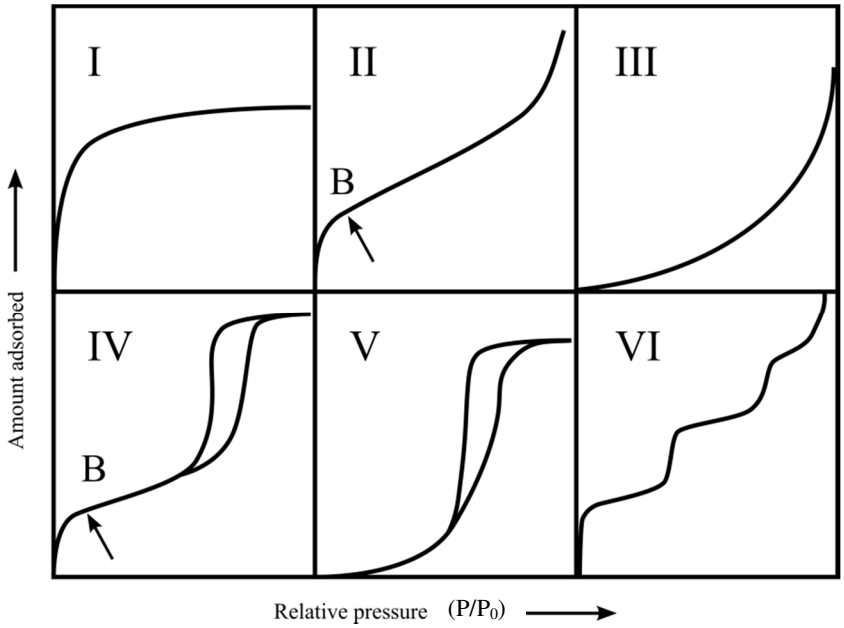

Figure 2.6. Types of physisorption isotherms [43].

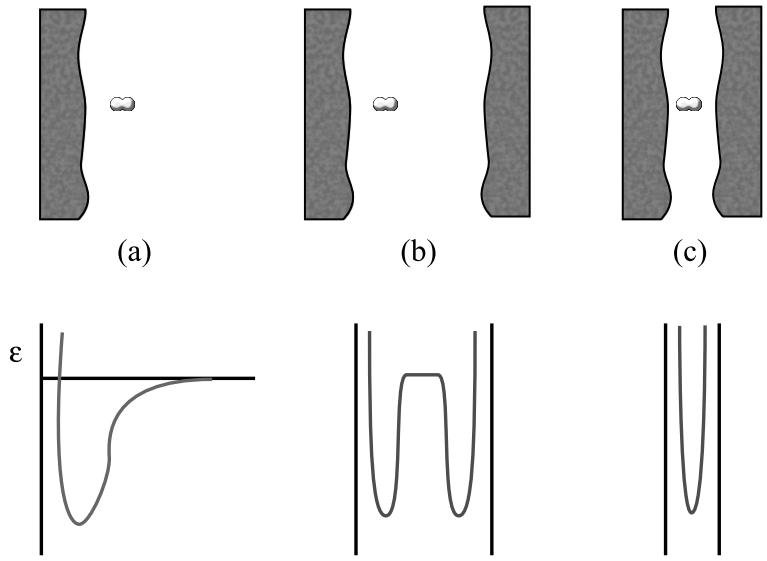

Figure 2.7. Adsorption potential (ε) on a) planar (or macropores) surface, b) mesopores and c) micropore [44].

The specific surface area and porosity of silica samples were determined using a Micromeritics TriStar 3000 equipment employing nitrogen as adsorbent at 77 K. Prior to the analysis, the samples were degassed for 240 min at 120 and 190 °C. From these

results the following parameters can be calculated: BET specific surface area (SSA_{BET}), external specific surface area (SSA_E), microporous (or internal) specific surface area (SSA_{MP}), average particle size (d), pore size in the adsorption branch (d_{p_A}), pore size in the desorption branch (d_{p_D}) and pore size distribution (PoSD). These parameters are calculated with the Tristar II software [45] using the methods described below.

2.2.4.1 BET Specific surface area

The most commonly used specific surface area determined by gas physisorption is the SSA_{BET}, which is based on the theory of Brunauer–Emmett–Teller [46]. They proposed a method to estimate the volume of gas adsorbed on a solid as a monolayer.

As was mentioned previously, during the gas adsorption, the more energetic sites are covered first. Before the adsorbate completely covers the surface, the formation of a second adsorbed layer starts. Actually, a pressure where only one layer completely covers the surface of the solid does not exist. However, the BET theory makes the theoretical estimation of the number of gas molecules required to form a monolayer possible. Brunaer, Emmett and Teller proposed the following equation for describing the multilayer gas on solid materials [46]:

$$\frac{P}{V_a(P_0-P)}=\frac{1}{V_mC}+\frac{C-1}{V_mC}\left(\frac{P}{P_0}\right) \quad \text{or} \quad \frac{P/P_0}{V_a(1-P/P_0)}=\frac{1}{V_mC}+\frac{C-1}{V_mC}\left(\frac{P}{P_0}\right), \qquad \textbf{(2.7)}$$

where V_a is the volume of gas adsorbed, V_m the volume of gas adsorbed when the entire surface is covered by a monolayer, P/P_0 is the relative pressure (i.e., P the pressure of the adsorbate and P_0 saturation pressure) and C is the BET constant. For most solids, when the isotherm data are plotted using Eq. (2.7), it results in a straight line between 0.05 and 0.3 P/P_0. Micromeritics software establishes a linear regression between 0.05 and 0.20 resulting in:

$$a=\frac{1}{V_mC} \quad \text{and} \quad b=\frac{C-1}{V_mC}, \qquad \textbf{(2.8)}$$

operating:

$$V_m=\frac{1}{a+b}, \qquad \textbf{(2.9)}$$

where a and b are the intercept and slope of the line. Therefore, the SSA of gas monolayer can be calculated using:

$$SSA_m = SSA_{BET} = \frac{V_m P}{RT} N_A CSA = \frac{1}{a+b} \frac{P}{RT} N_A CSA \ , \qquad \textbf{(2.10)}$$

where CSA is the cross-sectional area with a value of 0.162 nm^2 for nitrogen.

When sufficient volume of gas has been adsorbed to form a monolayer on the solid, the fraction of surface, $(\theta_0)_m$, not covered by any molecule is dependent on the BET constant and is given by [44]:

$$(\theta_0)_m = \frac{\sqrt{C}-1}{C-1}, \qquad \textbf{(2.11)}$$

for C values around 100, the fraction of surface not covered when sufficient gas has been adsorbed to form a monolayer is 0.091.

In the adsorption region of relative pressures close to a completed monolayer (0.05-0.3), the BET theory and experimental isotherms have a good agreement because the ratio V_a/V_m is close to unity for C values between 3 and 1000 [44], resulting in a powerful and convenient method for the estimation of surface area. Although the BET theory is the most extended and useful method to estimate the SSA, some of the assumptions made are not exempt of criticism, such as: 1) the surface is considered energetically homogenous; 2) the influence of lateral adsorbate interactions is ignored; and 3) the heat of adsorptions of the second and higher layers is assumed to be equal to the heat of liquefaction [44]. The BET equation fails to predict the adsorption behavior at high relative pressures (> 0.3) because these suppositions are not valid anymore. Furthermore, the BET model is not appropriate for microporous adsorbents, neither for solids with mesoporosity between 2 and 4 nm, because it is difficult to separate the process of mono-multilayer adsorption from micropore filling [4,44,47-49].

2.2.4.2 t-plot method

The t-plot method is based on the concept of a homogenous statistical thickness (t) of the adsorbate on the adsorbent surface. Although the thickness of the adsorbate layer is never uniform, constant film thickness is usually assumed. The monolayer depth of a closely packed hexagonal layer of nitrogen molecules is considered to be 3.54 Å [44]. Therefore, the statistical thickness of the adsorbed film is:

$$t(\text{Å}) = 3.54 \cdot n_m = 3.54 \frac{W_a}{W_m}, \quad \textbf{(2.12)}$$

where W_a is the weight adsorbed and W_m is the necessary weight adsorbed to form a monolayer on the adsorbent. The ratio W_a/W_m represents the theoretical value of the number of monolayers covering the adsorbent. Modifying this equation using the liquid volume and the surface area results in:

$$t(\text{Å}) = \frac{V_{liquid}}{SSA} = \frac{V_g\left(\frac{cm^3\,STP}{g}\right) \cdot \rho_F\left(\frac{cm^3\,liq}{cm^3\,STP}\right)}{SSA\left(\frac{cm^2}{g}\right)} \cdot 10^8 \frac{\text{Å}}{cm}, \quad \textbf{(2.13)}$$

where V_{liquid} is the volume of liquid adsorbed, V_g the volume of gas adsorbed and ρ_F the density factor between the gas and liquid nitrogen with a value of 0.0015468; STP refers to standard temperature and pressure (i.e., 0 °C and 1 bar).

The t-plot method is based on the comparison of an isotherm of microporous materials with a standard type II isotherm (i.e., as exhibited by a non-porous or macropores adsorbent) [50,51]. De Boer [51] obtained a master t-curve for nitrogen at 77 K identical for a wide variety of adsorbents, provided no capillary condensation occurs and no narrow pores are present. This curve is commonly used as a reference curve for texture determinations and can be described perfectly by the equation of Harkins and Jura [52] in the P/P_0 range of 0 to 0.75, where the quantity adsorbed is related to the statistical thickness of the adsorbed film.

$$\log\left(\frac{P}{P_0}\right) = 0.034 - \frac{13.99}{t^2} \ . \quad \textbf{(2.14)}$$

This equation can also be expressed as:

$$t\,(\text{Å}) = \sqrt{\frac{13.99}{0.034 - \log\frac{P}{P_0}}} \ . \quad \textbf{(2.15)}$$

An example of the adsorption isotherm and t-plot curve of a material with microporosity and mesoporosity is shown in Figure 2.8 [44].

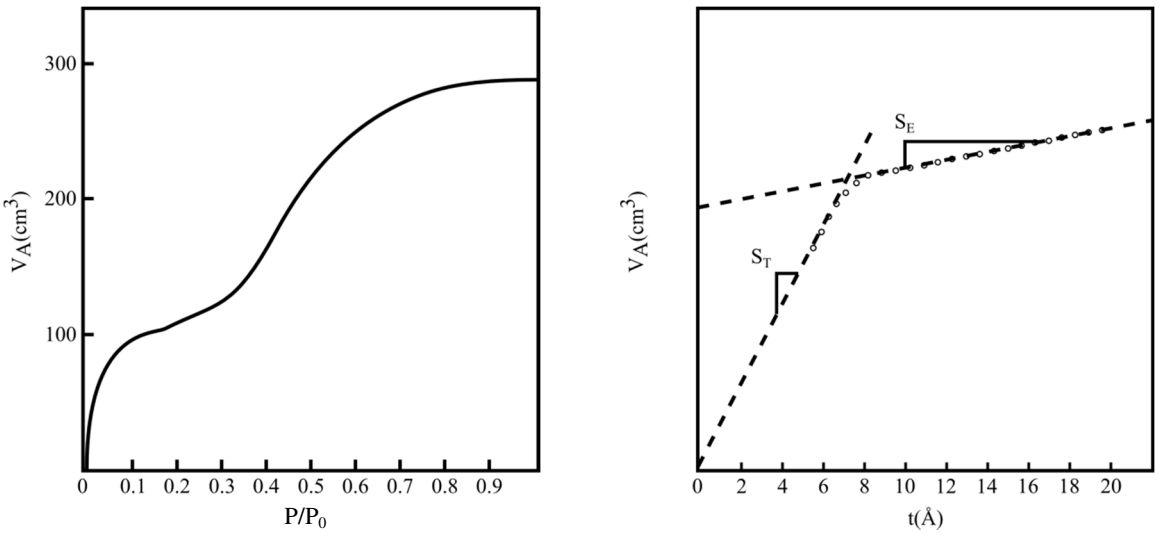

Figure 2.8. Adsorption isotherm and t-plot curve of a micro and mesoporous material [44].

At the beginning of t-plot curve (i.e., small values of t), its slope (S_T) is related to the adsorbed layer within large pores and complete filling of smaller pores. The total specific surface area (SSA_T) can be determined as follows:

$$SSA_T(m^2/g) = S_T \cdot \rho_F . \quad \textbf{(2.16)}$$

Likewise, the SSA_E of the wide pores (without taking into account the micropores) is obtained from the slope of the upper linear portion of the t-plot (S_E).

$$SSA_E(m^2/g) = S_E \cdot \rho_F . \quad \textbf{(2.17)}$$

S_E is related to the development of a statistical thickness in all pores except in the micropores, which are filled at lower values of t, in other words, at lower P/P_0 values. The difference between the two areas (S_T and S_E) is the area in the micropores (SSA_{MP}).

$$SSA_{MP} = SSA_T - SSA_E . \quad \textbf{(2.18)}$$

Without sufficient data points at low relative pressures, the S_T cannot be calculated. In these cases, the SSA_{BET} is used to estimate the SSA_{MP}:

$$SSA_{MP} = SSA_{BET} - SSA_E . \quad \textbf{(2.19)}$$

The software of the equipment TriStar 3000 uses the t-plot method to determine the SSA_E. The linear portion used to obtain the SSA_E is between 0.35 and 0.50 nm (default values specified by the software). This range starts when the theoretical values of the gas monolayer (0.354 nm for N_2) is reached and finishes shortly afterwards. Figure 2.9 shows an example of a t-plot curve where the thickness range between 0.35 and 0.5 was used to obtain the SSA_E.

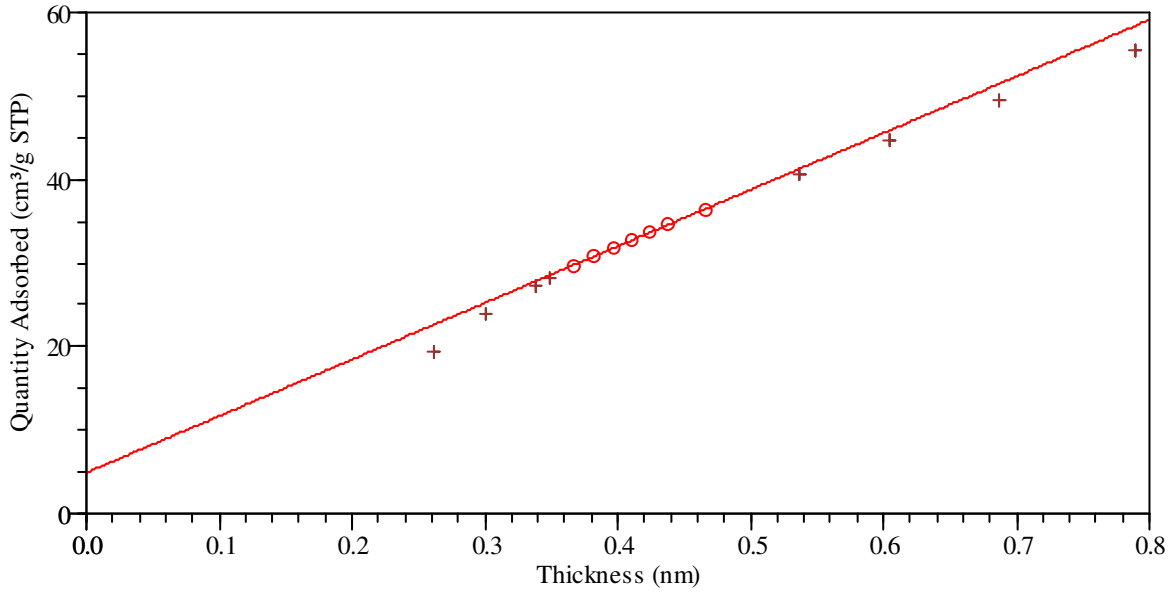

Figure 2.9. Example of the t-plot curve using a t range between 0.35 and 0.5 nm.

STP refers to standard temperature and pressure.

2.2.4.3 Average particle size calculated from the specific surface area

The mean particle size can be calculated from the geometrical relationship between surface area and mass:

$$d\ (nm) = \frac{6000}{SSA \cdot \rho}, \qquad \textbf{(2.20)}$$

where d is the mean particle size of nano-silica considering spherical particles (nm), ρ the density of the material, which is 2.2 (g/cm^3) for nano-silica, and SSA the surface area (m^2/g). This particle size is an average value considering that the particles are spherical and not porous. In the case that the clusters formed by the grouping of non-porous primary particles are present, and the porosity of the clusters is due to the assembly of the primary particles, the particle size of the primary particles could be calculated using Eq. (2.20).

2.2.4.4 BJH Model

Barret, Joyner and Halenda [53] proposed a method for calculating the pore size distribution (PoSD) from the isotherm data using the Kelvin equation and the thickness of the adsorbed layer, known as the BJH method. The Kelvin equation [54] relates the pore size with critical condensation pressure (also known as capillary condensation) in the mesopores.

$$\ln\left(\frac{P^*}{P_0}\right) = -\left(\frac{2\cdot\gamma\cdot\nu\cdot\cos\alpha}{R\cdot T\cdot R_m}\right), \qquad \textbf{(2.21)}$$

where P* is the critical condensation pressure, γ the surface tension of the liquid, ν the molar volume of the condensed liquid, α the contact angle between the solid and the condensed phase, R_m the mean radius of curvature of the liquid meniscus, T the temperature (77 K for nitrogen) and R the ideal gas constant.

The BJH method is based on an imaginary emptying of condensed liquid in the pores. A pore filled with condensed liquid can be described with three zones: the core, the adsorbed layer and the walls of the pore [45]. The core evaporates all at the same time when the critical pressure, which is calculated using the Kelvin equation, for that pore radius is reached. The adsorbed layer is composed of adsorbed gas that is removed stepwise with each pressure step; the thickness of this layer can be defined by Equation (2.15).

The BJH method is one of the most common methods used to determine the PoSD because of its simplicity. However, it presents several drawbacks. 1) In micropores the concept of capillary condensation is no longer valid [44,48]. That is because the Kelvin equation does not consider the influence of the adsorption potential (see Figure 2.7) on the position of the pore condensation transition [44], and also because it is (erroneously) assumed that the pore fluid has the same properties as the bulk fluid. 2) For pores narrower than 10 nm curvature effects should be taken into account, which means that the statistical thickness should not be used [44]. 3) When the adsorbent has a random distribution of interconnected pores, the tensile strength effect (TSE) occurs, resulting in a different behavior for the adsorption and the desorption branch, which abruptly closes the hysteresis. The impact of the forced closure due to TSE can be even higher if pore network effects occur and wider pores have to be emptied through narrower pores. A comparison between the PoSD obtained from the adsorption and desorption branch can be used as a criterion to assess the nature of this phenomenon [55]. Pore size distribution studies using the BJH method concluded that the this method underestimates the pore size for pores narrower than 10 nm [44,56].

2.2.4.5 Analysis conditions

The olivine nano-silica samples were dried at 105 °C just after they were produced and stored in closed plastic containers. The gas physisorption equipment was employed with liquid nitrogen at 77 K (boiling point of N_2). The evacuation conditions (temperature and time) were studied to find the optimum conditions for olivine nano-silica. Initially, the temperature chosen in the analyses was 120 °C, using a low temperature to degas the sample as was proposed by Lieftink [30]. Later on, a higher temperature (i.e., 190 °C) was used in order to be sure that the physically adsorbed water was removed [5]. In addition, analyses of the same silicas after two years were performed to check the evolution of the dried nano-silica with time.

The influences of these parameters on the SSA_{BET} of the olivine nano-silica are collected in Table 2.3, where STD refers to the standard deviation, RSD to the relative standard deviation and variation to the change between the same nano-silica sample, but at two different conditions. The pretreatment conditions with sample NS-17 show that the SSA_{BET} remains constant once the evacuation time is above 240 minutes at 120 °C. Therefore, 240 minutes can be considered the optimum time. It can also be observed that there is a marked decrease (38%) in the SSA_{BET} when the silica was measured shortly after the preparation and two years later using the same conditions. The evacuation temperature affects the SSA_{BET} as well, resulting in higher surface areas (increase between 17 and 31%) at 190 °C than at 120 °C. The repeatability of the analysis was studied analyzing the samples at the same conditions between 3 and 5 times, showing an average and a maximum RSD of 2% and 5%, respectively.

2.2.5 Positron annihilation lifetime spectroscopy

The IUPAC [41] defines a positron as a positively charged electron and positronium as an atom-like pair of particles consisting of a positron and an electron. Positron annihilation lifetime spectroscopy (PALS) is a characterization technique to determine the pore size of materials. Using quantum mechanical models [57,58], information about the pore size can be obtained from the PALS.

In porous materials, a fraction of energetic positrons injected into samples forms positroniums (Ps) [59]. The ground state of positronium has two possible configurations (i.e., para-Ps with the spins of the positron and electron antiparallel, and ortho-Ps with parallel spins) depending on the relative orientation of the spins of the electron and positron. In addition to positroniums, free positrons co-exist in porous materials. The positrons annihilate around 450 ps [59]. The singlet para-Ps has a mean lifetime of 125 ps and decays preferentially into two γ-ray photons of 511 keV [59]. The ortho-Ps will self-annihilate into γ-rays around 140 ns [60]. However, when they are located within pores, their lifetimes are shortened by the effect of the molecular electrons of the wall pores.

Once the lifetimes of ortho-Ps are known, the pore size can be determined using the Tao-Eldrup model:

$$\tau_{o-Ps} = 0.5\left[1 - \frac{R}{R+\Delta R} + \frac{1}{2\cdot\pi}\cdot\sin\left(\frac{2\cdot\pi\cdot R}{R+\Delta R}\right)\right]^{-1}, \qquad \textbf{(2.22)}$$

where $\tau_{o\text{-}Ps}$ is the lifetime of ortho-Ps in ns, 0.5 is a constant value in nanoseconds, R is the pore size and ΔR is the thickness of homogenous electron layer in which the ortho-Ps annihilate.

Table 2.3. Influence of the evacuation time and temperature on the SSA_{BET} of several number of analyses.

Samples	Evacuation time (min)	Evacuation temperature (°C)	SSA_{BET} (m^2/g)	STD (m^2/g)	RSD (%)	Variation (m^2/g)	Variation (%)
NS-17	140	120	216.9	10.7	4.9	-	-
	240	120	275.9	5.0	1.8	-	-
	900	120	277.9	3.6	1.3	-	-
	240[1]	120	171.8	1.7	1.0	-104.1[2]	-37.7
NS-HP	240	120	363.0	8.0	2.2		
	240	190	424.5	12.0	2.8	61.5[3]	16.9
NS-14-3F	240	120	178.4	-	-		
	240	190	233.3	-	-	54.9[3]	30.8
NS-14-4F	240	120	270.6	-	-		
	240	190	323.9	-	-	53.3[3]	19.7
NS-14-5F	240	120	291.0	-			
	240	190	341.7	6.6	1.9	50.7[3]	17.4
NS-14-6F	240	120	263.2	-	-		
	240	190	343.1	6.7	2.0	79.9[3]	30.3

[1]This analysis was performed two years after the silica was prepared. [2]The variation for this sample is the difference between the SSA_{BET} degassed at 240 minutes two years after the sample was prepared and after the sample was produced. [3]The variation for this sample is the difference between the SSA_{BET} degassed at 120 °C and 190 °C.

The ^{22}Na radioisotope, generally employed as a positron source in the laboratory frame, emits a positron together with a 1.27 MeV birth γ-ray. The positron implanted into the sample annihilates with the electron, providing 511 keV annihilation γ-rays. The average lifetimes at individual positron states are measured as the time difference between the birth and 511 keV annihilation γ-rays. The analysis of PALS was done by Dr. Sato, who has used the PALS technique in several studies with nano-silica [39,40]. The PALS

equipment used in this PhD thesis consists of a positron source and a digital oscilloscope-based system (LeCroy WaveRunner 6050) employing photomultiplier tubes (HAMAMATSU H6610) with BaF_2 scintillators (Oyo Koken) at room temperature. The time resolution of the system is 180 ps full width at the half maximum (FWHM). For each spectrum at least $1.0 \cdot 10^6$ coincident counts are registered. After subtracting the background, positron lifetime spectra are numerically analyzed by the POSITRONFIT code.

Figure 2.10 shows a PALS spectrum of olivine nano-silica. A PALS spectrum contains the following lifetime constituents: 1) a component related to the annihilation of free positrons with a lifetime around 450 ps; 2) a component related to the annihilation of o-Ps in vacuum with a lifetime around 140 ns; and 3) components related to the annihilation of o-Ps in pores with lifetimes between 10 and 30 ns depending on the pore size (they can be seen in Figure 2.10).

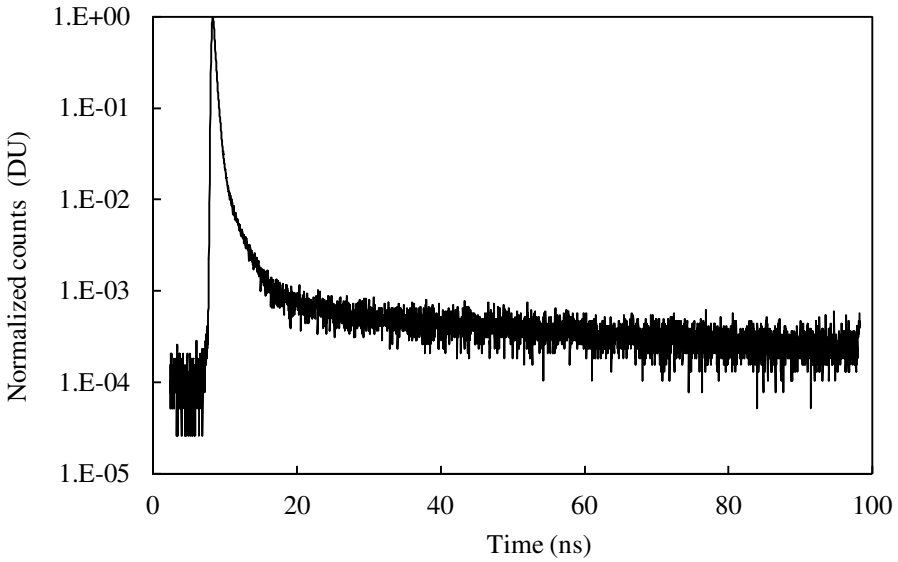

Figure 2.10. Example of PALS spectrum.

The pore range that the PALS technique can measure depends on the model used. The Tao-Eldrup model [57,58] gives accurate pore sizes up to approximately 1 nm radius [61]. Even though several models have been proposed to determine the pore size of materials above 2 nm [61-64], at the moment, there are no models widely accepted that can accurately assess the mesoporosity of materials.

2.2.6 Nuclear magnetic resonance spectroscopy

Nuclear magnetic resonance spectroscopy (NMR) is a characterization technique that uses the magnetic properties of certain atomic nuclei to determine the physical and chemical properties of the atoms surrounding the magnetic nuclei. The NMR active isotope (the

atomic nucleus) used in this research is ^{29}Si with a spin number of 1/2. The most important parameter determined by NMR is the chemical shift [65]. The chemical shift (δ) refers to the variations of nuclear magnetic resonance frequencies of the active isotope (in this case ^{29}Si) due to the distribution of electrons in the surrounding atoms. This parameter is sensitive to the bonding angles and bond lengths of the silica structure [66]. Thus, the different number of siloxane bridges and of hydroxyl groups can be established by NMR. Q^2, Q^3 and Q^4 are the silicon atoms with different number of siloxane bridges (see Figure 2.11). The chemical shift is related to a reference signal, which in the case of this research is tetra-methylsilane. Figure 2.11 shows an example of the ^{29}Si NMR spectra of the olivine nano-silica, with the area of the peaks of Q^2, Q^3 and Q^4.

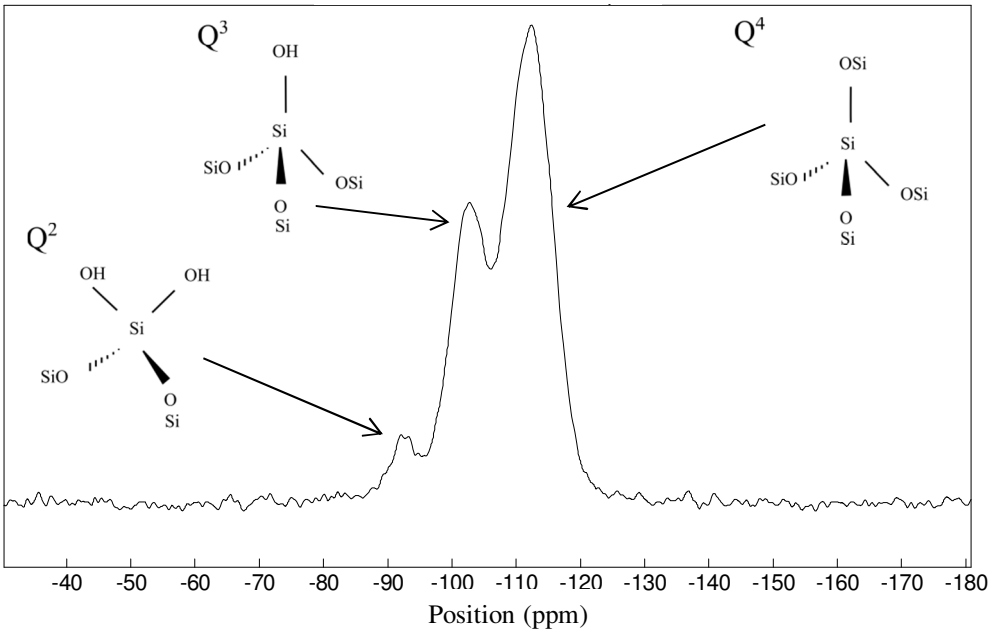

Figure 2.11. Example of the ^{29}Si NMR spectra of the olivine nano-silica.

From the Q values, the silanol content, which is one of the main parameters of nano-silica particles, can be calculated following the procedure described by Leonardelli [67]:

$$f_g = \frac{Q^2}{Q^2 + Q^3}, \tag{2.23}$$

$$f_s = \frac{Q^2 + Q^3}{Q^2 + Q^3 + Q^4}, \tag{2.24}$$

$$\alpha_{OH} = f_s \cdot \frac{1 + f_g}{SSA_{BET}} \cdot \frac{N_A}{M_{SiO_2} + M_{OH} \cdot f_s (1 + f_g)}, \tag{2.25}$$

where f_g is the fraction of Q^2 silanol sites, f_s the fraction of all silanol sites, N_A the Avogadro's number, SSA_{BET} the specific surface area determined by the BET method [46], M_{SiO_2} the molar mass of silica (i.e., 60.06 g/mol), M_{OH} the molar mass of hydroxyl groups (i.e., 9 g/mol) and α_{OH} the silanol content (OH/nm^2).

The NMR analyses were carried out at the University of Valencia. The equipment used was a 400 Bruker Avance III spectrometer, equipped with a wide bore magnet of 9.4 T, and a 4 mm DVT probe, which operated at 79.5 MHz. The spinning rate was 10 KHz and the magic angle was adjusted using a sample of KBr. The ^{29}Si MAS spectra have been acquired at 300 K with a $\pi/2$ pulse of 4 μs and a relaxation delay of 30s. The sweep width was 64 KHz, and the numbers of scans 2900. No proton decoupling was applied.

Chapter 3. The dissolution of olivine for nano-silica production – experimental data

3.1 Introduction

The study of the kinetics of dissolution of olivine in acid is addressed in Chapters 3 and 4. In Chapter 3, the experimental data of the dissolution of olivine is presented, and in Chapter 4 a kinetic model is proposed. The study of the dissolution of olivine is essential for the large-scale production of nano-silica for two reasons: 1) for the industrial production of olivine nano-silica, as for any industrial process, the assessment of the reaction kinetics is needed in order to predict the time required to achieve a desired conversion degree; and 2) the properties of olivine nano-silica (i.e., specific surface area, aggregated/agglomerated state, etc.) depend on the kinetics of the dissolution of olivine [30]. The production of nano-silica via the olivine dissolution has not been industrially performed yet and is still under development. Hence, data about this production process are limited, Jonckbloedt [12,25] being the only researcher who studied the dissolution of olivine under the olivine nano-silica conditions. Jonckbloedt's kinetic model of the dissolution of olivine will be further discussed in Chapter 4, but for the purpose of this chapter it is sufficient to mention that he did not consider the specific surface area of olivine, nor the chemical and mineralogical composition of the dunite employed.

As mentioned in Chapter 1, olivine refers to the mineral $(Mg,Fe)_2SiO_4$ and dunite refers to a rock where at least 90% of the volume consists of olivine. The remaining 10% of dunite ores can consist of pyroxenes, amphiboles, micas, carbonates, serpentines, etc.

The dissolution of olivine in acid follows Eq. (1.4). The kinetics of the dissolution of olivine depends on the surface area of olivine, hydrogen ion activity and temperature. In many dissolution studies, pure olivines were used [9,11,19,22,24]. These olivines were handpicked; subsequently, they were thoroughly cleaned to remove any fine materials from the surface. However, for the production of olivine nano-silica [12], commercial dunite rocks –and sometimes even a by-product material with an olivine content lower than 90 wt.% (see Greek dunites in Chapter 2)– are employed because this process focuses on the industrial production of silica. The commercial dunites contain other components besides olivine. Therefore, the determination of the specific surface area associated with the olivine and the mineralogical composition of the dunite is required for the dissolution studies. The mineralogical characterization should focus on: 1) the content of minerals that consume a considerable amount of acid (besides olivine), such as carbonates; 2) the content of minerals that will not react with acid, or will react much slower than olivine; and 3) the olivine content. The lack or inadequate characterization of the dunite rock could lead to an incorrect kinetic model.

The first part of the study of the olivine dissolution consists of three items: 1) the material characterization focusing on the specific surface area (SSA) and the mineralogical composition; 2) the surface characterization of olivine before and after dissolution; and 3) the experimental data about the dissolution curves. The olivine content, the SSA calculated according to Brantley [68] and the information about the silica layer obtained in this chapter will be used in Chapter 4, where a kinetic model of the olivine dissolution for nano-silica production will be proposed.

3.1.1 Specific surface area and roughness factor

The specific surface area of olivine is one of the main parameters influencing the olivine dissolution kinetics so its determination is basic for the study of the dissolution kinetics. A geometric specific surface area (SSA_G) can be estimated from the particle size distribution of olivine assuming the grains are spherical (see Eq. (2.4)). The ratio between the surface area and the geometric surface area has typically been called the surface roughness [69,70]. A roughness factor (λ), also named surface roughness, can be calculated from a microscopic analysis technique (e.g. gas physisorption using the BET equation, SSA_{BET}) to estimate SSA and a macroscopic analysis technique (e.g. light scattering) to estimate SSA_G [69,71]:

$$\lambda = SSA/SSA_G \, . \tag{3.1}$$

The surface roughness is higher than unity because the elementary particles are usually not spherical and because some minerals are porous. In the case of porous materials, the surface area of a mineral grain can be expressed in terms of the external surface area, SSA_E, and internal surface area, SSA_I [68,71]:

$$SSA = SSA_E + SSA_I = SSA_G \cdot \lambda_E + SSA_I \, . \tag{3.2}$$

This equation can be applied to materials of varying grain size if the surface roughness and internal surface area are both assumed to be independent of the grain size. Brantley and Mellot [68] proposed an equation which can be used to estimate either the SSA as a function of the grain size for impurity-free, laboratory-ground primary silicates without significant porosity or the external surface area of porous silicates:

$$\log SSA_{Br} = b + m \cdot \log(d) \, , \tag{3.3}$$

where SSA_{Br} is the specific surface area in cm^2/g, b is 5.2 ± 0.3, m is -1.1 ± 0.2 and d is the grain size in μm, in the case of olivine. This equation considers that λ is slightly dependent on the grain size.

3.1.2 Literature review on the olivine properties in dissolution studies

Some properties of olivines, such as the forsterite/fayalite (Mg_2SiO_4/Fe_2SiO_4) ratio, olivine content, specific surface area and roughness factor, used by different authors, are summarized in Table 3.1. The roughness factor (λ) of the olivines studied is in the range of 2 to 67 (see Table 3.1), while the roughness factor of freshly crushed silicates should be around 7 [71]. There are four studies where a roughness factor above 20 was reported [68,72-74]. These high roughness factors are the result of the high SSA_{BET} due to measurement errors or because the materials have a higher SSA_{BET} than expected. The measurement errors can be attributed to either the gas used in the physisorption analysis or the magnitude of the surface area. Analyzing samples using nitrogen as an adsorbate results in values 40% higher than the values obtained using krypton [68]. When the total surface area of the sample analyzed is smaller than 5 m^2 and nitrogen is used, problems concerning the accuracy arise [75]. On the other hand, the high SSA_{BET} can be due to 1) the presence of porous materials, 2) fine particles or 3) bodies with cracks and etch pits. The SSA_{BET} is most affected by the presence of porosity, which can be due to the olivine itself or to the presence of other porous minerals. Most likely, the presence of other porous minerals leads to porosity because, as was stated by Brantley [68], olivine is usually not mesoporous or microporous [68]. When, for instance, traces of porous minerals are present, the SSA_{BET} of the material is much higher than the SSA_{BET} of the olivine, whereas it does not affect the SSA_G. Furthermore, Brantley [68] proved the BET method is not always a reliable technique for assessing the SSA of olivine. Thus, if λ of the freshly crushed olivine is higher than 10, a careful determination of the material should be carried out to demonstrate the absence of other minerals that could contribute more to the SSA_{BET} than the olivine. Another possibility would be to use Eq. (3.3) to determine the SSA_{Br} related to olivine of a dunite rock.

The most probable reason for the high λ for the olivines studied by Grandstaff [18], Brantley [68] and Haug [74] is the presence of other minerals besides olivine that are porous. In the case of the olivine used by Herk [73], it is likely to be due to the pre-dissolution step to etch the mineral.

The mineral composition of olivine (forsterite/fayalite ratio) is also a key factor of the dissolution of olivine, since fayalite is six times more reactive than forsterite [21]. However, because the forsterite content of olivine is about 92% (normally expressed as Fo92) in most studies, this factor has not been taken into account in the dissolution rate. In the case of Norwegian olivine, the dunite rocks have a forsterite content in the range of

92 to 93% [76]. The forsterite content can be estimated from the X-ray diffraction data [77] using:

$$\text{Fo}\ (\%) = 4233.91\text{-}1494.59 \cdot d_{130} \pm 4\%\,, \qquad \textbf{(3.4)}$$

where d_{130} is the position of the 130 peak in Å. The Fo calculated from Eq. (3.4) is very sensitive to position shifts of the peak, having an error of 4%.

Table 3.1. Summary of the literature data on the properties of olivine used in the dissolution studies.

Author	Olivine[1]	Fo[2] (%)	Hand[3]	m_{ol} (%)	d (μm)	d_A (μm)	Gas	SSA_{BET} (cm^2/g)	λ
Grandstaff [18]	HB	81	NO	95	74-194	134	-	9300	66.7
van Herk [73]	DW	93	NO	99.9	105-125	115	N2	6300	38.8
Wogelius [21]	SCA	91	-	-	250-420	335	Kr	307	5.5
Jonckbloedt [25]	NO	93	NO	92.6	63-300	182	Kr	-	-
Awad [22]	SCA	91	YES	100	1 mm cubes	-	-	-	-
Chen [24]	SCA	91	YES	100	75-150	113	Kr	340	2.0
Pokrovsky [9]	SCA	91	YES	100	50-100	75	Kr	800	3.2
Rosso [10]	GM	92	NO	-	250-350	300	N2	405	6.5
Oelker [11]	SCA	89	YES	100	50-100	75	Kr	800	3.2
Hänchen [19]	SCA	91	YES	100	90-180	135	N2	797	5.8
Olsen [20]	GM	92	NO	-	250-350	150	Eq. (5)[4]	528	4.2
Brantley [68]	SCA	-	-	-	250-500	375	Kr	329	6.6
Brantley [68]	TS	-	-	-	250-500	375	Kr	2340	46.9
Haug[5] [74]	NO[3]	93	NO	95	74-147	111	N2	4700	27.8

[1]Where HB stands for Hanauma Bay, Hawai; DW for Dreiser Weiher, West Germany; SCA for San Carlos, Arizona; NO for Norway; GM for Green Mountain, North Carolina; and TS for Twin Sisters Mountain, Washington. [2]Fo stands for forsterite content. d refers to particle diameter and d_A average particle diameter. [3] Hand refers to handpicked. [4]SSA was calculated using Eq. (3.3). [5]This olivine was not used in the dissolution studies, but it originates from Norwegian mines like the dunites used in this study.

3.2 Materials and methods

In this chapter, two types of olivine dissolution experiments are presented: 1) a set of experiments to assess the kinetics of the dissolution of olivine; and 2) a set of experiments to establish the extent of the olivine dissolution and the olivine content. In addition, surface characterization experiments after the dissolution of olivine were also conducted. The purpose of the surface characterization experiments was to study the surface of the

olivine grains, focusing mainly on the presence or absence of a silica layer on the olivine grains after the reaction with acids.

Olivine dissolution experiments were carried out around 50, 70 and 90 °C with crushed dunite rocks of different fractions in a vigorously stirred, thermostated reactor of one liter to evaluate its dissolution kinetics. The temperature was kept constant by circulating water from a thermostat through a double wall. Particularly, in the initial state of the experiments, the temperature was rather difficult to control for the most rapidly executed experiments, resulting in an oscillation of up to ± 3 °C for short time intervals. The reagents used were 500 ml of 3M sulfuric acid and the equivalent stoichiometric amount of olivine (previously dried). The concentration of hydrogen ions was determined by titration with a 0.05 M $Na_2B_4O_7$ solution at regular time intervals.

Two Norwegian dunite rocks were used in this study as was mentioned in Chapter 2. One was supplied by North Cape minerals (CRS), and the other one by Eurogrit (GL50). Dunite CRS and GL50 are commercialized as slag conditioner and as abrasive material, respectively. Both materials were analyzed by XRD, XRF, combustion infrared analysis, thermogravimetric analysis (TGA), laser light scattering (LLS) and nitrogen physisorption. Dunite GL50 was also characterized by scanning electron microscopy (SEM) in order to observe the texture and morphology of this material prior to dissolution and after dissolution with and without stirring. A Micromeritics TriStar 3000 device using nitrogen and with an evacuation time of 240 min at 120 °C was used for the gas physisorption analyses [43]. Two SEM devices were used: 1) a FEI XL-30 FEG-SEM equipped with a Schottky field emission gun operated at 20 keV and with an EDAX® energy-dispersive spectroscopy (EDS) device, and 2) a FEI Quanta 600 FEG-SEM with a Schottky field emitter gun (at voltage of 10 keV).

The particle size of CRS and GL50 as received was in the range of 63-2000 μm and 100-500 μm, respectively. Dunite CRS was cleaned to remove impurities and to obtain different fractions. The cleaning steps performed were: wet sieving, ultrasound (US) treatment with ethanol to remove the fines, and again wet sieving. This material was named CRS-US. Dunite GL50 was used without cleaning treatments because 1) this material had fewer impurities, and 2) for practical considerations in order to assess the validity of the developed kinetic model when using commercial dunites.

In order to determine the olivine content, the reactivity of both dunites was studied. This was performed at 90 °C in acidic solutions with a molar ratio of hydrogen ions to olivine two times higher than that required by stoichiometry (molar ratio of hydrogen ion to olivine, $R_{H/ol}$, around 8) in order to establish the olivine content. The reagents used were 500 ml of 3M sulfuric acid and approximately 60 g of dunite. The particle sizes of the dunites investigated were in the range 300-500 μm and 100-500 μm for CRS-US and GL50, respectively. The initial molar ratio of hydrogen ions to olivine was doubled to complete the reaction within short times. The reagents were kept together in the reactor

only long enough for all the olivine to be consumed and to minimize the reaction of the slow weathering silicates. The water evaporated during the reaction was around 9 g (1.5 g of water evaporated per hour) and was neglected, assuming a constant reaction volume. After the reaction, the residue was collected and weighed. This residue was cleaned 3 times with 500 ml of distilled water in order to remove any particles of colloidal silica. Subsequently, the residue was analyzed by XRD to check for the presence of olivine.

From these experiments, the olivine content (w_{ol}) in the dunites was calculated following:

$$w_{ol}(\%) = \frac{m_{ol}}{m_{du}}, \tag{3.5}$$

$$m_{ol} = n_{ol} \cdot M_{ol} = \left[n_{H^+con}(\text{mol}) - 2n_{MgCO_3}(\text{mol}) \right] \cdot M_{ol}, \tag{3.6}$$

where m_{ol} is the mass of olivine, m_{du} the mass of dunite, n_{ol} the number of moles of olivine, M_{ol} the molar mass of olivine, n_{H^+con} the number of moles of hydrogen ions consumed and n_{MgCO_3} the number of moles of magnesite.

The characterization of the olivine surface was performed by scanning electron microscope (SEM) using olivine GL50 with a particle size between 100 and 500 μm. A stoichiometric amount of this olivine reacted with 3M sulfuric acid at 90 °C for 3 hours. Three olivine samples were analyzed: one before the dissolution, one after the dissolution in an unstirred reactor and the third one after the dissolution in a vigorously stirred reactor. The conditions of the olivine dissolution in a vigorously stirred reactor are similar to the conditions employed in the experiments conducted to assess the kinetics of the dissolution of olivine.

3.3 Material characterization

3.3.1 Chemical and mineralogical composition

The forsterite content, calculated with Eq. (3.4), was 93.1, 91.7 and 93.8% for CRS, CRS-US and GL50, respectively, being in agreement with the range reported by Osland for Norwegian dunites [76]. Hereafter, these dunites are considered to be rich in Fo93 olivine. Table 3.2 lists the theoretical composition, the molecular formula and the molar mass of a Fo93 olivine, with and without part of the iron replaced with nickel. This table shows that the MgO content should be 51.6%, and that there should not be any loss on ignition (LOI) for a pure Fo93 olivine. However, the commercial dunites used in this study contain other minerals than olivine. Some of these minerals should be rich in aluminum and chromium (see Table 3.3). The nickel content is related to the olivine mineral, resulting in a chemical composition of $(Mg_{1.86}Fe_{0.133}Ni_{0.007})SiO_4$ for the olivine. GL50 and CRS-US

have similar contents of MgO and exhibit a similar LOI, meaning similar contents of olivine.

Table 3.2. Chemical composition of olivine Fo93 with and without replacement of nickel for iron.

Name	Formula	M (g/mol)	MgO	FeO	SiO_2	NiO	MgO	Fe_2O_3	SiO_2	NiO
Olivine (Fo93)	$(Mg_{1.86}Fe_{0.14})SiO_4$	145.11	51.65	6.94	41.41	-	51.26	7.65	41.10	-
Olivine (Fo93)	$(Mg_{1.86}Fe_{0.133}Ni_{0.007})SiO_4$	145.13	51.64	6.59	41.41	0.36	51.27	7.27	41.11	0.36

All concentrations are expressed in wt.%.

Table 3.3. Chemical composition of commercial dunites CRS, CRS-US and GL50.

Name	d (μm)	MgO	Fe_2O_3	SiO_2	Cr_2O_3	Al_2O_3	NiO	MnO	CaO	Na_2O	K2O	LOI	Other Oxides
CRS	63-2000	47.41	7.84	41.42	0.31	0.75	0.33	0.12	0.34	0.06	0.01	1.29	0.12
CRS-US	63-2000	47.59	8.28	40.96	0.33	0.64	0.35	0.11	0.29	0.04	0.07	1.19	0.15
CRS-US	300-500	48.46	7.9	40.67	0.25	0.65	0.36	0.10	0.2	0.02	0.05	0.89	0.45
GL50	100-500	48.78	7.4	40.91	0.26	0.52	0.35	0.10	0.09	0.02	0.04	0.73	0.80

Samples CRS-US was cleaned to remove the fines using ultrasounds.
All concentrations are expressed in wt.%.

The diffractograms of the samples CRS, CRS-US and GL50 are shown in Figure 3.1, where quartz was added as reference material to correct the difractogram displacement; for the sake of clarity only the range between 5 and 34 degrees (2θ) is shown. Olivine is the main mineral in dunites CRS, CRS-US and GL50 although there are other minerals present as well (see Table 3.4). These minor minerals are amphiboles (actinolite and hornblende), micas (phlogopite), serpentine minerals (chrysotile), chlorite, talc, carbonates and enstatite. Most of these minerals have been identified in other Norwegian dunites [74,78] and are the reason that the content of Al_2O_3 is between 0.5 and 0.8% and the LOI is between 0.7 and 1.3% (see Table 3.3). Magnesite was only found in the diffractogram of CRS; however, the combustion infrared analysis detected a small amount of carbonates (between 0.2 and 0.4%) in all the samples (see Table 3.5).

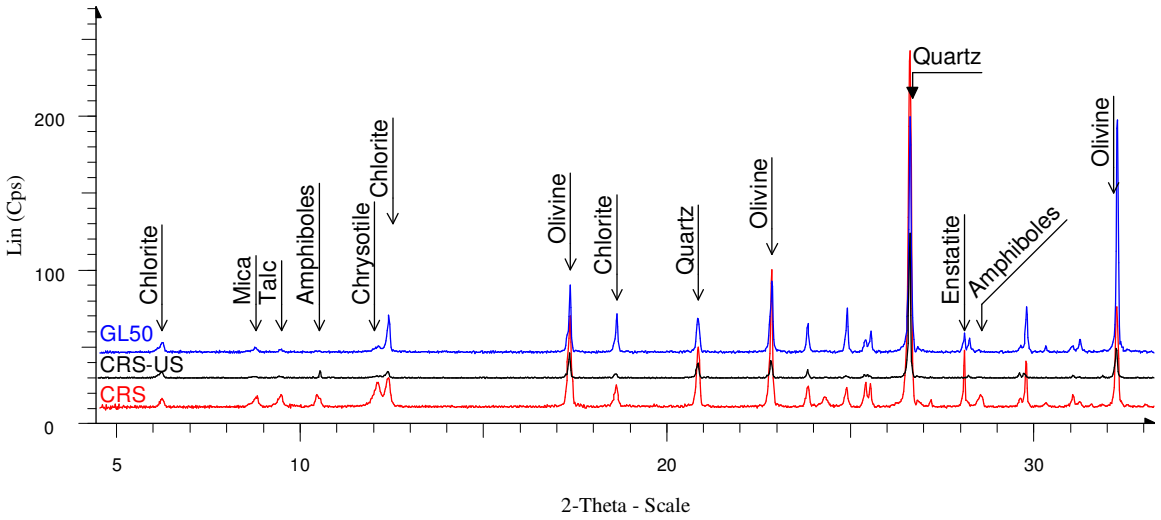

Figure 3.1. Diffractograms of dunites CRS, CRS-US and GL50 prior to dissolution.
Quartz was added as reference material.

Table 3.4. Mineralogical patterns found in the diffractograms (see Figures 3.1 and 3.4) of dunites CRS, CRS-US and GL50 before and after dissolution in acid.

Compound Name	PDF number	CRS	CRS-US	GL50	RE-CRS-US	RE-GL50
Olivine	01-079-1192	Y	Y	Y	N	N
Actinolite	00-041-1366	Y	Y	N	Y	Y
Hornblende	01-071-1062	Y	Y	N	Y	Y
Biotite	01-088-1899	Y	Y	Y	N	N
Phlogopite	01-085-2275	Y	Y	Y	N	N
Chrysotile	00-025-0645	Y	Y	Y	N	N
Chlorite, chromian	01-083-1381	Y	Y	Y	Y	Y
Talc	01-073-0147	Y	Y	Y	Y	Y
Magnesite	01-080-0101	Y	N	N	N	N
Enstatite ferroan	01-088-1911	Y	N	Y	Y	Y

PDF number refers to the powder diffraction file number from the PDF-2 Database,
Y present and N absent.

Figure 3.2 shows the TG analysis of CRS, CRS-US and GL50 using a heating rate of 1 °C/min. Table 3.6 lists the decomposition temperatures of the minerals present in the dunites. Table 3.7 summarizes the mass loss measured during the thermal analysis for CRS, CRS-US and GL50. The mass loss due to the decomposition of minerals is around 1.5% for CRS and 0.8% for CRS-US and GL50. Table 3.7 also shows the maximum possible amount of serpentine, calculated from the TG analyses, being around 0.4% for dunites CRS-US and GL50. The critical mass loss is displayed in the temperature interval between 450 and 650 °C. The minerals that decompose with this temperature interval are magnesite, talc and chlorite.

Table 3.5. Carbon content, magnesite content and magnesite LOI of dunites CRS, CRS-US and GL50.

Name	C-Total (%)	Magnesite[1] (%)	LOI[2] (%)
CRS	0.05	0.35	0.18
CRS-US	0.06	0.42	0.22
GL50	0.03	0.21	0.11

[1]Magnesite content calculated considering that all the carbon is present in this mineralogical form.
[2]LOI related to the magnesite decomposition.

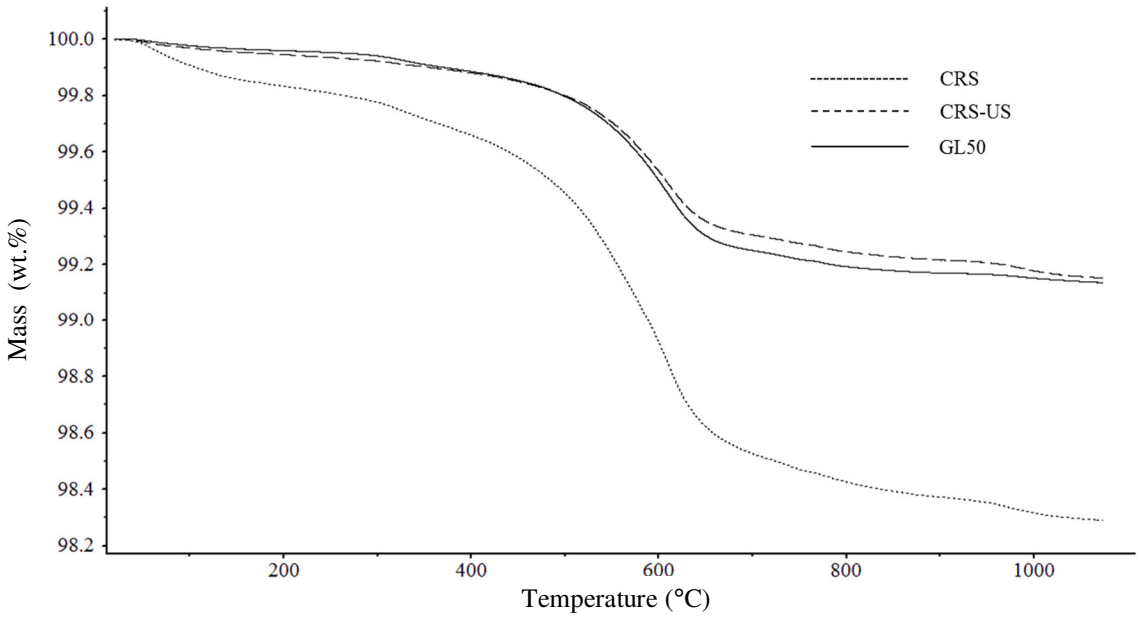

Figure 3.2. TG analyses of dunites CRS, CRS-US and GL50 prior to dissolution.

Table 3.6. Decomposition temperature of the minerals present in the dunites.

Mineral	Formula	Thermal decomposition (°C)	Reference
Actinolite	$Ca_2(Mg,Fe)_5Si_8O_{22}(OH)_2$	850	[79]
Phlogopite	$KMg_3Si_3AlO_{10}(OH,F)_2$	>1050	[80]
Serpentine	$Mg_3Si_2O_5(OH)_4$	650-720	[81]
Magnesite	$Mg(CO_3)$	570-610	[82]
Talc	$Mg_3(Si_2O_5)_2(OH)_2$	100-500 & 700-1000	[83]
Chlorite	$Mg_5Al_{0.75}Cr_{0.25}AlSi_3.O_{10}(OH)_8$	500-900	[84]

Table 3.7. Mass loss (wt.%) and serpentine content of the dunites in the TG analyses.

Samples	200-1000 (°C)	450-650 (°C)	650-720 (°C)	Serpentine[1] (wt.%)
CRS	1.52	0.96	0.09	0.78
CRS-US	0.77	0.51	0.05	0.43
GL50	0.81	0.56	0.05	0.43

[1]Serpentine content related to the LOI between 650 and 720 °C.

The other silicate minerals present in the dunites, react with acid much more slowly than olivine (see Table 3.8). Olivine reacts 50 times more rapidly than enstatite, which is the second fastest weathering silicate present. Thus, for short reaction times, the other silicates may be considered as inert materials regarding the consumption of hydrogen ions. Furthermore, the content of these other minerals is very small. Consequently, the hydrogen ion consumption will only be related to the content of olivine and carbonates.

Table 3.8. Dissolution rates of several silicate minerals at pH values of 2 and 25 °C.

Name	pH	Temperature (°C)	log r (mol cm^{-2} s^{-1})	log r^1 (mol cm^{-2} s^{-1})	Reference
Olivine	2	25	-12.0	-12.0	[20]
Hornblende	3.5	25	-15.6	-	[85]
Phlogopite	5	25	-16.4	-15.4	[86]
Serpentine	8	25	-15.7	-14.3	[87]
Chlorite	5	25	-16.5	-15.0	[88]
Talc	5	25	-16.0	-	[86]
Enstatite	2	25	-13.7	-13.7	[89]

Where r is the dissolution rate obtained from the literature at the pH and temperature of each different study and r^1 are the values calculated at pH = 2 and T = 25 °C.

Table 3.9 lists the experimental conditions of the reactivity experiments of dunites GL50 and CRS-US, the moles of hydrogen ion consumed and the olivine content determined using Eqs. (3.5) and (3.6). After 3 hours of reaction, the magnesite and olivine, which are the most reactive minerals, were completely consumed for GL50 as can be seen from Figure 3.3, where the hydrogen ion concentration remains constant after three hours. In order to be sure that all the olivine was consumed, the reaction time of the experiments was fixed at 5 hours for GL50. The reaction time for CRS-US was set one hour longer than for GL50 (6 hours) because the SSA_{Br} of GL50 is higher than for CRS-US. After reaction for 5 and 6 hours for GL50 and CRS-US, respectively the residual material was collected and analyzed by XRD. The diffractograms of these residue materials (see Figure 3.4) exhibited actinolite (amphiboles), chlorite, talc and enstatite for residue RE-2 (GL50) and RE-4 (CRS-US), but not olivine, which indicates that the olivine was completely

consumed. Neither mica nor serpentine minerals were found in the diffractograms. As these minerals dissolve slower than olivine and the reaction time is relatively short, mica and serpentine should still be present in the diffractograms. In fact, enstatite, which is more reactive than these minerals, is still present in the residue. Therefore, either mica and serpentine must have been removed during the cleaning steps of the residue, the sample analyzed was not representative of the total material or the content was below the detection limit. Another remarkable fact is that amphiboles were detected in the residue of GL50, whereas they were not detected in the material before the dissolution; this is due to either the sample analyzed before dissolution was not representative of the total material or the content was below the detection limit. After dissolution, olivine, which is the main mineral phase, has disappeared, making the relative content of other minerals higher.

Table 3.9. Experimental conditions of the reactivity experiments of dunites CRS-US and GL50, the moles of hydrogen ion consumed and the olivine content.

Name	$V_{H_2SO_4}$ (ml)	$[H^+]$ mol/L	Dunite	m_{du} (g)	T_r (°C)	$R_{H/ol}$	n_{H^+} (mol)	n_{ol} (mol)	w_{ol} (%)
RE-0	498.6	6.11	GL50	61.79	90.2	7.8	-	-	-
RE-1	501.9	6.05	GL50	62.25	90.1	7.9	1.523	0.381	88.8
RE-2	502.4	6.05	GL50	62.21	90.0	7.9	1.524	0.381	88.9
RE-3	501.6	6.08	CRS-US	62.29	90.3	8.0	1.529	0.382	89.1
RE-4	500.7	6.07	CRS-US	62.69	90.1	7.9	1.514	0.378	87.6

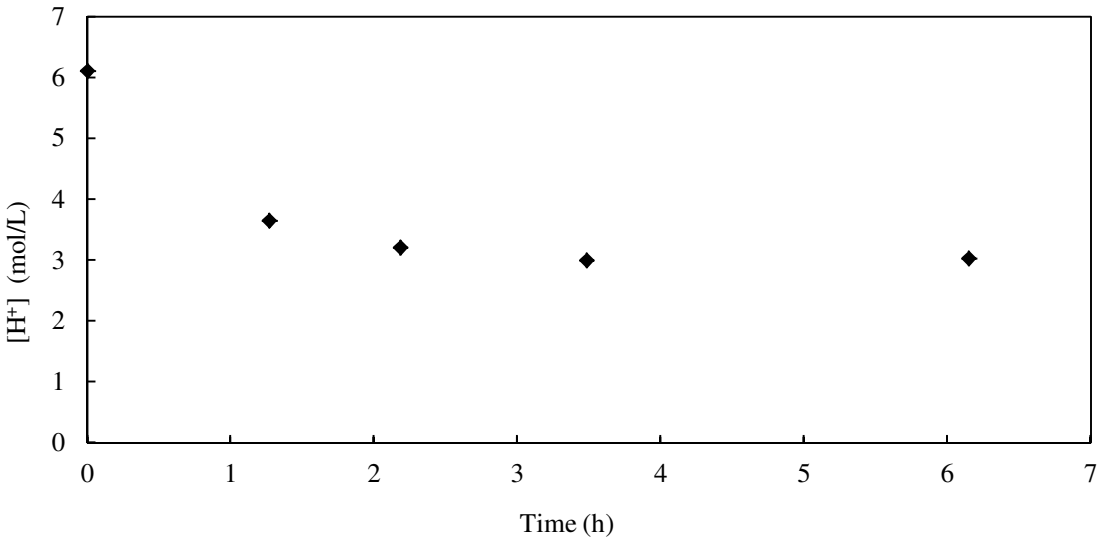

Figure 3.3. Dissolution curve of dunite GL50 at 90 °C: Experiment RE-0 (more details of this experiment can be found in Table 3.9).

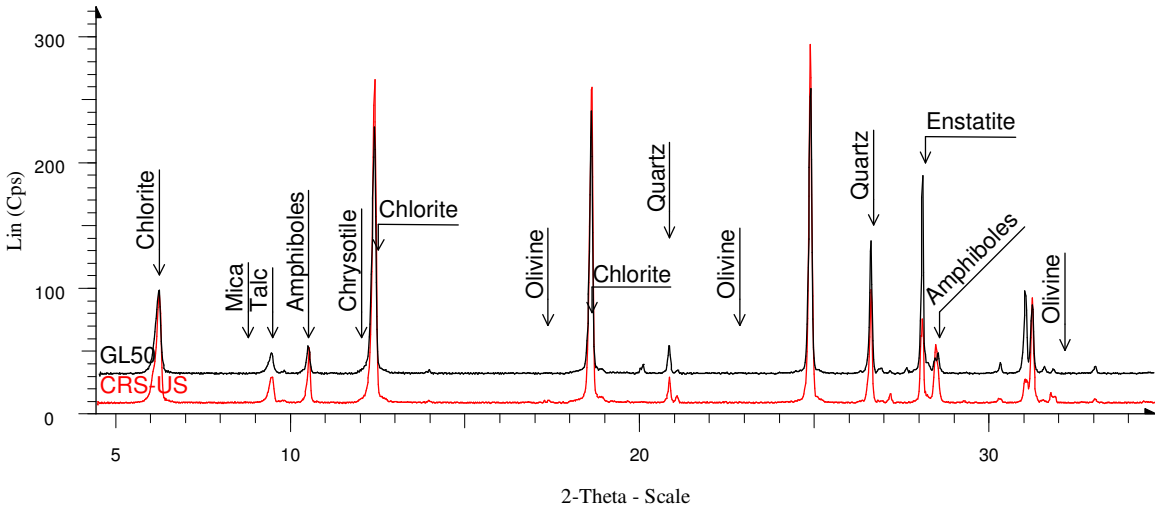

Figure 3.4. Diffractograms of the residue of dunites CRS-US and GL50 after dissolution.

Quartz was added as reference material.

The average olivine content determined from the reactivity experiments (see Table 3.9) is 88.9 and 88.4 wt.% for GL50 and CRS-US, respectively. Therefore, around 11 wt.% of the material of these dunite rocks consists of different minerals than olivine. Comparing the residual masses after the experiments, experimental (m_{exp}) and theoretical (m_{th}), it can be observed that these values are similar for both experiments (see Table 3.10). The experimental residue (m_{exp}) has a weight of 0.5 g or 7% higher than the theoretical residue because some silica, produced during the dissolution of olivine, was present within the residue. The good agreement between both residual masses confirms that the dissolution method is a reliable procedure for the determination of the olivine content in commercial dunites.

Table 3.10. Residual masses experimental and theoretically (after complete dissolution of olivine) of the reactivity experiments of dunites CRS-US and GL50.

Exp.	Dunite	m_{exp} (g)	m_{th} (g)
RE - 2	GL50	6.6	6.0
RE - 4	CRS-US	7.0	6.5

3.3.2 Specific surface area

Since dunite CRS had more impurities than dunite GL50 (see Tables 3.3-3.5 and 3.7), CRS of the fraction 125-500 µm was used to study the effect of the cleaning treatments on the SSA_{BET}. The specific surface areas of this material treated in different ways are shown in Table 3.11, where DS, WS and US refer to dry sieving, wet sieving and

ultrasound treatment in ethanol, respectively. As can be seen from the reduction in the $SSA_{BET,}$ using wet sieving instead of dry sieving leads to a substantial improvement in the removal of the fines. The ultrasound treatment step still reduces the specific surface area, but to a lower extent.

Table 3.11. BET specific surface area of CRS 125-500 after different treatments.

Name	Treatment	SSA_{BET} (m^2/g)
CRS-125-500	DS	1.109
CRS-125-500	WS	0.264
CRS-125-500	WS/US	0.143
CRS-125-500	WS/US	0.208
CRS-125-500	WS/US/WS	0.296
CRS-125-500	WS/US/WS/US	0.178

DS stands for dry sieving, WS for wet sieving and US for ultrasounds.

The average specific surface areas and the roughness factor of dunite CRS-US and GL50 are collected in Table 3.12. The particle size distributions of different fractions of CRS-US are plotted in Figure 3.5. When a mineral displays no porosity, the SSA_{BET} should increase with a drop of the particle size, and when a mineral is porous the SSA_E should rise with a decrease of the particle size. However, for SSA_E, this trend could not be observed due to measurement errors as can be seen from the high relative standard deviation (RSD). These high RSDs are due to the low total surface area of the samples (between 0.5 and 1.5 m^2), whereas the recommended surface area for this analysis is at least 5 m^2 [75]. The SSA_{BET} also breaks with this trend because the dunites exhibit porosity as can be seen from the hysteresis of the adsorption isotherm (Figure 3.6) and the positive values of SSA_{MP}. Usually, olivine is not porous [68], so it is likely that the porosity is due to the presence of other minerals. Therefore, in this case, the SSA_{BET} does not seem to be a reliable parameter to assess the specific surface area of the olivine because a small amount of impurities can significantly distort the SSA_{BET}. Furthermore, if the olivine were microporous, the dissolution rate would be much lower inside the pores (process controlled by diffusion) than outside (process controlled probably by surface reactions), and the SSA_{BET} would not be a reliable parameter either.

Table 3.12. Average specific surface areas (SSA_{BET}, SSA_E, SSA_{MP}, SSA_G, SSA_{Br}) and roughness factors (λ_{BET}, λ_{Br}) of dunites CRS-US and GL50.

	CRS-US 125-150	CRS-US 150-250	CRS-US 250-300	CRS-US 300-500	CRS-US 500-600	CRS-US 600-700	GL50[1] 100-500
d_A (µm)	138	200	275	400	550	650	300
SSA_{BET} (m^2/g)	0.309	0.149	0.284	0.174	0.174	0.260	0.280
SSA_E (m^2/g)	0.168	0.035	0.094	0.021	0.093	0.117	0.115
SSA_{MP} (m^2/g)	0.142	0.114	0.190	0.153	0.081	0.143	0.165
SSA_G (m^2/g)	0.011	0.008	0.006	0.004	0.003	-	0.006
SSA_{Br} (m^2/g)	0.068	0.046	0.033	0.023	0.018	-	0.038
λ_{Br}	6.4	6.2	6.0	5.8	5.8	-	6.1
λ_{BET}	29.1	19.8	50.9	43.4	57.4	-	44.8
RSD_{BET} (%)	9	17	12	34	0	33	14
RSD_E (%)	15	159	18	286	3	60	55
RSD_{MP} (%)	23	27	9	78	5	10	14

[1]This fraction was not measured by LLS because the grains settled too fast. The term d_A refers to the average particle size obtained from sieving. The cleaning treatment employed in CRS-US were: wet sieving, ultrasound treatment and again wet sieving.

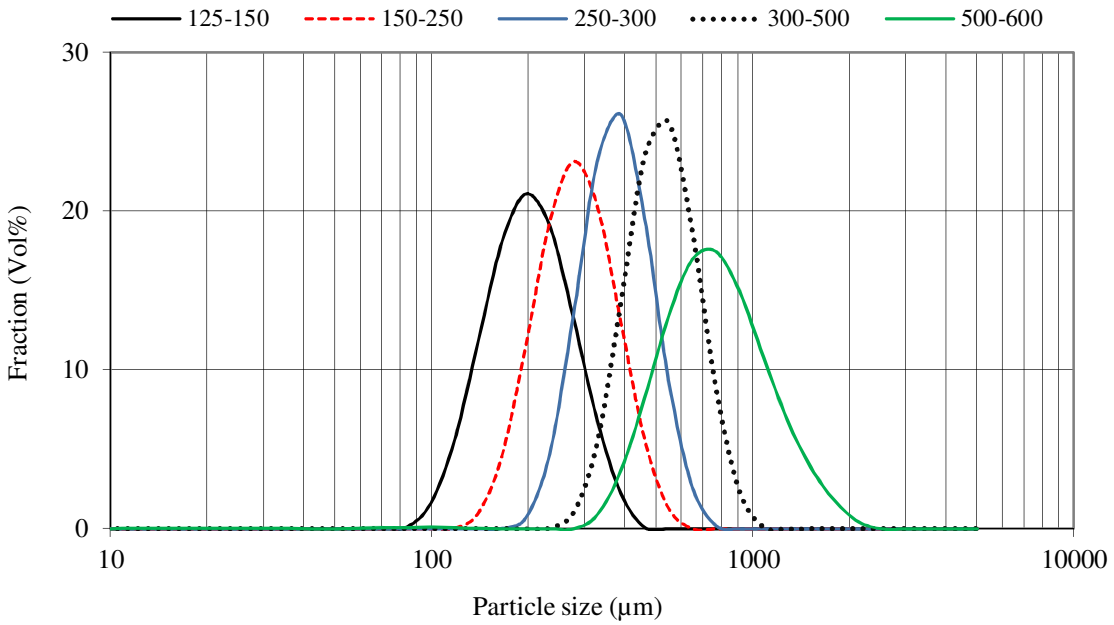

Figure 3.5. Particle size distribution, measured using LLS, of different fractions (125-150, 150-250, 250-300, 300-500, 500-600 µm) of dunite CRS-US.

The fractions of CRS-US were obtained by wet sieving.

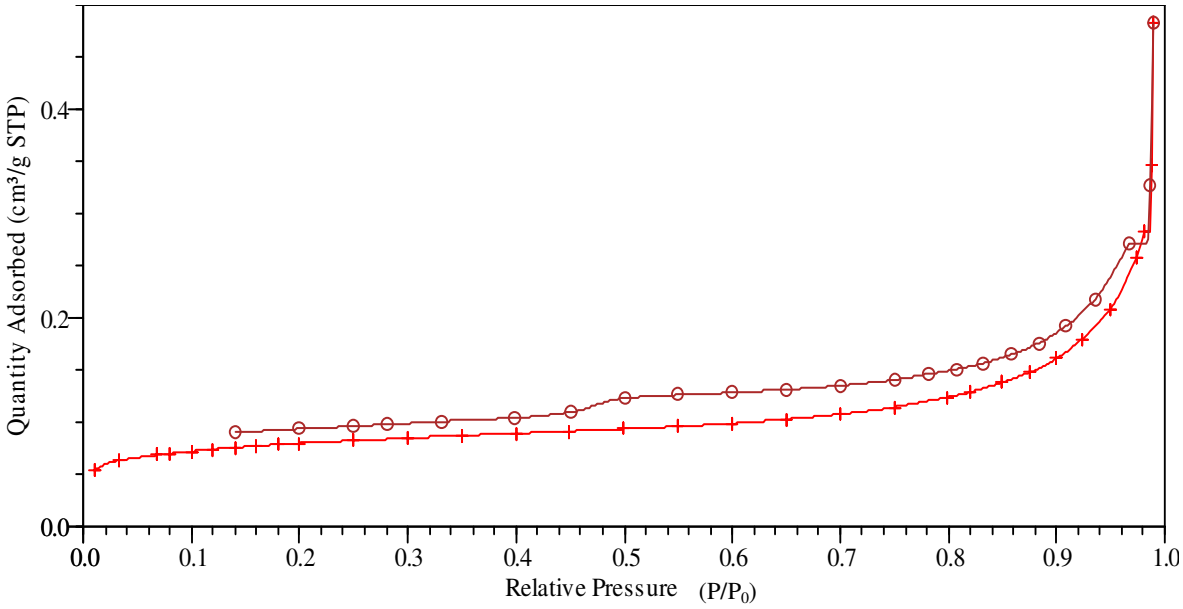

Figure 3.6. Nitrogen adsorption isotherm of dunite CRS-US 125-150.
The hysteresis loop is due to the difference between the adsorption and desorption curve.

The roughness factor calculated from the SSA_{BET} is in the range of 20 to 55, while the roughness factor calculated from the SSA_{Br} is around 7, which is in agreement with the values of White [71] for freshly crushed silicates. Thus, if λ_{BET} of the freshly crushed olivine is higher than 10, a thorough characterization of the material, to detect the presence of impurities, would be advisable. When other minerals are present together with olivine, the use of the SSA_{Br} instead of the SSA_{BET} for the olivine dissolution studies would be more reasonable. Even in the case that the only component in the material is olivine and the olivine grains are porous, the SSA_{Br} would be more useful for dissolution studies than the SSA_{BET}.

3.4 Surface characterization of olivine before and after the dissolution

SEM images were taken from GL50 grains before and after dissolution with and without stirring. The silica layer, detected by EDS analysis, can be visually identified because 1) the surface of olivine has a different texture than the surface of silica and 2) the silica layer exhibits shrinking cracks formed during the drying of the material. The molar ratio between metal ions and silicon (Me/Si) for an olivine grain is 2, and it would be 0 for a pure and thick silica layer. Layers with shrinking cracks exhibit ratios between 0.2 and 1.8. Values close to zero correspond to silica layers with a thickness of at least the excitation depth of the electron beam. Values close to 1.8 correspond to silica layers

much thinner than the excitation depth; that is because the material below the superficial layer is also taken into account in the EDS analysis.

Van Herk [73] and Jonckbloedt [25] also carried out SEM analyses of olivine grains dissolved in acid in a stirred reactor. Van Herk found a layer that presents shrinking cracks with a Me/Si ratio of 1.6, and Jonckbloedt did not find any silica layer.

Figure 3.7 shows SEM pictures of GL50 prior to dissolution, where the presence of particles smaller than 10 μm can be observed. These particles are not olivine and contribute greatly to the specific surface area. Figure 3.8, a – d, depicts images of the olivine grains after dissolution in an unstirred reactor. The presence of a silica layer on the surface of olivine can be observed in all the images, which is representative for most grains examined in this sample. Figure 3.8, c and d, were taken from the same spot but with different angles and magnifications. The thickness of the silica is larger than 700 nm for the grain in Figure 3.8, c and d. Figure 3.9, a - e, shows the olivine grains after dissolution in a stirred reactor. Etch pits and dissolution cracks can be observed in Figure 3.9, a and b. The presence of these features is indicative for a dissolution mechanism controlled by surface reaction [90]. Silica layers could not be perceived on most of the grains examined, and in the rare cases, where they were observed, they did not completely cover the olivine grains. Figure 3.9, c and d, are examples of these cases where a sheet silicate is in the matrix of olivine as an intergrowth, and the sheet silicate behaves as a shelter for the silica. Figure 3.9e shows an exfoliated sheet silicate that offers a protecting area to the silica particles from the stirring action. To conclude, a silica layer is covering most of the olivine grains when the dissolution takes place in an unstirred reactor; however, the presence of a silica layer is unusual when a stirred reactor is employed.

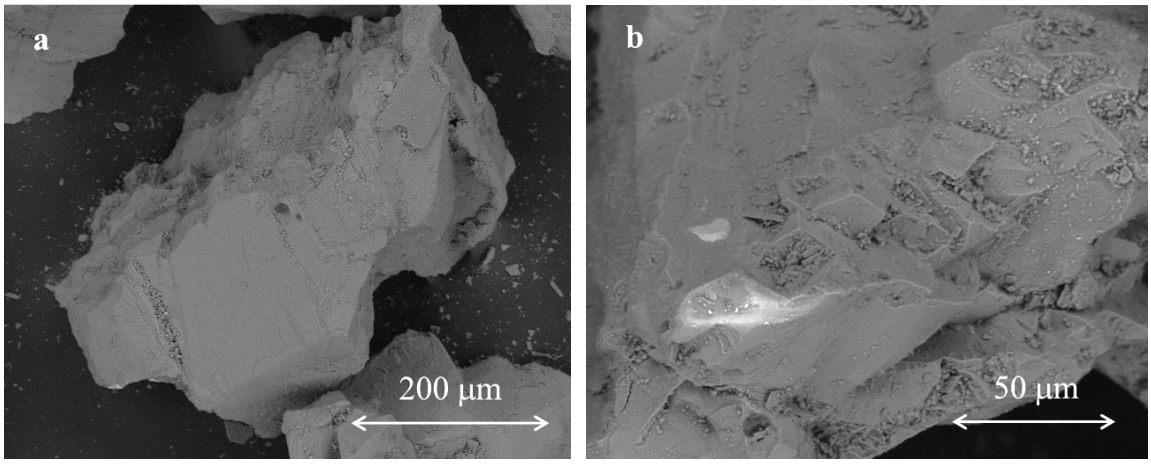

Figure 3.7, a and b. SEM pictures of dunite GL50 prior to dissolution.

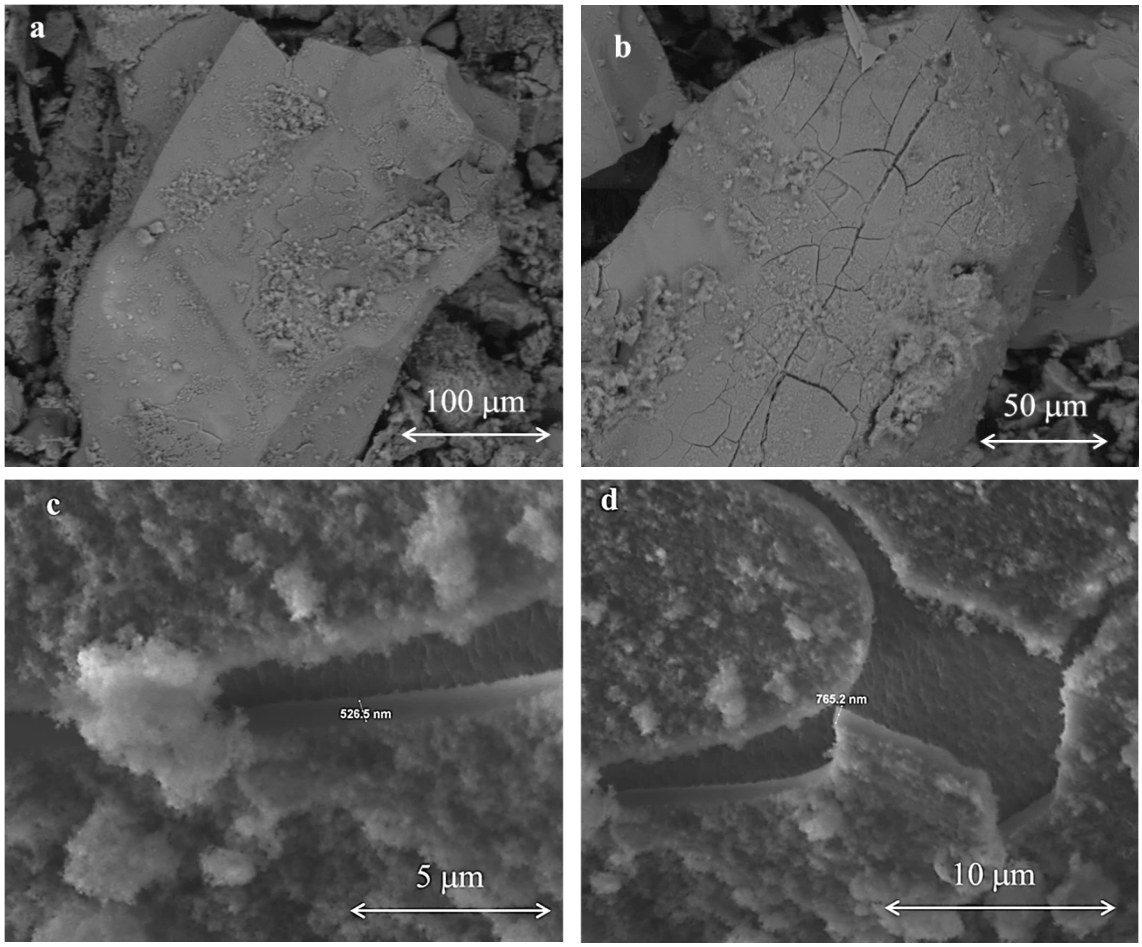

Figure 3.8, a – d. SEM pictures of GL50 after dissolution in an unstirred reactor.
The thickness of the silica layer in Figures c and d was 500 and 700 nm, respectively.

3.5 Data from dissolution experiments

This section presents data obtained in the dissolution experiments. From this data, a kinetic model is proposed in Chapter 4 for the dissolution of olivine in acid under the conditions of olivine nano-silica production. The variables of the experiments are the main parameters of the olivine dissolution kinetics (i.e., specific surface area, hydrogen ion activity and temperature), except for the concentration of hydrogen ion, which was set at the beginning of the experiment as 6M (i.e., 3M H_2SO_4). Therefore, different experiments were conducted changing the grain fraction of the dunite and temperature. In addition, two types of commercial dunites, both originating from Norway, were used to check if their dissolution behavior was similar.

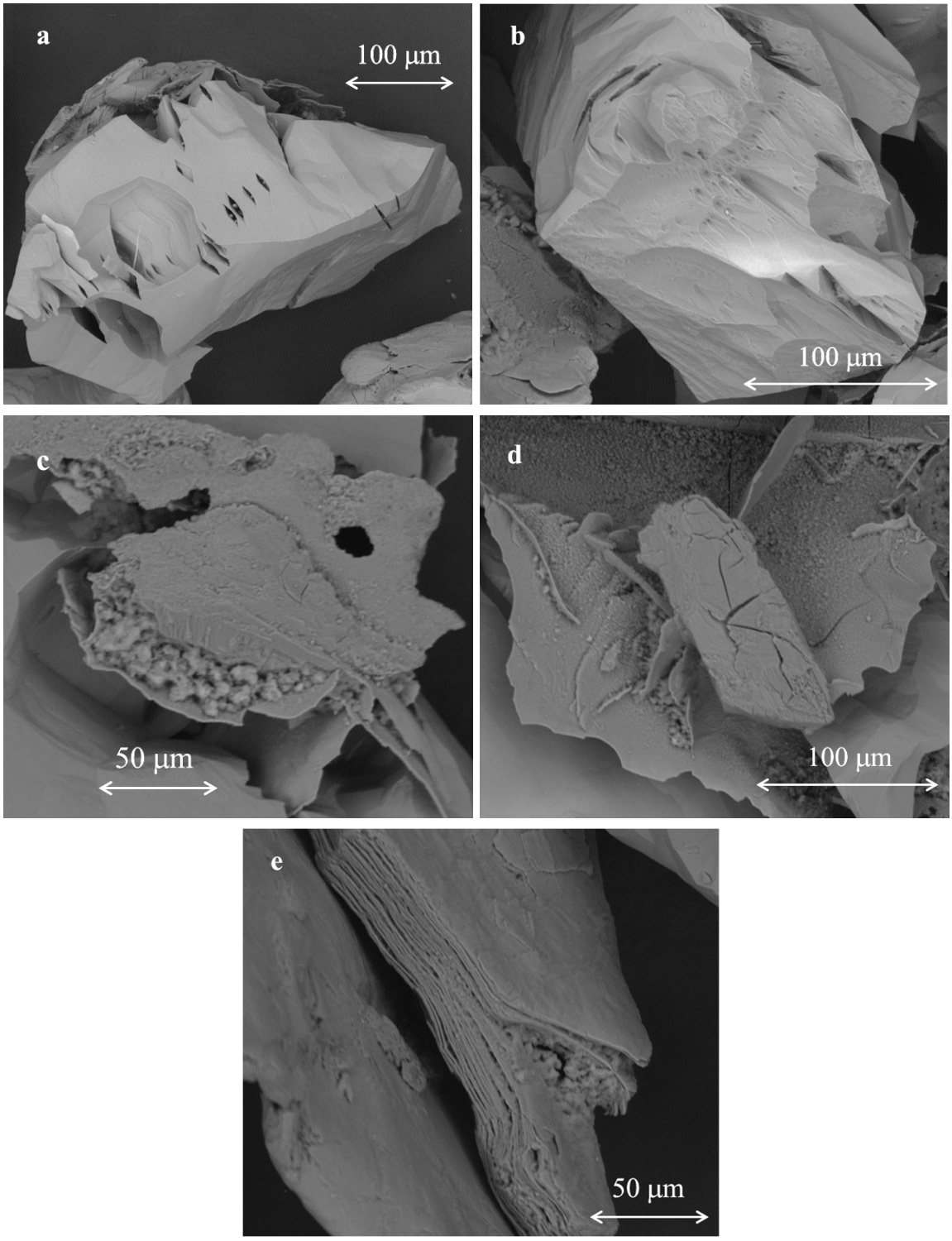

Figure 3.9, a - e. SEM pictures of dunite GL50 after dissolution in a stirred reactor.

In Figure 3.9, a and b, etch pits and dissolution cracks can be observed. In Figure 3.9, c – e, silica deposits can be found in protected sites offered by an inert (or less reactive) silicate mineral.

Table 3.13 lists the experimental conditions for all the experiments. Figures 3.10 - 3.12 show the hydrogen ion concentration versus time for different set of experiments with similar reaction temperatures using dunite CRS-US. Figure 3.13 represents the same type of graph for experiments using dunite GL50 at different temperatures. In addition, the experiment conducted at 70 °C (NS-14) was performed in a bigger reactor to see whether the scale-factor was playing a role in the kinetics. How all these parameters affect the dissolution kinetics is discussed in detail in Chapter 4, but from the experimental data, it can already be observed that the most influencing parameter for the dissolution of olivine is the temperature. An example of this is the required time to neutralize the hydrogen ion from 6M to 1M, which is around 2200 and 200 minutes for experiments performed at 50 and 90 °C, respectively.

Table 3.13. Experimental conditions of dissolution of dunites in 3M sulfuric acid.

Sample	Olivine	d_A (µm)	Fraction (µm)	SSA_{Br}[1] (m^2/g)	T_r (°C)	Ratio H^+/Ol	$V_{H_2SO_4}$ (L)
NS-1	CRS-US	138	125-150	0.068	48.7	4.5	0.5
NS-2	CRS-US	200	150-250	0.045	52.0	4.0	0.5
NS-3	CRS-US	400	300-500	0.023	55.0	3.8	0.5
NS-4	CRS-US	200	150-250	0.045	70.2	4.0	0.5
NS-5	CRS-US	400	300-500	0.023	70.7	4.0	0.5
NS-7	CRS-US	275	250-300	0.032	87.7	4.2	0.5
NS-8	CRS-US	400	300-500	0.023	86.2	4.1	0.5
NS-9	CRS-US	200	150-250	0.045	50.6	4.1	0.5
NS-10	CRS-US	200	150-250	0.045	89.8	4.2	0.5
NS-11	GL50	302	250-355	0.034	90.0	4.2	0.5
NS-12	GL50	302	250-355	0.034	89.7	4.1	0.5
NS-13	GL50	302	250-355	0.034	89.9	4.1	0.5
NS-14	GL50	300	100-500	0.038	70.2	4.3	10

[1]SSA_{Br} prior to dissolution. The term d_A refers to the average particle size obtained from sieving, Fraction the olivine fraction used and ratio H^+/Ol the molar ratio of hydrogen ion to olivine.

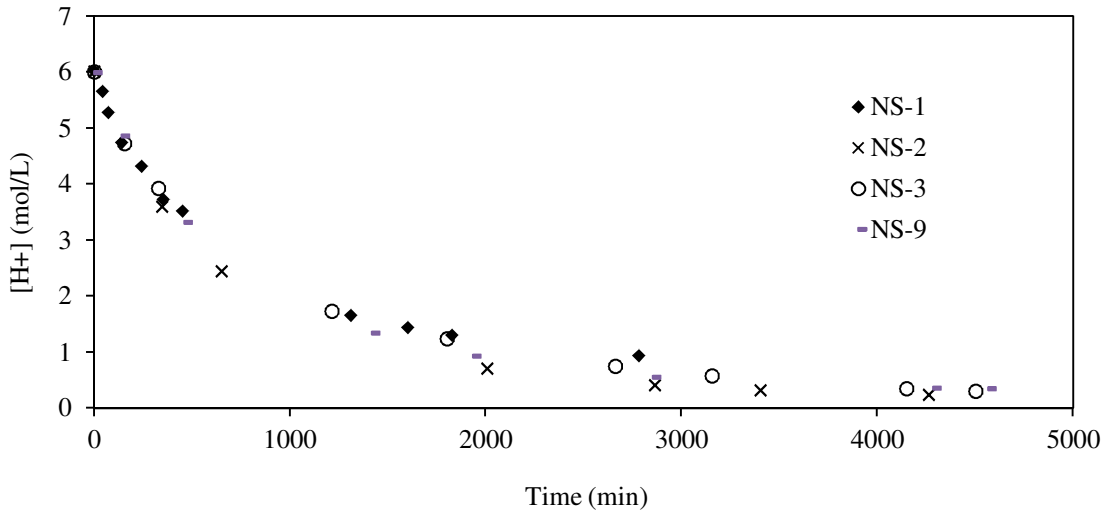

Figure 3.10. Dissolution curves of dunite CRS-US around 50 °C in 3M sulfuric acid.

The experimental conditions are presented in Table 3.13.

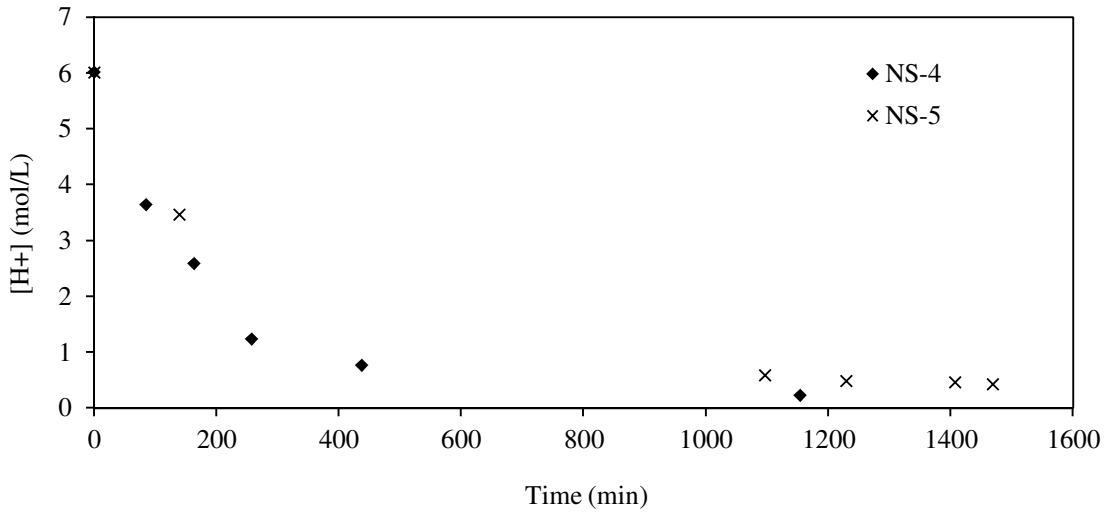

Figure 3.11. Dissolution curves of dunite CRS-US around 70 °C in 3M sulfuric acid.

The experimental conditions are presented in Table 3.13.

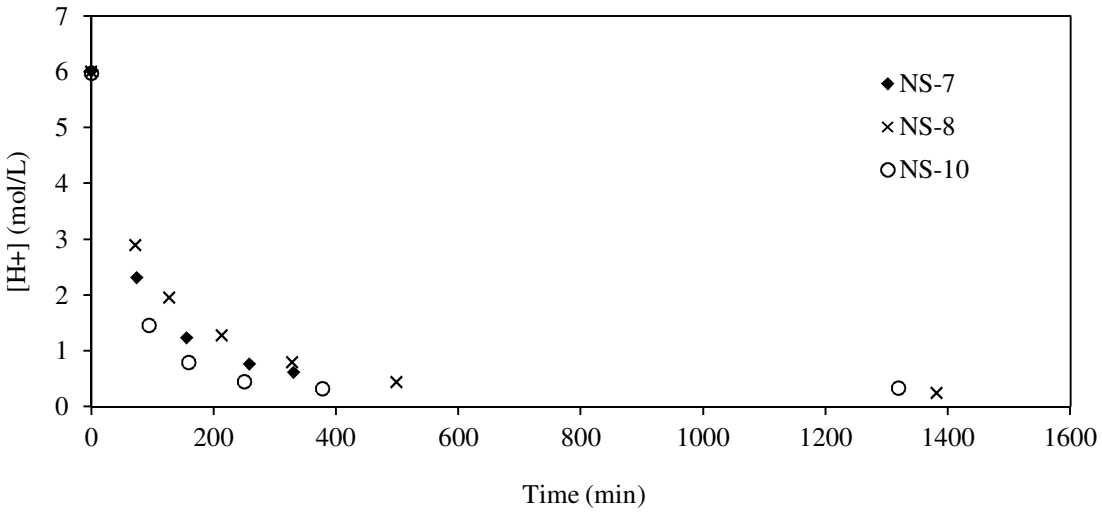

Figure 3.12. Dissolution curves of dunite CRS-US around 90 °C in 3M sulfuric acid.

The experimental conditions are presented in Table 3.13.

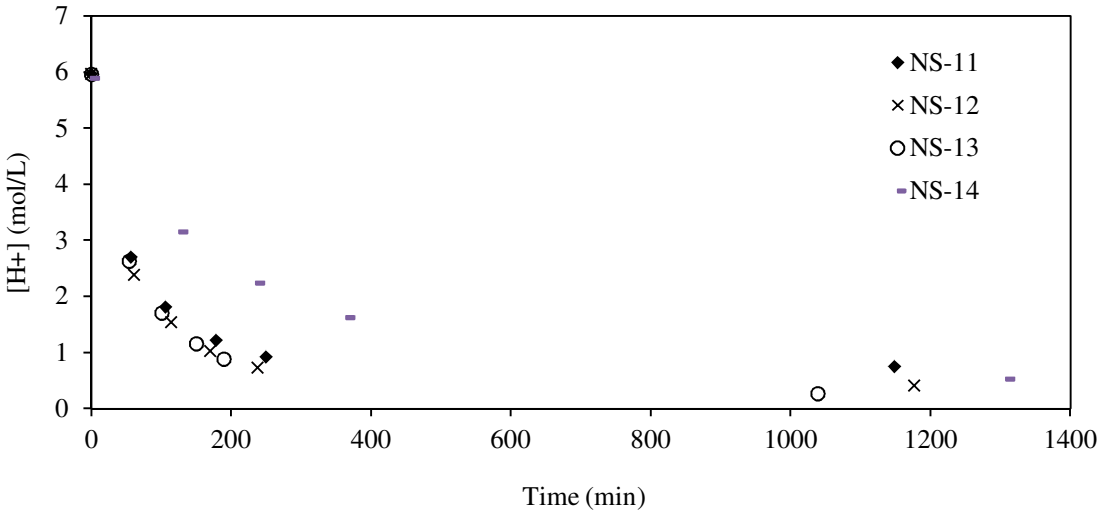

Figure 3.13. Dissolution curves (NS-11, NS-12 and NS-13 around 90 °C and NS-14 around 70 °C) of dunite GL50 in 3M sulfuric acid.

The experimental conditions are presented in Table 3.13.

3.6 Conclusions

To study the kinetics of the dissolution of olivine in acids, the commercial dunites need to be adequately characterized. The characterization of dunite needs to focus on the mineralogical composition and the specific surface area of the material. The mineralogical composition should be centered on the amount of olivine, unreactive silicates and carbonates.

Besides the olivine, the XRD analyses revealed small amounts of other minerals in both dunites studied here such as mica and serpentine. The content of carbonates measured by combustion infrared analysis is 0.4 and 0.2 wt.% for CRS-US and GL50, respectively. The average olivine content from the reactivity experiments is 88.4 and 88.9 wt.% for CRS-US and GL50, respectively.

The roughness factor of the dunites studied calculated with the SSA_{BET} is in the range of 20 to 55, whereas the expected value should be around 7. These high values are due to the presence of porous and finely divided species. Since olivine is usually not porous, it is likely that the porosity is due to the presence of other minerals. Even in the case that the only component in the material were olivine and the olivine grains were porous, the SSA_{Br} would be more useful for dissolution studies than the SSA_{BET}. In any case, the SSA_{BET} is not a reliable parameter to use in the kinetic study of the dissolution of olivine because the porosity of the samples and the large error in the measurement. Thus, it appears that the equation proposed by Brantley [68] is more suitable to calculate the SSA of the olivine grains.

SEM pictures of olivine GL50 before dissolution show that some finely divided species are present together with the olivine. After dissolution in an unstirred reactor, most of the olivine grains examined were covered by a silica layer. The silica layer measured on the grains was thicker than 700 nm. When the reactor was stirred, olivine grains with etch pits and dissolution cracks were observed, and only on rare occasions silica was found.

The olivine content, the SSA_{Br} and the information about the silica layer will be used in the next chapter, where a kinetic model of the olivine dissolution for the nano-silica production will be proposed.

Chapter 4. The kinetics of the dissolution of olivine in acid

4.1 Introduction

In this chapter a kinetic model of the dissolution of olivine for nano-silica production is proposed, using the experimental data presented in Chapter 3. The dissolution of olivine in acid follows Eq. (1.4). As was mentioned in the previous chapter, a kinetic model for the dissolution of olivine is essential for the basic understanding of the process and the upscaling of the nano-silica production. Many researchers have studied the dissolution of olivine under normal weathering conditions (above pH 1, a dissolved olivine fraction smaller than 10% and a solid content below 50 g/L) [9-11,18-24]. These researchers agree that the dissolution mechanism is controlled by surface reactions, and the kinetics depends on the hydrogen ion activity, surface area of olivine and temperature:

$$r = k_T \cdot a_{H^+}^n = A \cdot \exp\left(\frac{-E_a}{R \cdot T}\right) \cdot a_{H^+}^n , \qquad \textbf{(4.1)}$$

where r is the dissolution rate ($mol \cdot cm^{-2} \cdot s^{-1}$), k_T the rate constant ($mol \cdot cm^{-2} \cdot s^{-1}$), A the pre-exponential factor ($mol \cdot cm^{-2} \cdot s^{-1}$), E_a the activation energy (kJ/mol), R the gas constant ($8.314 \cdot 10^{-3}$ $kJ \cdot mol^{-1} \cdot K^{-1}$), T the temperature (K), a_H^+ the hydrogen ion activity and n the reaction order. A summary of the kinetic parameters together with the experimental conditions found in the literature can be seen in Table 4.1. The values of E_a range from 25 to 105 kJ/mol, n from 0.33 to 1.1, and r from $2 \cdot 10^{-13}$ to $5 \cdot 10^{-12}$ $mol \cdot cm^{-2} \cdot s^{-1}$. However, the most frequently mentioned value for the reaction order is around 0.5, and the activation energy is in the range between 43 and 80 kJ/mol.

There are several studies in which the dissolution parameters are out of these ranges. The study of Grandstaff [18] is one of them, with values of E_a of 38 kJ/mol and n of 1.1. The different values established by this author could be the result of the high roughness factor of the studied dunite (see Table 3.1); this roughness factor is due to the presence of other minerals with higher specific surface area (SSA) than olivine. Van Herk [73] also reported anomalous activation energy values of 30 kJ/mol together with high values of the roughness factor. Chen [24] reported a value of E_a of 126 kJ/mol, which is surprisingly high, and an reaction order of 0.7, which is also relatively high. He conducted experiments only at one temperature, obtaining the activation energy by combining his results with experiments from the literature [21,23]. In addition, the roughness factor was 3 times smaller than the expected roughness factor for freshly

crushed silicates [71]. For these reasons his results can be considered to be unreliable. The remainder of the dissolution studies in Table 4.1 display similar values of k_T and n.

Table 4.1. Summary of the olivine dissolution kinetics in the literature.

A	E_a	k_T [1]	n	r [1]	Solid content (g/L)	Frac. Dis. (%)	Acid	pH	Ref.
1.53E-04	38.1	3.2E-11	1.10	2.0E-13	2	6.6	HCl	3-5	[18]
6.71E+02	79.5	7.9E-12	0.50	7.9E-13	0.1-10	-	HCl	2-10	[21]
-	25.0	-	0.33	-	-	80-99	HCl	1-3	[73]
-	30.0	-	0.43	-	-	80-99	H_2SO_4	1-3	[73]
-	66.5	-	0.33	-	250	90-99	H_2SO_4	-0.5-1	[12]
-	71.5	-	-	-	-	10<	H_2SO_4	1-2	[22]
-	125.6	-	0.70	-	0.5-3	2	HCl	2-5	[24] [2]
-	-	-	0.50	2.0E-12	4-16	5<	HCl	1-8	[9]
3.46E-04	42.6	1.2E-11	0.50	1.2E-12	30	-	HNO_3	2-4	[10]
1.90E-01	63.8	1.3E-12	-	1.3E-12	3-8	-	HCl	2	[11]
8.54E-02	52.9	4.6E-11	0.46	5.5E-12	0.5-10	0.05-99	HCl, H_2CO_3	2-12	[19]
-	-	9.3E-12	0.46	1.1E-12	50	-	HNO_3	1-4	[20]
1.13E+02	70.5	5.0E-11	0.46	6.0E-12	-	-	-	-	[91] [3]

A, k_T, and n are given in $mol \cdot cm^{-2} \cdot s^{-1}$, E_a in kJ/mol and n dimensionless units. [1]Calculated at pH=2 and T=25 °C. [2]Experiments were done only at 65 °C and E_a was calculated by comparing these results with the literature. [3] This study statistically obtained the kinetic parameters from 22 investigations.

Although the dissolution of olivine has been widely studied, only Jonckbloedt [25] conducted experiments under conditions relevant for the production of nano-silica. These conditions included a negative pH to accelerate the reaction as well as a high solid content and an elevated conversion degree to increase the amount of nano-silica produced per batch. Under these conditions, the study of the olivine dissolution is still problematic for the following reasons: 1) the concentration of hydrogen ions cannot be maintained constant because of the lack of pH sensors that could operate in such an aggressive environment; 2) the viscosity rises during the experiment [32]; 3) the olivine surface area substantially decreases over time; 4) the quantity of silica released is much higher than the silica solubility [92].

Jonckbloedt studied the dissolution of olivine in 3M sulfuric acid with a stoichiometric amount of olivine and without keeping the pH level constant [12]. He also proposed a model for these conditions where the olivine particles shrink over time:

$$\frac{d[H^+]}{dt}\ (mol/min) = -\exp\left(\frac{-E_a}{R \cdot T}\right) \cdot 1.92 \cdot 10^8 \cdot SSA_G \cdot a_{H^+}{}^{0.33}, \qquad \textbf{(4.2)}$$

where E_a is 66.5 kJ/mol and SSA_G (geometric specific surface area) is expressed in m^2/g. The particle shrinkage was incorporated into Jonckbloedt's model by means of the SSA_G, which changed over time. Although Jonckbloedt's model was a considerable step forward in the elucidation of the kinetics of the dissolution of olivine under the conditions of olivine nano-silica production, there are several points on which more effort could have been attempted: 1) Jonckbloedt did not follow the standard equation (i.e., Eq. (4.1)) for the dissolution of olivine; 2) the specific surface area and the mineralogical composition of the olivine employed were not reported, so Jonckbloedt's results cannot be compared with the other studies; 3) the specific surface area used was the geometric, whereas, as was mentioned in Chapter 3, the SSA_{Br} (see Eq. (3.3)) would have been a better estimation of the real external specific surface area of olivine; 4) he obtained the kinetic parameters by fitting the plot of "log ($d[H^+]/dt$)" versus "$-m \cdot \log(\text{mol } [H^+]) - n \cdot \log(\text{act } [H^+])$", which is a peculiar procedure. It would have been much simpler to obtain the kinetic parameters by fitting the data of the dissolution curve to Eq. (4.1); and 5) the reaction order is lower than in most of the dissolution studies. In addition to these points, the mass transport mechanism should be more deeply investigated because there are some controversial points in Jonckbloedt's work [12]: 1) the mass transfer through the liquid film was calculated considering a stagnant liquid and an effective diffusivity instead of the mass-transfer coefficient (k_L) obtained from Sherwood's number; 2) the change in the viscosity of the slurry was not taken into account when calculating the mass transfer through the liquid film.

In this chapter, a kinetic model for the dissolution of olivine under the nano-silica production conditions is developed. Before proposing a model, the mechanism of the olivine dissolution focusing on the possible resistances to the transport is studied. Once it is concluded that the mechanism dominating the process is the surface reaction, a model is developed using Eq. (4.1) to fit the experimental data of the rate of consumption of hydrogen ions. The change in the olivine surface area is incorporated in the model using a roughness factor based on the Brantley equation. Finally, this model is compared with the ones from the literature.

4.2 Mechanism of the olivine dissolution

4.2.1 Solubility, nucleation and polymerization of silica

The mechanism controlling the dissolution of olivine in acid depends on the mixing device, reaction kinetics, silica concentration, silica solubility, silica polymerization and fluid properties.

The solubility of silica at the pH level of 1 is 150 mg/L or 2.5 mmol/L [92]. Once the silica concentration is above this value, silica starts to nucleate and condensate. At the olivine nano-silica production conditions, 218 grams of olivine (1.5 moles) per liter of acid are used. Once this material has reacted with the acid, 90 (stoichiometric calculations) grams of silica are released to the medium. The silica starts to condensate when the conversion degree, X, is 0.1664%, which happens 4 seconds after the reaction has started at 90 °C (see Table 4.2). Therefore, it can be considered that solid particles of silica are present during the whole experiment. The primary particles formed in a silicic acid solution are around 5 nm [4,93]. These silica particles grow forming siloxane bonds as described by [4]:

$$\equiv Si-OH + OH-Si\equiv \rightarrow \equiv Si-O-Si\equiv + H_2O. \quad \textbf{(4.3)}$$

Table 4.2. Time to release 2.5 and 135 mmol/L by the dissolution of olivine.

Sample	T_r (°C)	t_1 (sec)	t_2 (min)
NS-2	52.0	90	55
NS-10	89.8	4	3.4

Where t_1 and t_2 are the required time to produce 2.5 and 135 mmol/L of silica.

The formation of siloxane bonds is catalyzed by the concentration of hydrogen ion [4]. Gorrepati [93] stated that the silica particles grow over time in acidic media reaching sizes above 500 nm. She also stated that silica particles reach a diameter of 200 nm after 100 minutes in an 8M HCl solution at 5 °C with a silica concentration of 135 mmol/L, while the particles need almost seven days in a 2M HCl solution. Under the olivine nano-silica production conditions (3M H_2SO_4, T ~ 90 °C, and initial and final silica concentration of 0 and 1500 mmol/L, respectively), the temperature and silica concentration are much higher than in Gorrepati's experiments, except at the beginning of the experiment (3.4 minutes passed in experiment NS-2 to release the same amount of silica that was used in Gorrepati's experiments); therefore, the polymerization kinetics should be faster once the silica is released.

4.2.2 Possible resistances to the transport

The most common reaction models in leaching and dissolution of solids are shown in Figure 4.1. Model (a) illustrates a spherical particle that shrinks over time without any layer covering the surface. Model (b) shows a spherical particle in which the core shrinks over time, but the solid layer covering the surface of the cores increases over time; therefore, the size of the particle (core plus solid layer) remains constant. Model (c)

describes a spherical particle where the core shrinks over time together with a solid layer of constant thickness. More details about these models can be found in [94-96].

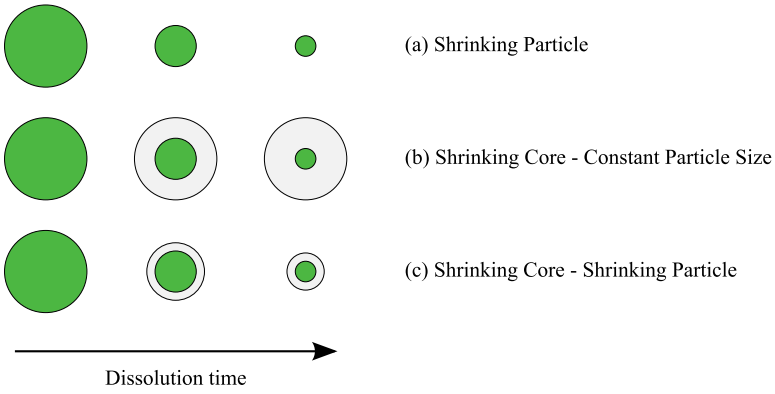

Figure 4.1. Dissolution models of solid particles [96].

When a solid layer covers the grains of olivine there are 3 possible resistances to the transport of ions from the bulk liquid to the olivine surface and vice versa: 1) diffusion through the liquid film, 2) diffusion through a solid layer and 3) reaction on the surface. When all the resistances influence the dissolution of olivine, the shrinking of the core spherical particles can be described in analogy with Levenspiel [94]:

$$\frac{d(R_{ol})}{dt} = -\frac{[H^+]/(4\cdot\rho_{ol})}{\frac{R_{ol}^2}{R_{ol+\theta_{Si}}^2\cdot k_L} + \frac{\theta_{Si}\cdot R_{ol}}{R_{ol+\theta_{Si}}\cdot D_e} + \frac{1}{k_T}}, \qquad \textbf{(4.4)}$$

where R_{ol} is the core radius of olivine grains, $R_{ol+\theta_{Si}}$ the radius of the olivine grain covered by a solid layer, θ_{Si} the thickness of the solid layer, k_L the mass-transfer coefficient in the liquid film, D_e the effective diffusion coefficient through the solid layer, k_T the reaction rate constant of the olivine dissolution and ρ_{ol} the olivine density. In steady state, the molar flux in each step should be equal to the others:

$$N = r = N_L = N_{so}\ , \qquad \textbf{(4.5)}$$

where N is the overall flux rate for the dissolution of olivine, r is the reaction rate, N_L is the molar flux through the liquid layer and N_{so} is the molar flux through the solid layer, all of them in $mol\cdot s^{-1}\cdot cm^{-2}$.

4.2.3 Literature review on solid layers

The formation or lack thereof of a solid layer around the olivine particles is of great interest when tackling the kinetics of the dissolution of olivine and has been investigated by many authors [9,12,18,73,96-102]. Table 4.3 summarizes different studies about the dissolution of olivine where a solid layer was investigated.

Table 4.3. Summary of the studies where the presence of a silica layer around the olivine particles was investigated

Solid content (g/l)	Stirring	Si/Dep layer	SEM/TEM	θ_{Si} (nm)	Reference
250	N	Y	Y	-	[12]
250	Y	N	Y	-	[12]
6	Y	Y	XPS	1	[98]
2	Y	N	Y	-	[18]
4	Y	Y	Y	-	[73]
-	Y	Y	Y	-	[100]
4-16	Y	N	Y	-	[9]
50-100	MS	Y	XPS	<2	[99]
-	N	N	Y	-	[101]
-	N	Y	Y	-	[97]
100	N	Y	Y	<40	[102]

Si/Dep layer refers to the presence or lack thereof of a solid layer and θ_{Si} the silica layer thickness.

A silica layer was only found by Schott [98], van Herk [73] and Bearat [100] in a stirred reactor using SEM, TEM or X-ray photoelectron spectroscopic (XPS) techniques. Schott found a thin layer of 10 Å that was unstable and did not grow over time; he also stated that this layer did not inhibit the diffusion. Van Herk found a silica layer partly covering some of the olivine grains. Bearat also found a passivating silica layer and that the passivation effect of the silica could be decreased by increasing the abrasion between the particles. In the same study [100], the influence of the solid content on the conversion degree was studied, concluding that the conversion increased up to a solid content of 10 wt.%, after which it remained constant. The fact that the conversion remained constant implies that either the silica layer was completely removed or its thickness was constant and, therefore, incapable of being reduced any further by abrasion.

Silica layers cover the surface of olivine only on rare occasions when the slurry was vigorously stirred (more details are provided in Chapter 3). Under these mixing conditions, silica is removed from the surface of olivine. The detachment of the silica layer from the olivine grains depends on the fluid and mixing properties, and the pH of the slurry. The increase of the solid content improves the abrasion, detaching the silica layer from the olivine [97,100]. In addition, at low pH, the polymerization of silica is

enhanced [4,93] increasing the removal of the silica layer as well. Under the olivine nano-silica production conditions, the presence of a silica layer is more unlikely than in the studies reported in the literature because 1) the solid content is higher, and, therefore, the abrasion, and 2) the polymerization is faster.

4.2.4 Diffusion through the liquid film as the limiting step

When the diffusion through the liquid film controls the process, the hydrogen ion concentration around the particle can be described by Figure 4.2 and Eq. (4.6).

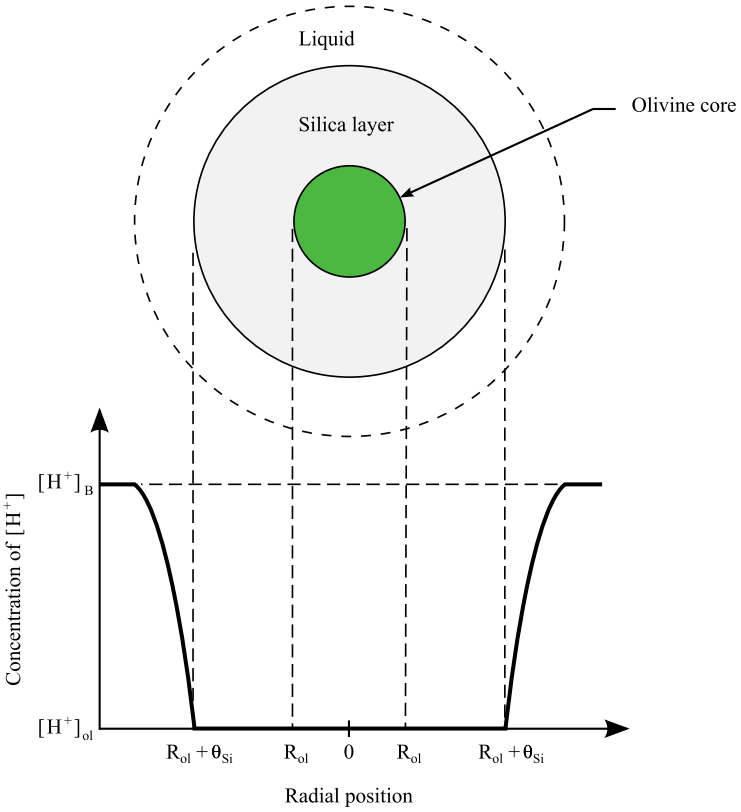

Figure 4.2. Diagram of a reacting olivine particle when the diffusion through the liquid film is the rate limiting step [94].

$$N_{L,H} = k_L \cdot \left([H^+]_B - [H^+]_{ol}\right) \approx k_L \cdot [H^+]_B \,, \qquad \textbf{(4.6)}$$

where $N_{L,H}$ is the molar flux of the hydrogen ion through the liquid layer, $[H^+]_B$ the concentration of hydrogen ions in the bulk liquid and $[H^+]_{ol}$ the concentration of hydrogen ions on the surface of olivine. In the case that the diffusion through the liquid film controls the process, the surface reaction resistance, and, therefore, $[H^+]_{ol}$, can be neglected. The Sherwood's number (Sh) for diffusion from a sphere into a stagnant medium is described by:

$$Sh = \frac{k_L \cdot d}{D} = 2, \quad \textbf{(4.7)}$$

where k_L is the mass-transfer coefficient, d the particle diameter and D the diffusion coefficient.

For forced convection, the important hydrodynamic variables are the relative velocity between the solid and the liquid, also known as slip velocity (v_s), and the rate of renewal of the liquid layer around the solid particle [103]. The mass-transfer coefficient can be estimated following the procedure explained in [103]. This coefficient is calculated using an empirical equation for solid particles suspended in an agitated vessel when a significant density difference exists [104]. In this procedure, the free settling velocity (v_t) – which refers to the decantation speed of a solid particle in a stagnant fluid – is used instead of the slip velocity.

$$Sh = \frac{k_L \cdot d}{D} = 2 + 0.44 \cdot Re^{1/2} \cdot Sc^{0.38}, \quad \textbf{(4.8)}$$

$$Re = \frac{\rho_L \cdot v_s \cdot d}{\mu}, \quad \textbf{(4.9)}$$

$$Sc = \frac{\mu}{\rho_L \cdot D}, \quad \textbf{(4.10)}$$

where Re is the Reynolds number, Sc the Schmidt number, μ the viscosity and ρ_L the density of the liquid. Equation (4.8) is valid for solid-liquid systems where the particles settle faster than $5 \cdot 10^{-4}$ m/s. The free settling velocity can be calculated following [103]:

$$v_t = \left(\frac{4 \cdot g \cdot (\rho_{ol} - \rho_L)}{3 \cdot C_D \cdot \rho_L} \right)^{1/2}, \quad \textbf{(4.11)}$$

where g is the gravitational constant and C_D the drag coefficient. C_D, is a function of the Reynolds number and particle shape [103]. The drag coefficients of spherical particles for the different flow regimes are listed in Table 4.4.

Table 4.5 lists the density and viscosity at 20 °C of the slurry during the dissolution of olivine in acid under the following conditions: 3M H_2SO_4, a solid content of 250 g/L and at 70 °C. The viscosity was measured with a Haake Rotovisco RV 20 at a shear rate of 64 s^{-1}, which is similar to the average shear rate (calculated following the procedure in [103]) in the reactor. The flux of hydrogen ions through the fluid film for different conditions, using the initial concentration of hydrogen ion in the calculations, is listed in Tables 4.6 -

4.8. The diffusion coefficients used in these calculations are in the range 10^{-8} to 10^{-10} m^2/s, which are typical values for liquids [13]. For some of the calculations in Tables 4.6-4.8, the free settling velocity is smaller than $5 \cdot 10^{-4}$ m/s; therefore, Eq. (4.8) is not valid. This equation can be used when the olivine particle size is bigger than 28, 126 and 150 μm for the conditions in Tables 4.6 - 4.8, respectively. When the velocity is lower than $5 \cdot 10^{-4}$ m/s, the Sherwood number is close to two, which is the value for spheres in a stagnant fluid, and this equation is still used as an (under)estimation. In the real case, the slurry is vigorously agitated and the mass-transfer coefficient will be always higher than the values obtained using the method with the free settling velocity. The slowest mass-transfer rate calculated through the liquid film at the beginning and at the end of the dissolution (see Tables 4.6 and 4.8) is $1 \cdot 10^{-5}$ and $2 \cdot 10^{-6}$ $mol \cdot s^{-1} \cdot cm^{-2}$, respectively.

Table 4.4. Hydrodynamic regimes for settling spherical particles [103].

Regime	Reynolds Number	C_D Expression
Laminar	0-0.3	$C_D = 24/Re$
Intermediate	0.3-1000	$C_D = 24/(Re^{0.6})$
Turbulent	>1000	$C_D = 0.445$

Table 4.5. Density and viscosity of the slurry during the olivine dissolution at 20 °C.

Time	ρ_{Sl} (kg/m^3)	μ_{Sl} (Pa·s)
At the beginning of reaction	1180	0.0017
5< X <50	1276	0.0332
End of reaction	1364	0.0452

At the beginning of the reaction, the ρ and μ of the slurry refer to the density and viscosity of 3M H_2SO_4 found in [105]. X refers to the conversion in %. The viscosity was measured at a shear rate of 64 s^{-1}.

Table 4.6. Mass-transfer of hydrogen ions at the initial conditions.

ρ_{Sl} (kg/m^3)	μ_{Sl} (Pa·s)	D (m^2/s)	d (μm)	v_t (m/s)	Re	Sc	Sh	k_L (m/s)	$N_{L,H}$ ($mol \cdot s^{-1} \cdot cm^{-2}$)
1180	0.0017	1.00E-09	10	6.51E-05	4.52E-04	1.44E+03	2.15	2.15E-04	1.29E-04
1180	0.0017	1.00E-09	50	1.63E-03	5.65E-02	1.44E+03	3.66	7.32E-05	4.39E-05
1180	0.0017	1.00E-09	100	1.23E-02	8.54E-01	1.44E+03	8.45	8.45E-05	5.07E-05
1180	0.0017	1.00E-09	500	7.74E-02	2.69E+01	1.44E+03	38.17	7.63E-05	4.58E-05
1180	0.0017	1.00E-08	100	1.23E-02	8.54E-01	1.44E+02	4.69	4.69E-04	2.81E-04
1180	0.0017	1.00E-09	100	1.23E-02	8.54E-01	1.44E+03	8.45	8.45E-05	5.07E-05
1180	0.0017	1.00E-10	100	1.23E-02	8.54E-01	1.44E+04	17.47	1.75E-05	1.05E-05

Table 4.7. Mass-transfer of hydrogen ions between 5 and 50% conversion.

ρ_{Sl} (kg/m^3)	μ_{Sl} (Pa·s)	D (m^2/s)	d (μm)	v_t (m/s)	Re	Sc	Sh	k_L (m/s)	$N_{L,H}$ (mol·s^{-1}·cm^{-2})
1276	0.033	1.00E-09	10	3.18E-06	1.22E-06	2.60E+04	2.02	2.02E-04	1.21E-04
1276	0.033	1.00E-09	100	3.18E-04	1.22E-03	2.60E+04	2.73	2.73E-05	1.64E-05
1276	0.033	1.00E-09	500	7.95E-03	1.53E-01	2.60E+04	10.19	2.04E-05	1.22E-05
1276	0.033	1.00E-08	100	3.18E-04	1.22E-03	2.60E+03	2.31	2.31E-04	1.38E-04
1276	0.033	1.00E-09	100	3.18E-04	1.22E-03	2.60E+04	2.73	2.73E-05	1.64E-05
1276	0.033	1.00E-10	100	3.18E-04	1.22E-03	2.60E+05	3.76	3.76E-06	2.25E-06

Table 4.8. Mass-transfer of hydrogens ion at the end of the reaction.

ρ_{Sl} (kg/m^3)	μ_{Sl} (Pa·s)	D (m^2/s)	d (μm)	v_t (m/s)	Re	Sc	Sh	k_L (m/s)	$N_{L,H}$ (mol·s^{-1}·cm^{-2})
1364	0.045	1.00E-09	10	2.22E-06	6.71E-07	3.32E+04	2.02	2.02E-04	1.21E-04
1364	0.045	1.00E-09	100	2.22E-04	6.71E-04	3.32E+04	2.60	2.60E-05	1.56E-05
1364	0.045	1.00E-09	500	5.56E-03	8.39E-02	3.32E+04	8.65	1.73E-05	1.04E-05
1364	0.045	1.00E-08	100	2.22E-04	6.71E-04	3.32E+03	2.25	2.25E-04	1.35E-04
1364	0.045	1.00E-09	100	2.22E-04	6.71E-04	3.32E+04	2.60	2.60E-05	1.56E-05
1364	0.045	1.00E-10	100	2.22E-04	6.71E-04	3.32E+05	3.43	3.43E-06	2.06E-06

4.2.5 The diffusion through a silica layer as the limiting step

When the diffusion through a silica layer controls the process, the hydrogen ion concentration around the particle is illustrated by Figure 4.3 and described by:

$$N_{so,H} = D_e \frac{[H^+]_B - [H^+]_{ol}}{\theta_{Si}} \approx D_e \frac{[H^+]_B}{\theta_{Si}}, \qquad \textbf{(4.12)}$$

Where $N_{L,H}$ is the molar flux of the hydrogen ion through the liquid layer, D_e the effective diffusion coefficient and θ_{Si} the thickness of the silica layer. In the case that the diffusion through the silica layer controls the process, the surface reaction resistance and $[H^+]_{ol}$ can be neglected. Daval [102] studied the formation of a silica layer around the olivine grains in small unstirred capsules finding a 40 nm layer around the olivine grains with a D_e of $3 \cdot 10^{-22}$ m^2/s. Safari [96] developed a mathematical model for the leaching of zinc ores containing silicates where a silica layer covering the ores was taken into account. The values obtained from Safari's model are a D_e that depends on the temperature for the diffusion through a silica layer of 1.2 μm:

$$\ln D_e = -12.92 - \frac{28167.83}{R \cdot T}, \qquad \textbf{(4.13)}$$

where R is 8.314 J ·mol^{-1} K^{-1}. At 90 °C, the D_e is 2.2·10^{-10} m^2/s. In Perry's Handbook [13] the diffusion coefficient through solids given is in the range of 10^{-10} and 10^{-34} m^2/s and the reference value proposed is 10^{-14} m^2/s.

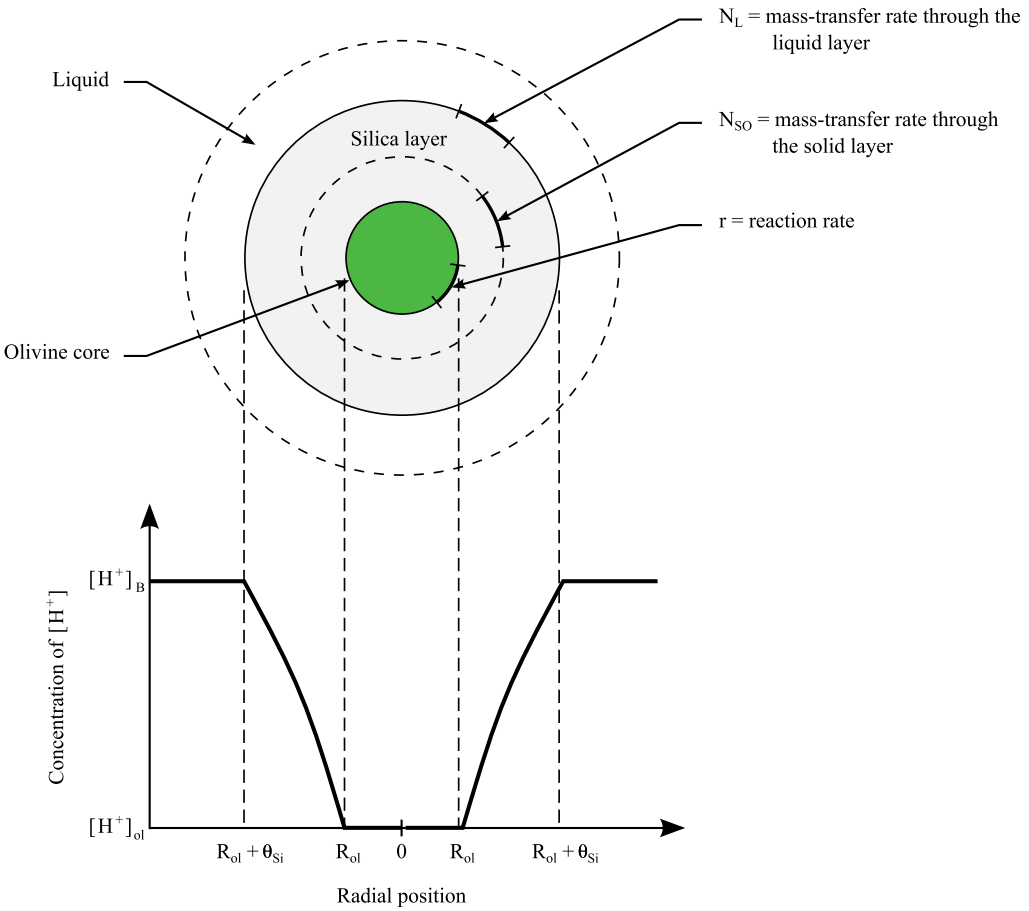

Figure 4.3. Diagram of a reacting olivine particle when the diffusion through the silica layer is the limiting step [94].

Table 4.9 lists the flux of hydrogen ions through a silica layer for the three different diffusion coefficients [13,96,102]. There is a significant difference between the fluxes in this table because the Daval diffusion coefficient is 10^{12} times lower than the Safari diffusivity, while both layers are made up of silica. This reflects the difficulty of obtaining an effective diffusion coefficient.

Table 4.9. Hydrogen ion flux through a silica layer.

D_e (m^2/s)	3.00E-22	2.17E-10	1.00E-14
Reference	**Daval [102]**	**Safari [96]**	**Perry HB [13]**
θ_{Si} (nm)	N_{so} ($mol \cdot s^{-1} \cdot cm^{-2}$)	N_{so} ($mol \cdot s^{-1} \cdot cm^{-2}$)	N_{so} ($mol \cdot s^{-1} \cdot cm^{-2}$)
1	1.80E-13	1.30E-01	6.00E-06
10	1.80E-14	1.30E-02	6.00E-07
50	3.60E-15	2.61E-03	1.20E-07
500	3.60E-16	2.61E-04	1.20E-09

4.2.6 Overall resistance

The overall hydrogen ion flux is in the range of $1.82 \cdot 10^{-9}$ to $1.31 \cdot 10^{-10}$ and $3.12 \cdot 10^{-8}$ to $1.28 \cdot 10^{-9}$ $mol \cdot cm^{-2} \cdot s^{-1}$ for experiments NS-2 and NS-10 at the beginning and at the end of the reaction (see Table 4.10), respectively. The slowest hydrogen ion flux through the fluid film at the beginning and at the end of the reaction, calculated in Tables 4.6 and 4.8, is 10^{-5} and $2 \cdot 10^{-6}$ $mol \cdot s^{-1} \cdot cm^{-2}$, respectively. Thus, the resistance due to the liquid film can be neglected because the transport through it is much faster than the overall flux. The resistance due to the silica layer could not be neglected in the case that a silica layer would actually exist and the value of D_e would be $3 \cdot 10^{-22}$ $m^2 \cdot s^{-1}$ or smaller. However, the presence of a silica layer under the olivine nano-silica process conditions is unlikely due to the vigorous agitation, high solid content (250 g/L) and strongly acidic medium, which improves the abrasion and increases the polymerization of silica. SEM pictures of the olivine grains (taken under the dissolution conditions presented in Chapter 3) show that only on rare occasions the olivine grains were partly covered by silica. In addition, etch pits and dissolutions cracks were also found in the pictures, which are indicative of a rate controlled by surface reaction [90]. Thus, it can be considered that the overall flux is controlled only by the surface reaction. In the case that a silica layer would cover the olivine grains, which is unlikely, the overall flux would involve both steps, the surface reaction and the diffusion through the silica layer.

Table 4.10. Species flux for experiments NS-2 and NS-10 at the beginning and at the end of the reaction.

Sample	$Fraction_{Ol}$ (μm)	T_r (°C)	$N_{ol,1}$ ($mol \cdot s^{-1} \cdot cm^{-2}$)	$N_{ol,2}$ ($mol \cdot s^{-1} \cdot cm^{-2}$)	$N_{H,1}$ ($mol \cdot s^{-1} \cdot cm^{-2}$)	$N_{H,2}$ ($mol \cdot s^{-1} \cdot cm^{-2}$)
NS-2	150-250	52.0	4.54E-10	3.27E-11	1.82E-09	1.31E-10
NS-10	150-250	89.8	7.80E-09	3.21E-10	3.12E-08	1.28E-09

$N_{ol,1}$ and $N_{ol,2}$ are rate of the consumption of olivine and $N_{H,1}$ and $N_{H,2}$ are the molar fluxes (per cm^2) of hydrogen ions, at the beginning and at the end of the experiments, respectively.

4.3 Surface reaction model

4.3.1 Hydrogen ion activity

The evolution of different species with the conversion degree for the olivine dissolution is plotted in Figure 4.4. Silica is not plotted in this graph because its concentration is constant once the solubility value is reached, which happens almost immediately (Table 4.2). Using these concentrations as inputs for the PHREEQC model [106] the activity of the hydrogen ions was calculated. Figure 4.5 plots the calculated hydrogen ion activity versus the pH of the solution at 20, 50 and 90 °C.

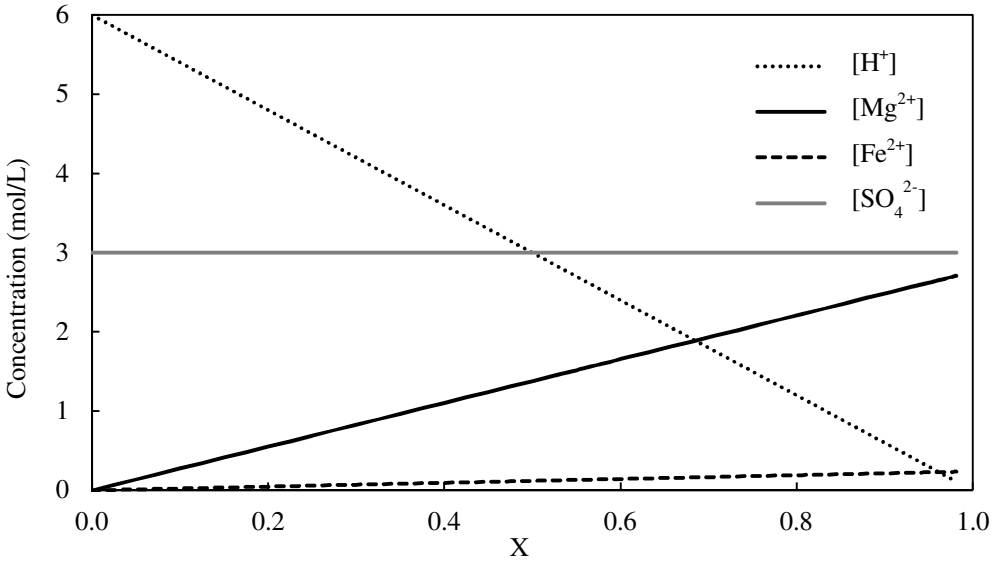

Figure 4.4. Estimated evolution of $[H^+]$, $[Mg^{2+}]$, $[Fe^{2+}]$ and $[SO_4^{2-}]$ against the conversion degree of the olivine dissolution in 3M sulfuric acid.

In order to incorporate the hydrogen ion activity in the model without the use of the PHREEQC software-model, the activity curves were fitted to two polynomial equations below and above a pH of -0.4 for temperatures between 20 and 90 °C:

$$-\log[a_{H^+}] = a_4 \cdot pH^4 + a_3 \cdot pH^3 + a_2 \cdot pH^2 + a_1 \cdot pH + a_0 \,. \qquad \textbf{(4.14)}$$

The constants of Eq. (4.14) are a function of the temperature and can be fitted with another polynomial equation:

$$a_i = b_{2i} \cdot T^2 + b_{1i} \cdot T + b_{0i} \,. \qquad \textbf{(4.15)}$$

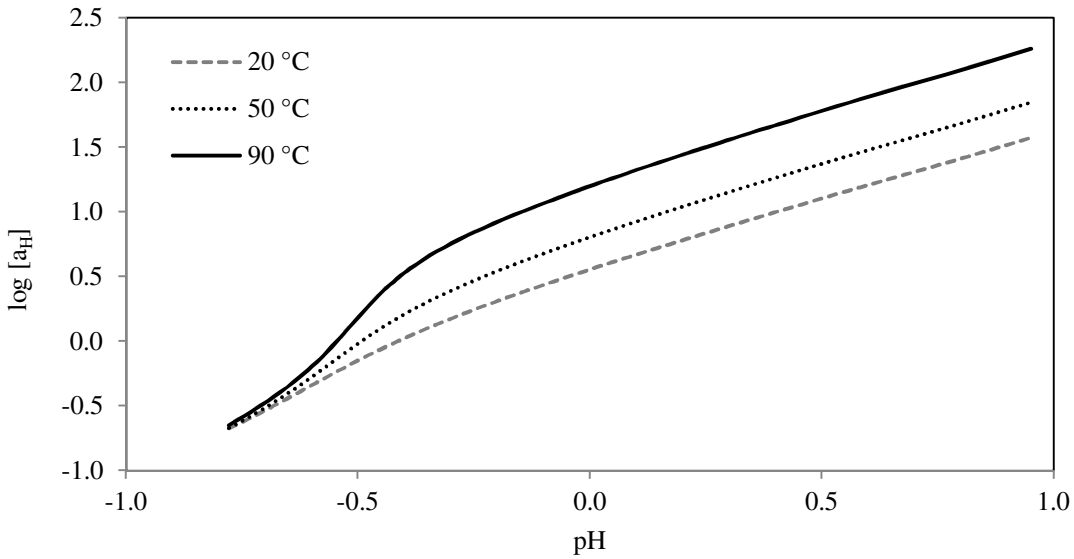

Figure 4.5. Hydrogen ion activity calculated using the PHREEQC model [106], versus the pH of the solution at 20, 50 and 90 °C.

The fitting constants of Eq. (4.15) are listed in Tables 4.11 and 4.12. From these results, the constants of Eq. (4.14) can be obtained, and, with them, the hydrogen ion activity can be calculated for different pH values and temperatures.

Table 4.11. Fitting constants of Eq. (4.15) for pH < -0.4 and the determination coefficient.

	a_4	a_3	a_2	a_1	a_0
b_2	-1.381E-02	-3.197E-02	-2.678E-02	-9.523E-03	-1.191E-03
b_1	4.942E-01	9.994E-01	7.090E-01	2.170E-01	2.901E-02
b_0	-3.787E+00	-8.638E+00	-7.405E+00	-1.260E+00	1.510E-01
R^2	0.9999	1.0000	1.0000	1.0000	1.0000

Table 4.12. Fitting constants of Eq. (4.15) for pH > -0.4 and the determination coefficient.

	a_4	a_3	a_2	a_1	a_0
b_2	-9.476E-06	6.474E-06	1.165E-05	-1.337E-05	2.124E-05
b_1	-3.102E-03	6.379E-03	-5.246E-03	2.997E-03	6.958E-03
b_0	-2.150E-02	1.121E-01	-1.587E-01	1.115E+00	4.069E-01
R^2	0.9994	0.9995	0.9997	0.9999	1.0000

4.3.2 Shrinking core model and specific surface area

As was stated in Chapter 3, the specific surface area is calculated with the Brantley equation using the geometric particle size distribution (PSD_G). Because the fraction dissolved is in the range of 0 to 99%, the specific surface area of olivine significantly changes over time. Therefore, a shrinkage model should be used that takes into account the particle size reduction. The best model in this case, where no solid layer is involved, is the shrinking particle (Figure 4.1). The particle size reduction (ΔR) as a function of the olivine consumed, considering spherical particles, can be described by:

$$\Delta R = \sqrt[3]{\frac{3}{16\cdot\pi}\cdot\frac{n_{H^+_{con}}\cdot M_{ol}}{\rho_{ol}}} = 1.3921\cdot\sqrt[3]{n_{H^+_{con}}}\,, \qquad \textbf{(4.16)}$$

where $n_{H^+_{con}}$ is the number of hydrogen ions consumed by the olivine and M_{ol} the molar mass of olivine. Using this equation, the PSD_G with the conversion degree can be obtained and, likewise, the SSA_{Br}. However, the equation proposed by Brantley was obtained for laboratory-ground primary silicates and not for weathered silicates. Because there is no better alternative to estimate the SSA of weathered olivine, the SSA_{Br} equation is employed here. In addition, the use of the Brantley equation (see Eq. (3.3)) gives erroneous values when most of the olivine (above 80%) is consumed as can be seen in Figure 4.6. The cause of this is a calculation issue that appears because: 1) a discrete particle size distribution is used; 2) the difference between ΔR and R is extremely small, which gives an extraordinary high surface area; and 3) the Brantley equation is logarithmic. Figure 4.7 shows the variation of the relative roughness surface area, λ/λ_i, with the olivine consumed, where the same calculation problem can be observed. An expression that determines the λ without this problem can be obtained by fitting the relative roughness surface below 80% of the olivine consumed (m_{ol_con}) to a polynomial equation and multiplying it by the initial (prior to dissolution) roughness factor:

$$\lambda = \lambda_i\cdot\left[A\cdot(m_{ol\_con})^5 + B\cdot(m_{ol\_con})^4 + C\cdot(m_{ol\_con})^3 + D\cdot(m_{ol\_con})^2 + E\cdot(m_{ol\_con})^2 + 1\right] \textbf{(4.17)}$$

The constants of this equation are listed in Table 4.13. Because the relative roughness surface areas show similar trends, this equation can be used to calculate the roughness factor for all the dunite fractions used in the dissolution experiments after shrinking. Therefore, using Eq. (4.17), the specific surface area for all the different PSD of olivine during the reaction can be estimated.

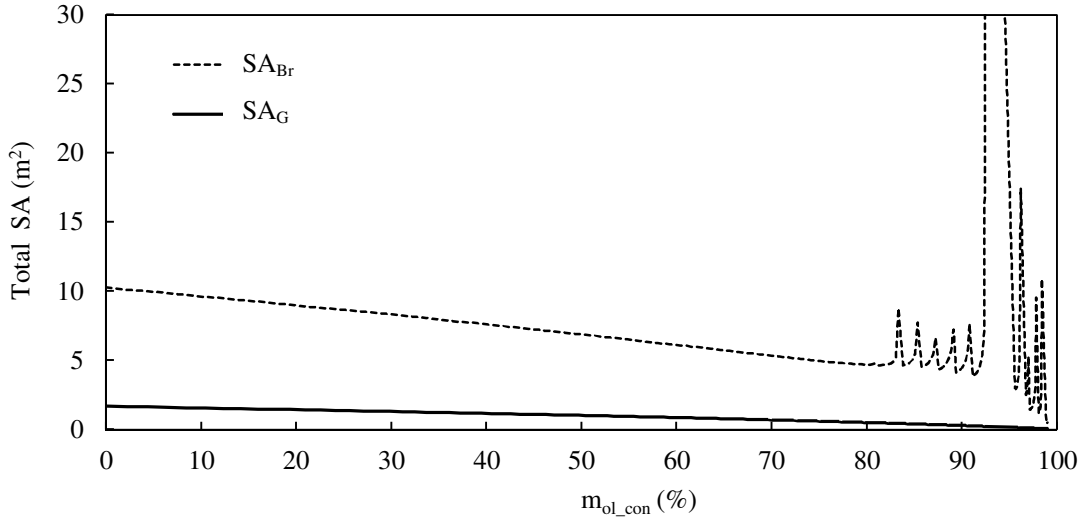

Figure 4.6. Evolution of the total surface areas, SA_{Br} and SA_G, with the olivine consumed for experiment NS-4 (220 g/L of olivine in 3M H_2SO_4).

The amount of olivine is calculated from the dunite quantity and its olivine content.

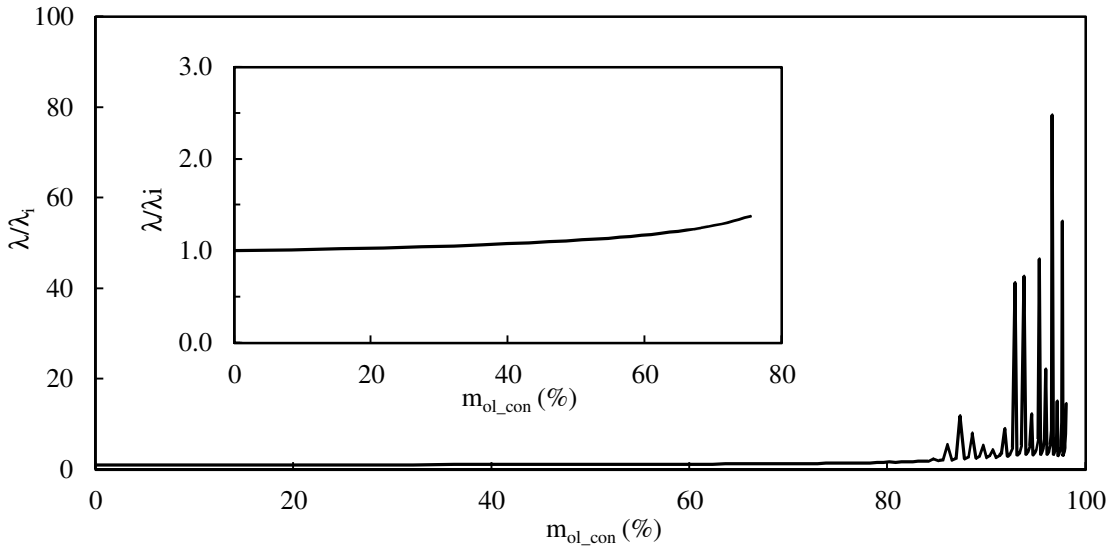

Figure 4.7. Variation of the relative roughness surface area, λ/λ_i, with the olivine consumed for experiment NS-4.

Table 4.13. Fitting constants of Eq. (4.17).

A	B	C	D	E
2.9795E-09	-5.2239E-07	3.2821E-05	-8.2023E-04	8.0935E-03

It is remarkable that the relative roughness surface area (λ/λ_i) shown in Figure 4.7 slightly increases with the mass of olivine consumed (i.e., the conversion degree), whereas the

expected trend for λ/λ_I of silicates should be a decrease with the conversion degree. This difference is not only because the Brantley equation was obtained for laboratory-ground primary silicates, but also because this equation considers that λ is dependent on the grain size.

4.3.3 Mass balance

In addition to the hydrogen ion activity and the specific surface area of the shrinking cores, a mass balance is required in order to develop a model for the experimental data of the hydrogen ion concentration. A mass balance over the hydrogen ions results in:

$$[H^+](t) = [H^+]_i - (4 \cdot r \cdot SSA) \cdot \Delta t \,, \qquad \textbf{(4.18)}$$

where $[H^+]$ is the hydrogen ion concentration, r the dissolution rate, SSA the specific surface area of olivine and t the time.

The model proposed in this Chapter studies the changes of the hydrogen ion concentration with time. The programming language used to develop the model was Visual Basic. This model includes three parts: the mass balance of the hydrogen ion (Eq. (4.18)), the shrinking core model of the olivine grains (Eq. (4.16)) and the olivine dissolution kinetics (Eq. (4.1)). The experimental variables of this model are the specific surface area of olivine, the reaction temperature and the hydrogen ion activity. The model factors that need to be calculated from the fitting to the experimental data are the kinetic parameters k_T and n.

4.4 Results

The kinetic parameters, k_T and n (see Eq. (4.1)), can be obtained by fitting the model based on Eq. (4.18) to the experimental results. For each dissolution experiment, a set of parameters that minimize the error between the kinetic model and the experimental data was obtained. Figure 4.8 shows the experimental data and two calculated dissolution curves for the n values of 0.35 and 0.5, and a rate constant of $3.45 \cdot 10^{-9}$ ($mol \cdot cm^{-2} \cdot s^{-1}$) for experiment NS-8. The calculated dissolution curve of n = 0.5 gives better results than the curve of 0.35.

Table 4.14 lists the values of k_T and n that produced the best fit for experiments NS-1 to NS-10, where dunite CRS-US (see Chapter 3) was used. The calculated dissolution curves, obtained using the best fitting values of k_T and n, are shown in Appendix II. The activation energy and the pre-exponential factor can be calculated from a linear regression of the logarithm of k_T versus the inverse of the temperature, as can be seen in Figure 4.9. In this figure, experiment NS-3 was not included in the linear regression because it did

not follow the general trend. The linear regression closely fits the logarithmic values resulting in a determination coefficient above 99%. Working out this equation results in a pre-exponential factor of 856 (mol·cm^{-2}·s^{-1}) and an activation energy of 78.5 (kJ/mol):

$$r = 856 \cdot \exp\left(\frac{-78.5}{R \cdot T}\right) \cdot a_{H^+}^{0.5} . \qquad \textbf{(4.19)}$$

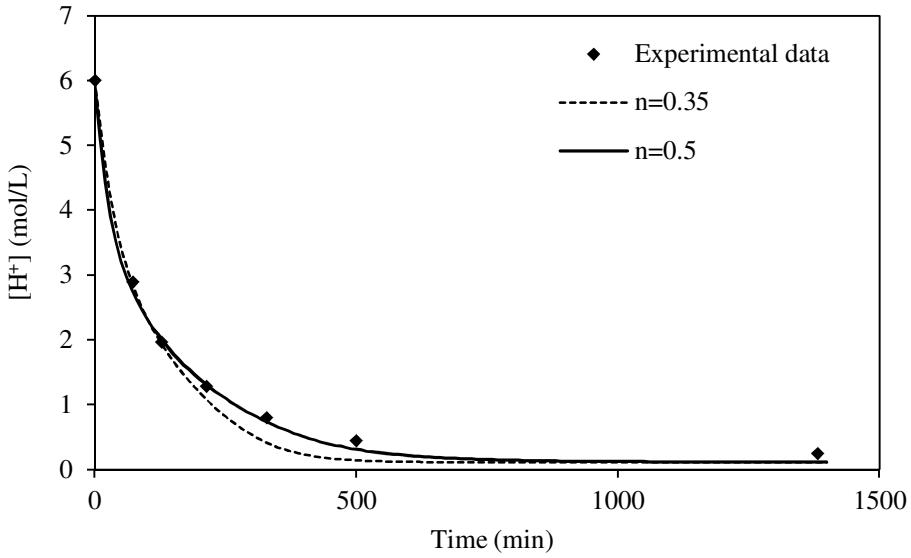

Figure 4.8. Experimental data and calculated dissolution curves for n of 0.35 and 0.5 and k_T of 3.45 ·10^{-9} (mol·cm^{-2}·s^{-1}) for experiment NS-8.

Table 4.14. Values of k_T and n producing the best fitting for experiments NS-1 to NS-10 using dunite CRS-US.

Experiment	k_{T_fit} (mol·cm^{-2}·s^{-1})	n	T (°C)
NS-1	1.45E-10	0.5	48.75
NS-2	2.10E-10	0.5	52.07
NS-3	3.00E-10	0.5	51.11
NS-4	9.30E-10	0.5	70.21
NS-5	1.04E-09	0.5	70.67
NS-7	4.10E-09	0.5	88.51
NS-8	3.45E-09	0.5	86.19
NS-9	1.95E-10	0.5	50.57
NS-10	3.90E-09	0.5	89.75

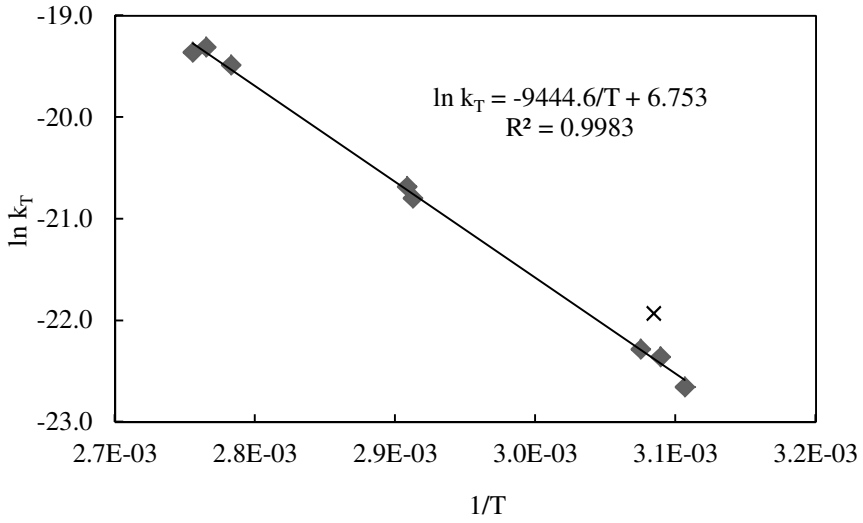

Figure 4.9. Logarithm of k_T versus the inverse of the temperature for experiments with dunite CRS-US.

Experiment NS-3 is not included in the regression.

Table 4.15 lists the rate constants calculated using Eq. (4.19) and the error between the k_{T_fit} and k_{T_cal}. The average error in k_{T_cal} −excluding experiment NS-3− is 5%.

Table 4.15. Rate constants calculated and the error between the k_{T_fit} and k_{T_cal}.

Experiment	k_{T_cal} (mol·cm^{-2}·s^{-1})	Error (%)
NS-1	1.549E-10	6.85
NS-2	2.090E-10	0.46
NS-3	1.919E-10	36.02
NS-4	9.701E-10	4.32
NS-5	1.006E-09	3.23
NS-7	3.901E-09	4.86
NS-8	3.296E-09	4.46
NS-9	1.828E-10	6.27
NS-10	4.266E-09	9.38

Comparing the reaction constant (k_{T_cal}) of NS-1 and NS-10 at 49 and 90 °C, the reaction at 90 °C is 27 times faster than at 50 °C. Table 4.16 shows the temperature rise needed to double the rate of reaction for activation energies in the range 40 to 78.5 kJ·mol^{-1}, which is the E_a range found in the literature for the olivine dissolution (see Table 4.1). At 40 kJ·mol^{-1} (smallest activation energy found in the literature), the required temperature rise to double the reaction rate is considerably higher than at 78.5 kJ·mol^{-1}. Thus, the higher

the E_a is, the more temperature-sensitive the kinetics is. This means that the model proposed here with an E_a of 78.5 kJ·mol^{-1} is more sensitive to the temperature than the models in the literature (except in the study of Wogelius [21]). Usually, chemical reactions are more temperature-sensitive than the physical steps (e.g. diffusion transport).

Table 4.16. Temperature rise needed to double the rate of reaction for activation energies in the range 40 to 78.5 kJ/mol.

Ea (kJ mol^{-1})		40	50	60	70	78.5
		Temperature rise (°C)				
T (°C)	25	13.4	10.7	8.8	7.5	6.7
	50	15.8	12.5	10.4	8.8	7.9
	90	20	15.9	13.1	11.2	10

This kinetic model was also used with experiments NS-11 to NS-14, where dunite GL50 was employed. Table 4.17 presents the fitted and calculated reaction constants for these experiments as well as the error between the two values of k_T. In experiments NS-11, -12 and -13, where the same dunite fraction was used (see Chapter 3), the fitted rate constant is around 8% smaller than the calculated rate constant. The error in experiment NS-14, where another dunite fraction and a reaction volume 20 times larger was used, is around 7% higher than the calculated rate constant. The average error between k_T calculated and fitted for experiments conducted with dunite GL50 is 7.6%.

Table 4.17. Fitted and calculated reaction constants for experiments with dunite GL50 and the error between these two k_T.

Exp.	T (°C)	k_{T_fit} (mol·cm^{-2}·s^{-1})	k_{T_cal} (mol·cm^{-2}·s^{-1})	Error (%)
NS-11	90.0	3.950E-09	4.343E-09	9.96
NS-12	89.7	4.000E-09	4.253E-09	6.34
NS-13	89.9	4.020E-09	4.319E-09	7.44
NS-14	70.2	1.040E-09	9.691E-10	6.81

4.5 Discussion

The kinetic parameters E_a and n obtained for the model proposed here are in the range found in the literature. The activation energy is slightly higher than in most of the kinetics studies (except for the work of Chen [24], where the E_a is dubious as is explained before), only being above this value the E_a reported by Wogelius [21]. Comparing with the E_a

obtained by Jonckbloedt [12], the activation energy in the experiments performed in this study is 18% higher, which makes the developed model more temperature-sensitive than Jonckbloedt's model. The reaction order found here agrees with most of the data from the literature, but disagrees with the kinetic model of Jonckbloedt.

The reaction order of 0.5 was explained by Rosso [10] as the formation of an activated complex, where two hydrogen ions attach to each of the two bridging oxygen atoms, and, simultaneously, water molecules displace the Mg-O bonds. This activated complex should be less rigid than the olivine structure, breaking down to aqueous species. Rimstidt [91] stated that the forsterite dissolution involves chain reactions with several elementary reaction stages. Thus, the reaction order (likewise the kinetic parameter A and E_a) here obtained should be considered as apparent values of the overall process.

The rate constant and the dissolution rate, calculated with the model developed, at 25 °C and pH of 2 are presented in Table 4.18. The dissolution rate agrees with the results from the literature showing the validity of the kinetic model. Unfortunately, the dissolution rate of the model proposed here cannot be compared with the one of Jonckbloedt because he did not report the SSA_G. The kinetic model developed (obtained using dunite CRS-US) can also be used for dunite GL50 with an error of 7.6%. In addition, an experiment with a reaction volume 20-times larger (NS-14) was also well described by Eq. (4.19), confirming the robustness of the model.

Table 4.18. Dissolution rate and rate constant calculated using Equation (4.19).

T (°C)	pH	k_{T_cal} ($mol \cdot cm^{-2} \cdot s^{-1}$)	r ($mol \cdot cm^{2} \cdot s^{-1}$)
25	2	1.51E-11	1.51E-12

4.6 Conclusion

Several assumptions have been made about the dissolution of olivine in acid under the conditions of nano-silica production such as: 1) the process is not controlled by the diffusion through a silica layer but by the surface reaction; 2) the olivine particles shrink over time as the shrinking particle model describes (Figure 4.1a); and 3) the specific surface area of olivine can be estimated using the roughness factor based on the Brantley equation. In order to avoid calculation problems generated when entering the SSA_{Br} in the model, the evolution of the relative roughness factor with the consumption of olivine was determined (Figure 4.7 and Eq. (4.17)). From the good correlation between the experimental data and the proposed model it can be inferred that the assumptions made are reasonable.

In this study an activation energy of 78.5 kJ/mol and a reaction order of 0.5 were obtained. This activation energy is slightly higher than that reported in most kinetics studies. The

dissolution rate and rate constant at pH value of 2 and 25 °C are $1.5 \cdot 10^{-12}$ mol·cm^{-2}·s^{-1} and $1.5 \cdot 10^{-11}$ mol·cm^{-2}·s^{-1}, respectively, which are comparable to the values found in the literature.

The average error between k_{T_cal} and k_{T_fit} is 5%, which shows a good agreement between the present model and the olivine dissolution experiments for dunite CRS-US. The average error of k_{T_cal} for dissolution experiments performed with dunite GL50 is slightly higher (7.6%).

This kinetic model can be applied, with good accuracy, to predict the olivine dissolution under the nano-silica production conditions for other dunite materials than those used in this work, and for other reaction volumes. Therefore, it can be used in the industrial production of nano-silica to predict the evolution of the conversion over time.

Chapter 5. Properties of olivine nano-silica

5.1 Introduction

As mentioned in Chapter 1, a wide range of silica products is presently manufactured for various applications. World demand for specialty silicas is rising 5.6% per year to reach 2.8 million metric tons in 2016, and in economic terms, the market is expected to grow by 7.5% to reach $6.4 billion in 2016 [3]. Nowadays, there are two main commercialized routes for the productions of synthetic amorphous silica, which are the thermal route and the wet route (see Chapter 1) [1]. In these production methods, a high temperature process is involved (above 1000 °C). To reach these temperatures huge amounts of fuel are consumed making these processes: a) non-sustainable because of the scarcity of fuels; b) not environmentally friendly because of the huge amount of CO_2 emitted; and c) expensive because of the fuel price.

An alternative synthesis route to the commercial production methods of amorphous nano-silica with low energy requirements (reaction temperature below 100 °C and exothermic reaction) is the dissolution of olivine in acid. The dissolution of olivine, which follows Eq. (1.4), yields a slurry consisting of a mixture of magnesium/iron salts, amorphous silica, unreacted olivine and inert minerals. Once the reaction is complete, the unreacted olivine and inert minerals are removed from the final suspension by sedimentation. Subsequently, the silica can be cleaned from the magnesium/iron salts by washing and filtering.

When a stoichiometric amount of olivine is placed in a reactor together with 3M sulfuric acid, 1.5 moles of silica will be produced. The concentration of the hydrogen ion, silica and olivine in the slurry (but not in the solution) versus the conversion degree is plotted in Figure 5.1. Once the silica concentration is above the solubility value, which is 150 mg/L at the pH level of 1 [92], silica starts to nucleate and condensate. This concentration is reached for a conversion of 0.1664% (see Chapter 4 and Table 4.2), which already occurs after 4 seconds of reaction in experiment NS-10 (at 90 °C) and after 90 seconds in experiment NS-2 (at 52 °C). Therefore, it can be assumed that the nucleation starts from the beginning of the experiment. The primary particles formed in a silicic acid solution are around 5 nm [4,93]. These silica particles grow forming siloxane bonds as described by Eq. (4.3). The silica condensation reaction below the isoelectric point mainly depends on the hydrogen ion concentration and temperature; the presence of other ions in the solution also influences the condensation reaction, however, its effect is less significant [4,93]. As was stated in Chapter 4, Gorrepati found that silica particles grow to 200 nm in 100 minutes in an 8M HCl solution at 5 °C and with an initial concentration of 135 mmol/L [93].

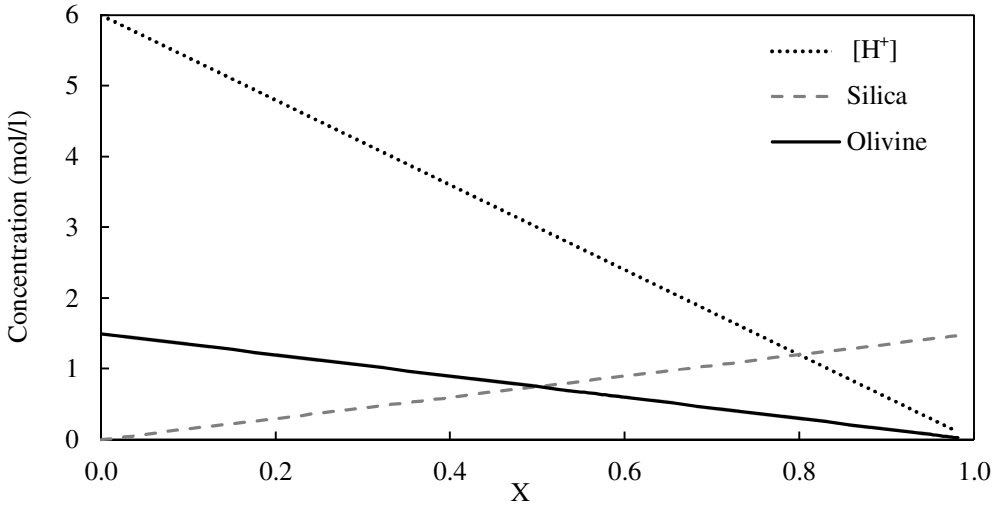

Figure 5.1. Species concentration versus the conversion degree for the dissolution of olivine in 3M sulfuric acid.

The texture of nano-silica is a complex topic reviewed by several researchers [28,29,32,107], but only Lieftink [30,32] studied in depth the nano-silica produced from olivine. Although Lieftink [30] provided interesting results, more data about the following items are desired: i) the effects of the process variables (surface area of olivine, hydrogen ion activity and temperature) on the textural properties of the resulting nano-silica; ii) the influence of the mode of operation on the process, particularly on the process yield; iii) the chemical composition of nano-silica produced in order to establish the impurities left.

In the previous chapters, attention was paid to the kinetics of the dissolution of olivine for the production of nano-silica. The main purpose of this chapter is to assess the properties of the nano-silica synthesized (i.e., specific surface area, porosity and content of impurities), in order to demonstrate that amorphous porous nano-silica can be produced satisfactorily by the dissolution of olivine in acid. An additional aim is to present new data and more details about the influence of the process conditions on the textural properties (i.e., size of the primary particles and size and shape of the agglomerates), separation efficiency, and content of impurities of the nano-silica produced.

5.2 Review of the olivine nano-silica

The main researcher in this area, Lieftink [30], who studied the texture of the silica produced by the dissolution of olivine, showed that variation of the production rate and the total reaction time led to different silica textures. Thus, Lieftink stated that the silica texture generated during the reaction of olivine is mostly determined by the dissolution rate of olivine. The dissolution of olivine in acid depends on the surface area of olivine,

hydrogen ion activity and temperature (see Chapter 4 and Eq. (4.19)). Therefore, increasing the surface area of olivine, hydrogen ion activity and/or temperature will increase the reaction rate.

Lieftink [30] stated that when the dissolution of olivine exhibited a slow rate, particle growth occurred; and when the dissolution proceeded rapidly, particle growth occurred as well, but slower. Particle growth proceeded according to a particle agglomeration model, which implies that the final cluster size was determined by the rate of formation of 2 nm particles (primary particles formed after nucleation) and the agglomeration of these particles into clusters. Therefore, when the 2-nm particles were produced rapidly, the probability of agglomeration of two small particles was larger than the probability of accommodation of small particles into a larger, growing particle.

Another factor which influences the texture of nano-silica, especially the specific surface area, is the amount of magnesium sulfate. The separation and washing of the olivine nano-silica increases its specific surface area and its pore volume. Washing does not affect the texture of the silica, but removes the magnesium sulfate from the pores. Therefore, the washing of olivine nano-silica can be considered as the extraction of magnesium sulfate from the porous system. Lieftink [30] reported that seven washing steps using 100 ml of demineralized water were needed to remove almost all magnesium sulfate from 750 ml of colloidal nano-silica, increasing the surface area from 50 to 300 m^2/g.

The specific surface area (SSA_{BET}), external specific surface area (SSA_E) and reaction time (t_r) of the olivine nano-silica produced by Lieftink [30] at different temperatures are presented in Table 5.1. This olivine nano-silica presented a SSA_{BET} in the range of 140 to 400 m^2/g and exhibited micropores, mesopores and macropores [30].

Table 5.1. Specific surface area of the olivine nano-silica prepared by Lieftink in the temperature range between 40 and 90 °C [30].

	Coarse (425-1000 μm)			Fine (90-425 μm)		
T (°C)	**SSA_{BET} (m^2/g)**	**SSA_E (m^2/g)**	**t_r (h)**	**SSA_{BET} (m^2/g)**	**SSA_E (m^2/g)**	**t_r (h)**
40	140	110	145.8	227	151	71.7
50	-	-	62.5	-	-	7.2
70	280	186	22.5	310	209	5.7
90	340	263	4.3	399	312	2.5

where coarse and fine refers to the olivine particle size.

5.3 Process yield of the olivine nano-silica

The process yield (Y_{NS}) is defined as the proportion between the amount of nano-silica produced experimentally (m_{NS_exp}) and the potential nano-silica present in the olivine calculated theoretically (m_{NS_th1}):

$$Y_{NS}(\%) = \frac{m_{NS\_exp}}{m_{NS\_th1}} \cdot 100 . \quad \textbf{(5.1)}$$

The theoretical nano-silica is expressed as:

$$m_{NS\_th1} = m_{ol} \cdot M_{SiO_2} / M_{ol} , \quad \textbf{(5.2)}$$

where m_{ol} is the mass of olivine, and M_{SiO_2} and M_{ol} are the molar masses of silica and olivine, respectively. The m_{NS_exp} is calculated with:

$$m_{NS\_exp} = m_{NS\_exp\_im} \cdot w_{SiO_2} , \quad \textbf{(5.3)}$$

where $m_{NS\_exp\_im}$ (g) is the total mass of nano-silica dried at 120 °C (i.e., silica with impurities) and w_{SiO_2} (%) the silica content or silica mass fraction of the dried material, which can be determined if the other compounds present in the material are known. Besides silica, silanol groups, physisorbed water and sulfates can also be found in this dried nano-silica.

When silica is thermally treated, the physisorbed water is removed at about 150 °C. At 200 °C, all the physisorbed water from the surface has evaporated, but the silanol groups still remain. Above this temperature, silanol groups condense releasing water according to Eq. (4.3). This happens in 3 different steps: i) at 450-500 °C vicinal groups, which structure is represented in Figure 5.2, condense; ii) at 600-800 °C internal silanol groups (also commonly called structurally bound water, see Figure 5.2) condense; and iii) up to about 1000-1100 °C, only the isolated silanol groups remain on the silica surface [6]. Iron and magnesium sulfate decompose at around 460 and 800 °C [108], respectively; and sulfuric acid decomposes at 340 °C [109].

The silica content, w_{SiO_2}, can be calculated from thermogravimetric analysis (TGA) as the difference between the final mass fraction of the TGA at 1100 °C and the oxide content with:

$$w_{SiO_2}(\%) = \left(w_{1100} - w_{MgO} - w_{FeO}\right) \Big/ \left(100 - w_{20-120}\right), \quad \textbf{(5.4)}$$

where w_{20-120} is the mass fraction loss in the interval 20-120 °C due to the release of water adsorbed by the nano-silica.

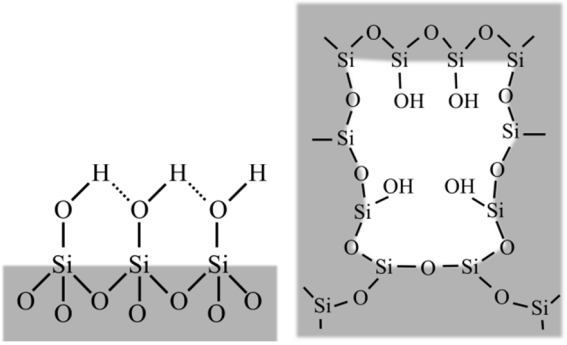

Figure 5.2. Representation of silanol groups: a) vicinal silanols and b) internal silanol groups of silica [5].

The fourth oxygen is above or below the plane of the paper.

Another important parameter of the process is the separation efficiency (E_{Sep}) defined as the proportion between the mass of nano-silica produced experimentally and the mass of the nano-silica that can be potentially produced from the reacted olivine (m_{NS_th2}):

$$E_{sep}(\%) = \frac{m_{NS\_exp}}{m_{NS\_th2}} \cdot 100 . \qquad \textbf{(5.5)}$$

In this case the theoretical amount of nano-silica is expressed as:

$$m_{NS\_th2}(g) = n_{H\_neu} \cdot M_{SiO_2} / 4 , \qquad \textbf{(5.6)}$$

where n_{H_neu} is the amount of hydrogen ions neutralized.

Generally, the process yield depends on the conversion degree of the reaction and on the separation efficiency of the post reaction treatments. Because in the olivine nano-silica experiments presented here almost all the olivine reacts with sulfuric acid, the yield depends mainly on the amount of nano-silica lost in the separation steps. When the separation is performed by filtration, which is the most common method to separate the silica from the sulfate salts, the process yield depends on the time required to produce the silica cake and the properties of the silica cake. For the olivine nano-silica process, Jonckbloedt [12] reported a production of 65 g of nano-silica per kg of 3M sulfuric acid and 190 g of olivine, resulting in a separation efficiency of 67%. This value is calculated from the amount of $[H^+]$ neutralized because no data about the purity of olivine was reported.

5.4 Materials and methods

The dunite rock used in this chapter was CRS-US (see Table 3.3). The desired grain size fractions were obtained by wet-sieving. Then, the sieve fractions were ultrasonically treated with ethanol to remove any adhering fines. Approximately 88.4 wt.% of the rock was olivine with the composition $(Mg_{1.86}Fe_{0.133}Ni_{0.007})SiO_4$, with a forsterite content of 93% and a molar mass of 145.13 g/mol.

Experiments were carried out at 50, 70 and 90 °C with dunites of different size fractions (the experimental method used is described in more detail in Chapter 3). The neutralization reaction was stopped when the concentration of $[H^+]$ reached 0.1 mol/L when it was stopped. Subsequently, the stirrer was switched off and the slurry was left for ten minutes, after which the silica suspension was separated from the solid residue by sedimentation. After that, the resulting suspension was washed with 500 ml of 0.1 M sulfuric acid solution and filtered over a Buchner funnel with a vacuum pump (P_{abs} = 0.2 bar). Sulfuric acid was chosen as the rinsing liquid to prevent oxidation of iron. The washing and filtering processes were repeated four times, except in cases where too much silica escaped with the filtrate.

The nano-silica produced dried at 105 °C was characterized by ICP-MS, combustion infrared analysis, TG analysis, gas physisorption and TEM. The TG analysis was corrected for buoyancy effects; the temperature was increased gradually from room temperature to 1100 °C at 1 °C/min, keeping it constant for two hours at 200 °C and 1100 °C (see Chapter 2 for more details). The evacuation conditions prior to the gas physisorption analysis were 120 °C for 240 minutes.

The purity of the silica can be calculated with:

$$P_{Si}(\%) = 100 - w_{im}\ , \qquad \textbf{(5.7)}$$

where w_{im} is the mass fraction of impurities (i.e., sulfates and metallic ions), considering that sulfur is in the sulfate form.

5.5 Results

5.5.1 Experimental conditions

The experiments carried out are shown in Table 5.2 together with the amount of reagents used ($m_{H_2SO_4}$ and m_{ol}), molecular ratio of hydrogen ions/olivine, average particle size of olivine, d_{ol}, and reaction temperature, T_r. The neutralization curves of these experiments are presented in Appendix II.

Table 5.2. Initial conditions of the olivine nano-silica experiments.

Sample	$m_{H_2SO_4}$ (g)	m_{ol} (g)	Ratio H^+/Ol	d_{ol} (µm)	T_r (°C)
NS-1	589.1	109.8	4.5	138	48.7
NS-2	593.5	125.0	4.0	200	52.0
NS-3	555.8	121.7	3.8	400	55.0
NS-4	532.7	112.6	4.0	200	70.2
NS-5	593.9	122.9	4.0	400	70.7
NS-6	594.2	113.1	4.4	550	69.9
NS-7	593.7	119.4	4.2	275	87.7
NS-8	592.3	121.5	4.1	400	86.2

3M sulfuric acid was used in all the experiments.

Table 5.3 shows the key parameters for the production of nano-silica. These parameters are the $[H^+]_{final}$ at which the reaction was stopped, reaction time, t_r, time required to reach $[H^+]$ of 1M, aging time, t_{ag}, amount of unreacted olivine, m_{ol_unr}, olivine conversion, X_{ol}, and filtration steps. The aging time was calculated as the difference between the total reaction time and the time when 90% of the olivine was consumed.

Table 5.3. Parameters of the production of olivine nano-silica.

Sample	$[H^+]_{final}$ (mol/L)	t_r (h)	t_r $[H^+]$ = 1M (h)	t_{ag} (h)	m_{ol_unr} (g)	X_{ol} (%)	Filt. Steps
NS-1	0.93	46.0	43.4	11.5	4.6	95.1	2
NS-2	0.24	71.0	29.7	35.8	5.0	95.4	4
NS-3	0.31	75.0	37.2	5.9	10.0	90.6	3
NS-4	0.23	19.2	5.8	10.6	4.5	95.4	4
NS-5	0.27	42.2	10.1	25.3	3.7	96.6	4
NS-6	0.65	63.7	33.6	32.6	1.4	98.3	4
NS-7	0.62	6.0	3.5	1.9	4.9	93.5	4
NS-8	0.25	23.0	4.7	17.2	2.3	97.8	3

The times required to reach the $[H^+]$ of 1M (conversion degree around 83%) versus the average particle size of olivine at the different temperatures are plotted in Figure 5.3. The reaction time required decreased when the temperature increased and when the average particle size of olivine declined. The value of the reaction time required for the NS-1 experiment is not presented in this figure. This reaction time was unexpectedly long compared with the rest of the experiments at 50 °C, because the ratio (H^+/Ol) was too high and also because the temperature was the lowest. The high ratio of (H^+/Ol) was due to smaller amount of olivine used in this experiment, which means that most of the olivine is consumed and the pH is still significantly low.

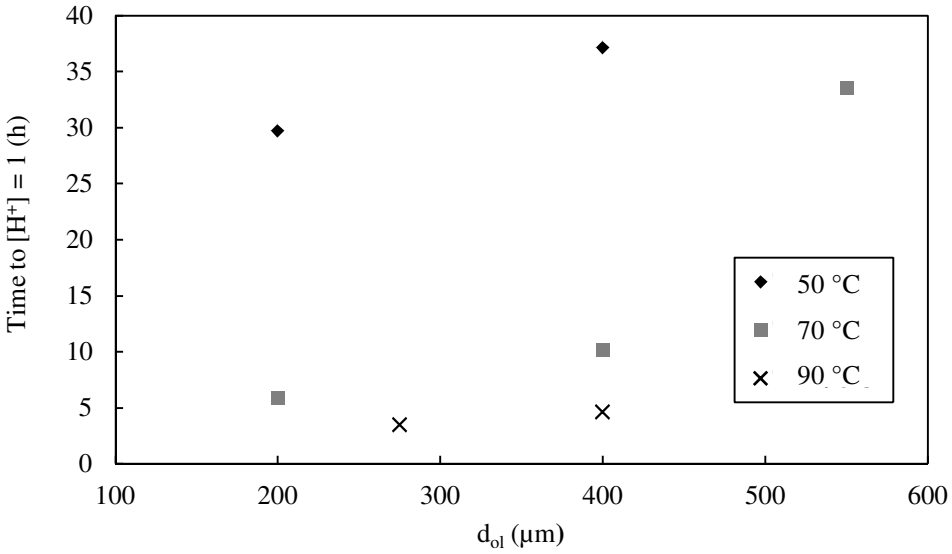

Figure 5.3. Time to reach [H^+] of 1M versus the average particle size of olivine.

For industrial applications, the synthesis process can be carried out under fast kinetic conditions to decrease the required reaction time. Only three hours are required to produce nano-silica at 87 °C, which is a reasonable industrial reaction time. The reaction time can be reduced even further by operating at higher temperatures, higher H^+/Ol ratios or using olivine with higher surface area.

5.5.2 Properties of the olivine nano-silica

The adsorption isotherms and t-plot curves of different silicas are shown in Figures 5.4 and 5.5, respectively. Figure 5.4 represents the adsorption isotherm of NS-1 and NS-2 since these samples had the lowest and the highest SSA_{BET}. The adsorption isotherm curves of all the olivine nano-silicas have similar shapes, but the volumes of gas adsorbed are higher for samples of higher specific surface areas.

The adsorption isotherm of olivine nano-silica can be classified as type IV with H1 hysteresis loop [43,110]. This adsorption isotherm is typical for mesoporous materials and is related to capillary condensation taking place in mesopores [43]. Hysteresis H1 is associated with porous materials consisting of agglomerates with narrow pore distributions [43].

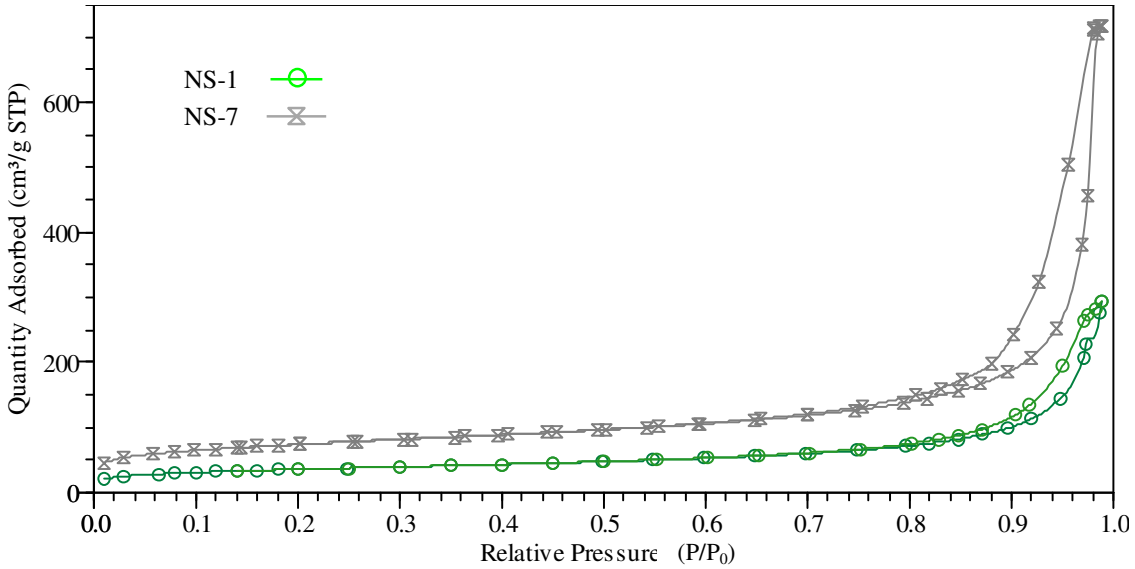

Figure 5.4. Adsorption isotherms of the olivine nano-silica NS-1 and NS-7.

STP refers to standard temperature and pressure.

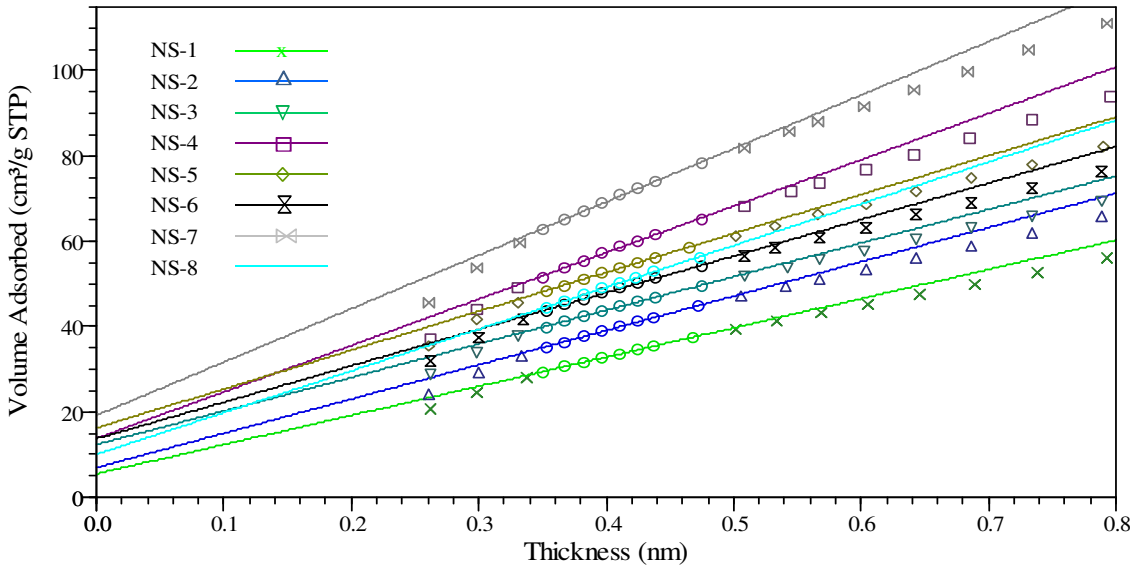

Figure 5.5. t-plot curves of olivine nano-silica.

Where circles have been used to represent the fitted data. STP refers to standard temperature and pressure.

Table 5.4 shows the values of the surface area, average pore size using the BJH [53] method from the adsorption and the desorption isotherm, average particle size and ratio between SSA_{MP} and SSA_{BET} of the olivine nano-silica. The specific surface areas for samples produced at 50, 70 and 90 °C are shown in Figure 5.6. As was mentioned previously, Lieftink [30] stated that the SSA_{BET} of the olivine nano-silica increases with the rate of the olivine dissolution. That means, the SSA_{BET} of nano-silica rises with the reaction temperature, the specific surface area of olivine and the $[H^+]$. This trend is not so

pronounced, but it can be observed in the experiments performed at 70 °C (NS-4 to NS-6), where the SSA_{BET} decreases with the average diameter of the olivine grains (related to the specific surface area of olivine). The same trend is appreciated in the experiments performed at 90 °C but not in the experiments at 50 °C or the experiments with similar olivine particle size (i.e., d_{ol} = 400 μm). The reasons for not observing this trend are that the temperature in these experiments (particularly in experiments NS-1, NS-2, and NS-3) was not constant, the final concentration of $[H^+]$ was slightly different, but most importantly, the number of filtration steps, and, therefore the sulfate content, was not constant.

Table 5.4. Surface area, pore size, particle size and ratio SSA_{MP}/SSA_{BET} of the olivine nano-silica.

Sample	SSA_{BET} (m^2/g)	SSA_{MP} (m^2/g)	SSA_E (m^2/g)	d_{p_A} (nm)	d_{p_D} (nm)	d_{BET} (nm)	d_E (nm)	SSA_{MP}/SSA_{BET} (%)
NS-1	131	27	104	21	21	26	21	21
NS-2	150	27	123	18	17	22	18	18
NS-3	165	43	122	18	18	22	17	26
NS-4	218	52	166	18	17	16	13	24
NS-5	198	58	139	19	19	20	14	29
NS-6	179	47	132	28	24	21	15	27
NS-7	266	72	194	25	22	14	10	27
NS-8	185	36	149	18	17	18	15	19

d_{p_A} and d_{p_D} are the average pore size from the adsorption and desorption branch. d_{BET} and d_E are the average primary particle sizes determined from Eq. (2.20) using SSA_{BET} and SSA_E, respectively.

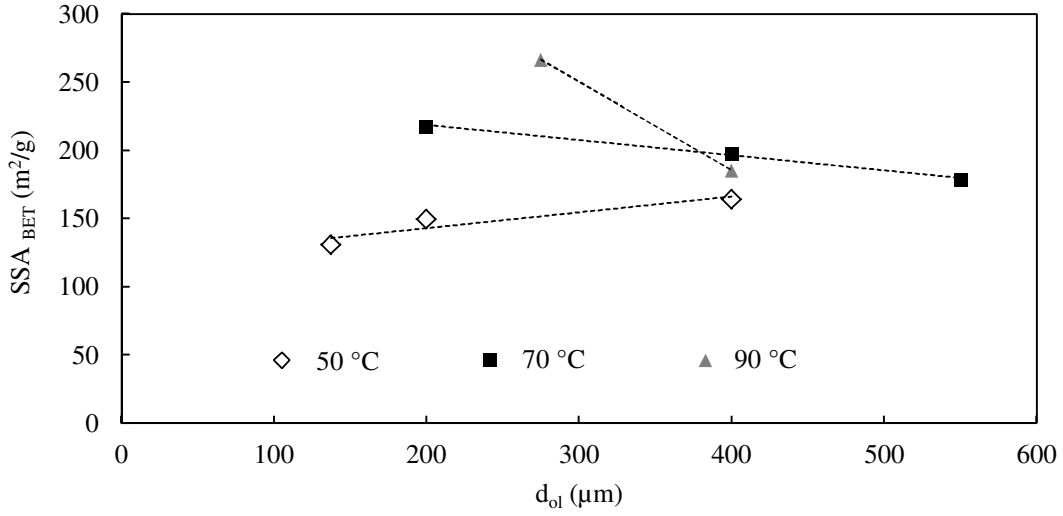

Figure 5.6. Specific surface area of olivine nano-silica against the particle size of olivine for experiments at 70 and 90 °C.

The chemical composition and the purity of silica (calculated with Eq. (5.7)) are shown in Table 5.5. The purity of silica includes the content of silica and silanol, and it is above 95% except for NS-1 and NS-8.

Table 5.5. Chemical analysis (in mass %) of the olivine nano-silica.

Sample	S (%)	Na (%)	Mg (%)	Al (%)	Ca (%)	Cr (%)	Fe (%)	Ni (%)	P_{Si} (%)
NS-1	3.89	0.00	1.88	0.02	0.05	0.00	0.36	0.02	86.01
NS-2	1.18	0.00	0.18	0.01	0.03	0.00	0.04	0.00	96.20
NS-3	1.26	0.01	0.29	0.02	0.08	0.00	0.06	0.00	95.76
NS-4	1.17	0.00	0.16	0.01	0.03	0.00	0.03	0.00	96.26
NS-5	1.19	0.00	0.26	0.02	0.04	0.00	0.05	0.00	96.06
NS-6	0.92	0.02	0.39	0.04	0.05	0.01	0.05	0.00	96.68
NS-7	1.36	0.00	0.28	0.02	0.04	0.00	0.06	0.00	95.52
NS-8	2.16	0.00	0.96	0.03	0.03	0.00	0.15	0.01	92.34

Where P_{Si} is calculated using Eq. (5.7).

TEM images (89 kx magnification) are shown in Figures 5.7 and 5.8, for NS-1 and NS-7, respectively. Figures 5.7 and 5.8 show a material of particle size between 10 and 50 nm. The highly agglomerated state, typical for silicas produced at low pH, can be seen in both silicas. This highly agglomerated state is because the silica particles agglomerate. Sample NS-1 was more agglomerated than sample NS-7, probably because in experiment NS-1 the reaction time was longer, giving more time to the silica to agglomerate.

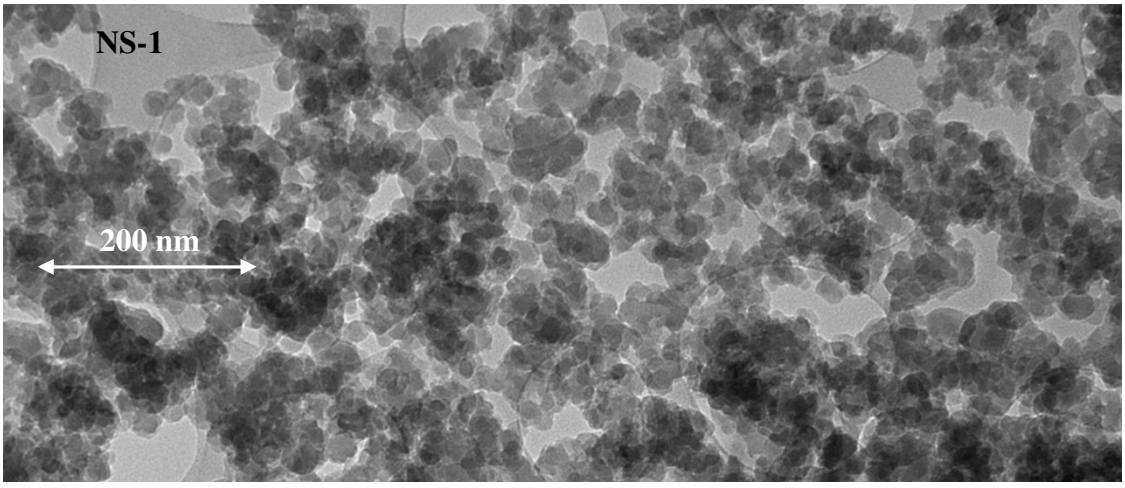

Figure 5.7. TEM picture (89 kx) of olivine nano-silica NS-1.

The primary particle size of the silicas derived from the SSA, Eq. (2.20), is in the range of 14 to 26 nm and of 10 to 21 nm for d_{BET} and d_E, respectively. In addition, the average pore diameters (calculated using the BJH method), d_{p_A} and d_{p_D}, are in the same range as

the primary particles, showing that the porosity is due to the voids between the primary particles in the agglomerate. Therefore, olivine nano-silica can be considered as an agglomeration of primary particles and as a (meso)porous material (the silica pore structure is studied in more detail in Chapter 8). In addition, the SSA_{MP} does not exhibit a particular trend regarding the SSA_{BET} (see Table 5.4), and the ratio SSA_{MP}/SSA_{BET} is almost constant, being in the interval 18 to 29%.

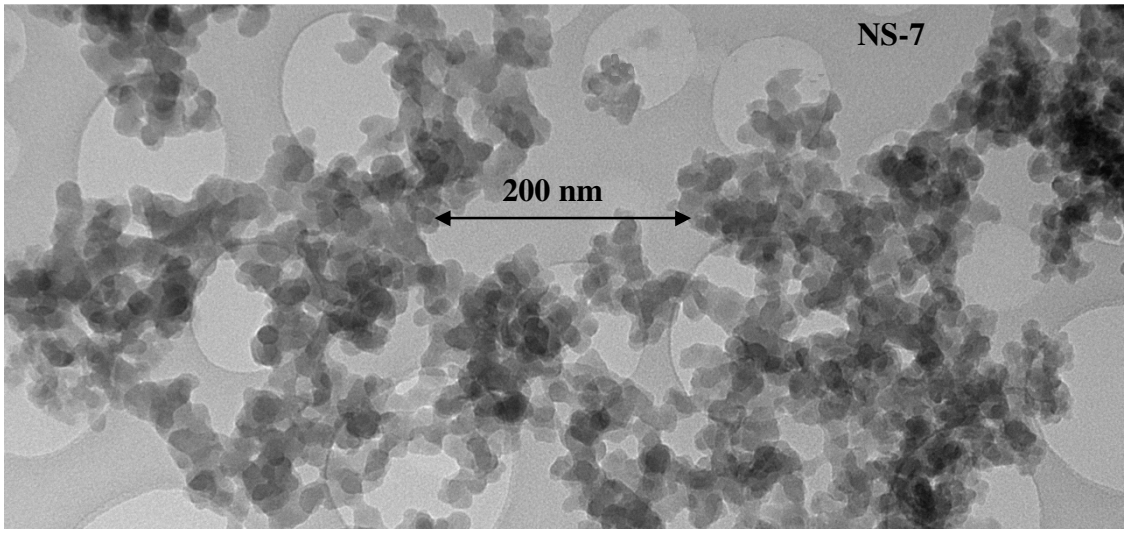

Figure 5.8. TEM picture (89 kx) of olivine nano-silica NS-7.

Table 5.6 shows the number of moles of sulfur, n_S, magnesium, $n_{Mg,}$ and iron, $n_{Fe,}$ together with the mass fraction of total sulfate, w_{SO4_T}, of sulfate related with olivine, w_{SO4_ol}, of free sulfate, w_{SO4_H2SO4}, and ratio magnesium/metal ions. The term w_{SO4_ol} refers to the equivalent amount of sulfate salts ($MgSO_4$ and $FeSO_4$). The free or extra sulfate, w_{SO4_H2SO4} is calculated from the difference between w_{SO4_T} and w_{SO4_ol}. The n_s, n_{Mg} and n_{Fe} are plotted in Figure 5.9. The number of moles of these three components follows a similar trend, exhibiting higher sulfate values (and also magnesium and iron values) for samples with fewer washing steps.

The w_{SO4_T} and the filtration steps carried out for the different samples are shown in Figure 5.10. The w_{SO4_T} decreases with the filtration steps. In addition, the free sulfate could be easily removed adding extra filtration steps with distilled water. Therefore, additional steps of washing with water would reduce the total sulfate, increasing the purity of the nano-silica. In fact, some experiments with 6 washing steps, the last three of them with distilled water, have shown purities above 99% (see next chapter).

Another interesting point is that the ratio of magnesium/metal ions in the silica remains stable with an average value of 0.93, which is identical to the value for dunite CRS-US (see Chapter 3). It means that the magnesium and iron salts are adsorbed on the nano-

silica with the same ratio as present in the olivine and that they are desorbed with the same ratio during washing as well.

Table 5.6. Sulfate content and ratio magnesium/metal ions of the olivine nano-silica.

Sample	n_S (mol/100g)	n_{Mg} (mol/100g)	n_{Fe} (mol/100g)	$w_{SO_4\_T}$ (%)	$w_{SO_4\_ol}$ (%)	$w_{SO_4\_H_2SO_4}$ (%)	$n_{Mg}/(n_{Fe}+n_{Mg})$
NS-1	0.121	0.077	0.006	11.655	8.05	3.60	0.92
NS-2	0.037	0.007	0.001	3.535	0.77	2.77	0.92
NS-3	0.039	0.012	0.001	3.775	1.26	2.51	0.92
NS-4	0.036	0.007	0.001	3.506	0.69	2.82	0.93
NS-5	0.037	0.011	0.001	3.565	1.09	2.48	0.93
NS-6	0.029	0.016	0.001	2.756	1.62	1.14	0.95
NS-7	0.042	0.012	0.001	4.075	1.21	2.86	0.92
NS-8	0.067	0.040	0.003	6.472	4.07	2.40	0.93

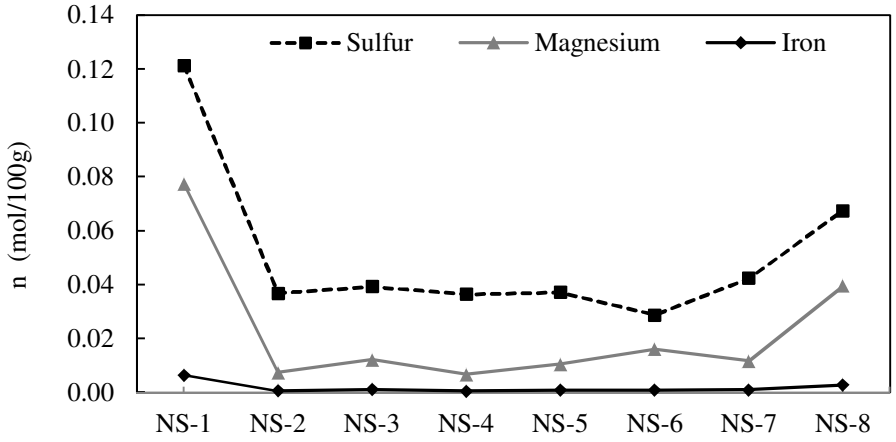

Figure 5.9. Molar composition of S, Mg and Fe of the olivine nano-silica.

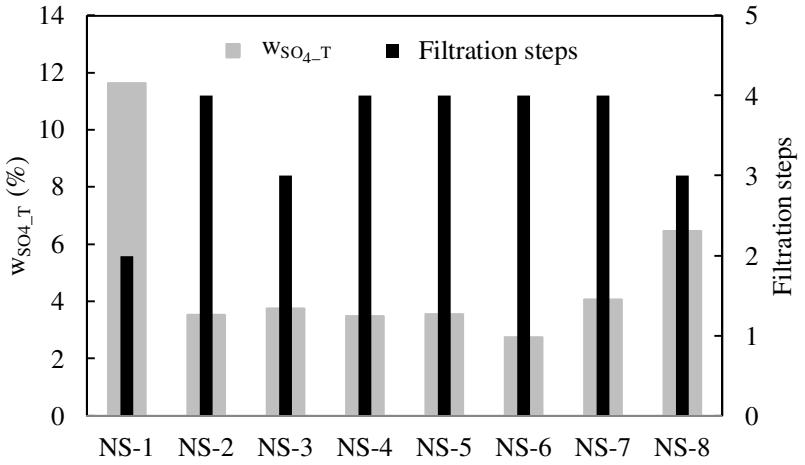

Figure 5.10. Total sulfate and number of filtration steps of the olivine nano-silica.

5.5.3 Process yield of the olivine nano-silica

The TG analyses of NS-1, NS-2, NS-5 and NS-8 and the DTG of NS-1 are shown in Figure 5.11. The higher mass loss of NS-1 is related to the higher amount of sulfates. The TG curves of NS-3, NS-4, NS-6 and NS-7 are similar to the NS-5 curve, showing comparable values of sulfates. Five TG analyses of the sample NS-3 were conducted, showing a relative standard deviation (RSD) of 5.0% in the loss on ignition between 400 and 1100 °C.

The process yield (Y_{NS}), separation efficiency (E_{sep}) and the purity of silica are estimated using Eq. (5.1), Eq. (5.5) and Eq. (5.7), respectively. These parameters are shown in Tables 5.7 and 5.8. The silica purity presented here (P_{Si}*) is estimated from the TG analysis, instead of the ICP analysis. The values of purity obtained by the TG analysis are only slightly higher than the purity values calculated from the ICP analysis. This difference is because the sulfate content calculated from the ICP analysis is slightly higher than the values from the TGA analysis.

Table 5.7. The silica content and the purity of silica (P_{Si}*) of the olivine nano-silica.

Sample	w_{1100} (%)	w_{MgO} (%)	w_{FeO} (%)	$w_{20\text{-}120}$ (%)	$w_{H_20\_A}$ (%)	w_{OH} (%)	w_{SiO_2} (%)	P_{Si}* (%)
NS-1	77.86	3.12	0.46	8.59	9.34	4.19	81.26	87.80
NS-2	86.96	0.30	0.05	7.27	7.76	4.36	93.41	98.74
NS-3	85.20	0.48	0.08	8.25	9.09	3.95	92.25	97.68
NS-4	87.17	0.27	0.04	6.78	7.24	4.43	93.18	98.53
NS-5	84.13	0.42	0.06	9.81	10.52	4.07	92.75	98.24
NS-6	85.84	0.64	0.06	9.38	9.65	2.87	93.94	97.65
NS-7	89.85	0.47	0.07	3.65	4.38	4.46	92.69	98.15
NS-8	81.34	1.60	0.20	9.81	10.66	3.80	88.20	94.01

w_{H20_A} is the water loss fraction between 20-200 °C and w_{OH} water loss fraction between 400-1100 °C subtracting the amount of w_{MgO} and w_{FeO}. P_{Si*} is the silica purity from the TG analysis (Eq. (5.7)).

The amount of nano-silica produced experimentally, theoretically and the process yield are plotted in Figure 5.12. The yield was in the range of 66 to 83%, except for the first experiment where it was 54%. The separation efficiency was in the range 71 to 88% with the exception of the first experiment. The process yield is only slightly higher than the separation efficiency, which means that the main factor affecting the process yield is the separation efficiency, and that is because more than 90% of the olivine has reacted with the acid in every experiment (see Table 5.3). The separation efficiency for NS-1 was unexpectedly low, possibly due to the high value of $[H^+]$. Although in the present study nano-silica was produced with a higher yield than the yield reported by Jonckbloedt [12], this parameter should be further improved, because around 30% of the produced material

was lost during the filtration. In order to increase the nano-silica recovery, a more efficient separation process should be employed. The separation process depends on the properties of the silica cake obtained during the filtration and on the time involved in producing the filter cake. The time is controlled by the texture of the nano-silica. Thus, the faster a filter cake is formed, the higher the yield will be.

Table 5.8. Process yield and separation efficiency of the olivine nano-silica.

Sample	$m_{NS\_exp\_im}$ (g)	m_{NS_exp} (g)	m_{NS_th1} (g)	Y_{NS} (%)	m_{NS_th2} (g)	E_{sep} (%)
NS-1	26.72	21.71	40.16	54.06	38.20	56.84
NS-2	39.61	37.00	45.71	80.95	43.61	84.84
NS-3	31.91	29.44	44.51	66.13	40.35	72.96
NS-4	35.00	32.61	41.19	79.18	39.30	83.00
NS-5	36.70	34.04	44.95	75.73	43.42	78.39
NS-6	35.10	32.97	41.35	79.74	40.65	81.11
NS-7	39.01	36.16	43.66	82.81	40.84	88.53
NS-8	35.11	30.97	44.44	69.69	43.45	71.27

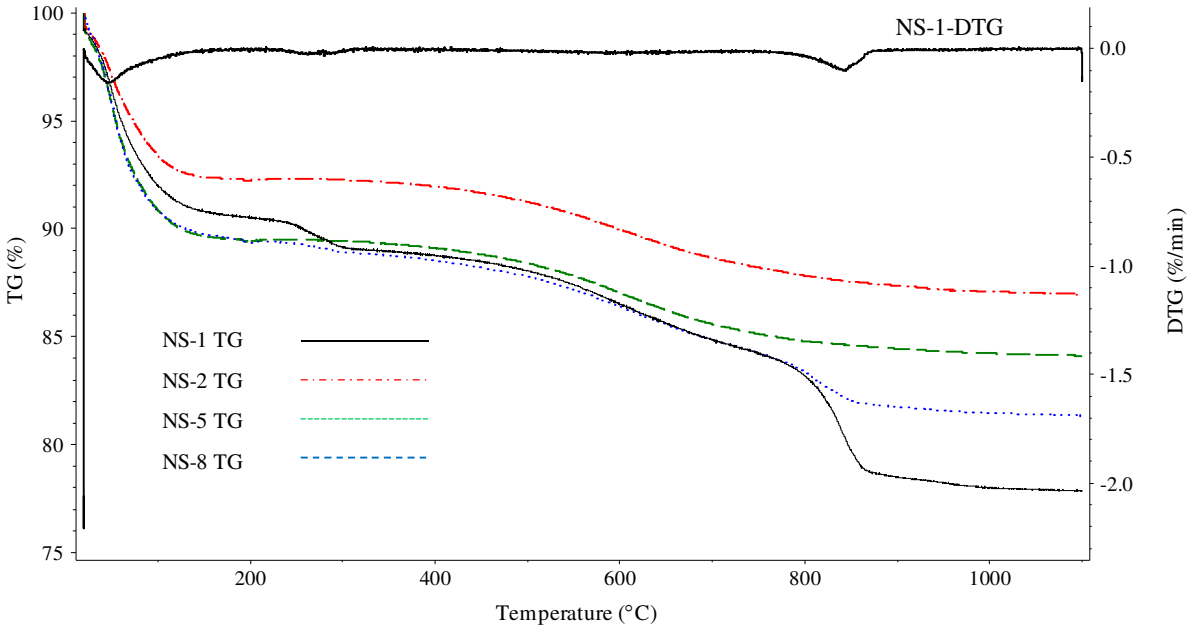

Figure 5.11. TG and DTG analyses of the olivine nano-silica.

The SSA_{BET} versus the E_{sep} is plotted in Figure 5.13. The general trend is that the E_{sep} increases with the SSA_{BET}. Therefore, it can be stated that the specific surface area of nano-silica influences the separation efficiency. The E_{sep} of experiment NS-2 is depicted in a different color, because its values were higher than expected. The reason why the E_{sep}

was higher than expected is the long aging time of this experiment compared with the short aging time of the rest of the experiments carried out at 50 °C. A plausible explanation for the phenomenon of increasing E_{sep} with the aging time would be that nano-silica particles agglomerate more with the aging time, forming the filter cake faster and losing less material. However, the primary particle size of the material does not change during the aging. In other words, the specific surface area of nano-silica remains constant, but larger clusters are formed, facilitating the filtration and enhancing the silica yield. This phenomenon could be used to improve (time and efficiency) the separation process of the nano-silica.

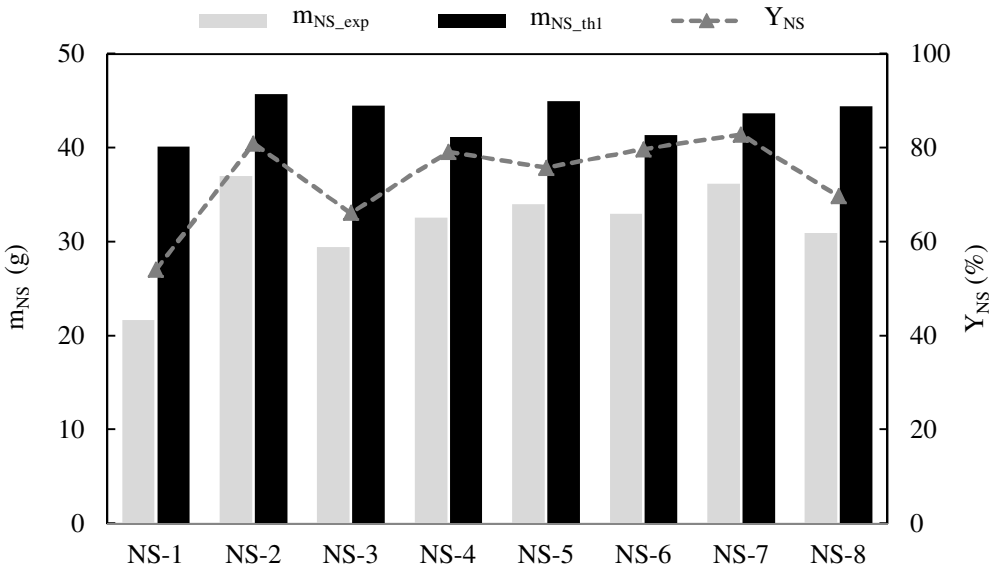

Figure 5.12. Yield and experimental and theoretical masses of olivine nano-silica.

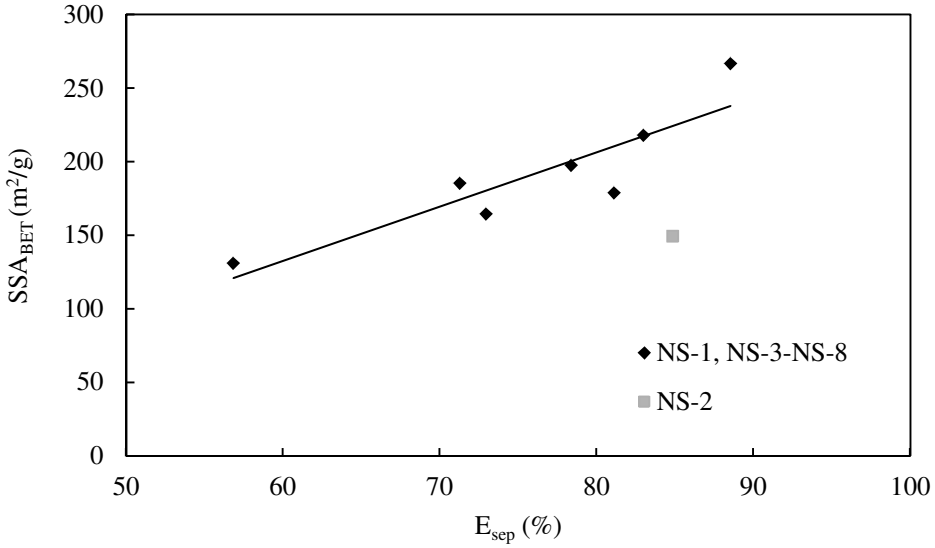

Figure 5.13. Specific surface area of olivine nano-silica versus separation efficiency.

5.5.4 Comparison of different amorphous nano-silicas

Table 5.9 summarizes the physical and chemical properties of pyrogenic silica [1], precipitated silica [1] (see Table 1.1), olivine silica produced by Lieftink [30] (at temperatures between 40 and 90 °C) and the olivine nano-silica produced in the current study. All of them have a purity above 95%, high SSA_{BET} and small particle size. Olivine nano-silica is the material with smaller pore size diameter. The main difference between the two olivine nano-silicas is that the nano-silica prepared here features a slightly smaller specific surface area than Lieftink's nano-silica. This difference in the surface area of olivine nano-silica is due to the kinetics of the dissolution of olivine, and probably also due to the content of impurities. The latter hypothesis cannot be confirmed since Lieftink did not report the chemical composition of the silicas, but additional filtration steps would reduce the content of impurities and increase the specific surface area. Lieftink [30] produced nano-silicas with shorter reaction times than the nano-silica presented here, as can be seen from the reaction times in Tables 5.1 and 5.3, which means that he stopped the reaction at lower conversions.

Table 5.9. Summary of the properties of different amorphous nano-silica [1,30].

Parameters	Pyrogenic [1]	Precipitated [1]	Lieftink [30]	This work
Purity, SiO_2 (%)	>99.8	>95	-	>95
SSA_{BET} (m^2/g)	50-400	30-500	100-400	100-300
d_1 (nm)	5-50	5-100	8-25	10-25
d_p (nm)	None	>30	>10	>10

An XRF analysis of the olivine nano-silica produced by Jonckbloedt [12] with waste sulfuric acid is shown in Table 5.10. The value of the loss on ignition includes the water condensed from the nano-silica as silanol groups. Considering that the mass of water released is around 5%, the silica content is still under 85%, which is much lower than the purity of nano-silica produced in this study.

Table 5.10. Chemical analysis of the olivine nano-silica produced by Jonckbloedt [12].

SiO_2	Al_2O_3	Fe_2O_3	MnO	MgO	CaO	Na_2O	K_2O	TiO_2	P_2O_5	LOI
78.5	<0.22	0.19	<0.006	0.3	<0.13	0.21	<0.05	2.09	0.01	11.94

5.6 Conclusions

The synthesis of nano-silica by the dissolution of olivine is a feasible method to produce amorphous porous nano-silica. The olivine nano-silica prepared in this chapter has a specific surface area between 100 and 300 m^2/g and a primary particle size between 10 and 25 nm. These particles are agglomerated in clusters forming a porous material with an average pore diameter (obtained using the BJH method) between 17 and 28 nm. The impurity content is below 5% after three cleaning steps and can be further decreased by performing additional washing steps using water (silicas of a lower sulfur content and higher SSA_{BET} are presented in the next chapter).

The specific surface area of olivine nano-silica depends on the kinetics of the reaction of olivine and the amount of magnesium sulfate in the porous material. Thus, increasing the reaction temperature, surface area of olivine, activity of the hydrogen ions and/or number of washing steps results in an increase in the nano-silica surface area. In this way, different types of nano-silica can be produced by changing the process conditions. The influence of the kinetics of the olivine dissolution on the specific surface area of the nano-silica is less straightforward than was stated by Lieftink [30], being much more apparent the effect of sulfates on the SSA.

The separation efficiency (E_{sep}) increases with the specific surface area of the nano-silica and aging time. Even if the E_{sep} is higher than that reported by Jonckbloedt [12], it could still be improved by accelerating the build up of the cake during the filtration and/or modifying the properties of the cake. One way to obtain a better filter cake is to keep the slurry aging for several hours before the filtration. Thus, there is more time for the nano-silica to agglomerate, leading to a more efficient separation process. Another possibility would be to add a recovery step to the filtration process.

The results presented in this chapter demonstrate that the dissolution of olivine in sulfuric acid is a feasible method to produce an amorphous porous nano-silica. Therefore, the olivine dissolution process is a convenient alternative to the traditional methods of nano-silica production. The next chapter continues with the properties of olivine nano-silica for materials with lower sulfur content. Additionally, it addresses the method to tailor the properties of the olivine nano-silica by means of a hydrothermal treatment.

Chapter 6. The influence of process conditions and Ostwald ripening on the SSA of olivine nano-silica

6.1 Introduction

Nanotechnology and nanomaterials have attracted great attention in the previous years as can be seen from the fact that the number of patents in this field has increased by 600% from 1992 to 2002 [111] and the annual global turnover is estimated to increase up to €1.5 trillion by 2015 [112]. The specific surface area (SSA) is a crucial parameter conferring special properties to nanomaterials. This is because materials with a large surface area possess a large surface energy, and, thus, they are thermodynamically unstable or metastable [113]. Therefore, the application of nano-materials strongly depends on the SSA making it one of the most relevant parameters to study. Olivine nano-silica is agglomerated in clusters forming a porous 3-D network structure of a high SSA. The agglomerated state of this silica can be beneficial for some applications where high-porous agglomerates are needed, such as nano-silica for ink-jet paper or catalytic materials. However, no research has been carried out focusing on tailoring the SSA of olivine nano-silica in order to meet with the requirements of different applications.

The main purpose of this chapter is to analyze the influence of the process conditions during nano-silica production by the dissolution of olivine, and the subsequent ripening treatment on the SSA_{BET} in order to assess the possibility of tailoring olivine nano-silica. The results obtained here demonstrate that olivine nano-silica (with purity above 99%) in the range of 90 to 400 m^2/g can be produced using an Ostwald ripening treatment at 20 °C. An additional aim of this chapter is to present new data about the evolution of the density and viscosity of the slurry over time and the preparation of silica dispersions by means of physical methods (i.e., high shear mixing and ultrasonic methods). The evolution of the density and viscosity is important not only because this information can contribute to the understanding of the physical and chemical changes occurring during the dissolution of olivine, but also because the viscosity and the density are essential parameters for the scale-up of the industrial production. The breaking up or deagglomeration of silica is a key factor to prepare colloidal dispersions, which is one of the most valuable product forms of nano-silica.

In the previous chapter, olivine nano-silicas with SSA_{BET} between 100 and 300 m^2/g, primary particles between 10 and 25 nm and purities above 95% were reported. The primary particles were agglomerated in clusters forming a porous material with an average pore diameter measured by Barrett-Joyner-Halenda (BJH) method above 10 nm. In addition, it was stated that the SSA_{BET} of olivine nano-silica depends on the kinetics of the reaction of olivine and the amount of magnesium sulfate remaining in the material. The current chapter focuses on the following points: 1) washing steps required to obtain

purities above 99%; 2) influence of the sulfates on the specific surface areas (SSA_{BET}, SSA_{MP} and SSA_{E}); 3) influence of the filtration pressure on the SSA; 4) influence of the conversion degree of the olivine dissolution on the SSA; 5) influence of the Ostwald ripening on the SSA; and 6) influence of the mechanical treatments (high shear mixer and ultrasound devices) on the particle size distribution of silica.

6.2 Ostwald ripening theory

The Ostwald ripening process consists of a hydrothermal treatment at basic pH levels in order to modify the equilibrium of the solubility of silica. The solubility equilibrium is reached when the rate of dissolution is equal to the rate of the deposition/condensation. The solubility of silica depends on the solution pH, temperature, radius of curvature of the silica particles and content of impurities. In the olivine nano-silica case, the impurity content is not relevant due to the low content of magnesium and iron ions and the inability of sulfate ions to affect the solubility of the silica [4]. Regarding the pH and the temperature, the solubility of silica increases when these parameters rise [4]. In addition, the solubility of silica is higher for convex surfaces than for concave surfaces, and the radius of curvature has two main consequences for the solubility.

The first consequence is that in a dispersion with individual particles of two sizes, the smaller particles exhibit a higher solubility than the larger ones. Consequently, the concentration of dissolved silica is higher next to smaller silica particles than in the vicinity of larger silica particles. The concentration difference in the liquid solution leads to the silica transport from the regions with high to low concentrations. The second consequence is that in a dispersion with agglomerated and individual particles, the individual particles dissolve more than the agglomerates, and the deposition of silica proceeds most preferably at the point of contact between particles in the agglomerates due to the negative radius of curvature. These two consequences are graphically described in Figures 6.1 and 6.2. Thus, when a silica dispersion is not in equilibrium, the more soluble particles dissolve. Subsequently, the dissolved silica condenses on the surface of silica particles of lower solubility. The solution/deposition process will continue until a new equilibrium is established. Another important factor in the solubility equilibrium of silica is the particle size distribution. This can be easily illustrated with the following example: a monomodal narrow particle size distribution would not be affected by a change in pH from 4 to 11 because, although the solubility of silica is much higher at pH 11 than at pH 4 [4], when the size of all the particles is the same, the ripening stops.

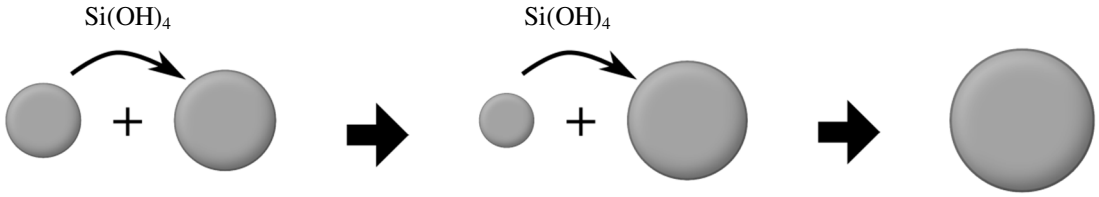

Figure 6.1. Ostwald ripening representation when two individual particles of different sizes are present in a dispersion.

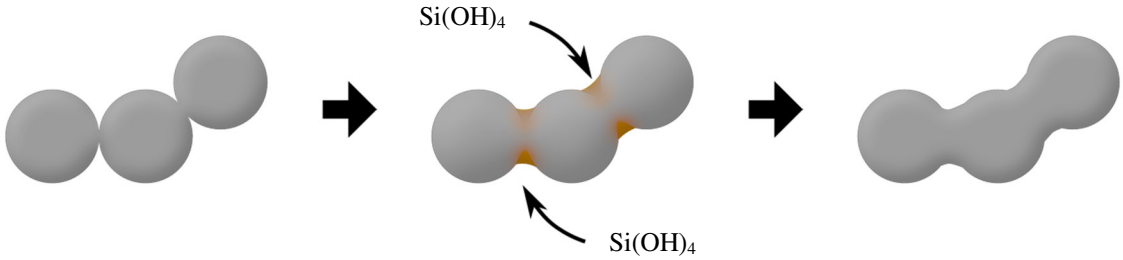

Figure 6.2. Ostwald ripening representation when aggregates are present in dispersion.

6.3 Materials and methods

The nano-silica synthesis experiments were carried out in a stirred glass thermostated reactor of one liter. The reagents used were 500 ml of 3M sulfuric acid and a stoichiometric amount of olivine, previously dried. The dunite rock used in this chapter was GL50 (see Chapter 2). The neutralization reaction was stopped when the concentration of $[H^+]$ reached 0.1M. Then, the silica suspension was separated from the solid residue by sedimentation. Subsequently, the slurry was washed and filtered either using a vacuum pump (P_{abs} = 0.2 bar) or filter press (P_{abs} = 3-5 bar). When the washing and filtration was performed employing a vacuum pump, the silica was redispersed after each step, whereas when the silica was filtered using a filter press, the washing and cleaning was performed in a continuous step.

The ripening experiments were performed in a stirred glass thermostated reactor of two liters with an olivine nano-silica supplied by Eurosupport (the Netherlands). This material was supplied in a cake form with a solid content around 20 wt.%. The Ostwald ripening treatment was carried out in an alkaline solution using either NH_4OH or NaOH. The pH was adjusted to the desired value and kept constant during the experiments. The experiments were carried out at 20 and 90 °C, in the pH range between 4.6 and 11, and with a silica content between 3 and 6 wt.%. A high shear mixer (Silverson multifunctional L5M laboratory mixer with a shear screen) and an ultrasound bath of 10 liters (Powersonic 1100d with an effective power of 200 W) were used in some of the experiments. During the ripening process, samples were taken at regular intervals to determine the pH of the solution and the SSA of the dried silica. The silica samples were filtered and dried in an oven at 110 ^oC for about 15 hours.

In addition to the Ostwald ripening experiments, silica dispersion tests in water were performed using an ultrasound equipment, which is more effective in breaking up the particles than the ultrasound bath. The ultrasonic device (Hielscher UP400S) was coupled with a 22 mm diameter sonotrode (model H22). The power of the ultrasound wave generation was in the range of 139-200 W with a frequency of 24 kHz. The amplitude of the sound wave was adjusted to 100% of the maximum (100 µm). Using ultrasound, 100 ml of slurry with 1 wt.% of solid content was sonically treated for several minutes. During this treatment, the dispersion was cooled down using a double walled vessel and a cooling liquid at 5 °C. The resulting silica dispersion was characterized by laser light scattering (LLS).

The nano-silica produced dried at 105 °C was characterized by nitrogen physisorption, transmission electron microscopy (TEM), X-ray fluorescence (XRF), combustion infrared analysis (determination of sulfur content) and LLS. The evacuation condition of the nitrogen physisorption analysis were 190 °C for 240 min.

6.4 Results

6.4.1 Influence of the process conditions

The olivine silicas were synthesized using different process conditions. The process conditions studied were the number of washing steps using a vacuum pump and the filtration pressure during the washing. Table 6.1 shows the specific surface areas (SSA_{BET}, SSA_{MP} and SSA_E), the increase in the SSA between samples with consecutive filtration steps, particle size (calculated using Eq. (2.20)) and average pore size in the adsorption branch (d_{p_A}) of the silicas; this table also shows the micropore volume (V_{MP}) and the pore volume in the adsorption branch(V_{P_A}).

Table 6.1. SSA, Variation of the SSA between samples with consecutive vacuum filtration steps, particle size, pore size, micropore volume and pore volume.

Sample	SSA_{BET} (m^2/g)	SSA_{MP} (m^2/g)	SSA_E (m^2/g)	ΔSSA_{BET} (%)	ΔSSA_{MP} (%)	ΔSSA_E (%)	d (nm)	d_{p_A} (nm)	V_{MP} (cm^3/g)	V_{P_A} (cm^3/g)
NS-14-3F	233	58	175	-	-	-	11.7	14.5	0.025	0.529
NS-14-4F	324	122	202	39	110	15	8.4	13.9	0.055	0.578
NS-14-5F	346	142	204	7	16	1	7.9	13.7	0.064	0.589
NS-14-6F	348	142	206	0	0	1	7.8	14.6	0.064	0.679
NS-HP	433	125	308	-	-	-	6.3	14.7	0.055	1.026

F refers to the number of washing/filtration steps and HP to high pressure filtration.

Table 6.2 presents the chemical composition, loss on ignition (LOI), purity of silica and conductivity of the filtrate. The purity of silica was calculated using:

$$P_{Si}(\%) = w_{SiO_2} + w_{LOI} - w_{SO_3}, \quad \textbf{(6.1)}$$

which was above 99% after five filtration steps, showing the good quality of the silica for the samples using vacuum filtration.

Table 6.2. Chemical composition, purity and conductivity of the olivine nano-silicas with different number of filtration steps, of a filter-pressed olivine nano-silica, and of the raw material used in the Ostwald ripening experiments.

Sample	SiO_2 (%)	Al_2O_3 (%)	Fe_2O_3 (%)	MgO (%)	CaO (%)	K_2O (%)	Cr_2O_3 (%)	LOI (%)	S (%)	Psi (%)	Cond. (mS/cm)
NS-14-3F	86.05	0.02	0.21	1.35	0.01	0.01	0.02	12.33	1.75	93.96	52.60
NS-14-4F	91.64	0.09	0.07	0.38	0.01	0.01	0.02	7.77	0.33	98.59	12.30
NS-14-5F	92.56	0.12	0.05	0.21	0.01	0.01	0.02	7.01	0.05	99.45	2.47
NS-14-6F	92.42	0.30	0.04	0.22	0.05	0.03	0.02	6.92	0.03	99.27	0.32
NS-HP	85.70	0.02	1.00	1.66	0.04	0.01	0.03	11.54	1.26	94.07	0.33
NS-RM	90.29	0.05	0.21	0.26	0.03	0.03	0.02	9.10	0.06	99.24	-

P_{Si} was calculated using Eq. (6.1). F refers to the number of washing/filtration steps, HP high pressure filtration and RM raw materials.

Table 6.3 presents the number of moles and masses of sulfur, magnesium and iron, where the magnesium and iron salts are in a monohydrate form at 190 °C [108] (temperature at which the evacuation, prior to the gas physisorption, was conducted). In addition, the total mass of impurities (w_{T_im}) is also presented in this table. It is noteworthy that the number of moles of magnesium is higher than the moles of sulfur for samples with low sulfur content, e.g., NS-5F, NS-6F. This is likely due to the different analysis techniques used to determine the content of oxides and sulfur. For these special cases, the number of moles of magnesium based on the sulfur content ($n^*_{Mg} = n_S$) was calculated, and the amount of iron was neglected.

The adsorption isotherm and the t-plot curve for silicas after different washing steps are shown in Figures 6.3 and 6.4, respectively. An increase in the specific surface areas (SSA_{BET}, SSA_{MP} and SSA_E) with the number of washing steps can be observed. During the washing and filtration, the sulfate salts, which are soluble, were removed from the silica. The sulfate salts were adsorbed on the surface of silica, and cleaning could be regarded as an extraction of the salts from the silica [30]. The specific surface area in the micropores for clean silicas (samples with 5 and 6 filtration steps) was 40% of the SSA_{BET}.

Table 6.3. The number of moles and mass fractions of sulfur, magnesium and iron of different olivine nano-silicas.

Sample	n_S (mol/g)	n_{Mg} (mol/g)	n_{Fe} (mol/g)	n_{Mg*} (mol/g)	w_{MgSO_4} (%)	w_{FeSO4} (%)	$w_{H_2SO_4}$ (%)	w_{T_im} (%)
NS-14-3F	5.277E-04	3.214E-04	2.543E-05	3.214E-04	4.4478	0.4321	1.7737	6.6536
NS-14-4F	1.027E-04	9.402E-05	8.743E-06	9.402E-05	1.3010	0.1015	0.0000	1.4013
NS-14-5F	1.563E-05	5.222E-05	6.276E-06	1.563E-05	0.2163	0.0000	0.0000	0.2163
NS-14-6F	9.349E-06	5.453E-05	5.005E-06	9.349E-06	0.1294	0.0000	0.0000	0.1294

Where $MgSO_4$ and $FeSO_4$ are in monohydrate form.

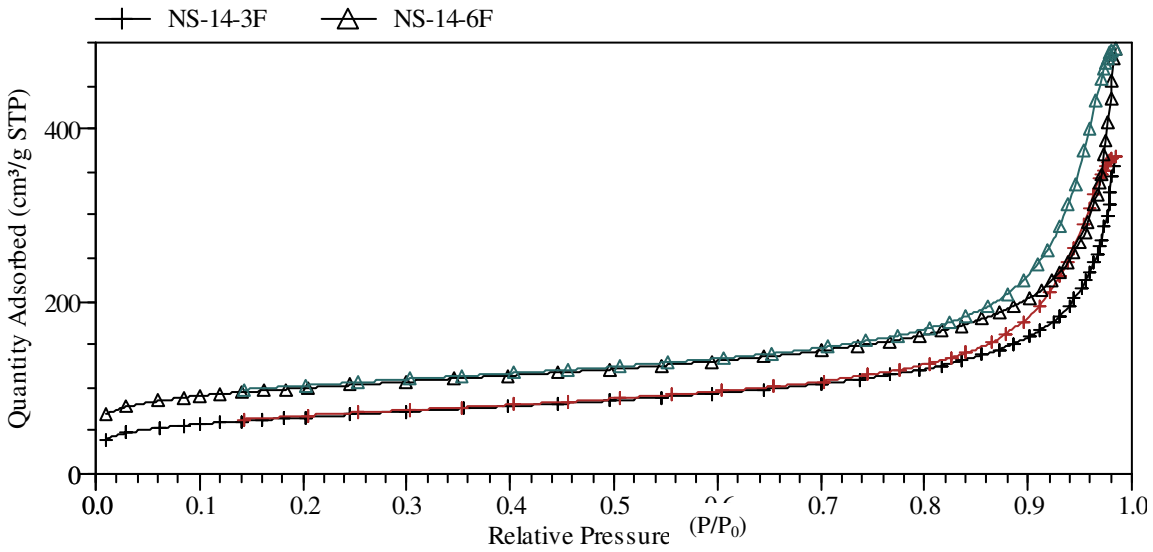

Figure 6.3. Adsorption isotherms of the olivine silicas for sample NS-14 with 3 and 6 filtration steps..

STP refers to standard temperature and pressure.

In order to investigate the influence of the sulfate salts on the SSA of silica, two hypotheses are proposed: 1) the only influence of the sulfates on the SSA_{BET} would be their mass, not having any direct effect in the SSA_{BET}. In that case, an SSA_{BET} of the sulfate-free silica (i.e., SSA_{BET}*) can be calculated taking into account that the impurity mass does not contribute to the SSA_{BET}:

$$SSA_{BET}^{*} = \frac{SSA_{BET}}{(1 - w_{T\_im})}; \qquad \textbf{(6.2)}$$

and 2) the sulfates are located in the micropores, partly blocking them. Thus, an SSA_{MP}* could be estimated using the following formula:

$$SSA_{MP}{}^{*} = \frac{SSA_{MP}}{1-\left(\phi_{T\_im}(\%)\right)/100}, \tag{6.3}$$

where ϕ_{T_im} (%) is the volume fraction between the total volume of impurities (V_{T_im}) and the total volume of the micropores (V_{T_MP}). Table 6.4 presents the following values: a) the SSA_{BET}*; b) volume of the impurities in the silica using the densities of magnesium and iron sulfate monohydrate (2.45 and 1.9 cm^3/g, respectively) as well as sulfuric acid (1.84 cm^3/g); c) total volume of the micropores (V_{T_MP}, see Eq. (6.4)), with consideration that sulfates are only found in those locations; d) the ratio of the impurity volume regarding this total volume; and e) the estimated SSA_{MP}*.

$$V_{T\_MP} = V_{MP} + V_{T\_im}\ . \tag{6.4}$$

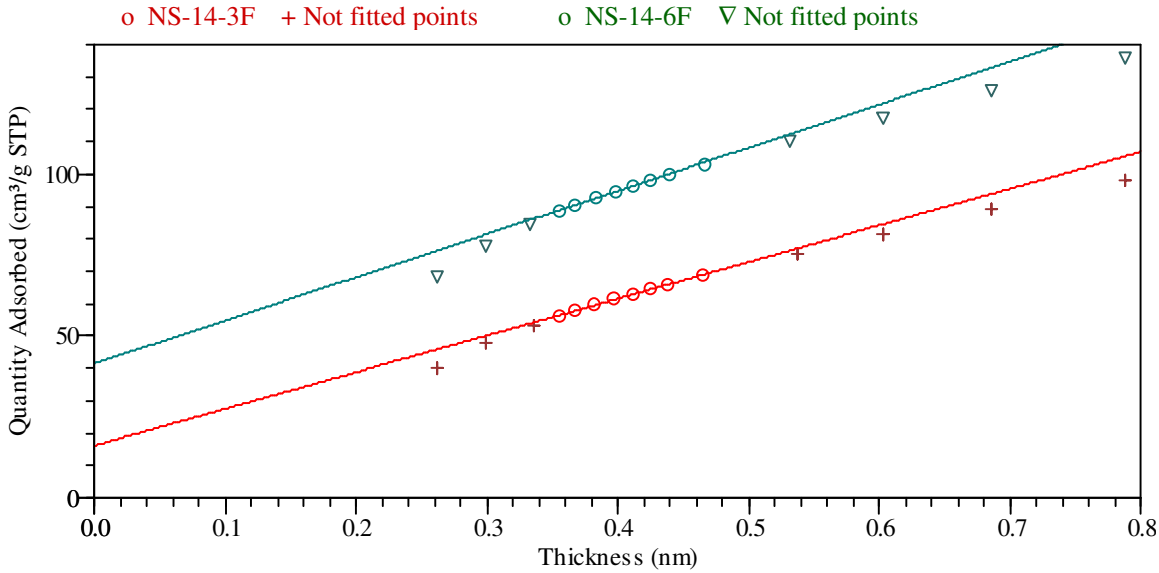

Figure 6.4. t-plot curves of sample NS-14 with 3 and 6 filtration steps.

In the case that the only influence of the sulfates on the SSA_{BET} would be their mass, the SSA_{BET}* should be constant for all the samples; however, SSA_{BET}* increases from 250 to 348 m^2/g. In the case that hypothesis 2 holds, the SSA_{MP}* should be constant for all the samples. Although the SSA_{MP}* increases from 127 to 149 m^2/g, the increase is much lower than in the case of hypothesis 1. Hypothesis 2 is also in agreement with the fact that between consecutive filtration steps, particularly between filtration steps 3 and 4, the SSA_{MP} had a higher increase (110%) than the SSA_E (15%).

Table 6.4. Estimation of SSA_{BET}* for a sulfate-free silica, volume of impurities, total volume in the micropores and SSA_{MP}*.

Sample	SSA_{BET} (m^2/g)	SSA_{BET}* (m^2/g)	V_{MgSO_4} (cm^3/g)	V_{FeSO_4} (cm^3/g)	$V_{H_2SO_4}$ (cm^3/g)	V_{T_im} (cm^3/g)	V_{T_MP} (cm^3/g)	ϕ_{T_im} (%)	SSA_{MP}* (m^2/g)
NS-14-3F	233	250	0.0182	0.0023	0.0096	0.0301	0.0551	54.61	127
NS-14-4F	324	329	0.0053	0.0008	0.0000	0.0061	0.0615	9.91	135
NS-14-5F	346	347	0.0009	0.0000	0.0000	0.0009	0.0652	1.36	149
NS-14-6F	348	348	0.0005	0.0000	0.0000	0.0005	0.0646	0.82	149

Where $MgSO_4$ and $FeSO_4$ are in monohydrate form.

SSA_{BET}* was calculated using Eq. (6.2) and SSA_{MP}* was calculated using Eq. (6.3).

The purity of sample NS-HP was lower than sample NS-6F (see Table 6.2) even though the conductivities of the filtrates were similar. This was due to the formation of preferential paths during the filtration of NS-HP, which makes the washing inefficient. Another remarkable fact of sample NS-HP was that in spite of its low purity content, this sample presented a high SSA. This could be due to the compression effect on the bulk structure of silica, which would be in agreement with the statement of Madeline [114] about the influence of pressure on the voids of a nanoparticle cake. This idea is also supported by the highest volume of the pores (V_{P_A}) of sample NS-HP (see Table 6.1). Thus, the fact that the specific surface area does not decrease but increase means that the filtration pressure was high enough to compress the pores of the material, but not high enough to collapse the pores. If the filtration pressure had been higher, the pores would have collapsed, resulting in a drastic drop of the SSA_{MP} and SSA_{BET}. Therefore, it can be stated that the filtration pressure is a key parameter influencing the specific surface area.

In addition to the experiments in which the number of washing steps and filtration pressure were modified, two batches of silica were produced. In these two experiments (NS-50 and NS-51) samples were taken at different times, or in similar fashion, at different conversion degrees, in order to check the influence of the conversion on the properties of silica (see Table 6.5). The conversion used in this chapter is based on the hydrogen ion, while in Chapter 5 the conversion is based on the olivine. The difference between the conversions calculated in either way is small since the amount of reagents (olivine and sulfuric acid) was close to the stoichiometry values, but with a little excess of the concentration of hydrogen ion. Figure 6.5 presents the adsorption isotherms of NS-50-S3 and NS-50-S4 with conversion degrees of 38 and 77%, respectively. Figure 6.6 shows the evolution of the specific surface area with the conversion.

Table 6.5. Silica batches at different conversions.

Sample	Temperature (°C)	Olivine	$Fraction_{Ol}$ (µm)	X (%)	S (%)	SSA_{BET} (m^2/g)	SSA_{MP} (m^2/g)	SSA_E (m^2/g)
NS-50-S3	50.4	GL50	100-500	38	0.2	517	137	380
NS-50-S4	50.4	GL50	100-500	77	0.33	325	132	193
NS-50-S5	50.4	GL50	100-500	90	0.16	310	139	170
NS-51-S4	70.5	GL50	100-500	81	0.4	375	124	251
NS-51-S5	70.5	GL50	100-500	94	0.05	354	143	210

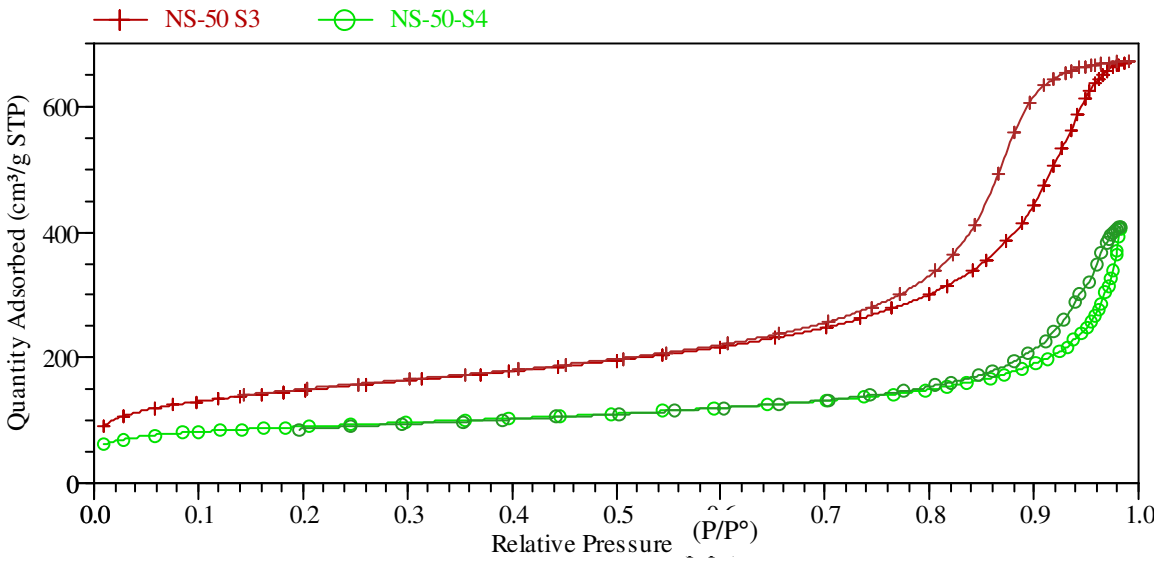

Figure 6.5. Adsorption isotherm of samples NS-50-S3 and NS-50-S4.

From the results shown in Table 6.5, it can be observed that the SSA_{BET} depends on the conversion degree (X). The SSA_{BET} decreases with the reaction time (as well as with the conversion) as can be observed in Figure 6.6. It is remarkable that a nano-silica with a SSA_{BET} above 500 m^2/g was produced (i.e., NS-50-S3) even at low reaction kinetics (reaction temperature of 50 °C), exhibiting a SSA_{BET} 200 m^2/g higher than for the same batch at higher conversion degrees. The adsorption isotherm curve of NS-50-S3 starts with higher adsorbed values, which means that this material is more microporous than NS-50-S4. Also, the slope of the BET region (i.e., relative pressure between 0.05 and 0.2), which is associated with the multilayer region, is steeper for samples with lower X. Surprisingly, in disagreement with the adsorption isotherm, the microporous surface area (calculated using the t-plot method with Eq. (2.19)) is almost constant for all the samples. This phenomenon is likely due to the fact that the SSA_{MP} was calculated with the BET specific surface area instead of the total specific surface area (see Eq. (2.19)) since no sufficient data in the low relative pressure range can be obtained with the TriStar 3000.

As was mentioned in Chapter 2 the SSA_{BET} cannot be correctly determined for microporous materials.

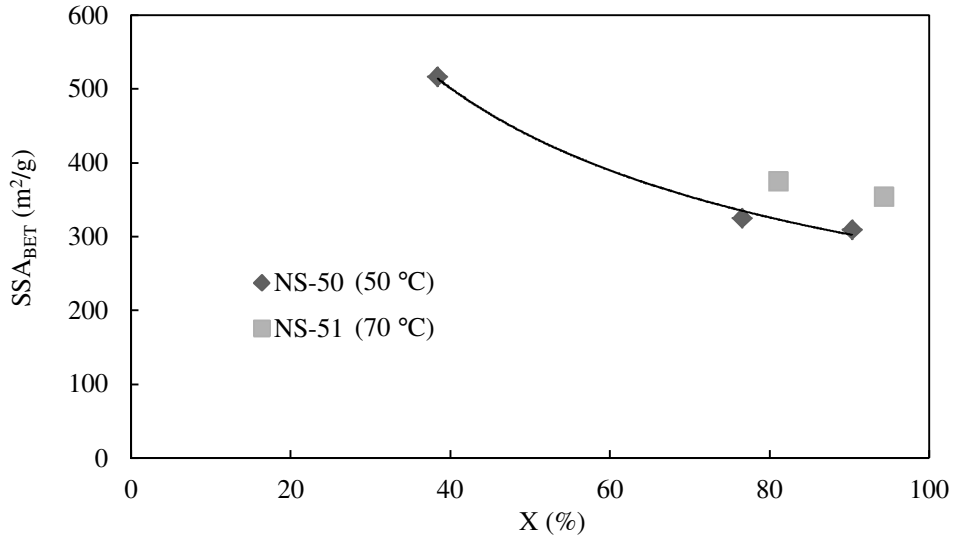

Figure 6.6. SSA_{BET} versus the conversion for experiments NS-50 and NS-51.

As was mentioned in the previous chapter, Lieftink [30] stated that the specific surface area of olivine depends mainly on the kinetics of the dissolution of olivine and the sulfate content of the silicas. However, in Chapter 5 it was found that although there is some influence of the olivine dissolution kinetics on the SSA_{BET}, it is not as clear as expected. In addition, the conversion degree influences significantly the SSA_{BET}, this factor resulting to be more important than the kinetics.

6.4.2 Evolution of density and viscosity of the olivine nano-silica slurry

During the NS-50 and NS-51 experiments, the evolution of the density and viscosity of the olivine nano-silica slurry was studied. The density was measured using 50 ml glass picnometers, and the viscosity was obtained with a Haake Rotovisco RV 20. The slurry was sampled after stopping the stirrer for approximately 2 minutes to let the coarse grains (olivine and other silicate minerals) settle. Tables 6.6 and 6.7 and Figure 6.7 show the density evolution of the slurry with the conversion.

The density increases by 15% over time (i.e., with the conversion) from the initial value of the 3M sulfuric acid (1.18 mg/L) to the final value (1.36 mg/L). At 40% conversion the density reaches a local maximum in both experiments, this effect being more significant for NS-50. This phenomenon could be due to a density change of some of the species (Fe, Mg and silica species) in the slurry with the pH, but further research is still needed to clarify this.

Table 6.6. Evolution of the density of batch NS-50 with the conversion.

sample	time (h)	$[H^+]$ (mol/L)	X (%)	ρ (g/ml)
0	0.0	6.09	0.00	1.180
1	1.3	5.36	11.87	1.198
2	4.3	3.97	34.82	1.294
3	5.9	3.75	38.41	1.260
4	25.9	1.43	76.52	1.319
5	48.6	0.59	90.34	1.349

Table 6.7. Evolution of the density of batch NS-51 with the conversion.

sample	time (h)	$[H^+]$ (mol/L)	X (%)	ρ (g/ml)
0	0.0	6.02	0.00	1.180
1	0.6	4.54	24.61	1.214
2	1.0	3.64	39.57	1.276
3	2.4	2.60	56.84	1.280
4	5.9	1.14	81.13	1.317
5	25.6	0.08	98.63	1.364

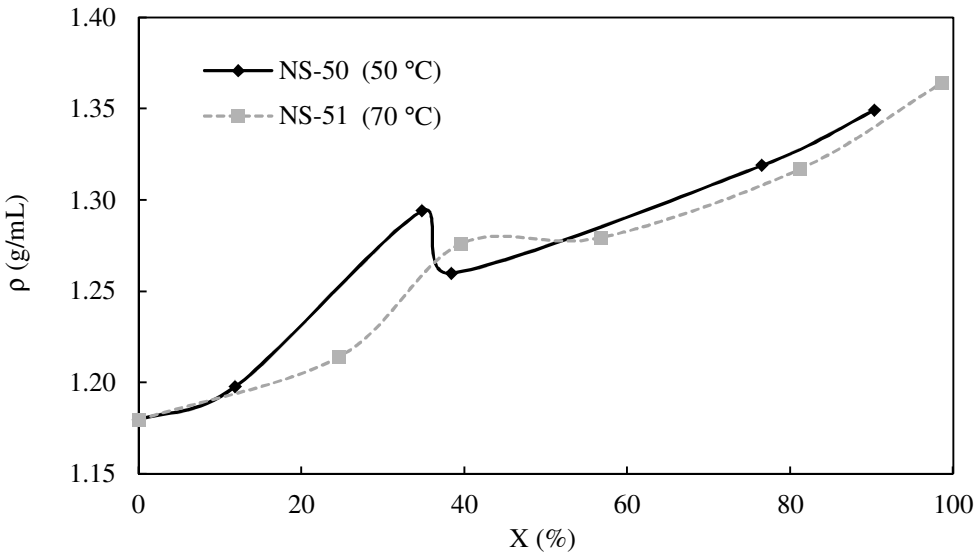

Figure 6.7. Evolution of the density of batches NS-50 and NS-51 with the conversion.

The viscosity of the slurry is an important parameter for two reasons: 1) knowledge of the viscosity is required for the industrial design of the facilities (type of reactor, stirrer, pumps, etc.); and 2) it provides information about possible changes in the slurry. However, continuous measurement of the viscosity inside the reactor is difficult due to the corrosive environment (pH, temperature and abrasion). Lieftink [30] found that the

viscosity of the slurry initially increased (at low conversion degrees) passing through a local maximum. After this increase, the viscosity dropped returning to the initial value. He reported the time which preceded the appearance of a "gel phase" (using Lieftink's terminology) and the time the "gel phase" was present (see Table 6.8). This gel phase was identified visually, observing the movements of the mineral grains over time. He stated that the beginning and duration of the gel phase depend on the reaction rate of the dissolution of olivine. In addition, he concluded that the gel phase started when the concentration of silica was about 0.05 mol/L, and it disappeared when the colloidal particles grew [30].

Table 6.8. Appearance and duration time of the "gel phase" for different temperatures and olivine fractions as measured by Lieftink [30].

T (°C)	$Fraction_{Ol}$ (μm)	Reaction time (min)	Onset viscosity (min)	Viscosity duration (min)
90	425-1000	260	18	40
90	90-425	150	10	20
70	425-1000	1350	40	35
70	90-425	340	23	20
70	>90	100	7	90
40	425-1000	8750	260	150
40	90-425	2800	200	1200

Table 6.9 and Figure 6.8 show the evolution of the viscosity of batch NS-51 slurry with the conversion. As was mentioned in Chapter 4, the average shear rate in the impeller region (calculated following the procedure in [103]) is around 64 s^{-1}. The viscosity trend shows an increase with the conversion for shear rates between 64 and 181 s^{-1}, rising the viscosity from 1.8 (viscosity of sulfuric acid) to 45 mPa·s (viscosity of the slurry with conversions above 90%). At low conversions (samples NS-51-1 and NS-51-2), the viscosity passed through a local maximum at low shear stress as can be seen in Figure 6.9, which shows that the slurry features the phenomenon of yield stress. In the case of dispersions, yield stress occurs when particles start to flocculate forming an extended network.

Further research with viscometers working at low shear rates and with higher sensitivity at viscosities as low as that of sulfuric acid would be required to ensure the presence of yield stress for this type of slurry. Comparing sample NS-51, which was performed at 70 °C with a dunite fraction of 100-500 μm, with the experiments of Lieftink (see Table 6.8), it can be seen that the beginning and duration time of the local maximum of the viscosity (or gel phase) are within the same range. However, at shear rates above 64 s^{-1}, the viscosity local maximum at low conversion degrees cannot be observed.

Table 6.9. Evolution of the slurry viscosity (mPa·s) of batch NS-51 with the conversion degree.

Sample		0	1	2	3	4	5
γ (s^{-1})	**23**	1.8	58.2	58.2	19.2	14.5	43.9
	38	1.8	41.8	40.7	19.7	19.1	43.2
	64	1.8	33.2	33.2	18.9	22.4	45.2
	108	1.8	25.0	25.2	18.6	23.0	44.8
	181	1.8	20.3	20.3	18.2	23.7	45.4
	302	1.8	17.5	17.5	17.8	24.1	45.0
	505	1.8	15.5	15.6	17.1	24.0	43.9
time (h)		0.0	0.6	1.0	2.4	5.9	25.6
$[H^+]$ (mol/L)		6.02	4.54	3.64	2.60	1.14	0.08
X (%)		0.00	24.61	39.57	56.84	81.13	98.63

Where the value of sample 0 is the viscosity of 3M sulfuric acid [105].

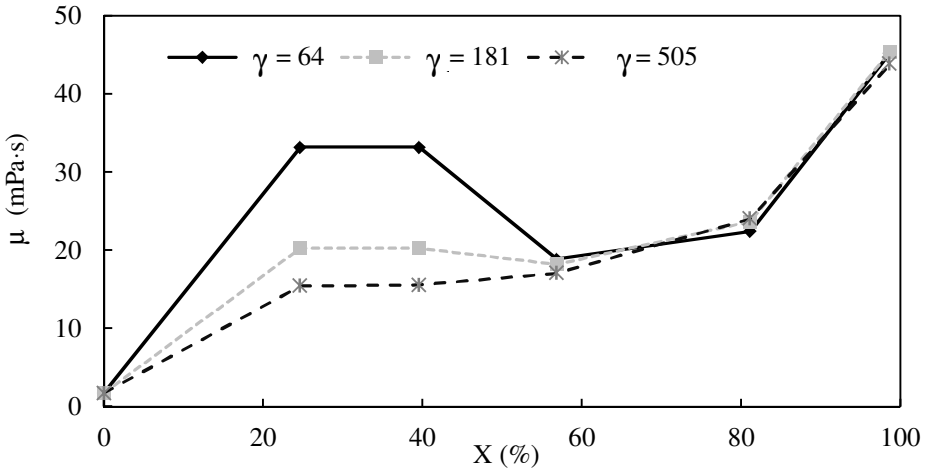

Figure 6.8. Evolution of the slurry viscosity of batch NS-51 with the conversion.

Where γ is the shear rate in s^{-1}.

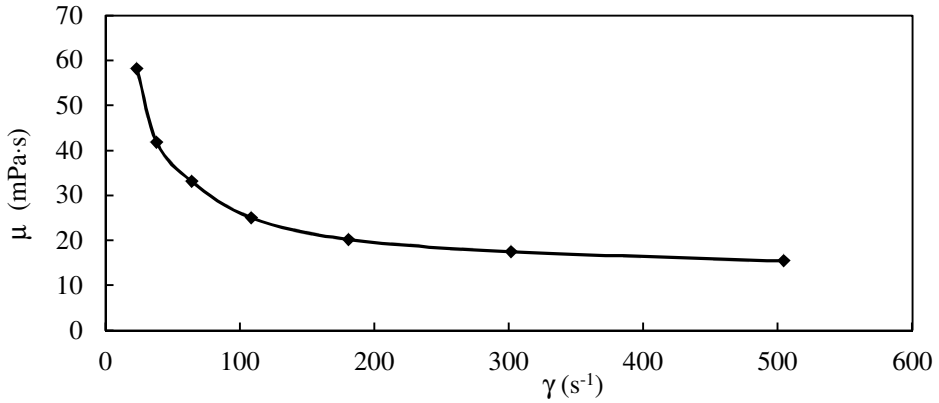

Figure 6.9. Slurry viscosity of sample NS-50-S1 versus the shear rate.

6.4.3 Ostwald ripening experiments

The experimental conditions of the ripening tests are shown in Table 6.10, giving the average values of the reactor temperature, pH, silica mass percentage and the base used. Table 6.11 lists the specific surface areas, specific surface area variations or reductions after the ripening treatment and primary particle size (calculated using Eq. (2.20)) of nano-silica for the ripened samples.

Table 6.10. Experimental conditions of the ripening tests using a normal and high shear mixer.

Sample	T (°C)	pH	m_{SiO_2} (%)	Base	HM Speed (rpm)
RP-1	89	8.4	4.4	NH_4OH	-
RP-2	90	10.0	3.1	NH_4OH	-
RP-3	90	8.3	2.6	NaOH	-
RP-4	90	9.6	3.3	NaOH	-
RP-5[1]	90	10.0	6.6	NaOH	5000
RP-6	RT	9.0	3.1	NaOH	1200
RP-7	RT	9.0	3.1	NaOH	5000
RP-8	RT	9.0	3.0	NaOH	7500
RP-9	RT	4.6	3.1	-	5000
RP-10	RT	7.1	3.1	NaOH	5000
RP-11	RT	11.0	3.0	NaOH	5000

RT refers to room temperature and HM to high shear mixer.

[1] In RP-5 the high shear mixer was used for 10 min in order to break the silica lumps faster.

The parameters of the ripening experiments were the type of solution, pH, silica percentage, temperature, reaction time, and type and speed of mixer. As can be seen in Table 6.11, the type of solution and silica percentage do not affect the final SSA_{BET}. In the first four experiments (RP-1 to RP-4), it was noticed that the silica lumps did not disappear earlier than after three hours, but after 10 minutes with the high shear mixer, the lumps were gone. The speed of the high shear mixer did not affect the final surface area (see RP-6, RP-7 and RP-8). Therefore, it can be stated that the high shear mixer cannot alter the final result of the SSA_{BET} during the Ostwald ripening, but it accelerates the ripening process. The pH and temperature are the most important factors influencing the final properties of the silica due to the enhancement of its solubility.

The influence of the temperature can be seen comparing experiments RP-3 and RP-4 (pH 8.3 and 9.6 at 90 °C), where the SSA_{BET} decreased as much as 133 m^2/g, to experiment RP-6 (pH 9 and 20 °C), where the SSA_{BET} dropped only up to 197 m^2/g. The influence of the pH is illustrated in Figure 6.10, where the SSA_{BET} of the samples ripened at room temperature decreases with the pH (90 m^2/g at pH=11). Figure 6.11 shows the reduction of the SSA_{MP} and SSA_E during the Ostwald ripening. As can be seen from these curves,

the decrease of the SSA_{MP} is greater than the decrease for SSA_E involving samples with a small reduction of SSA_{BET}. For Sample RP-11, 89% of the micropore area is reduced producing a material of low porosity.

Table 6.11. Specific surface area, specific surface area variation and particle size of the ripened olivine nano-silica.

Sample	Time (h)	SSA_{BET} (m^2/g)	SSA_{MP} (m^2/g)	ΔSSA_{MP} (%)	SSA_E (m^2/g)	ΔSSA_E (%)	d_{p_A} (nm)	d_{p_D} (nm)	d_{BET} (nm)
NS-RM	-	341	102	-	239	-	17	16	8
RP-1	6.0	140	20	80	120	50	20	19	19
RP-1	22.0	124	19	81	105	56	17	16	22
RP-2	3.0	150	22	78	128	47	20	19	18
RP-2	6.0	135	18	82	117	51	19	19	20
RP-3	1.5	181	25	75	156	35	21	20	15
RP-3	6.0	133	18	82	115	52	23	22	20
RP-4	6.0	133	19	81	114	53	18	17	21
RP-5	0.2	159	19	82	140	41	22	20	17
RP-5	6.0	139	19	81	120	50	20	19	20
RP-6	0.2	209	29	71	180	25	20	20	13
RP-6	1.0	197	27	73	170	29	21	20	14
RP-7	0.2	200	28	72	172	28	21	20	14
RP-7	1.0	199	26	74	173	28	22	21	14
RP-8	0.2	203	28	72	174	27	22	20	13
RP-8	1.0	191	26	74	165	31	23	22	14
RP-9	1.0	347	105	-	242	-	17	17	8
RP-10	1.0	283	70	31	212	11	19	19	10
RP-11	0.2	141	16	84	124	48	25	23	19
RP-11	1.0	90	12	89	79	67	28	26	30
RP-11*	2.0	101	12	88	89	63	27	24	27

RM refers to the raw material used. *In sample RP-11 an ultrasound bath was used for 1 hour.

In addition to the specific surface area results, particle size distribution (PSD) analyses were carried out (see Table 6.12 and Figure 6.12) for the samples where the high shear mixer was used and for the slurry of nano-silica produced by the dissolution of olivine. The slurry of olivine nano-silica was sampled after a conversion degree around 90% was reached. Subsequently, the stirring was stopped to let the mineral grains settle. The d_{50} of the slurry was 110 μm. Since it is not certain that all the mineral grains have been removed from the slurry, it is not known whether these large particles are mineral grains or nano-silica clusters, or both. The PSD of the ripened dispersions shifted to smaller particles than present in the olivine nano-silica slurry. The d_{50} sizes of silica clusters of the ripened samples were in the range of 13 to 18 μm. In experiment RP-11, where the

sample was treated in an ultrasonic bath for 60 minutes, the d_{50} size was reduced by as much as 9 µm. These nano-silica dispersions exhibit particle sizes in the microrange but not in the nanorange. However, this olivine silica is still considered as a nanomaterial (or nanostructured materials) due to its high specific surface area.

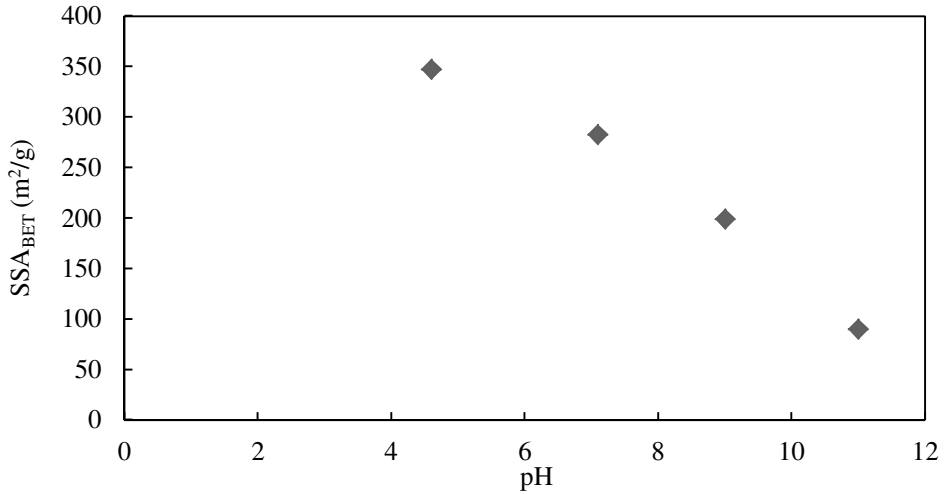

Figure 6.10. Reduction of the SSA_{BET} after the Ostwald ripening treatment using the high shear mixer.

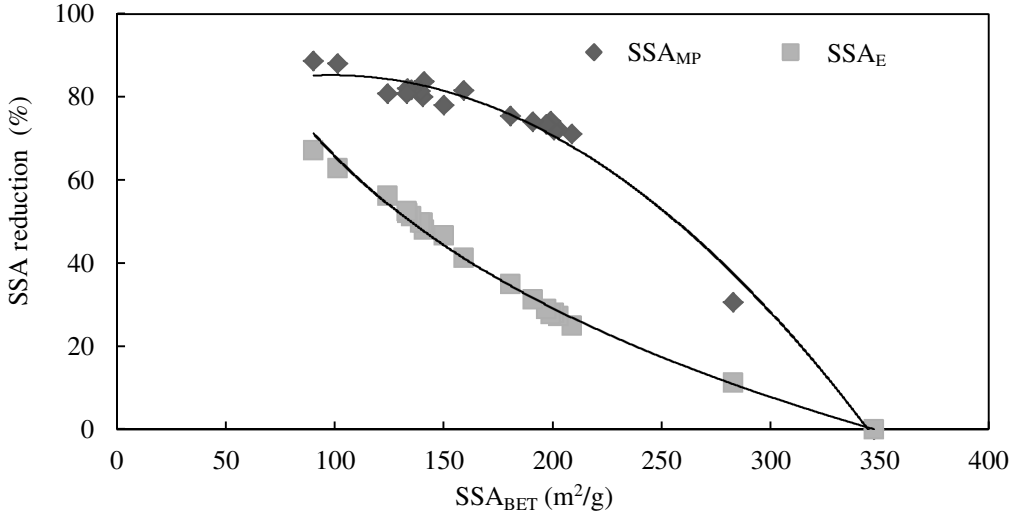

Figure 6.11. Reduction of the SSA_{MP} and SSA_E after the Ostwald ripening treatment using the high shear mixer.

Table 6.12. d_{10}, d_{50} and d_{90} of the ripened olivine nano-silica dispersion.

Sample	time	d_{10} (µm)	d_{50} (µm)	d_{90} (µm)
RP-6	10	6.9	16.9	36.0
RP-6	60	6.8	17.5	43.2
RP-7	10	6.3	15.0	31.6
RP-7	60	6.1	13.0	25.0
RP-8	10	5.7	13.8	32.7
RP-8	60	4.9	10.9	24.6
RP-9	60	6.0	14.1	31.5
RP-10	60	6.7	15.7	35.9
RP-11	10	6.54	14.5	29.2
RP-11	60	6.04	14.1	29.7
RP-11[1]	60	4.76	9.8	19.0

[1] In sample RP-11 an ultrasound bath was used for 1 hour.

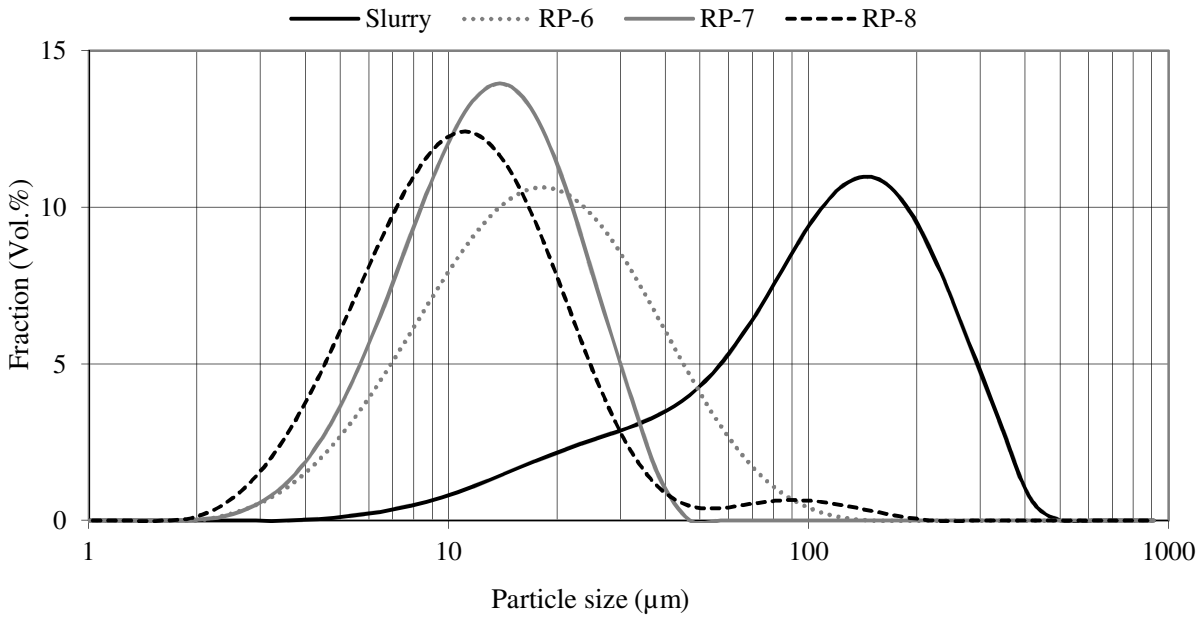

Figure 6.12. Particle size distributions of different olivine nano-silica dispersions after the Ostwald ripening treatment and of the olivine nano-silica slurry.

Where Slurry refers to the nano-silica slurry produced by the olivine dissolution.

TEM photographs of RP-1 are shown in Figure 6.13. Agglomerates are still present and the edges of the silica clusters seem to be more rounded than in samples without ripening (see Figures 5.7 and 5.8).

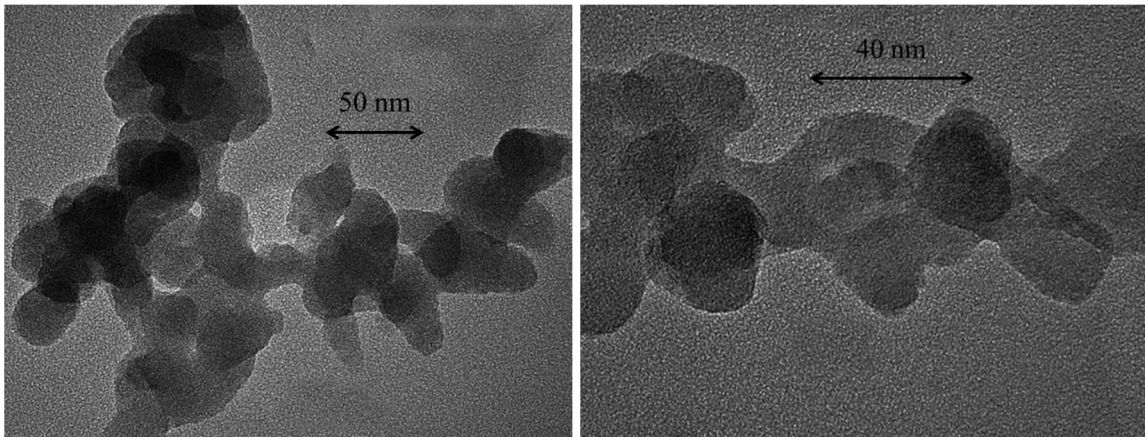

Figure 6.13. TEM photographs (250 kx and 430 kx, respectively) of olivine nano-silica after the Ostwald ripening treatment.

Although the Ostwald ripening treatment of the olivine nano-silica was successful in tailoring the SSA, this treatment was not able to break the agglomerates into nano-particles, not even when the high shear mixer was used. In addition, the ripening treatment is also likely to reinforce the silica structure since soluble silica deposits on the point of contact between particles.

6.4.4 Preparation of a silica dispersion using ultrasounds

Silica dispersions with 1 wt.% solid content in demineralized water were prepared using the following steps: high shear mixing for 5 minutes at 5000 rpm, and ultrasonic treatment with the Hielscher UP400S device for 0 (i.e., no ultrasonic treatment), 5 or 20 minutes (see Table 6.13). The PSD results of the three dispersions are shown in Figure 6.14. Ultrasonification periods longer than 20 minutes were not used because the temperate of the dispersion increased with the treatment duration.

Table 6.13. Silica dispersions in water using a high shear mixer and ultrasonic device.

Dispersion	Material	t_{HM} (min)	t_{US} (min)	d_{10} (μm)	d_{50} (μm)	d_{90} (μm)
D-1	NS-50-S4	5	0	6.96	13.20	23.70
D-2	NS-51-S5	5	5	2.01	5.00	23.24
D-3	NS-51-S5	5	20	0.21	5.96	20.30

Where t_{HM} and t_{US} refer to the treatment time of the high shear mixer and ultrasonic devices.

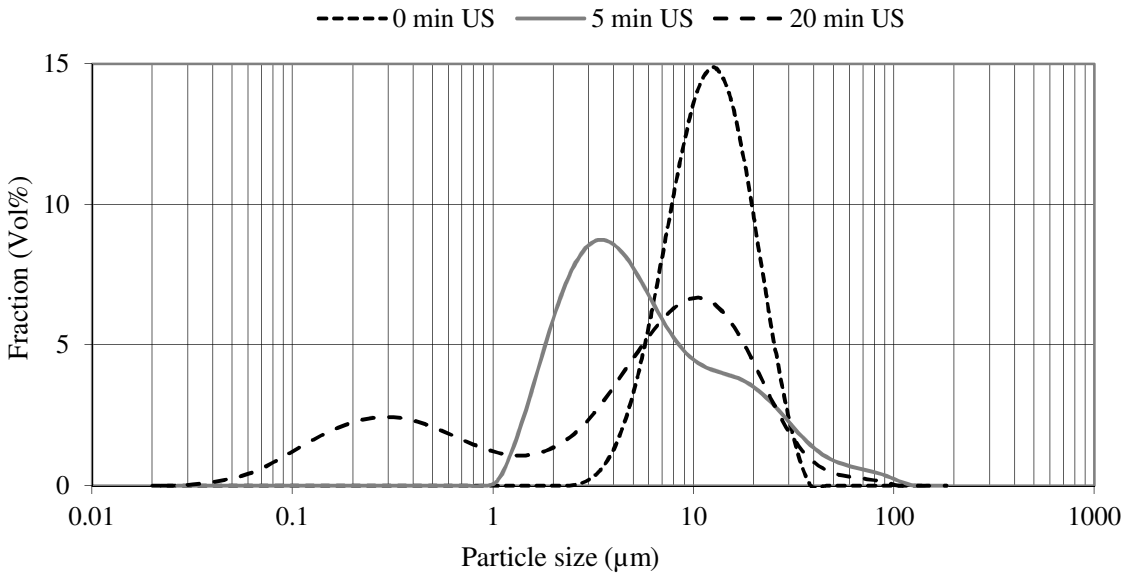

Figure 6.14. Particle size distribution of silica dispersions in water prepared by treatment with a high shear mixer and ultrasonic device for 5 and 20 minutes.

When only the high shear mixer was used (dispersion D-1), the particle size distribution was in the range of micrometers, being 3 µm the smallest clusters measured. After 5 minutes of ultrasonification, the d_{50} decreased from 13 to 5 µm (see Table 6.13), but the d_{90} remained unchanged and no particles below 1 µm were produced. The best result was obtained after 20 minutes of ultrasonification, where 28% (by volume) of the agglomerates was in the range of nanometers with aggregates as small as 30 nm. Therefore, the silica clusters can be broken up producing particles in the nanometer range by means of ultrasonification. The possibility of producing dispersions with nano-silica particles is very interesting in order to have the possibility of preparing colloidal dispersions, which is one of the high-valuable commercial products of nano-silica. Further research is still needed to optimize the breaking process of the silica clusters to increase the amount of small agglomerates.

6.5 Discussion

In Section 6.4.3, the results of the ripening of olivine nano-silica are presented showing a drastic decline of the specific surface area as well as a minor decrease in terms of the size distribution of the silica clusters. In addition, TEM photographs revealed that the edges of the ripened silica clusters are more rounded. These changes are due to the Ostwald ripening, where the solubility equilibrium is shifted, and they can be explained by the following hypothesis: the smallest individual silica particles (in the case that individual particles are present in the dispersion) exhibit the highest solubility. Consequently, the concentration of dissolved silica is higher next to smaller silica particles than in the

vicinity of larger silica particles. Then, part of the soluble silica condensates at the points of lower solubility, which are the contact points between the primary particles in the agglomerates. When the individual particles have been removed from the dispersion, and the equilibrium is not yet reached, the external parts of the agglomerates dissolve to condensate afterwards at the contact points between particles. This process continues until the equilibrium is established and there are no silica particles with different solubilities anymore.

This proposed hypothesis can explain why the agglomerates are still present after the ripening experiments; the decrease of the SSA_{MP} is greater than that of the SSA_E for samples exhibiting a small reduction of SSA_{BET}, and the edges of the silica particles seem more rounded (see Figure 6.13). The silica agglomerates are still present after the ripening because the high shear mixer can neither break them into individual particles nor can they dissolve during the ripening. In fact, the agglomerates are likely to be even mechanically stronger since the dissolved silica condenses on junctions between the silica particles strengthening their union. The SSA_{MP} is reduced more than the SSA_E for samples with a small reduction of SSA_{BET} because the soluble silica first condenses within the micropores. As the ripening progresses, the reduction of SSA_{MP} proceeds more slowly and the reduction of SSA_E accelerates, mainly due to the fact that the most accessible SSA_{MP} has already been filled with silica.

The solubility of silica should not be increased above pH 11 because the ion concentration would be two high (e.g., Na^+), which is undesirable for some applications, but most important because above this high pH silica dissolves massively forming ions (e.g., $HSiO_3^-$). Therefore, the SSA_{BET} cannot be further reduced by raising the pH level. An alternative method to further reduce the SSA_{BET} could be to add active silica to the solution. This method is known as the building-up process [4,115,116] and is based on a continuous ripening of nano-silica due to the continuous addition of active or reactive silica. Using this method it is possible to further grow the nano-silica particles, but it has the inconvenience that the agglomerates cannot be broken since the active silica will deposit on the silica clusters.

Further research should be performed to study the effect of the Ostwald ripening treatment on silica dispersions ultrasonically prepared, so that the large agglomerates (e.g., silica dispersions with a PSD below 1 μm) are not present. From these experiments, similar reductions of the SSA_{BET} as after the Ostwald ripening treatment performed here could be expected, but with smaller sizes of silica clusters.

6.6 Conclusions

The process conditions of the olivine nano-silica production have a strong influence on the final specific surface area of this material. The process conditions and the ripening treatment influence the properties of nano-silica in different ways. 1) The cleaner the

nano-silica is, the higher its specific surface area is, reaching values between 300 and 400 m^2/g for olivine silicas of a low content of salts and, hence, silica purities above 99%. The sulfate salts are located in the pores of the silica clusters, blocking them and drastically reducing the SSA_{MP}. 2) The higher the filtration pressure is, the higher the surface area will be. This is due to a reduction of the pore volume. However, if the applied pressure is too high, it is likely that the pores of the material collapse, reducing the SSA_{BET}. 3) The smaller the conversion degree is, the higher the SSA_{BET} is. Silicas with surface areas above 500 m^2/g were produced at slow reaction rates (50 °C) and conversions of 38% (see sample NS-50-S3). And 4) the ripening process diminishes the specific surface area of nano-silica by 75%, and a further reduction in the SSA_{BET} could be achieved if the material would be treated gradually using the building-up process. In addition, this treatment removes the microporous surface area of the samples almost completely.

Although the combination of the high shear mixing and the Ostwald ripening treatment of the olivine nano-silica is successful in tailoring the SSA_{BET} and partly reducing the particle size of the agglomerate, this treatment is not able to break the agglomerates into nano-particles. In fact, the agglomerates are likely to be even stronger since soluble particles condense on the junctions between particles, strengthening their union.

The ultrasonic treatment can break apart the silica agglomerates, producing individual aggregates as small as 30 nm. However, this process should be optimized to increase the amount of dispersed particles in the nanometer range. This optimization could be done using longer ultrasonification times (but intermittently to prevent the temperature from rising too high) or separating the dispersion in different size fractions so that the ultrasounds treatment would be more effective. An alternative would be to use a colloid mill, which is usually more effective in breaking up the clusters than an ultrasonic device. Even though the deagglomeration process still has to be optimized, it is clear that the olivine nano-silica clusters can be broken using mechanical techniques. Therefore, these techniques make possible the production of stable colloidal dispersions using olivine nano-silica.

To conclude, the results shown here demonstrate that the SSA_{BET} of olivine silica can be tailored to meet the requirements of different possible applications. This tailoring can be done by changing the filtration pressure, controlling the conversion degree of the olivine dissolution and/or performing ripening treatments after the production process has been completed. Thus, the typical SSA_{BET} for a clean nano-silica (~350 m^2/g) can be modified in the range 90 to 500 m^2/g.

Chapter 7. Development of the olivine nano-silica particles

7.1 Introduction

The most important properties of silica powder are the particle structure (i.e., size, shape and aggregate/agglomerate ratio), pore structure (i.e., size and pore interconnection) and surface chemistry. That is because these parameters influence the properties of silica, and, therefore, its possible applications. In Chapters 5 and 6, the properties of olivine nano-silica are reported, showing that this material is structured in large porous clusters of high surface area. Understanding the formation process of these clusters (under the olivine nano-silica process conditions) might provide useful knowledge to improve the tailoring of the nano-silica properties, control the particle growth and explain the difference properties between olivine silica and commercial silicas.

The formation process of commercial silicas produced using the wet route (i.e., silica gel, precipitated and colloidal silica) has been thoroughly studied by many researchers [4-6,26-28,31,117-122]. However, only a few of them have studied the polymerization below the isoelectric point [26,28,30,93,118], and no research has been done under the olivine nano-silica conditions.

Lieftink [30] investigated the texture of silica produced under the olivine nano-silica conditions. These conditions are negative pH, slow and continuous silica release and sulfate salts concentrations around 3M. He measured the particle size of olivine nano-silica using TEM, resulting in particles sizes between 6 and 20 nm in agreement with values calculated from the SSA_E using Eq. (2.20). Nevertheless, the silica particles in the TEM micrographs [30] seemed to be grouped in clusters, and single particles with sizes between 6 and 20 could not be observed. In addition, Lieftink [30] stated that a stable colloidal dispersion was obtained for olivine nano-silica. He specified that stable colloidal silica particles were obtained during the dissolution of olivine. He also stated that these colloids were likely to be stabilized by steric repulsion via two possible mechanisms: 1) the formation of a strongly adsorbed hydration layer; and 2) the formation of a sulfate layer adsorbed on the silica where water molecules could be adsorbed [30]. However, the only results that Lieftink reported to support this theory on the stabilization were the particle size measured using TEM and the decrease of the viscosity, which was visually identified (see Chapter 6). In addition, Gorrepati [93] found that silica particles prepared from waterglass grew to clusters of 3 μm in 4000 minutes in 4M hydrochloric solutions at 5 °C (see Figure 7.5). Therefore, Lieftink's statement about stable colloidal silica particles is considered to be doubtful.

This main aim of this chapter is to clarify the mechanism of the silica polymerization under the olivine nano-silica production conditions in order to understand the influence of

the polymerization on the textural properties of the silica. A secondary objective is to study the zeta-potential of dispersed olivine nano-silica particles, and compare it with other types of silica. An additional objective is to explain why gelling does not take place under these conditions.

This chapter is structured in three parts: 1) literature review on the mechanisms involved in the particle polymerization and stability of silica; 2) zeta potential studies of olivine nano-silica; and 3) polymerization studies of olivine nano-silica.

7.2 Literature review

7.2.1 Dispersion stability of colloidal particles

A colloidal dispersion (the definition of a colloidal dispersion can be found in Appendix I) is stable when its properties remain constant over time, which means that colloids do not grow with time nor the dispersion becomes a gel. The forces that can be present between colloidal particles are electrostatic, van der Waals and steric [6,123]. The electrostatic forces between particles are attractive when the particles have charges of opposite sign and repulsive when the charge has the same sign. The electrostatic repulsion is due to the overlap of electric double layers of the same sign. The van der Waals forces refer to the attractive or repulsive forces between molecular entities (or between groups within the same molecular entity) other than those due to bond formation or to the electrostatic interaction of ions or of ionic groups with one another or with neutral molecules [41]. The DLVO theory [124,125] proposes the following expression for the total potential:

$$V_T = V_A + V_R \,, \qquad \textbf{(7.1)}$$

where V_T is the total potential, V_A is the attractive potential and V_R is the repulsive potential, which does not take into account steric forces. When the attractive potential is higher than the repulsive potential, the colloidal dispersion is unstable; otherwise, the colloidal dispersion is stable. In addition to the potentials taken into account in the DLVO theory, steric stabilization should be considered as well since it is the main mechanism in the stability of some colloidal dispersions. Steric stabilization occurs when there is a layer on the surface of the colloidal particles that prevents the particles to come closer than a certain limit.

The effect of gravity should also be considered in stabilization studies when the particles dispersed in a liquid are bigger than one μm. The ratio of gravitational to brownian forces determines which factor dominates the dispersion process [126,127]:

$$\frac{\text{Gravitational force}}{\text{Brownian force}} = \frac{r^4 \cdot \Delta\rho \cdot g}{k_B \cdot T}, \qquad \textbf{(7.2)}$$

where r is the particle radius, $\Delta\rho$ the density difference between the dispersed and continuous phases, g the acceleration due to the gravity, k_B the Boltzmann constant and T the absolute temperature. When this ratio is higher than one, sedimentation is likely to occur even if the electrostatic repulsion is very high; when this ratio is lower than one, the Brownian force is the dominant factor. The radius of silica at 20 °C to make this ratio the unity can be estimated ($\Delta\rho$ is 1200 kg/m^3), resulting in 766 nm. Thus, when the silica particles are larger than 1.5 μm, some sedimentation is likely to occur, which makes the dispersion unstable. When the gravitational force dominates the process, the sedimentation rate of the particles can be slowed down decreasing the $\Delta\rho$ and increasing the viscosity

7.2.2 Zeta potential and isoelectric point

The isoelectric point is defined by the IUPAC as the value at which the net electric charge of an elementary entity is zero [41]. According to a review performed by Parks [128], the isoelectric point of silica is the range between pH 0.5 and 3.7, being commonly considered that the isoelectric point is around pH 2 [128]. The isoelectric point depends on the type of silica (crystalline or amorphous) and presence of impurities [129]. Below this pH, the silica particles are positively charged, and above this pH they are negatively charged.

Figures 7.1 and 7.2 present zeta potential curves of monodisperse amorphous silica with an average diameter around 400 nm for different chloride salts with concentrations of 0.001M and 0.1M [129]. When the salt concentration is 0.001M, the isoelectric point is at the pH value of 2 for all the chloride salts. On the other hand, when the salt concentration is increased, the isoelectric point is shifted to higher pH values.

7.2.3 Polymerization of silica

Iler [4] stated that the polymerization of silica consists of three stages: 1) nucleation of particles; 2) growth of the nucleus forming bigger particles: and 3) linking of particles into branched chains and networks. Silica particles grow following a condensation reaction of the silanol groups according to Eq. (4.3) [4].

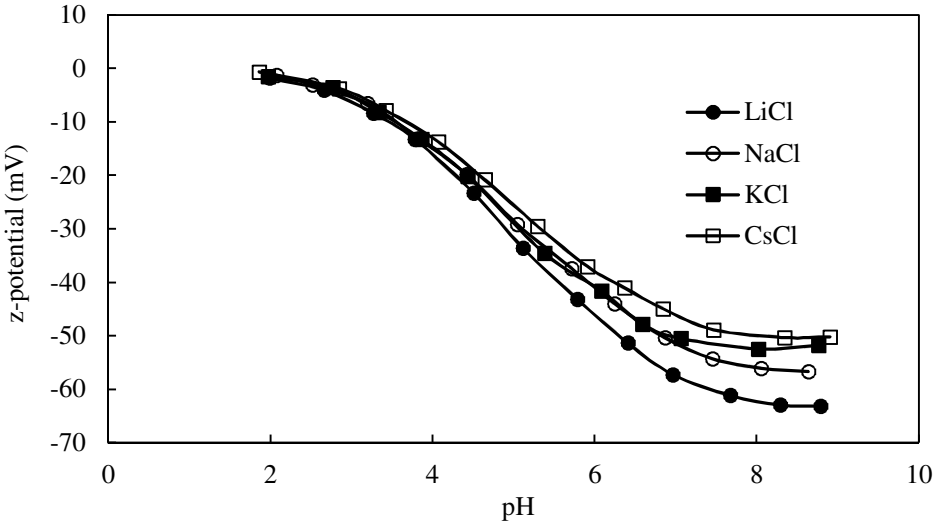

Figure 7.1. Zeta potential of amorphous silica in 0.001M chloride dispersions [129].

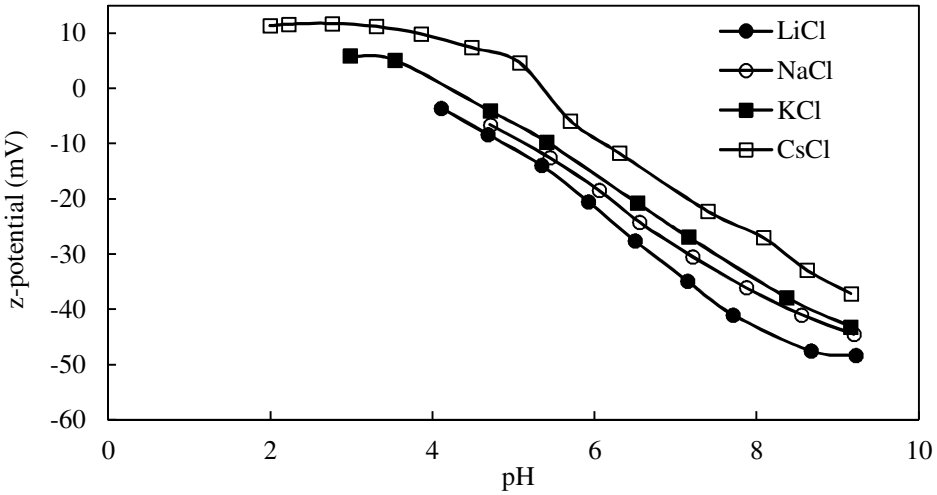

Figure 7.2. Zeta potential of amorphous silica in 0.1M chloride dispersions [129].

7.2.3.1 Supersaturation and nucleation

Before the silica nucleation takes place, the solution needs to reach a supersaturated state. The supersaturation ratio at which the nucleation starts can be defined as:

$$S = \frac{[Si]_{sup}}{[Si]_{eq}}, \tag{7.3}$$

where S is the supersaturation ratio, $[Si]_{sup}$ the silica concentration at the supersaturation point and $[Si]_{eq}$ the silica concentration at the equilibrium (i.e., solubility of silica).

The solubility of silica depends on the type of silica, temperature, pH, particle size and presence of other compounds in the dispersion [4], the most influencing parameters being the pH and the temperature. Goto [130] studied the influence of the temperature and pH on the solubility of amorphous silica particles of 5 nm (see Figure 7.3). Alexander [92] studied the solubility of amorphous silica in water in the pH range between 1 and 11, obtaining a solubility value around 150 ppm at pH 1 and 25 °C.

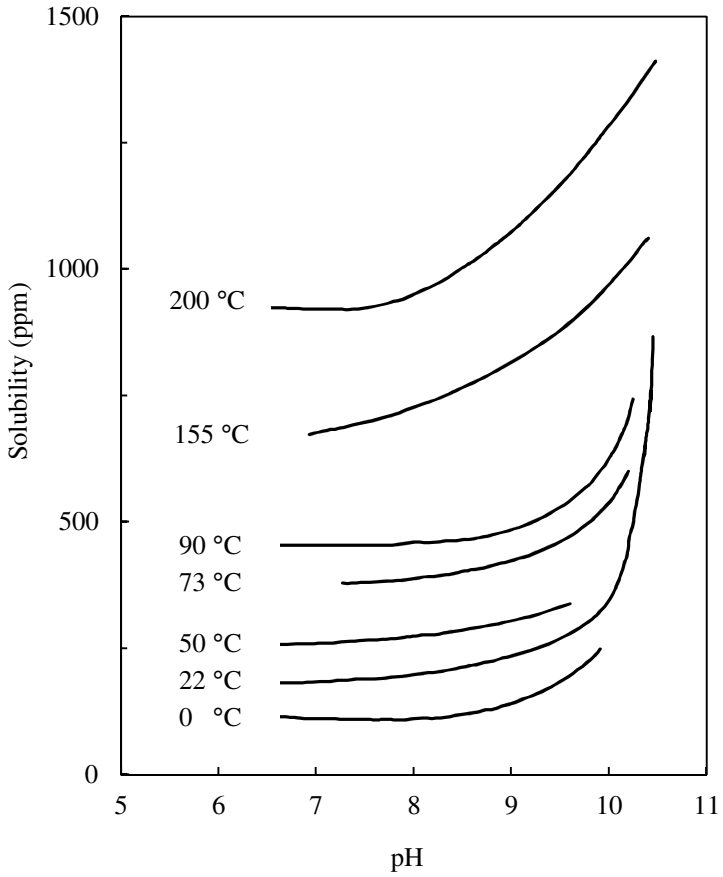

Figure 7.3. Solubility of amorphous silica particles of 5 nm at different temperatures and pH values [130].

The nucleation of silicic acid (also referred as silica monomers) has been studied by many researchers [4,26,27,120-122,131] following the disappearance rate of silicic acid using the molybdate method. This method determines photometrically the concentration of molybdate-reactive silica. Molybdate-reactive silica includes dissolved simple silicates, monomeric silica and silicic acid and an undetermined fraction of polymeric silica [132]. More details about this method can be found in [4,132,133].

Table 7.1 summarizes the literature data about the supersaturation ratio. The supersaturation ratio of silica is in the range 1 to 10, except for the study conducted by

Gorrepati [131], who estimated theoretically a supersaturation ratio of 25 for a critical nucleus of 5 nm.

Table 7.1. Supersaturation ratios of silica.

pH	T (°C)	S	Reference	
8	-	5-10	Marsh	[134]
5	95	2-3	Makrides	[135]
2	90	6.3	Alexander	[92]
-	-	25 [1]	Gorrepati	[131]

[1] This value was estimated theoretically [131].

Okkerse [26,31] studied the disappearance of silicic acid (or what he called low-molecular silicic acid) of 0.25 wt.% (~2500 ppm) waterglass solutions in the pH range between 1 and 5. He found that the disappearance rate was minimal at about pH 2, and increased linearly with the hydrogen ion concentration below pH 2. At lower pH levels than the isoelectric point, silica condensates following reaction Eq. (4.3), where the hydrogen ions catalyze the reaction creating an intermediate species carrying a positive electrostatic charge [6,26]:

$$\equiv SiOH_2^+ + HO-Si\equiv \rightarrow \equiv Si-O-Si\equiv + H^+ + H_2O. \qquad \textbf{(7.4)}$$

Okkerse [26,31] proposed a condensation rate at pH below the isoelectric point for silicic acid depending on the hydrogen ion concentration and the concentration of dissolved silica:

$$r_{con} = k_{con}\cdot(f[Si(OH)_4]_i)\cdot[H^+]\cdot[Si(OH)_4]^3\,, \qquad \textbf{(7.5)}$$

where r_{con} is the condensation rate and $f[Si(OH)_4]_i$ is a parameter proportional to the concentration of silicic acid at the beginning of the experiment. Okkerse [26] also proposed that the rate of condensation of silicic acid with silica of higher molecular weight is slower than the rate of condensation between two units of silicic acid. Therefore, when waterglass is added to an acidic solution with a pH below 2, the rate of formation of nuclei is higher than the rate of deposition of silicic acid on silica of high molecular weight.

Weres [121] performed experiments on the rate of disappearance of silicic acid using waterglass solutions with silica concentrations between 500 and 1200 ppm, pH in the range 2.5 to 8 and NaCl concentrations up to 1M. He stated that silica nucleation is

homogenous (i.e., nucleation does not take place in preferential locations), provided no colloidal silica particles are in the medium, which is in agreement with Iler [4]. Weres [121] affirmed that the nucleation rate depends on the concentration of silicic acid, temperature and the ionization of the silica, which likewise depends on the pH of the solution and the ionic strength. This statement was also confirmed by Chan [120].

Fleming [27] conducted experiments on the disappearance rate of silicic acid in the presence of colloidal silica using waterglass solutions with silica concentrations between 100 and 500 ppm, pH in the range 4 to 8 and NaCl concentrations up to 1M. He found a supersaturation level of 200 ppm. Fleming [27] concluded that the disappearance of silicic acid follows two mechanisms depending on the supersaturation level: below 200 ppm, the silicic acid coats the surface of the colloidal silica and the disappearing rate is relatively low; and above 200 ppm the disappearing rate is much higher.

Gorrepati [131] studied the polymerization of silicic acid using waterglass solutions with a silica concentration of 135 mmol/L (~12000 ppm) in HCl solutions between 2M and 8M, and up to 1M chloride salt concentration at 5 °C. She found a disappearance rate at pH levels far below the isoelectric point, depending on the concentrations of hydrogen ions and silica (in the absence of chloride salts):

$$r_{con} = k_{con} \cdot [Si(OH)_4]^2 , \qquad \textbf{(7.6)}$$

where k_{con} depends on the initial concentration of silicic acid and the hydrogen ion. In the literature, reaction orders of 2, 3 and 4 can be found [26,27,92,122,131,136]. Gorrepati [131] accounted these discrepancies for the different experimental conditions used (e.g., pH and temperature).

Figure 7.4 presents Gorrepati's results of the concentration of silicic acid and the particle size of silica [131]. She found that the silicic acid concentration drastically decreases at the beginning of the experiment, having being almost completely consumed after 20 minutes. On the other hand, the increase of the particle size is exponential, being more pronounced at the end of the experiment. From these results, Gorrepati concluded that the mechanism of the particle growth of silica is the aggregation of silica particles, and she ruled out that it would be due to addition of monomeric species

7.2.3.2 The formation of primary particles

Primary particles refer to the smallest colloidal particle (temporarily stable) that can be experimental observed. The size of the primary particles of silica is in the range of 1 to 6 nm [4,6,29,30,131,137-141]. The reasons for the difference between the sizes of the primary particles are that: 1) not all the researchers have used the same characterization methods; 2) the synthesis methods are different; 3) the synthesis conditions are different

(i.e., pH, temperature, silica concentration, etc.); and 4) the times when the analyses have been performed are different.

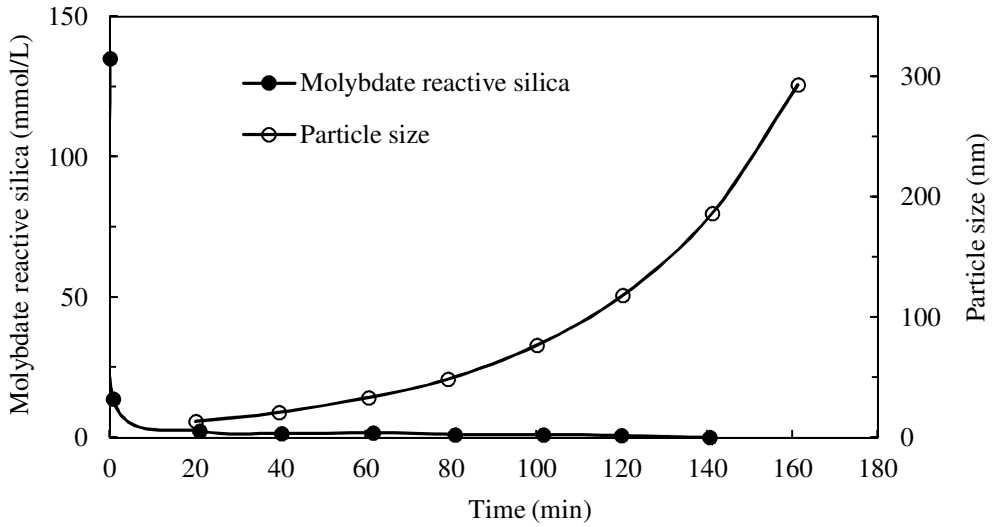

Figure 7.4. Evolution of silicic acid concentration and particle size in an 8M HCl solution at 5 °C [131].

Prior to the formation of the primary particles, oligomers should be formed. Iler [4] defined them as the low molecular weight polysilicic acids from trimers to perhaps octamers. He divided up the oligomer formation into the following steps: 1) condensation of silicic acid into dimers; 2) tetramer formation by combination of two dimers; 3) ring closure of tetramers; 4) henceforth monomer and dimer react preferentially with these more highly ionized species, increasing their molecular weight; simultaneously, wherever it is possible, silanol groups condense evolving to more compact, three-dimensional species, which are the precursors of the primary colloidal particles [4]. Iler stated that the nucleation process is reversible, and each polymer species is in equilibrium with a certain concentration of silica monomer in solution [4].

Once the oligomers are formed, a further increase in the particle size occurs rapidly if the solution is still supersaturated. A polycyclic oligomer is not actually considered as a silica particle because there is no anhydrous silica core. At this point, the monomers in the solution condense with the silanol groups of the oligomers until the oligomers remain as an anhydrous silica core. Monomers also condense with themselves forming a silica layer on the surface of the oligomers with the silicon atoms outwardly exposing silanol groups [4].

In molecular simulations performed by Iler [4], it was found that when monomers condensate on octamers or decamers to form a nearly anhydrous silica core surrounded by silicon atoms forming the external hydroxylated surface of the particle, the particle contained between 40 and 50 silicon atoms. This primary particle had a particle size

around 1.6 nm [4]. Okkerse [26] found that the size of the primary particles produced from the neutralization of waterglass was influenced by the rate and duration of the condensation reaction. A slow condensation reaction resulted in small silica particles, while at fast reactions larger primary particles were obtained. In acidic conditions, primary particles between 1 and 2 nm have been found [6,29,118,142].

Kelt [28] studied the hydrolysis of tetraethyl orthosilicate and the subsequent polymerization of silica at pH 1, 5 and 8 using ^{1}H and ^{29}Si NMR. He interpreted that silica grows forming linear oligomers instead of cyclic oligomers. Zerda [118] also studied the hydrolysis and polymerization of tetramethyl orthosilicate in the pH range between 1 and 9 using Raman spectroscopy and ^{29}Si NMR. At pH 1, the condensation reaction was catalyzed by the hydrogen ions according to Eq. (7.4) in agreement with Okkerse [26]. Zerda [118] proposed that at a pH level of 1 and at the beginning of the polymerization process, linear chains or weakly cross-linked branched structures of approximately 2 nm and low internal degree of condensation were produced.

He explained the formation of these chains with the following hypothesis: the condensation takes place in the least acidic silanols, which are the silicon atoms with the lowest number of condensed groups (e.g., in a chain the silicon atoms with less siloxane bonds are the edges) [118]. As the silica particle keep increasing in size, the silanol groups attached to the branched chains internally condense, and at the same time other silanols bind to the edge of the particles. In the last stages of this process, three dimensional growth becomes more dominant, leading to the formation of highly branched particles [118]. Thus, Kelt [28] and Zerda [118] found that, below the isoelectric point, the nuclei formation based on a ring structure proposed by Iler [4] does not take place.

7.2.3.3 Particle growth by aggregation

Based on the condensation model of Ordway [143], Iler [4] proposed a hypothesis about the reaction mechanism of silicic acid when some nuclei are present for pH values between 2 and 7. According to this hypothesis, silicic acid condenses preferentially at a location where the silicon atom has only one OH group because it is the most acidic and readily ionized [4]. When a certain amount of nuclei are present in the dispersion, the remaining silicic acid reacts preferentially with them because of its greater acidity and degree of ionization. As the concentration of silicic acid drops, the oligomers, which were in equilibrium with the higher silicic acid concentration, depolymerize. Subsequently, the newly dissolved silicic acid condenses on the nucleus [4]. On the other hand, Okkerse [26] and Gorrepati [131] found that, below the isoelectric point, the formation of nuclei is faster than the rate of condensation between silicic acid and high molecular weight particles.

Iler proposed that in the pH range between 2 and 7 silica colloids link together into branched chains to form three-dimensional network regions forming gels [4]. The

condensation follows a similar path as in Eq. (7.4), but instead of $Si(OH)_2^+$, SiO^- species are involved. The presence of silicic acid or silica monomers then plays a role in further cementing the particles together. In addition, Iler [4] pointed out that the presence of silicic acid may play a role in promoting the formation of the initial bond.

7.2.3.4 Overall particle growth of silica particles

The influence of the pH and salt concentration on the aggregation rate of silica monomers at pH far below the isoelectric point was studied by Gorrepati using waterglass [93]. She found that both parameters have an important influence on the aggregation rate of silica particles, as can be seen in Figures 7.5 and 7.6. Gorrepati [93,131] stated that the silica particle growth follows a two steps process: 1) formation of primary particles of 5 nm; and 2) aggregation of these particles.

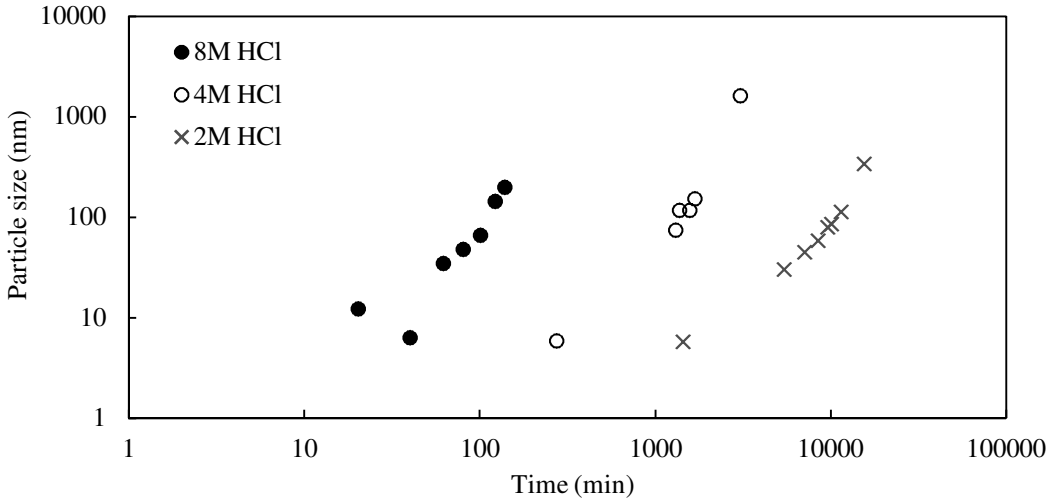

Figure 7.5. Size of the silica clusters over time for different HCl concentrations [93].

Depending on the state of the clusters, they could be classified as aggregates or agglomerates (definitions of them are provided in Appendix I).

The polymerization of silica proposed by Iler between pH 2 and 10 is summarized in Figure 7.7. This figure shows the reaction path to form the primary particles as well as the two possible growth routes depending on the pH and salt concentration, which result either in silica gel or a stable colloidal dispersion.

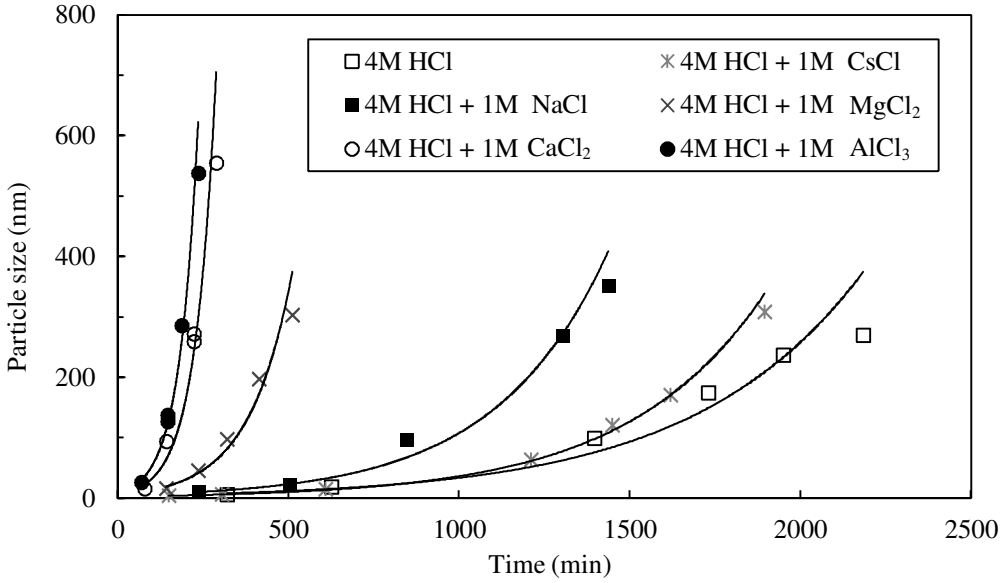

Figure 7.6. Size of silica clusters over time for 4M HCl solutions for different chloride salts [93].

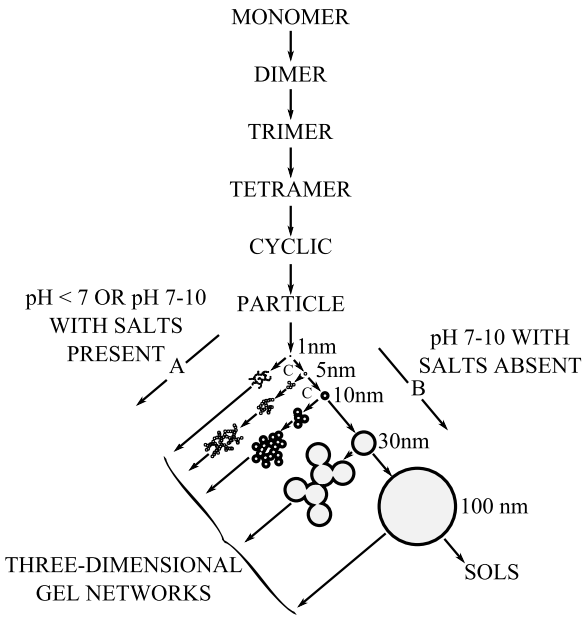

Figure 7.7. Polymerization behavior of silica between pH 2 and 10 [4].

Nano-silica produced from the olivine route polymerizes at similar conditions to Gorrepati's experiments because olivine nano-silica is produced far below the isoelectric point. Thus, the particle growth should follow a similar path to the one proposed by Gorrepati [93]. The main differences between the process of Gorrepati and the olivine nano-silica process are the type of acid used, temperature and the source of silica. The source of silica used by Gorrepati was waterglass [93], whereas the source of silica in this

study is the olivine mineral. The main difference between these two is that in the case of olivine, silica is released into the medium at the dissolution rate, whereas silica from waterglass is in the medium from the beginning.

Gorrepati also investigated the dissolution and precipitation of the zeolite mineral analcime. She studied the evolution of the concentration of silica particles smaller than 200 nm using ICP (see Figure 7.8). Gorrepati concluded that the silica produced from the dissolution of analcime precipitates in the same manner as the silica from waterglass. Therefore, she considered that the silica released during the analcime dissolution polymerized in the same way as waterglass silica [93,131].

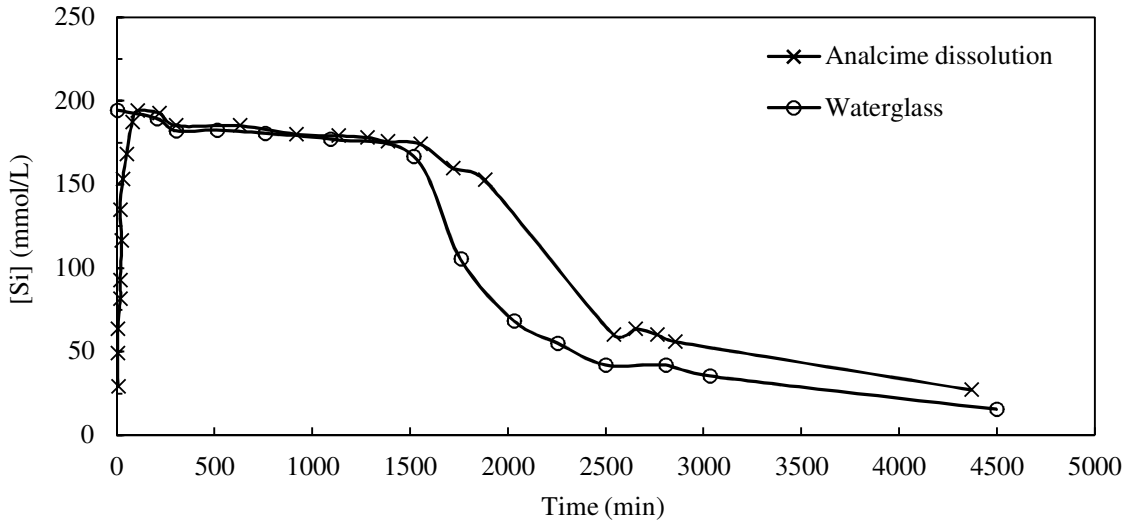

Figure 7.8. Evolution of the concentration of silica particles smaller than 200 nm using analcime and waterglass [131].

8 grams of analcime (particle size between 0.2-38 μm) were dissolved in 300 mL of 4M HCl at 5 °C. The dispersion was filtered using a 0.2 μm filter prior to the analysis.

7.2.4 Stability of colloidal silica and gelling

A central aspect of the chemistry of colloidal silica is the study of stabilization and gelling. The stability of colloidal silica has been investigated for several decades due to its importance and complexity. Colloidal silica is considered to behave anomalously in the sense that does not follow the DLVO theory [124,125]. The reason for this anomalous behaviour is that besides the van der Waals and electrostatic forces, the effect of the steric force and slow condensation rate at low ionization states (i.e., around the isoelectric point) should be taken into account. In the case of colloidal silica, stabilization by steric repulsion has been reported by several authors [6,144-152]. Two types of layers causing the steric repulsion have been proposed: a hydration layer and a silica layer.

Figure 7.9 summarizes the gelling behaviour of colloidal silica in the pH range between 0 and 14, and with and without 0.1M NaCl [4]. This figure shows that at pH 2, when the

ionization is the lowest, the colloid system is temporary stable. This is due to a steric repulsion [4,146-148,150,153], and also maybe due to the low ionization state of the silica, which makes the particle growth very slow [92]. The stability decreases with increasing pH between 2 and 7, and at pH 7, it starts to increase again. According to the DLVO theory, this stability rise is the result of a higher electrostatic charge. Above pH 10.5, silica starts to depolymerize because the solubility of silica increases exponentially since silicic acid is dissociated into ionic species. The presence of NaCl above pH 6 reduces the stability of the colloids. This decrease in the stability is due to the compression of the double layer as predicted by the DLVO theory. The type of salt and the size of silica colloids also have an important influence on the stability of silica [4,144,147-149].

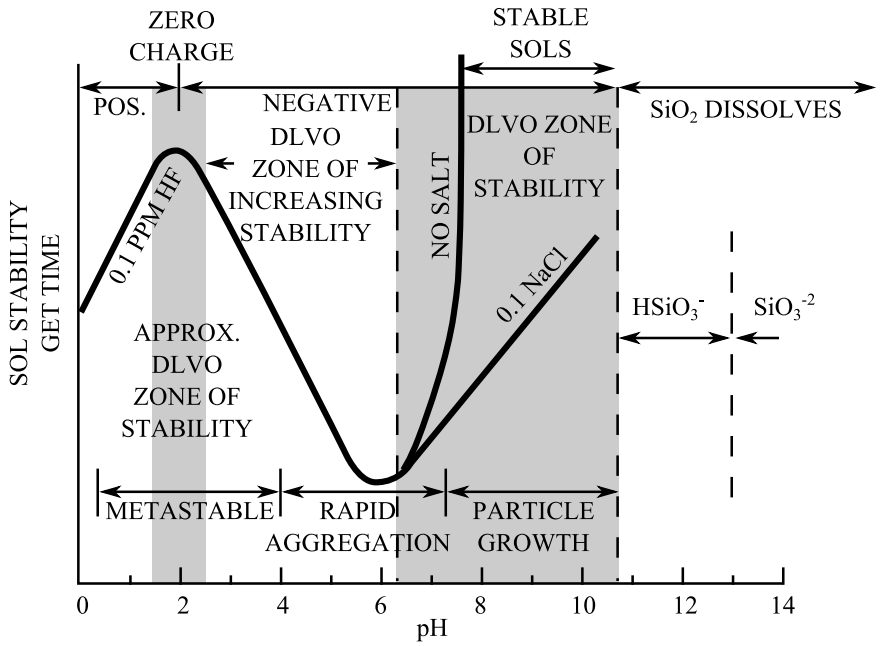

Figure 7.9. Gelling time of colloidal silica versus the pH of the solution with and without 0.1M NaCl [4].

A gel was defined by Iler [4] as the condensation of silica particles into siloxane chains, then branching and cross-linking to form a three-dimensional molecular network. Silica gels are commonly produced by acidification of waterglass immediately followed by depositing onto a moving belt where the gelation takes places in several minutes (Figure 1.7 shows the flow diagram of the silica gel production process) [2,6]. Silica gels can be produced in a wide pH range, but normally they are produced above the isoelectric point at pH conditions where gelling occurs fast. A silica gel under negative pH conditions was produced by Lambert [154]. He reported a gelling time around one hour for a colloidal dispersion with 12 nm particles and with 10% solid content in a 98% sulfuric acid solution [154]. This gelling time is much longer than the predicted time by the equation

derived by Yates [6,155]. When the silica colloids are of a considerable size, particularly at low pH, interparticle bonding is rarely observed [4]. Actually, particles larger than 100 nm over the whole pH range hardly gel, even in concentrated sols [4].

7.3 Materials and methods

The zeta potential of olivine nano-silica was studied with a dispersion of 1 wt.% of silica in distilled water. Batch NS-51-S5, the chemical composition of which is presented in Table 7.2, was used in these experiments. This dispersion was prepared using the high shear mixer at 5000 rpm for 3 minutes and the ultrasonic device (details of the high shear mixer and ultrasonic device are given in Chapter 6) at maximum power for 5 minutes. The pH of the dispersion was adjusted with NaOH and H_2SO_4 solutions.

Table 7.2. Chemical composition of cake NS-51-S5 measured by XRF and combustion infrared technique.

Sample	SiO_2 (%)	Al_2O_3 (%)	Fe_2O_3 (%)	MgO (%)	CaO (%)	K_2O (%)	Cr_2O_3 (%)	LOI (%)	S (%)	Psi (%)
NS-51-S5	89.72	0.25	0.64	0.14	0.01	0.03	0.08	9.13	0.05	98.72

The particle growth of silica during the olivine dissolution was investigated with Norwegian dunite GL40. GL40 has a similar chemical composition to GL50 (see Table 2.1), but its average particle size is smaller. In addition, GL40 was milled for 30 minutes in order to accelerate the olivine dissolution without speeding up the particle growth of nano-silica. These experiments were carried out at 20 °C, in a vigorously stirred, thermostated reactor of two liters with sulfuric acid. The amount of olivine used was selected to have a similar silica concentration to Gorrepati's experiments (135 mmol/L). The experimental variables were the concentration of sulfuric acid and surface area of olivine. The temperature of 20 °C was selected to slow down the particle growth in order to be able to track the particle size development. This low temperature also slows down the olivine dissolution reducing the release rate of silica. The concentration of hydrogen ions was determined by titration with a 0.05M $Na_2B_4O_7$ solution at regular time intervals, from which the amount of silica produced was calculated. The particle size (or cluster size) was measured with the Malvern ZS after passing the samples through a filter of 1 μm in order to avoid the presence of olivine particles in the dispersion. However, at the beginning of the experiment, some particles in the size range between 500 and 1000 nm were found. These particles were neglected because they were likely to be olivine particles. Table 7.3 lists the conditions of the nano-silica polymerization experiments.

The particle size measured with the Malvern ZS can be classified as aggregates or agglomerates depending on its stage (definitions of aggregate and agglomerate terms are provided in Appendix I). For example, at the beginning of the experiment, where sizes

below 100 nm are found, the silica clusters are likely to be aggregates, whereas at longer times, and, therefore, larger particle sizes, the silica clusters are likely to be agglomerates.

Table 7.3. Conditions of the nano-silica polymerization experiments.

Experiment	m_{ol} (g/L)	$[Si]_{eq}$ (mmol/L)	d_{50} (µm)	SSA_G (m^2/g)	SA_T (m^2)	$[H^+]$ (mol/L)	T (°C)
NS-PO-2	50	307	116	0.09	9.0	4.0	20
NS-PO-3	50	307	116	0.09	9.0	2.0	20
NS-PO-6	70	429	116	0.09	12.6	4.1	20

$[Si]_{eq}$ refers to the equivalent concentration of silica from the olivine amount, SSA_G geometric specific surface area, and SA_T total surface area of the olivine.

7.4 Results

7.4.1 Zeta potential

Table 7.4 lists the conductivity and zeta potential of nano-silica dispersions prepared with batch NS-51-S5. It was not possible to measure the zeta potential below pH 1 because the conductivity rose above 40 mS/cm resulting in problems with the measurements. Figure 7.10 shows the zeta potential versus the pH, where it can be seen that the isoelectric point is around a pH value of 1, being in the interval found by Parks [128]. The zeta potential profile is linear, the negative charge of the particles increasing with the pH. Zeta potentials of -30 mV – value at which colloids are commonly considered to be stabilized electrostatically – are obtained around pH 7.

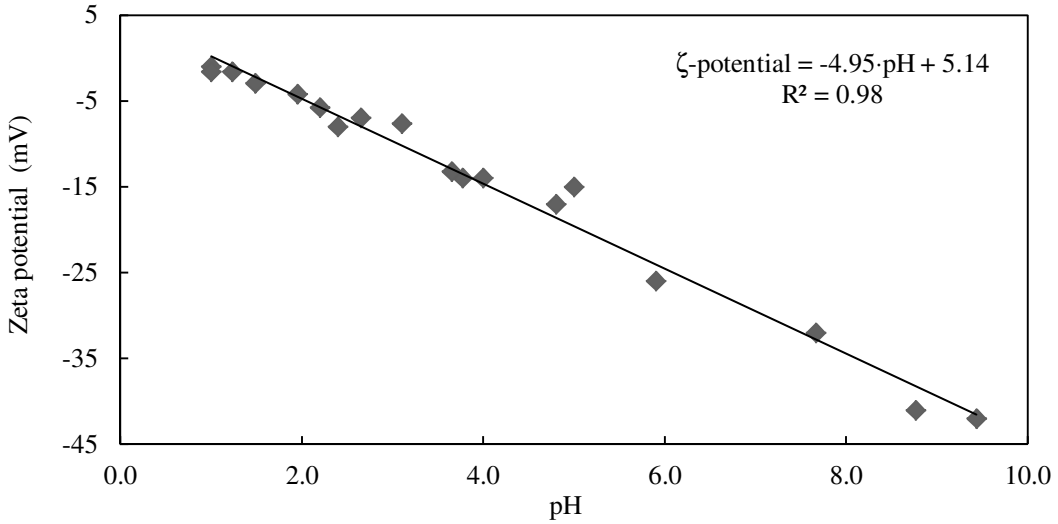

Figure 7.10. Zeta potential of nano-silica dispersions versus pH.

Table 7.4. Zeta potential of nano-silica dispersions at different pH values.

pH	Conductivity (mS/cm)	zeta potential (mV)
4.0	0.1	-14.0
7.7	0.1	-32.0
8.8	0.2	-41.0
9.4	0.2	-42.0
3.8	0.1	-14.0
4.8	0.1	-17.0
5.9	0.1	-26.0
2.4	1.8	-8.0
1.0	40.0	-1.0
5.0	0.3	-15.0
3.1	0.7	-7.6
2.2	3.0	-5.8
1.5	14.6	-2.9
1.0	45.0	-1.6
3.7	0.2	-13.2
2.7	1.2	-7.0
2.0	5.3	-4.2
1.2	26.0	-1.6

The zeta potential profile of olivine nano-silica (batch NS-51-S5) is similar to the results of Franks [129], except for few differences: 1) the zeta potential profile of olivine nano-silica does not feature a plateau at high pH values, while Franks' profile with 0.001M salt concentration does; 2) the isoelectric point is found at a lower pH level in the case of olivine nano-silica; and 3) the pH needs to be above 7 to obtain a negative charge on the silica particles leading to a zeta potential below -30 mV, whereas this zeta potential is obtained around pH 5 in Franks'dispersions (see Figure 7.1) [129]. These differences could be due to the presence of impurities such as aluminium and iron ions, which are ions that can change significantly the electrostatic charge of the silica surface [4].

7.4.2 Particle growth

Figure 7.11 plots the concentration of silica produced during the dissolution of olivine in the polymerization experiments. The quantity of silica produced is calculated stoichiometrically from the amount of hydrogen ions consumed. NS-PO-2 and NS-PO-6 showed similar production rates of silica, whereas the rate of NS-PO-3 is lower. This lower production rate is because the concentration of hydrogen ion for NS-PO-3 was 2M instead of 4M. On the other hand, it is remarkable than the particle growth of NS-PO-2 is slightly faster than that of NS-PO-6 since the total surface area of NS-PO-2 is supposed to be smaller.

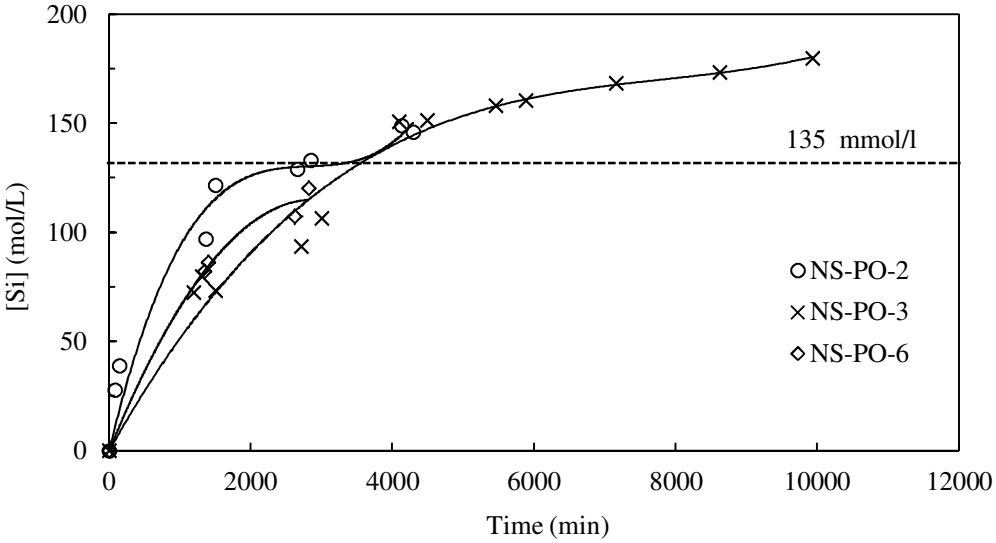

Figure 7.11. Silica produced over time for the particle growth experiments.

Where 135 mmol/L is the concentration used by Gorrepati [93].

Figure 7.12 presents the average particle size of silica over time during the particle growth experiments at 20 °C. Table 7.5 shows the estimated time and the amount of silica produced at the point where the average cluster size of silica was 60 and 100 nm for the three polymerization experiments. The cluster size of silica increased exponentially with time, reaching values above 400 nm after 4300 min for NS-PO-2. The growth rate of silica accelerated with the increase of the hydrogen ion concentration and amount of nano-silica released. In the case of the olivine nano-silica produced under the conditions used in Chapters 3-6 (3M H_2SO_4 and temperatures between 50 and 90 °C) the particle growth should be much faster than under the conditions of the polymerization experiments.

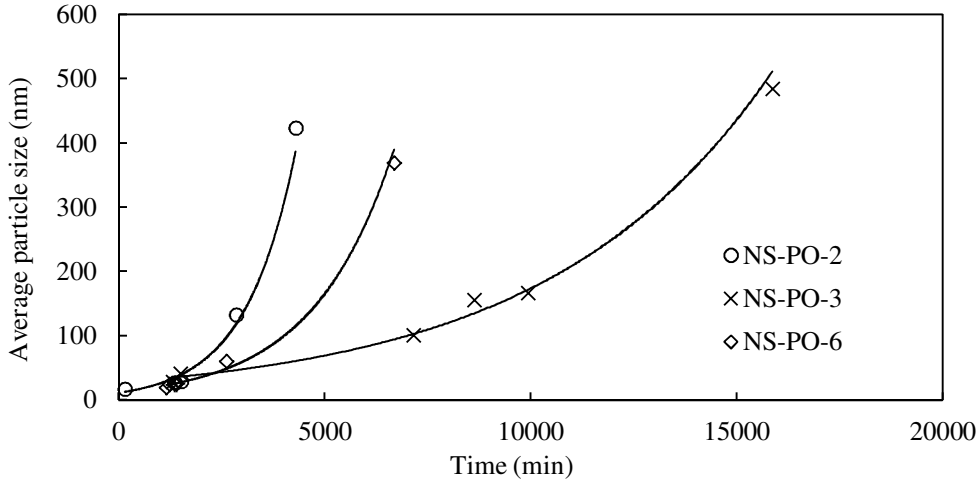

Figure 7.12. Growth of silica particles during the dissolution of olivine.

Gorrepati [93] found that using 135 mmol/L of waterglass and a 4M HCl solution, around 1300 minutes were required to obtain silica particles of 100 nm (see Figure 7.5) [93,131]. In the case of NS-PO-2, 2600 minutes passed before 100 nm silica particles were found. In addition, in the analcime experiments of Gorrepati [131] (see Figure 7.8), most of the zeolite had reacted after 100 minutes, whereas the cluster size of silica colloids from waterglass under similar conditions required around 1300 minutes to grow over 100 nm. Therefore, the dissolution time of the analcime regarding the time to obtain silica particles above 100 nm is rather short. In the case of the olivine, it is the opposite, the olivine dissolves slowly, only having been dissolved 42% of this material when the silica clusters have grown over 100 nm for experiment NS-PO-2. Thus, it can be concluded that the main reason for the slower particle growth of olivine silica is probably a slow release of silica into the medium.

The growth of the olivine silica clusters presents a trend similar to the one found in Gorrepati's experiments using waterglass, but with a lower particle growth rate. This similarity could mean that the mechanism of the particle growth of olivine nano-silica follows the same path as the silica particle growth from waterglass. However, further research would be necessary to verify this.

Table 7.5. Time and amount of silica produced for the formation of 60 and 100 nm silica particles during the polymerization experiments.

Experiment	d_A (nm)	time (min)	[Si] (mmol/L)	d_A (nm)	time (min)	[Si] (mmol/L)
NS-PO-2	60	2016	125.04	100	2639	130.89
NS-PO-3	60	4212	107.05	100	6989	150.78
NS-PO-6	60	3011	-	100	4011	-

d_A is the average particle size of silica determined by laser light scattering.

7.5 Discussion

As was mentioned previously, silica gels are commonly produced by the acidification of waterglass. This process is normally performed above the isoelectric point at pH conditions where gelling occurs fast, but also can be conducted under negative pH conditions [154]. However, a silica gel is not obtained during the dissolution of olivine under the conditions (temperature, pH and olivine concentration) employed in this study.

An explanation for the absence of gelling of large silica colloids was given by Iler [4], who stated that particles larger than 100 nm do usually not gel. He suggested that the mechanical force between the particles due to the Brownian motion is strong enough to break the newly formed siloxane bonds [4]. In experiment NS-PO-2, particles of 100 nm were formed after 2600 minutes. In addition, under the production conditions used in Chapters 3-6, the required time to form 100 nm particles would be even shorter.

Therefore, olivine silica grows fast to sizes over 100 nm, preventing the dispersion from gelling. Other possible reasons for the lack of gelling of olivine silica are: 1) the silica concentration of small silica colloids (i.e., smaller than 100 nm) is not high enough. In the case of complete conversion and 3M sulfuric acid (see Figure 5.1), the maximum amount of silica produced is around 9 wt.%; and 2) the vigorous mixing in the reactor to keep the olivine particles suspended makes gelling unlikely. In fact, during the olivine nano-silica experiments, gel formation on the reactor wall above the liquid level (where the slurry was not mixed) took place.

Another unclear aspect of olivine nano-silica is the increase of the viscosity at low conversion degrees (see Figure 6.8 and Table 6.8). Lieftink [30] considered that this increase of the viscosity was due to the formation of a gel-phase. He also concluded that the gel phase appeared when the concentration of silica was about 0.05 mol/L, and this gel phase disappeared when the colloidal particles grew. This explanation seems reasonable, but more experiments with more accurate determinations of the viscosity are required to confirm it.

7.6 Conclusion

The zeta potential of silica produced from the dissolution of olivine is linear in the pH interval between 1 and 9.5. The isoelectric point for olivine silica dispersions is around pH 1, being slightly lower than the values found in the literature for silica colloids [128]. Zeta potential values above 30 mV, which is usually considered the value to stabilize colloids electrostatically, are obtained when the pH value is above 7.

The cluster size of olivine silica grows up to 420 nm after 4300 minutes of reaction at 20 °C in 2M H_2SO_4solution. The particle growth should be much faster under the conditions described in Chapters 3-6 (>50 °C and 3M H_2SO_4), at which olivine dissolves within several hours. The particle growth shows a trend similar to the one found in Gorrepati's experiments using silica from waterglass, which could mean that the mechanism of the growth of olivine silica is due to the nucleation of primary particles and subsequent aggregation of these primary particles. Further research is needed to verify this hypothesis.

Olivine nano-silica does not gel. This behaviour of olivine silica can be due to three reasons: 1) silica polymerizes fast at 90 °C in 3M H_2SO_4 solution, forming particles above 100 nm in a short time; 2) the concentration of small silica colloids (i.e., below 100 nm) is low; and 3) the vigorous mixing in the reactor to keep the olivine particles suspended.

Chapter 8. Development of the pore structure of olivine nano-silica

8.1 Introduction

As was mentioned in the previous chapter, the most important parameters of silica powders are its particle structure (i.e., size and morphology), pore structure and surface chemistry. In Chapter 7 it is mentioned that olivine silica grows via a condensation route (Eq. (4.3)), and that silica clusters grow above 100 nm in about 2-day time at room temperature and 2M H_2SO_4 (see NS-PO-2 in Table 7.5). Under the conditions employed in Chapters 3, 4, 5 and 6, the growth occurs much faster resulting in silica agglomerates in the micrometer range as can be observed from Figures 6.12 and 6.14. These agglomerates are greatly porous featuring high specific surface areas.

The total porosity and pore structure of amorphous silica strongly affects the properties and functionality of silica. A specific pore structure is required for some applications, such as the use of porous silica in the field of catalysis or as dry agent. The main factor governing the specific surface area of porous silica, which is strongly related to the porous structure, is the size of the primary particles [26]. As was mentioned in the previous chapter, the size of the primary particles depends on the reaction rate and duration of condensation [26]. Besides the influence of the primary particles on the specific surface area of silica, the aggregation conditions (pH, temperature, amount of silica monomers and silica aggregates in the dispersion, etc.) and the production conditions of olivine nano-silica (impurity content, conversion degree, filtration pressure and ripening treatment) also affect the particle growth and pore structure.

The textural properties of pyrogenic, precipitated and silica gel are summarized in Tables 1.1 and 8.1. In the book of Bergna [6], the porosity of commercial pyrogenic, gel and precipitated silica were reviewed. Pyrogenic silica is essentially non-porous material formed by primary particles of 1 nm with a high coordination number. When this material is pressed, well defined mesopores are developed [156,157]. Precipitated silica is usually considered as macroporous, but to a small extent, also microporous [6]. Silica gels are likely to be mesoporous and/or microporous [6].

Okkerse [26] studied the properties of silica produced in the pH range from -1 to 10 using waterglass as a silica source. Some of his results are summarized in Figure 8.1, where it can be observed that the highest surface area was obtained between pH -1 and 5; at pH above 5, the SSA_{BET} was reduced drastically. Similar results have also been found by Plank [158] and Sing [159]. Okkerse [26] concluded that in the pH range between -1 and 5, the primary particle size of the silica gel was the same since the specific surface area was constant. The reason for this is that there are two opposite effects influencing the size of the primary particles: the reaction rate and reaction time. Thus, at pH 2, the reaction

rate was the slowest, resulting in the smallest primary particles, but the gelling time was also the longest, allowing the primary particles to become larger [26].

Table 8.1. Textural properties of different amorphous nano-silicas [6].

Parameters	Pyrogenic	Precipitated	Gel
Purity, SiO_2 (%)	>99.9	98-99	99.5
SSA_{BET} (m^2/g)	50-400	50-800	20-1000
d_1 (nm)	7-40	2-20	-
d_3 (μm)	-	3-3000	0.1-5000
Porosity	-	Macroporous	Micro and mesoporous

d_1 refers to the diameter of the primary particles, d_3 to agglomerate particles and d_p to pore.

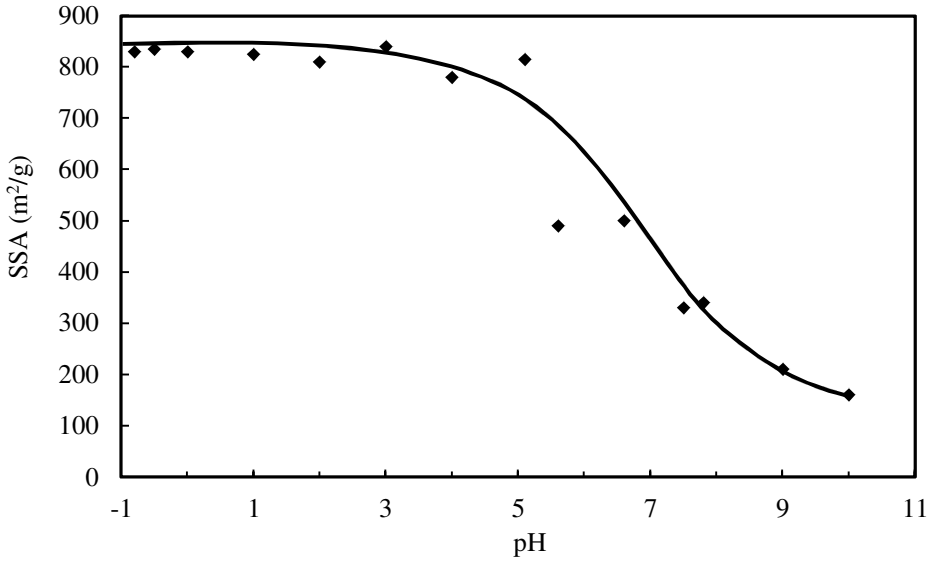

Figure 8.1. Influence of the pH on the SSA_{BET} of silica gel [26].

The pore structure of olivine nano-silica has only been studied by Lieftink [30]. He studied the pore size distribution (PoSD) of olivine nano-silica using nitrogen physisorption with two equipments: Micromeritics ASAP 2400 and ASAP 2010. The ASAP 2400 device was a standard equipment for gas physisorption in the relative pressure range between 0.01 and 0.99 and the ASAP 2010 device was used to study the microporosity at low relative pressures. The material was degassed at 100 °C overnight. This temperature is lower than the required temperature to remove all the physisorbed water, which is 190 °C (see Chapter 2). Thus, some of the pores of the silica could still be partly filled with adsorbed water. Lieftink studied the pore size distribution using the BJH method [30]. Because the BJH method does not give accurate results for pores below 10 nm (see Chapter 2), Lieftink estimated the microporosity using the t-plot [50,51], the

Dubinin [160] and the Saito methods [161]. These methods determine the total amount of microporosity, but they do not provide a pore size distribution. The findings of the nitrogen physisorption analysis performed by Lieftink can be summarized as follows: 1) at low conversion degrees (X) olivine nano-silica is microporous and mesoporous; 2) when the conversion progresses, macropores are also developed. Pore size distributions by mercury porosimetry were also determined, the results of which indicate that olivine nano-silica was mesoporous and macroporous [30].

The specific surface area determined by the BET method [46] using nitrogen can lead to inaccurate results when the sample is microporous (see Chapter 2) due to the method itself, and, in the case the pores are small enough, to the impossibility of nitrogen to penetrate the pores. Another way to determine the SSA is from the content of silanols, considering that the content of the surface silanol groups is constant when silica is fully hydroxylated (α_{FH}):

$$SSA_{NMR} = \frac{\alpha_{OH}}{\alpha_{FH}} \cdot SSA_{BET} , \qquad \textbf{(8.1)}$$

where α_{OH} is the silanol content determined using (in the case of this study) NMR and TG techniques. The NMR and TG techniques determine a total content of the silanol groups, including surface silanols, silanols on the micropores and silanols on internal surface areas (see Figure 5.2). According to Zhuravlev [162], the maximum extent of hydroxylation of silica is around 4.9 OH/nm^2. Zhuravlev determined this constant using the deuterium method, which is limited to surface silanols, and the SSA_{BET} using krypton as the adsorbate gas with a krypton surface area of 0.215 nm^2 [162]. In the determinations performed by Zhuravlev [162], the internal silanols and the silanols in pores narrower than 1 nm were neglected. Gallas [163] disagreed with the maximum silanol number determined by Zhuravlev and proposed a value of 8 OH/nm^2 for precipitated silicas. He determined the silanol content using the TG-IR technique and the SSA_{BET} using nitrogen as the adsorbate gas with a nitrogen surface area of 0.136 nm^2. Gallas attributed the difference in the silanol groups to the fact that Zhuravlev determined the SSA_{BET} using a krypton surface area higher than expected, resulting in higher values of SSA_{BET} and lower values of α_{OH} [162,163]. For olivine nano-silicas, Lieftink found a silanol content between 9 and 27 OH/nm^2 using NMR. He mentioned that this high silanol content was likely to be due to the presence of internal silanols and silanols in micropores. To conclude, a value of α_{FH} of 5 OH/nm^2 is used in this thesis for the estimation of SSA_{NMR} (Eq. (8.1)) because the Zhuravlev constant [162] is the most widely used silanol value for fully hydroxylated silicas, and to compare with the results of Lieftink [30], who also used this value in his determinations.

Lieftink [30] reported the pore structure and the SSA_{NMR} of olivine nano-silica. However, he studied the pore size distribution using the BJH method, and this technique is not suitable for the determination of pore sizes below 10 nm. Also, more data about the pore size distribution is desired in order to understand the influence of the process conditions (conversion degree, impurity content, hydrothermal treatment, etc.) on the pore structure of olivine nano-silica. Likewise, more data about the SSA_{NMR} is also desired.

In this chapter the pore structure of olivine nano-silica is studied using nitrogen physisorption with the BJH method and positron annihilation lifetime spectroscopy (PALS), so that the whole porous range can be determined. Furthermore, the influence of the process conditions on the porous structure and the SSA_{NMR} is investigated.

The results presented in this chapter show that olivine nano-silica is microporous, mesoporous and macroporous. The process conditions have an important influence on the textural properties of olivine nano-silica. Thus, the pore size distribution of olivine nano-silica can be tailored by changing the process conditions to match the requirements of different applications. In addition, a model describing the development of the olivine nano-silica structure is proposed.

8.2 Materials and methods

Nano-silicas prepared via the olivine route under different experimental conditions were analyzed to determine their pore structure and SSA_{NMR}. The pore structure was determined using the BJH method and PALS technique (more details about these two can be found in Chapter 2). The SSA_{NMR} was calculated from the α_{OH} values using Eq. (8.1); the α_{OH} was determined from the silica NMR spectrum (an example of the olivine nano-silica NMR spectrum can be seen in Figure 2.11) with Eq. (2.25). The SSA_{BET} used in this calculation was determined from gas physisorption analyses with degas temperatures of 120 and 190 °C for 4 hours.

The silanol number can also be determined from TG analysis. For this calculation two considerations have to be taken into account: 1) the mass loss involving water related to the silanol groups occurs in the temperature range between 400 and 1100 °C [6]; 2) there are two silanol groups per each water molecule evaporated. Thus, the silanol content can be calculated with:

$$\alpha_{OH}(OH/nm^2) = \frac{2 \cdot N_A \cdot \frac{w_{OH}{}^*}{100}}{M_{H_2O} \cdot SSA_{BET}}. \qquad \textbf{(8.2)}$$

Where N_A is the Avogadro's number, w_{OH}* is the water mass fraction (%) loss in the temperature interval 400-1100 °C for dried silicas at 200 °C and M_{H_2O} is the molar mass of water. Table 5.7 collects the water mass fraction loss in the range 400-1100 °C for silicas containing physically adsorbed water (w_{OH}), from which the w_{OH}* can be calculated:

$$w_{OH}*(\%) = w_{OH} \cdot \frac{100}{100 - w_{H_2O\_A}}, \quad \textbf{(8.3)}$$

where $w_{H_2O\_A}$ is the mass fraction loss between 20 and 200 °C.

8.3 Results

8.3.1 Pore size distribution of olivine nano-silica BJH

The main properties of the specific surface area and pore structure of different olivine nano-silicas are listed in Table 8.2. These properties are the specific surface areas (SSA_{BET}, SSA_{MP}, SSA_E), average pore size (d_{P_D}) and BJH volume of pores (V_{P_D}) from the desorption branch, and micropore volume (V_{MP}). Furthermore, the sulfur content and olivine dissolution conversion are also presented.

Figure 8.2 shows the BJH pore size distribution from the desorption branch of silica NS-14 after three and six filtration steps. The dashed line at 1.7 nm indicates the lower limit of the BJH method [53], however, as was mentioned in Chapter 2, this method underestimates the pores below 10 nm [44,55,164]. Even though the BJH method miscalculates the pores size distribution (PoSD) for pores smaller than 10 nm, it still can be used below this pore size for comparative purposes. The sulfur content of NS-14-3F and 6F was reduced from 1.75 wt.% to 0.03 wt.% by adding three additional washing steps, and the SSA_{BET} increased from 233 m^2/g to 348 m^2/g. The pore size distribution in both samples was between 2 nm and 100 nm. However, the sample with more sulfur featured a lower pore volume in this pore size range.

Table 8.2. Summary of the main properties of the SSA and pore structure of different olivine nano-silicas.

Samples	SSA_{BET} (m^2/g)	SSA_{MP} (m^2/g)	SSA_E (m^2/g)	d_{p_D} (nm)	V_{MP} (cm^3/g)	V_{P_D} (cm^3/g)	S (%)	X (%)
NS-14-3F	233	58	175	14.4	0.025	0.529	1.75	91
NS-14-4F	324	122	202	12.6	0.055	0.578	0.33	91
NS-14-5F	342	142	200	14.5	0.064	0.589	0.05	91
NS-14-6F	348	142	206	16.3	0.064	0.679	0.03	91
NS-HP	433	125	308	14.1	0.055	1.026	1.26	91
NS-50-S3	517	137	308	9.5	0.059	0.992	0.20	38
NS-50-S4	325	132	308	12.9	0.060	0.597	0.33	77
NS-50-S5	310	139	308	12.6	0.063	0.475	0.16	90
NS-51-S4	375	124	251	13.7	0.055	0.816	0.40	81
NS-51-S5	354	143	210	12.4	0.065	0.588	0.05	94
NS-RM	334	100	235	17.2	0.042	0.970	0.06	>90
RP-1-22h	124	19	105	16.3	0.008	0.439	0.06	>90
RP-9-1h	347	105	242	16.6	0.046	0.969	0.06	>90
RP-10-1h	283	70	212	18.8	0.030	1.026	0.06	>90
RP-8-1h	191	26	165	25.2	0.010	1.003	0.06	>90
RP-11-1h	90	12	79	25.7	0.004	0.581	0.06	>90

These samples were degassed at 190 °C for 4 hours. The conditions of the preparations of these samples are given in Chapter 6.

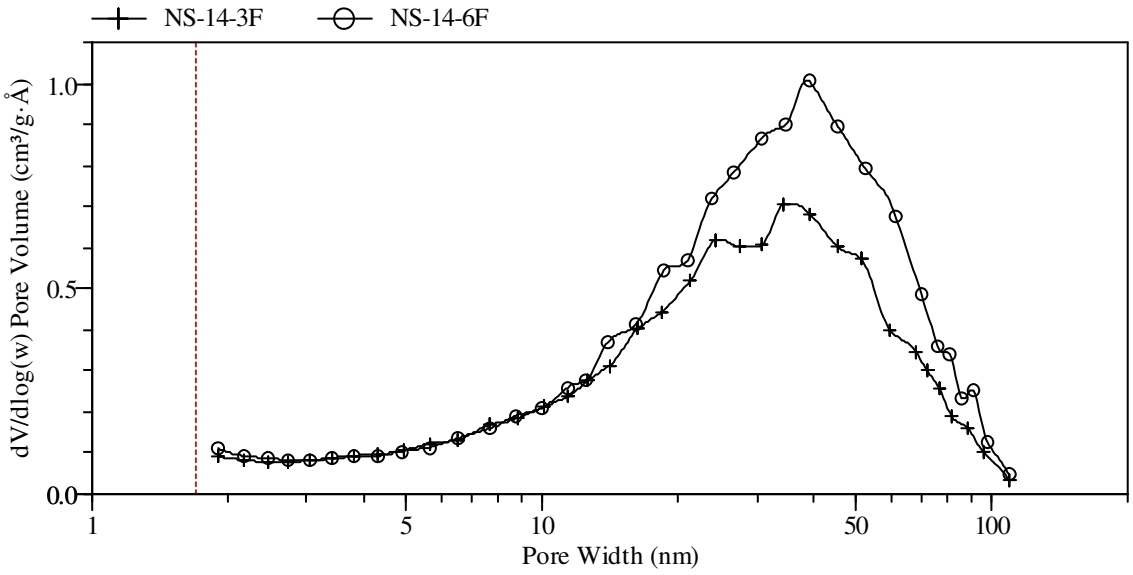

Figure 8.2. Pore size distribution determined by nitrogen physisorption and the BJH method for NS-14.

Figure 8.3 plots the BJH pore size distribution from the desorption branch of silica NS-HP, which was filtered using a filter press (P_{abs} = 3-5 bar) instead of vacuum filtration (P_{abs} = 0.2 bar). The PoSD of this sample was between 2 nm and 30 nm, showing a narrow peak and high pore volume around 20 nm. Thus, NS-HP did not exhibit macroporosity.

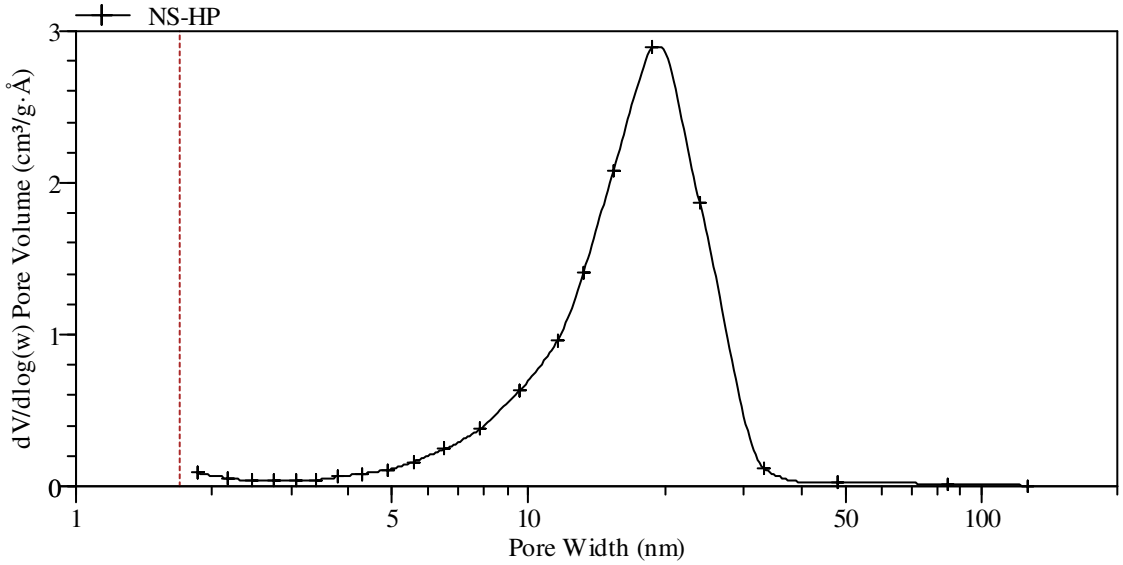

Figure 8.3. Pore size distribution determined by nitrogen physisorption and the BJH method for NS-HP.

Figure 8.4 plots the BJH pore size distribution from the desorption branch of silica NS-50 at different conversion degrees. The PoSD for the lowest X was between 2 and 50 nm with a high pore volume around 15 nm. The PoSD for NS-50-S4 and NS-50-S5 were in the range between 2 and 100 nm with a lower pore volume than the sample with the lower conversion (see Figure 8.8).

Figure 8.5 shows the BJH pore size distribution from the desorption branch of two ripened silicas (RP-1 at 22 hours and RP-11 at 1h) and the raw material (NS-RM) used in the ripening experiments. RP-1-22h was ripened for 22 hours at pH 8.4 and 90 °C, resulting in a SSA_{BET} of 124 m^2/g. RP-11-1h was ripened for 1 hour at pH 11 and at room temperature with a high shear mixer, resulting in a SSA_{BET} of 90 m^2/g. NS-RM and RP-1-22h featured a PoSD between 2 and 100 nm, but the pore volume was much lower in the ripened sample. The PoSD of RP-11-1h was in the range of 9 to 80 nm, the porosity below 9 nm being completely removed.

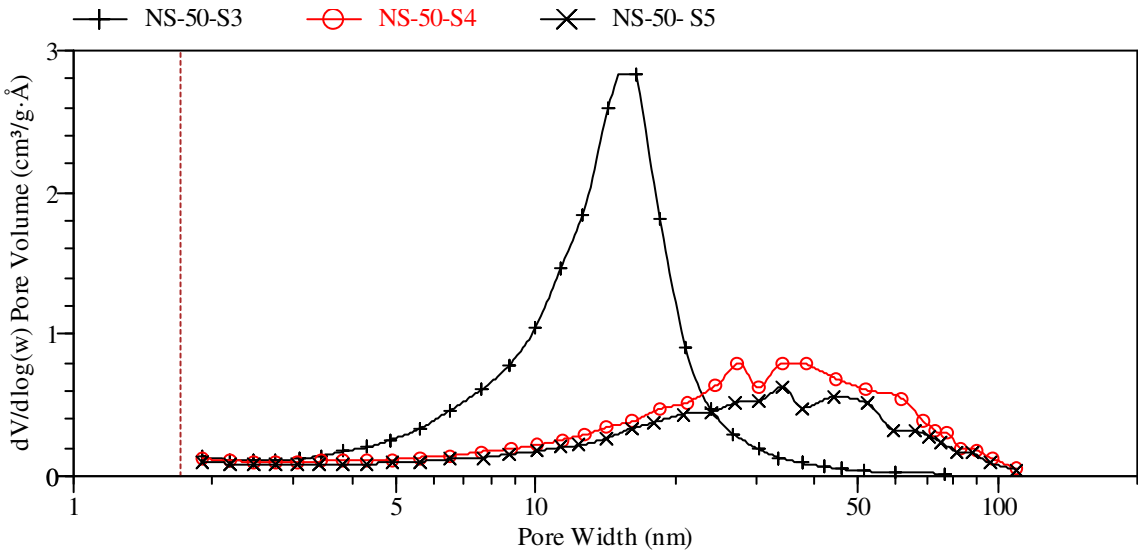

Figure 8.4. Pore size distribution determined by nitrogen physisorption and the BJH method for NS-50.

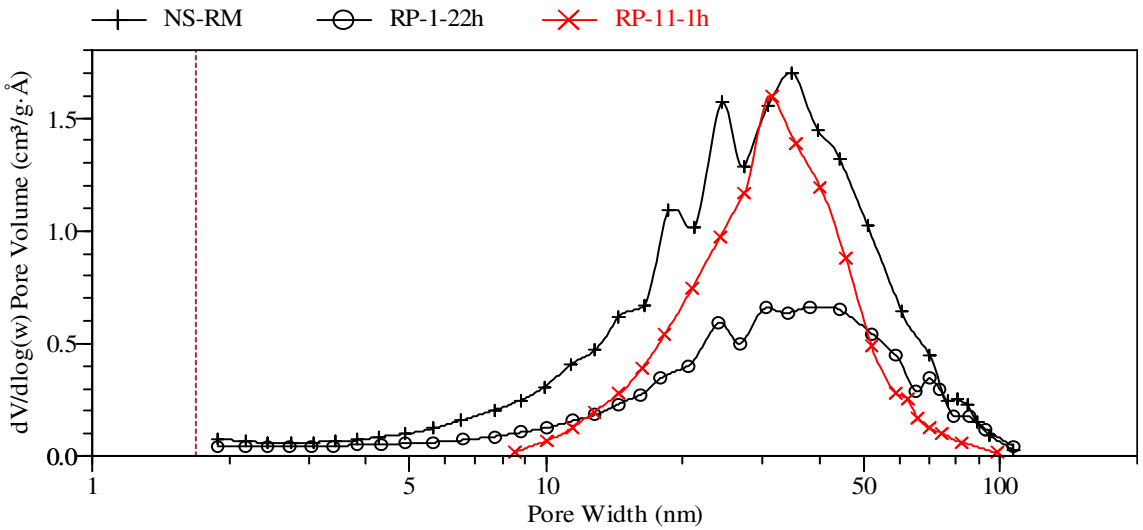

Figure 8.5. Pore size distribution determined by nitrogen physisorption and the BJH method for the ripening experiments and the raw material.

Figure 8.6 shows the micropore volume and the BJH pore volume for NS-14 after different washing and filtration steps. The micropore volume increased with the filtration steps by 155% (from sample NS-14-3F to NS-14-6F). This is because the impurities were mainly located in the micropores as was presented in Chapter 6. The biggest increase was found between steps 3 and 4. The BJH pore volume increased gradually with the filtration steps resulting in a rise of 28%. However, as can be observed from Figure 8.2, the pore size range did not change with the increase of the number of filtration steps, only the V_{P_D} was increased.

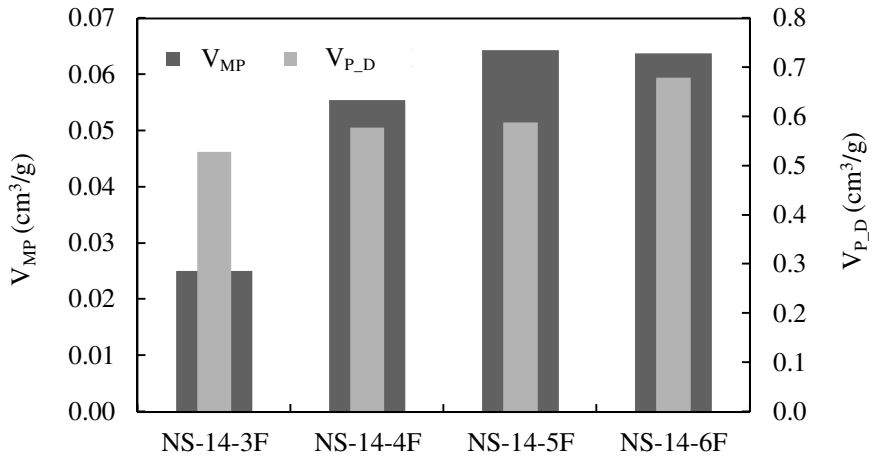

Figure 8.6. Micropore volume and pore volume determined for NS-14.

Figure 8.7 shows the micropore volume and the BJH pore volume for ripened nano-silicas where a high shear mixer was used. In this figure, the samples are organized from left to right in decreasing order of SSA_{BET}. RP-9-1h and RP-11-1h exhibited a SSA_{BET} of 347 m^2/g and 90 m^2/g, respectively. The micropore volume decreased with the ripening treatment, being greatly reduced for sample RP-11-1h. The BJH pore volume remained constant for samples RP-8, -9 and -10 and decreased for RP-11. Sample RP-1-22h also displayed a significant decrease of the BJH pore volume (see Table 8.2).

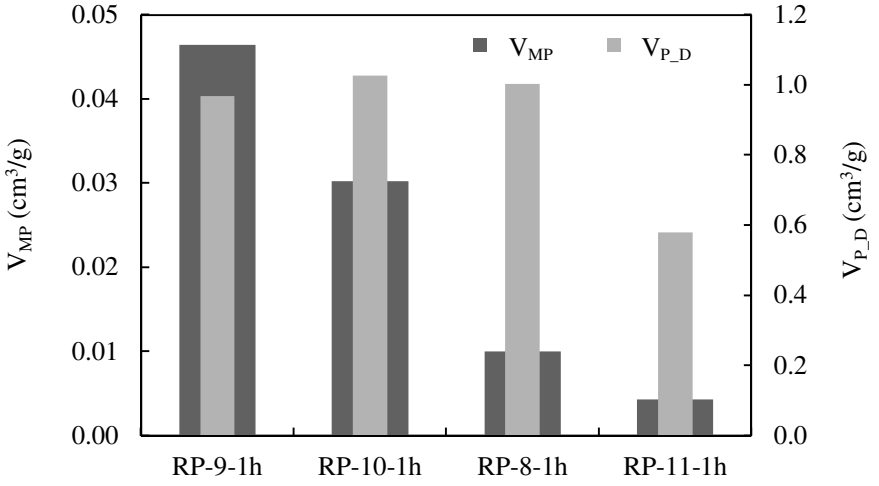

Figure 8.7. Micropore volume and pore volume determined by the BJH method for ripened olivine nano-silicas.

Figure 8.8 plots the pore volume versus the conversion degree for silicas NS-50 and NS-51; a) plots the micropore volume and b) the BJH pore volume from the desorption branch. The micropore volume remains almost constant for NS-50 and increases slightly

with the conversion degree for NS-51. The BJH pore volume decreases significantly with X for NS-50 and NS-51.

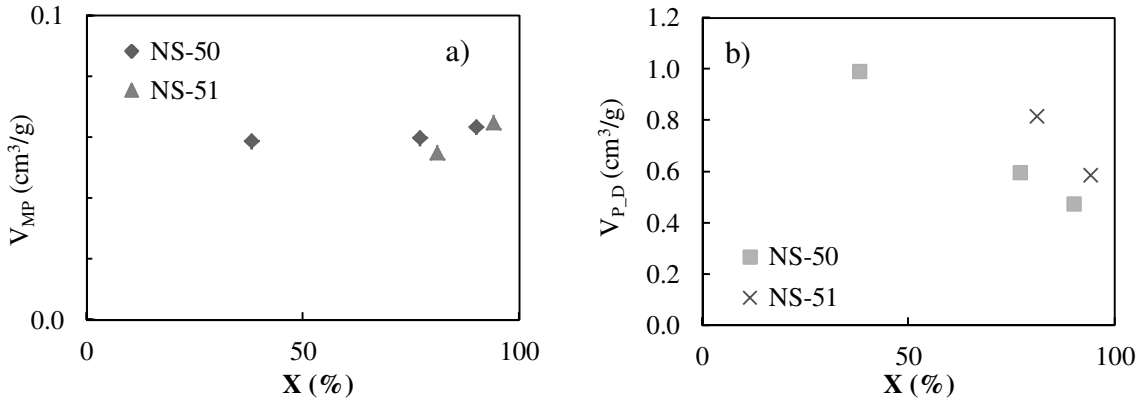

Figure 8.8. Pore volumes versus the conversion degree for NS-50 and NS-51; a) the micropore volume and b) the BJH pore volume.

For comparison with other studies where the silicas were analysed after degassing at 120 °C, Figure 8.9 plots the pore volumes of different silicas degassed at 190 and 120 °C; a) plots the micropore volume and b) the BJH pore volume from the desorption branch. Silicas degassed at 190 °C featured higher micropore volumes than silicas degassed at 120 °C. Carrott [165] found that the volume of the micropores of precipitated silica increased with the degassing temperature up to 200 °C. Bergna [6] explained that this phenomenon is the result of the removal of adsorbed water from fully hydroxylated microporous surfaces. On the other hand, the degassing temperature has no or little influence on the BJH pore volume.

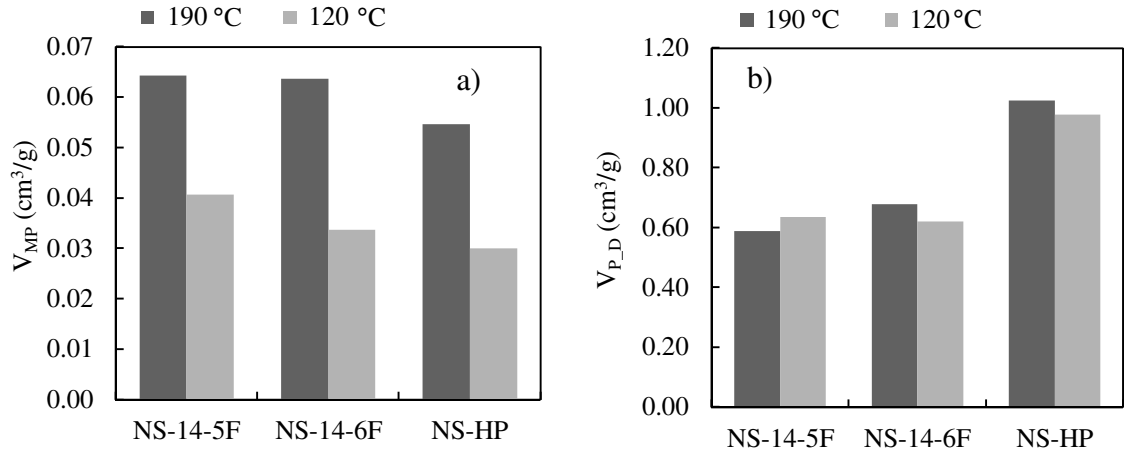

Figure 8.9. Pore volumes for different silicas evacuated at 190 and 120 °C; a) the micropore volume and b) the BJH pore volume.

To summarize, the pore size distribution (PoSD) of olivine nano-silica determined by the BJH method is in the range of 2 to 100 nm. The PoSD is influenced by the content of impurities, filtration pressure, conversion degree and ripening treatment. Thus, the PoSD of olivine silica can be tailored to match the requirements of different applications. This tailoring can be done by changing the filtration pressure, controlling the conversion degree and/or performing ripening treatments after the production process has been completed. Thus, the initial PoSD (2-100 nm) can be modified to a distribution of 9 to 30 nm.

8.3.2 Pore size measured by positron annihilation spectroscopy

The positron lifetime annihilation spectroscopy (PALS) technique measures the pore size and the intensity of each pore size. The pore intensity is related to the quantity of pores of each size. Thus, samples with higher intensity have larger amount of pores of the size involved. The results of PALS for different olivine silicas are listed in Tables 8.3-8.5 and in Figures 8.10-8.12. In the case of olivine nano-silicas two types of pores were found, pore 1 (p1) around 6 Å and pore 2 (p2) around 25 Å. The pore size and pore intensity determination of p2 is just above the limit of the Tao-Eldrup model [61]. Therefore, the results of p2 are likely to have associated a small error.

Table 8.3 reports the pore size (d_p) and pore intensity (I_p) of pores 1 and 2 of olivine nano-silicas produced during 2010 and 2011, which are reported in Chapters 5 and 6. This table also provides the conversion degree (X), sulfur content (S) and SSA_{BET}. Table 8.4 lists the pore size and pore intensity of nano-silicas NS-50 and NS-51 with different conversion degrees.

Table 8.5 gives the pore size and pore intensity of ripened olivine nano-silicas. All the PALS analyses were performed in 2013.

Table 8.3. Pore size and pore intensity for different olivine nano-silicas.

Sample	X (%)	S (%)	SSA_{BET} (m^2/g)	d_{p1} (Å)	I_{p1} [%]	d_{p2} (Å)	I_{p2} [%]
NS-1	84.55	3.89	131	5.6	10.1	22.8	2.1
NS-2	96.00	1.18	150	5.6	10.1	26.2	5.8
NS-4	96.18	1.17	218	6.0	13.5	26.2	5.0
NS-7	89.70	1.36	266	5.8	10.6	24.4	3.9
NS-8	95.84	2.16	185	5.8	10.4	24.2	3.6
NS-HP	91.42	1.26	425	6.2	8.2	27.0	10.4
NS-14-6F	91.07	0.03	348	5.8	10.9	26.4	11.8
NS-RM	>90	0.06	341	5.6	10.2	26.6	10.5

NS-1 to NS-8 were prepared during 2010 and 2011.

Table 8.4. Pore size and pore intensity for different olivine nano-silicas.

Sample	X (%)	S (%)	SSA_{BET} (m^2/g)	d_{p1} (Å)	I_{p1} [%]	d_{p2} (Å)	I_{p2} [%]
NS-50-S1	38.41	0.20	517	5.6	6.8	25.0	10.8
NS-50-S2	76.52	0.33	325	5.6	10.5	25.0	4.2
NS-50-S3	90.34	0.16	310	5.6	10.5	24.0	3.6
NS-51-S1	81.13	0.40	375	5.8	8.2	24.8	4.7
NS-51-S2	94.35	0.05	354	5.8	9.0	25.6	5.5

NS-50 and NS-51were prepared in 2013.

Table 8.5. Pore size and pore intensity for ripened olivine nano-silicas.

Sample	X (%)	S (%)	SSA_{BET} (m^2/g)	d_{p1} (Å)	I_{p1} [%]	d_{p2} (Å)	I_{p2} [%]
RP-1-22h	>90	0.06	124	6	8.8	23.8	5.2
RP-8-1h	>90	0.06	191	5.6	8.9	24.2	7.6
RP-9-1h	>90	0.06	347	5.6	8.3	24.0	8.2
RP-10-1h	>90	0.06	283	5.8	8.2	24.4	8.1
RP-11-1h	>90	0.06	90	5.6	8.3	24.2	2.2

The ripened nano-silicas were prepared in 2012.

Figure 8.10 plots the pore size of p2 (d_{p2}) pore size versus the sulfur content for different olivine nano-silicas. The trend for nano-silicas produced during 2010 and 2011 is that the pore size decreases with the sulfur content. Nano-silicas produced in 2013, do not follow this tendency. Although, all nano-silicas were dried overnight at 105 °C and stored in sealed plastic containers immediately after their preparation, it could be that the silica is still aging in this dried state. In fact, the aging of the dried silica is confirmed by the nitrogen physisorption results shown in Chapter 2, where the SSA_{BET} decreased by 38% after two years of storing the samples in plastic bottles.

Figure 8.11 represents the influence of the sulfur content on the intensity of pore 2. The pore intensity also decreased with the sulfur content for samples produced during 2010 and 2011, while this trend cannot be observed for samples produced in 2013.

Figure 8.12 shows the influence of the conversion degree on the intensity of pore 2, displaying a pronounced decrease with the X. Figure 8.13 plots the pore intensity of ripened olivine nano-silicas versus the SSA_{BET}. It can be observed that with the ripening, as the SSA_{BET} is reduced, the intensity of pore 2 is reduced as well. The decrease of the pore intensity is more pronounced when the SSA_{BET} is reduced below 200 m^2/g. On the other hand, the d_{p2} pore size was not influenced by the ripening treatment.

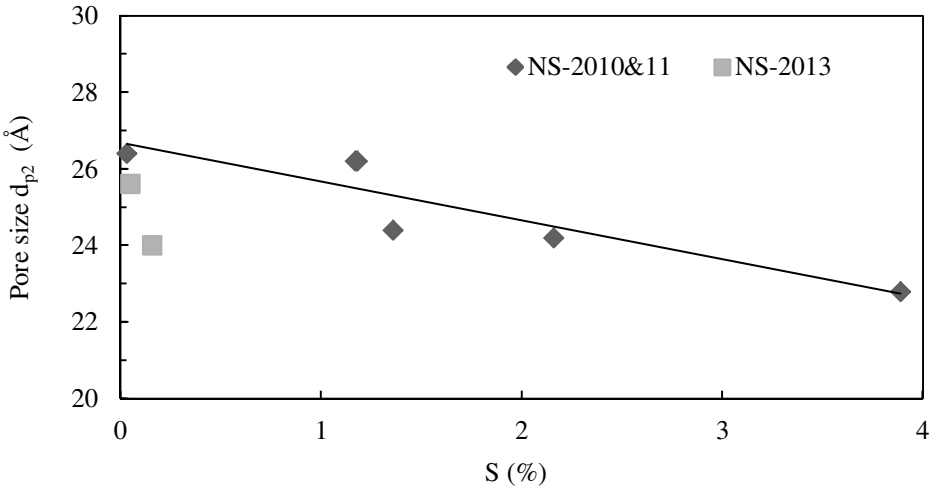

Figure 8.10. Size of p2 versus the sulfur content of different olivine nano-silicas.

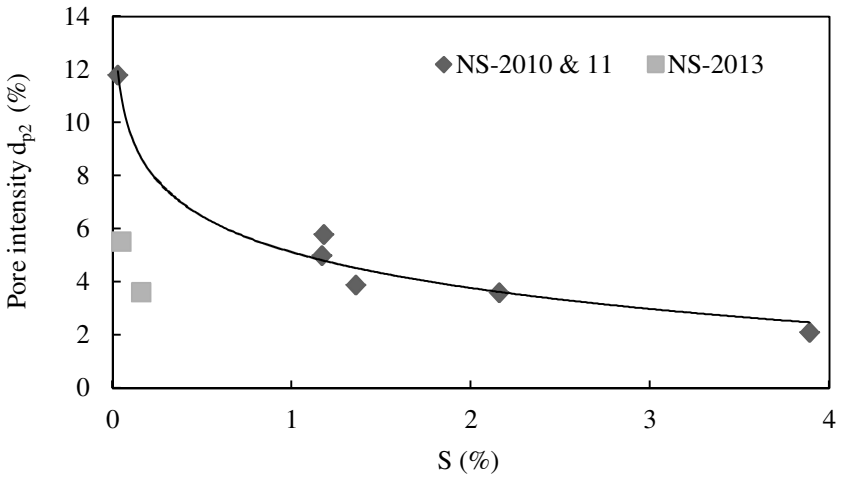

Figure 8.11. Intensity of p2 versus the sulfur content of different olivine nano-silicas.

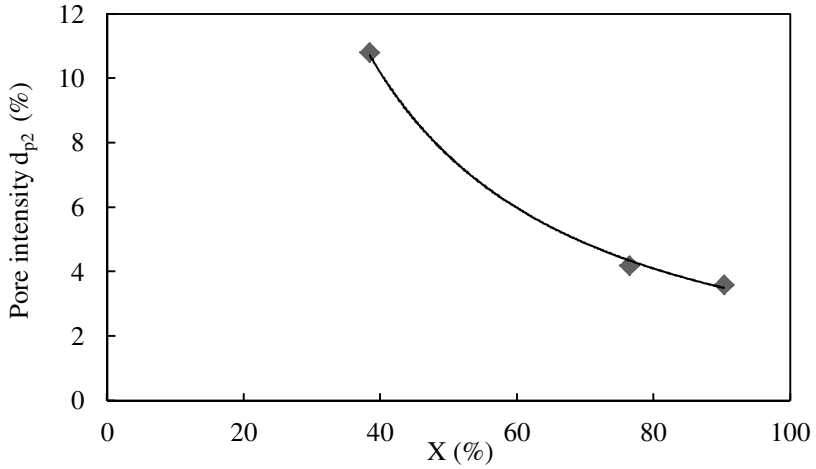

Figure 8.12. Intensity of p2 versus the conversion degree for NS-50.

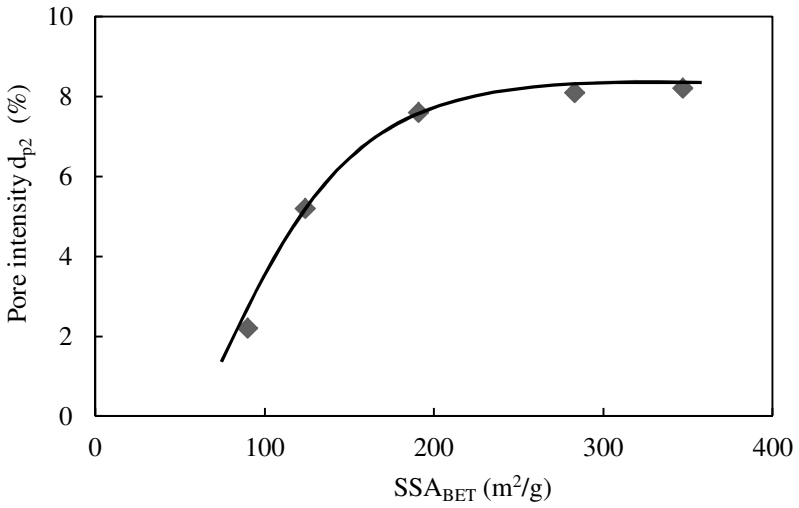

Figure 8.13. Intensity of p2 versus the SSA_{BET} for ripened olivine nano-silicas.

To conclude, two types of pores were found by PALS, one at around 6 Å (pore 1) and another one at around 25 Å (pore 2). Pore 1 is considered as an ultramicropore [44], while pore 2 is considered as a small mesopore [43]. The only trend that can be observed for pore 1 is that the pore intensity increases with the conversion degree for NS-50 and NS-51. On the other hand, the process conditions have a big influence on pore 2, which can be summarized as follows: 1) the pore size and intensity decrease with the sulfur content; 2) the pore intensity decreases with the ripening treatment, especially once the SSA_{BET} is reduced below 200 m^2/g; and 3) the pore intensity decreases with the conversion degree. Thus, pore 1 is not so much affected by the process conditions as pore 2. One way to explain the origin of these pores could be that pore 1 is intrinsic to the amorphous matrix of olivine nano-silica and pore 2 is related to the voids between the primary particles.

8.3.3 Silanol content and specific surface area measured by NMR

Tables 8.6-8.8 list the silanol content and the SSA_{NMR} calculated with Eq. (2.25) and Eq. (8.1), respectively. Additionally, the conversion degree, sulfur content and SSA_{BET} are also presented here. Table 8.6 provides the NMR results of the silicas discussed in Chapter 5. Table 8.7 gives the NMR results of some silica samples presented in Chapter 6. Table 8.8 shows the NMR results of silicas NS-50 and NS-51 (see Chapter 6). Table 8.9 lists the NMR results of ripened silicas mentioned in Chapter 6.

Table 8.6. Silanol number and SSA_{NMR} for different olivine nano-silicas degassed at 120 °C for 4 h.

Samples	X (%)	S (%)	SSA_{BET} (m^2/g)	α_{OH} (OH/nm^2)	Factor	SSA_{NMR} (m^2/g)
NS-1	85	3.89	131	23.0	4.6	602
NS-2	96	1.18	150	22.2	4.4	665
NS-3	95	1.26	165	19.3	3.9	634
NS-4	96	1.17	218	15.5	3.1	674
NS-5	95	1.19	198	17.0	3.4	672
NS-6	89	0.92	179	19.4	3.9	694
NS-7	90	1.36	266	13.2	2.6	706
NS-8	96	2.16	185	18.5	3.7	685

Where Factor refers to the ratio α_{OH}/α_{FH}.

Table 8.7. Silanol number and SSA_{NMR} for different olivine nano-silicas degassed at 190 °C for 4 h.

Samples	X (%)	S (%)	SSA_{BET} (m^2/g)	α_{OH} (OH/nm^2)	Factor	SSA_{NMR} (m^2/g)
NS-14-3F	91	1.75	233	14.3	2.9	668
NS-14-6F	91	0.03	343	10.9	2.2	745
NS-HP	91	1.26	433	8.9	1.8	773
NS-RM	>90	0.06	334	11.5	2.3	768

Table 8.8. Silanol number and SSA_{NMR} for silicas NS-50 and NS-51 degassed at 190 °C for 4 h.

Samples	X (%)	S (%)	SSA_{BET} (m^2/g)	α_{OH} (OH/nm^2)	Factor	SSA_{NMR} (m^2/g)
NS-50-S3	38	0.20	517	8.2	1.6	844
NS-50-S4	77	0.33	325	12.1	2.4	790
NS-50-S5	90	0.16	310	12.8	2.6	791
NS-51-S4	81	0.40	375	10.7	2.1	804
NS-51-S5	94	0.05	354	11.2	2.2	793

Figures 8.14 and 8.15 show the influence of the degassing temperature of the gas physisorption analyses on the α_{OH} and SSA_{NMR}. This is due to the influence of the degassing temperature on the SSA_{BET}, and, therefore, on the α_{OH} and SSA_{NMR} (see Equations (2.25) and (8.1)). The average values of SSA_{NMR} for silicas degassed at 120 °C and 190 °C are 666 and 775 m^2/g, respectively. In addition, it can be observed in Figure

8.15 that there is an upward linear trend for SSA_{NMR}, which means that the factors (i.e., process conditions) affecting the SSA_{BET} also have a positive influence on the SSA_{NMR}.

Table 8.9. Silanol number and SSA_{NMR} for ripened olivine nano-silicas.

Samples	SSA_{BET} (m^2/g)	α_{OH} (OH/nm^2)	Factor	SSA_{NMR} (m^2/g)
RP-1-22h	124	22.2	4.4	551
RP-8-1h	191	18.2	3.6	696
RP-9-1h	347	11.4	2.3	789
RP-10-1h	283	14.4	2.9	814
RP11-1h	90	40.3	8.1	725

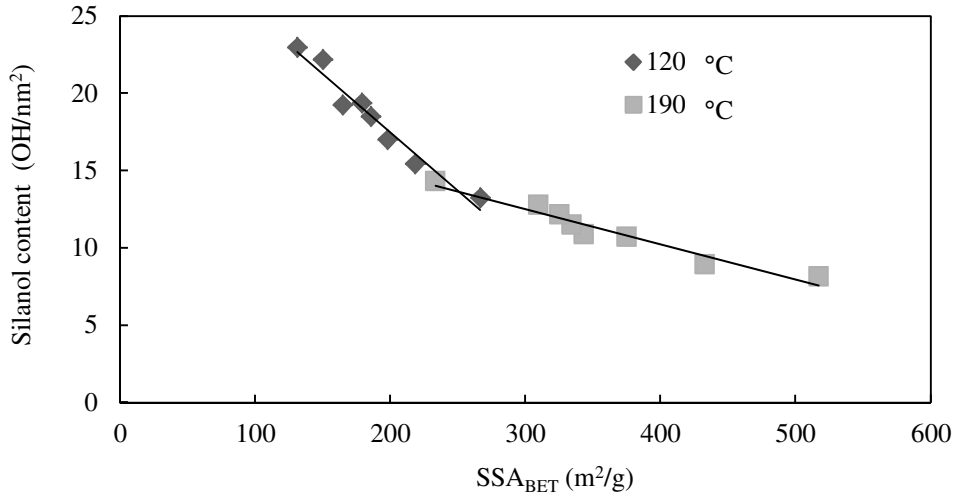

Figure 8.14. Silanol content versus SSA_{BET} for samples degassed at 120 and 190 °C.

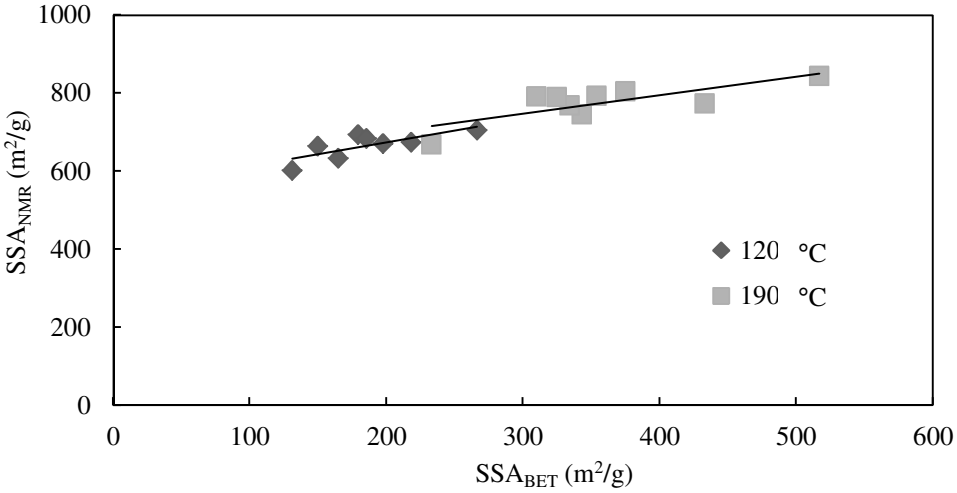

Figure 8.15. SSA_{NMR} versus SSA_{BET} for samples degassed at 120 and 190 °C.

Figures 8.16 and 8.17 show the influence of the conversion degree on the α_{OH} and SSA_{NMR} for silica NS-50. The silanol content increases with the X, whereas the SSA_{NMR} decreases slightly with it.

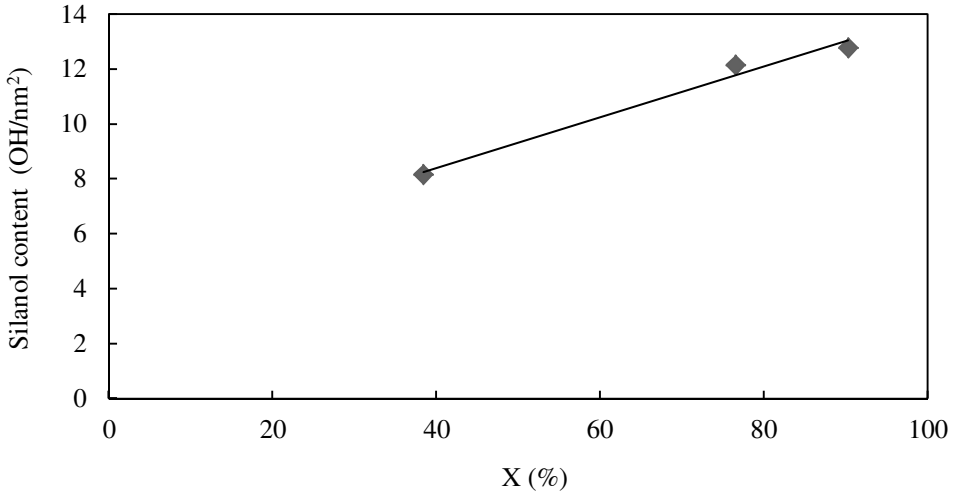

Figure 8.16. Silanol content versus conversion degree for sample NS-50.

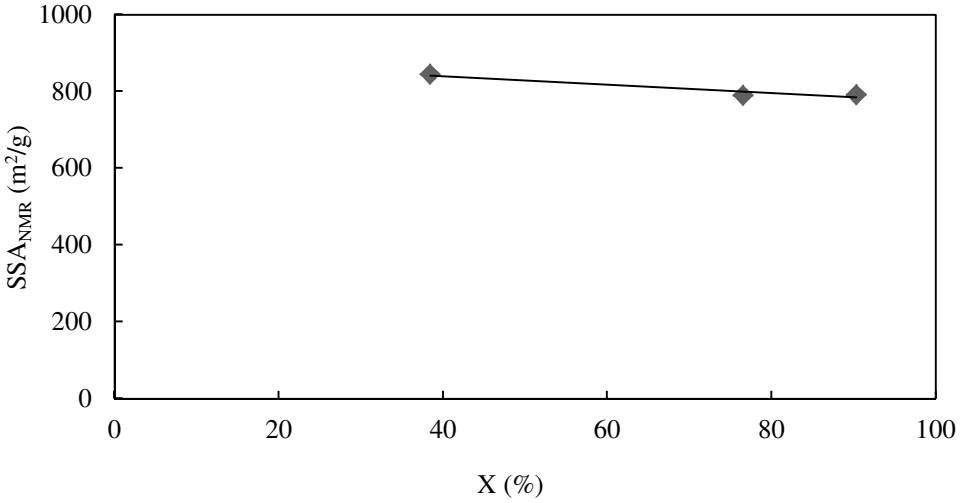

Figure 8.17. SSA_{NMR} versus conversion degree for NS-50.

Figure 8.18 plots the silanol content versus the SSA_{BET} for the ripened nano-silicas, where results measured on the raw material, samples treated with the high shear mixer (HM) and a sample after long ripening (without the HM) are presented. The silanol content rises with the ripening (i.e., with the reduction of SSA_{BET}). The highest silanol values were obtained for the samples with smallest SSA_{BET}, which are RP-1-22h and RP-11-1h with silanol values of 22 and 40 OH/nm^2, respectively. The silanol content for RP-11-1h was considerably higher than for RP-1-22h. This difference is likely to be either due to the

long ripening time of RP-1-22h or the high pH of RP-11-1h (see Table 6.10). Figure 8.19 represents the variation of the SSA_{NMR} with the SSA_{BET}. The SSA_{NMR} remains almost constant, increasing only slightly with the SSA_{BET}.

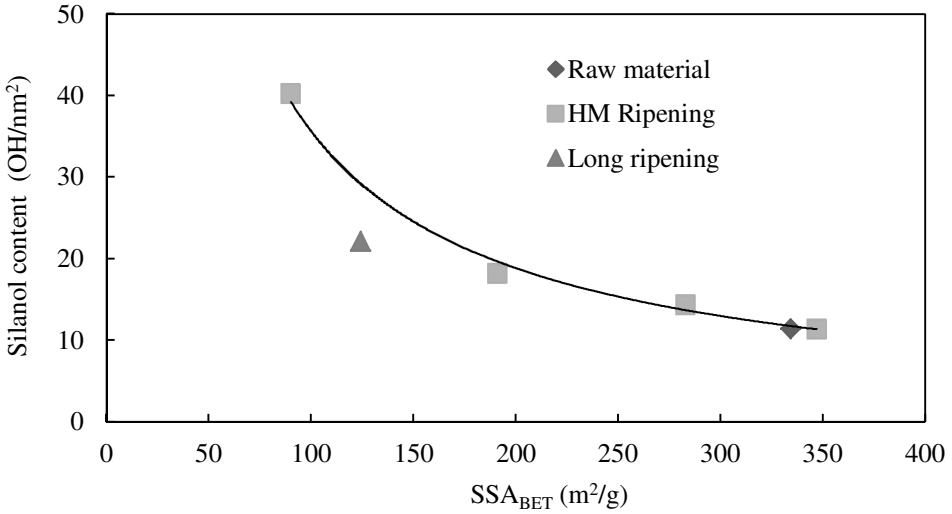

Figure 8.18. Silanol content versus SSA_{BET} for ripened olivine nano-silicas.
HM refers to samples prepared with the high shear mixer (RP-8 to RP-11) and long ripening to samples prepared without HM (RP-1 at 22 hours).

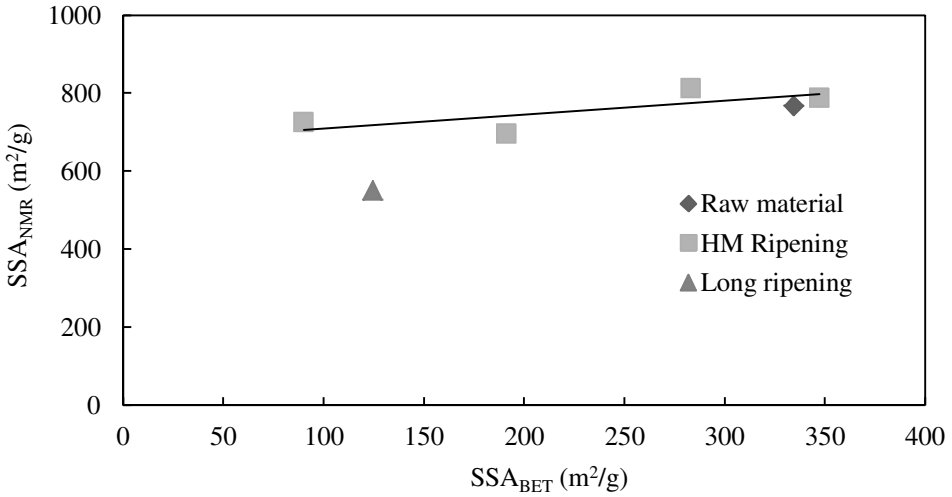

Figure 8.19. SSA_{NMR} versus SSA_{BET} for ripened olivine nano-silicas.

The silanol number was also calculated from TG analysis using Eq. (8.2) to compare them with the results obtained from NMR. These determinations were done for silicas NS-1 to NS-8. Figure 8.20 plots the silanol content from NMR and TGA analyses. Both determinations show similar results; however, the silanol content obtained from TG analysis is slightly lower than that from the NMR analysis.

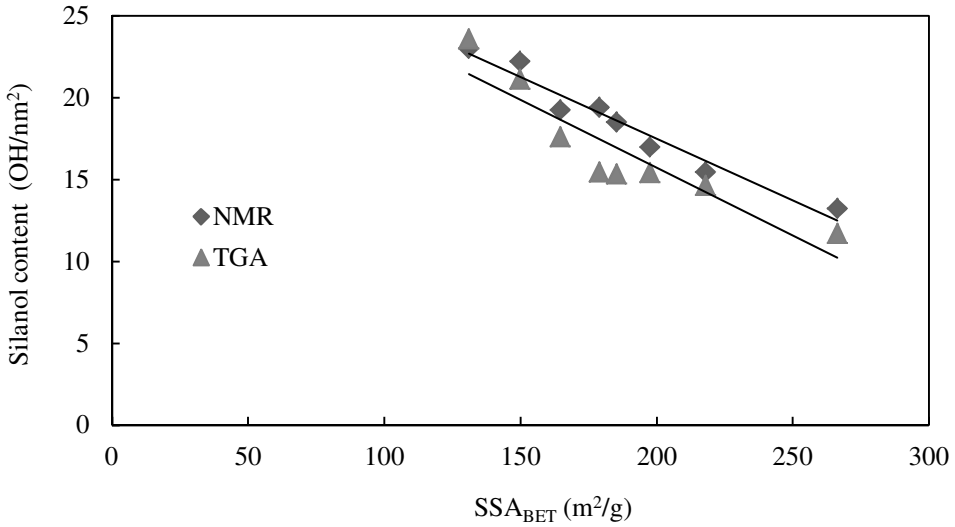

Figure 8.20. Silanol content determined from NMR and TG analyses versus SSA_{BET}.

To summarize, the silanol content is in the range of 13 to 22 OH/nm^2 for olivine nano-silicas dried at 120 °C and 11 to 13 OH/nm^2 for silicas dried at 190 °C. The α_{OH} of olivine silicas is higher than the values obtained by Zhuralev (4.9 OH/nm^2) [162], and also by Gallas (~8 OH/nm^2) [163], but similar to the values reported by Lieftink (9-27 OH/nm^2) [30]. The reason for these high silanol values is because the NMR technique determines the total amount of silanols, including silanols in the ultramicropores and internal silanols, but the SSA_{BET} does not take into account the internal surface area nor the area of micropores. The conditions of the olivine nano-silica production process have a considerable influence on the silanol values. The silanol content decreases with the purity and filtration pressure, and increases with the conversion degree of the dissolution of olivine and ripening treatment. Actually, silanol values as high as 40 OH/nm^2 were obtained for ripened silicas. The SSA_{NMR}, however, is much less affected by the process conditions than the $\alpha_{OH,}$ exhibiting slope which is nearly zero.

8.3.4 Precipitated silicas and pyrogenic silica

In this section the specific surface areas, pore size distributions and silanol contents of two precipitated silicas (Sipernat 50S and 310) and two pyrogenic silicas (Aerosil 200 and 380) are presented. Table 8.10 shows some physical properties from the material safety data sheet of the commercial products and some textural properties from the gas physisorption analysis. It is noteworthy that the result of the micropore volume for Sip 310 is negative, but since this is physically not possible, it is assumed zero. Another abnormal fact is that for the same sample, the SSA_{MP} is positive in disagreement with the V_{MP}. This is due to the calculation of the SSA_{MP} using Eq. (2.19), where the SSA_{BET} is

used as the total surface area, instead of Eq. (2.18), where the total surface area is determined from the t-plot.

Table 8.10. Main properties of precipitated and pyrogenic silicas.

	Data sheet			N_2 physisorption						
Silicas	**SSA_{BET} (m^2/g)**	**d_3 (μm)**	**P_{Si} (%)**	**SSA_{BET} (m^2/g)**	**SSA_{MP} (m^2/g)**	**SSA_E (m^2/g)**	**d_1 (nm)**	**d_{p_D} (nm)**	**V_{MP} (cm^3/g)**	**V_{P_D} (cm^3/g)**
Sip 50S	500.0	18.0	-	456.0	26.7	429.3	6.0	11.0	0.007	1.380
Sip 310	700.0	8.5	-	693.6	15.3	678.3	3.9	7.8	0.000	1.537
Aero 200	200.0	-	>99.8	216.8	8.7	208.1	12.6	12.9	0.001	0.582
Aero 380	380.0	-	>99.8	379.0	37.1	341.9	7.2	10.0	0.012	0.805

Where Sip refers to Sipernat, Aero to Aerosil, d_1 to the size of the primary particles (calculated using Eq. (2.20)) and d_3 to the agglomerate size.

Table 8.11 presents the pore sizes and pore size intensities obtained from the PALS analysis of Sipernat and pyrogenic silicas. Table 8.12 provides the silanol number and the SSA_{NMR} of Sipernat silicas. Pyrogenic silicas do not contain or contain very few silanol groups since the flame temperature of the production process is in the range of 1200 to 1600 °C [2].

Figure 8.21 presents the pore size distribution of Sipernat 50S and 310, both of them in the range of 2 to 100 nm, but Sip 310, which features a larger SSA_{BET}, has a higher pore volume in the mesopore range (5-50 nm) than Sip 50 S. Usually, precipitated silica is considered to be mainly macroporous [1,6], however, the pore size distribution clearly shows the presence of some pores in the range 2-50 nm.

Table 8.11. Pore size and pore intensity from PALS of precipitated and pyrogenic silicas.

Sample	**SSA_{BET} (m^2/g)**	**d_{p1} (Å)**	**I_{p1} (%)**	**d_{p2} (Å)**	**I_{p2} (%)**
Sip 50S	500	6	6.3	25.2	7.1
Sip 310	700	5.8	5.9	23.8	8.4
Aero 200	200	5.4	9.5	21.2	3.4
Aero 380	380	5.6	8.5	22.2	4.2

Table 8.12. Silanol number and SSA_{NMR} of precipitated silicas.

Samples	**SSA_{BET} (m^2/g)**	**fg (AU)**	**fs (AU)**	**α_{OH} (OH/nm^2)**	**Factor**	**SSA_{NMR} (m^2/g)**
Sip 50S	500	0.164	0.307	6.8	1.4	681
Sip 310	700	0.263	0.402	6.8	1.4	947

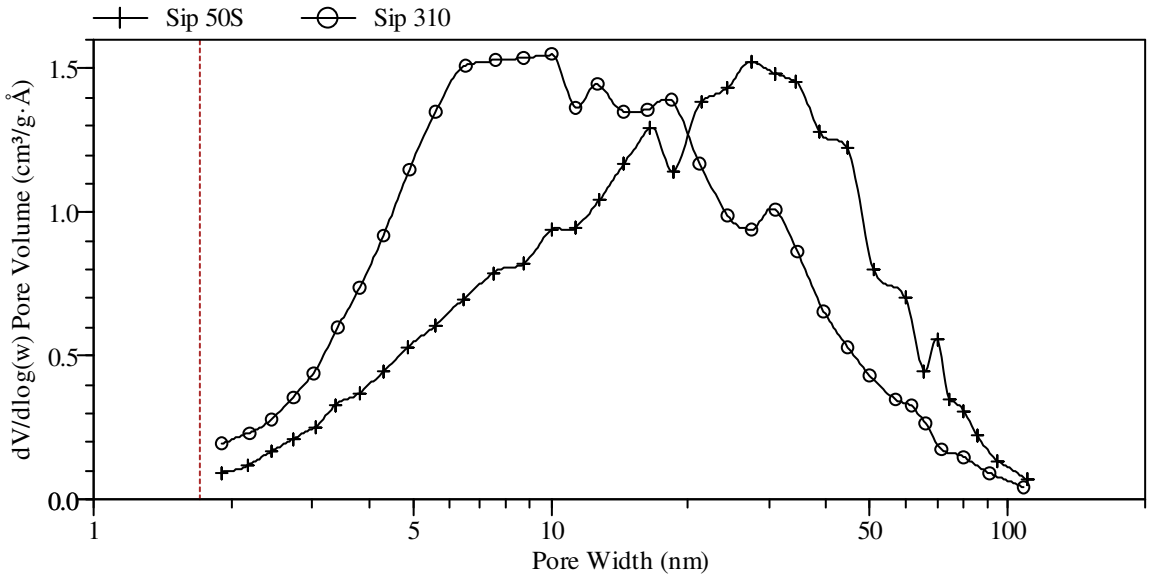

Figure 8.21. BJH pore size distribution of precipitated silicas.

Figure 8.22 shows the pore size distribution of Aerosil 200 and 380, which is in the range of 2 to 150 nm. The mesoporosity of this type of silica was unexpected since it is usually considered as non-porous silica [1,6,166] with type II physisorption isotherm, showing no hysteresis. However, when this material is pressed, mesopores are developed [156,157]. Lieftink [30] also found that Aerosil 200 was mesoporous with a similar pore size range and pore volume to the results presented here.

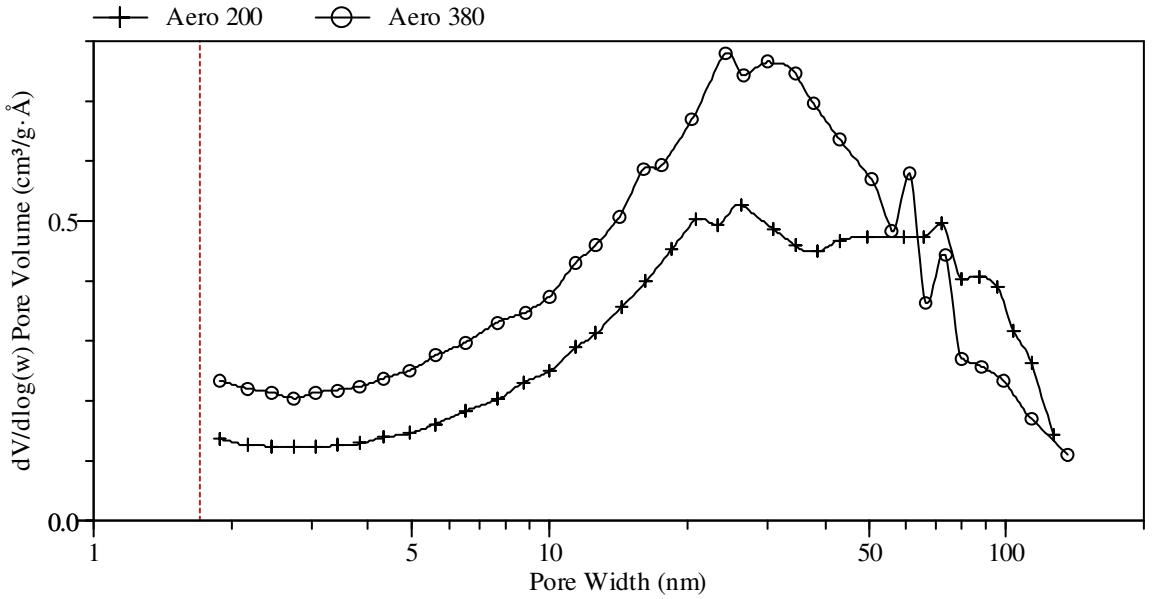

Figure 8.22. BJH pore size distribution of pyrogenic silicas.

Figures 8.23-8.25 present transmission electron microscope photographs of Sipernat 50S, Aerosil 200 and Aerosil 380, respectively. These samples have been prepared by ultrasonic dispersion in ethanol. It is possible that during the sample preparation in ethanol, neck formation between the silica particles of Aerosil occurred. All three types of silica are structured in 3D networks. In addition, in all the micrographs, voids can be found, which are related to mesoporosity and macroporosity.

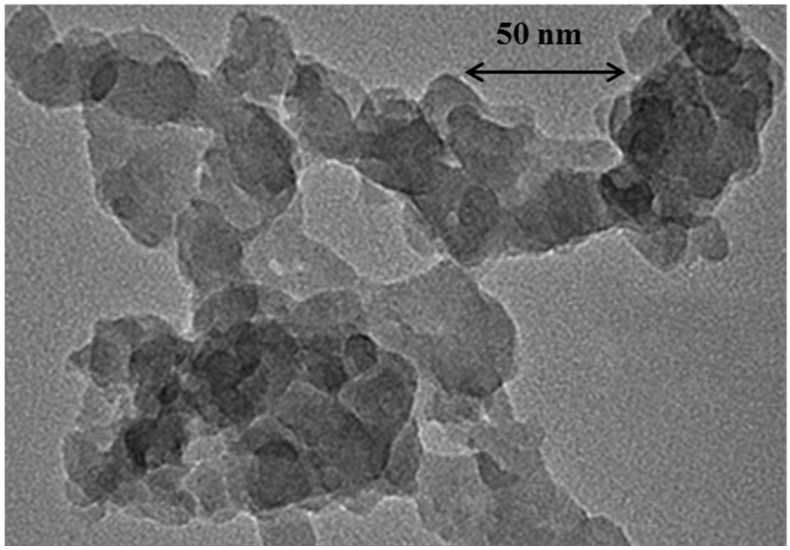

Figure 8.23. TEM photograph of Sipernat 50S (250 kx).

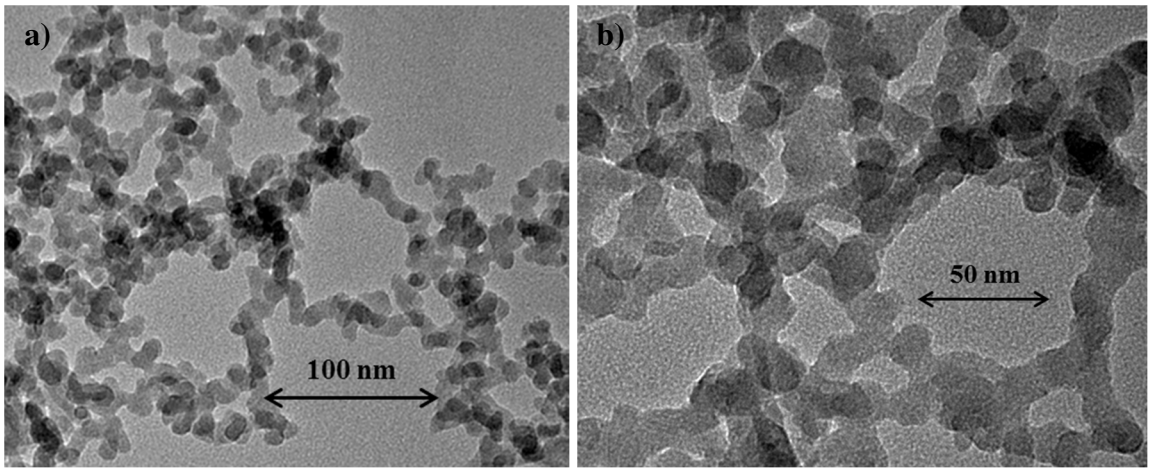

Figure 8.24, a and b. TEM photographs of Aerosil 200 (135 kx and 250 kx, respectively).

A comparison between the precipitated and olivine silicas reveals that: 1) the SSA_{BET} is higher for Sipernat 310 than for olivine silicas; 2) the V_{P_D} is considerably higher in the case of Sipernat silicas, which means that precipitated silicas have a higher content of mesopores and macropores; 3) the V_{MP} is much lower in the case of Sipernat silicas,

resulting in lower micropore surfaces areas; 4) the intensity of pore 1 measured by positron annihilation lifetime spectroscopy (PALS) is lower for precipitated silicas than for olivine silicas, while the intensity of pore 2 is in the same range; 5) the silanol content of Sipernat (~7 OH/nm^2) is lower than the silanol content of olivine silicas (~12 OH/nm^2 for samples degassed at 190 °C); 6) The SSA_{NMR} follows the order: Sipernat 310 > olivine nano-silica > Sipernat 50S, with an average value for olivine nano-silica of 780 m^2/g; and 6) both types of silicas form 3D network structures.

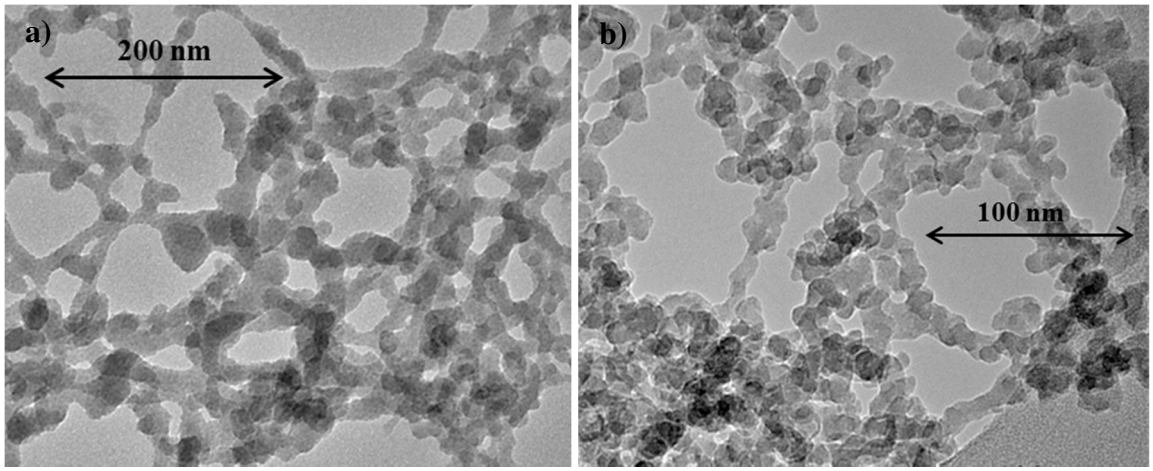

Figure 8.25, a and b. TEM photographs of Aerosil 380 (89 kx and 175 kx, respectively).

On the other hand, pyrogenic silicas exhibit similar SSA_{BET} and V_{P_D}, and lower V_{MP}. Regarding the PALS analysis, pyrogenic silicas show a similar intensity for pore 1 and a lower intensity for pore 2. Additionally, pyrogenic silicas also form 3D network structures.

The pore size ranges mentioned in the literature for precipitated and pyrogenic silicas are different from the PoSD obtained in this study. Mesoporosity was found for precipitated and pyrogenic silicas. There are two possible explanations for these results:

1) The evacuation temperature employed in this study removes all the physically adsorbed water so mesopores can take up gas. In fact, Carrott [165] found that the volume in the micropores of precipitated silica increased with the evacuation temperature up to 200 °C. Bergna [6] explained that this phenomenon is the result of the removal of adsorbed water on fully hydroxylated microporous surfaces.
2) It could be that at some steps during the production processes, mesoporosity is created. For example, this could happen if pyrogenic silica would be compressed after its production.

8.4 Discussion

Prior to analyzing how the pore structure develops with the conversion degree and ripening, a few aspects about the particle growth of silica should be recalled. The formation and particle growth of silica can be summarized (see Chapter 7) with the following steps: 1) Olivine dissolves releasing silica into the medium; 2) Soluble silica nucleates, and primary particles of 1 to 2 nm are formed; 3) The silica particles grow by condensation of hydroxyl groups (Eq. (4.3)) forming linear chains [118]; and 4) If the reaction continues, the chains keep growing, forming 3D networks. In addition to these points, it is important to remark that during the olivine dissolution reaction several processes occur at the same time such as the release of silica from the olivine, the continuous nucleation and formation of primary particles and the growth of silica. It is important to understand these processes since the properties of olivine nano-silica are affected by all of them.

The term growth of silica refers to both processes: aggregation and agglomeration (definitions of aggregation and agglomeration are provided in Appendix I). This term is used in this thesis because aggregation and agglomeration occur during the production of olivine nano-silica, but also because the frontier between them cannot be discerned so clearly.

Figure 8.26 presents the textural properties variation (SSA_{BET}, SSA_{MP}, SSA_{NMR} and V_{P_D}) in percentage versus the conversion degree. The SSA_{BET} and V_{P_D} decrease pronouncedly, the SSA_{NMR} decreases slightly, and the SSA_{MP} remains constant with increasing conversion degrees (X). SSA_{BET} shows a similar trend to V_{P_D} since SSA_{BET} is the sum of SSA_E, which is related to the BJH pore volume, and SSA_{MP}. The decrease of V_{P_D} with X can also be inferred from Figure 8.5, which shows that the PoSD is wider, but much flatter for higher conversion degrees. The decrease of the BJH pore volume with X means that the silica agglomerates become more compact due to a better packing of the particles. This is in agreement with the findings of Okkerse [141], who stated that a better packing was obtained for silicas gels after longer gelling times. Another interesting fact from the BJH PoSD is that the pore size becomes wider at higher conversions. This is in agreement with the findings of Lieftink [30], who found that olivine nano-silica at the beginning of the reaction was microporous and mesoporous, and with time, macropores were developed.

The SSA_{NMR} slightly decreases with the conversion degree, being almost constant. Since silica grows via a condensation route, it would be expected that the silanol number is reduced with the particle growth. This reduction occurs, but to a lower extent than for SSA_{BET} and V_{P_D}. The difference in the reductions of SSA_{NMR} and SSA_{BET} could be explained assuming that internal porosity is developed with the conversion degree as the result of condensation of two blocks of silica particles. Thus, this internal surface area is not available anymore for gas although the NMR analysis still detects the silanol groups

on these surfaces. In addition, the silanols in the ultramicropores are likely to remain unchanged.

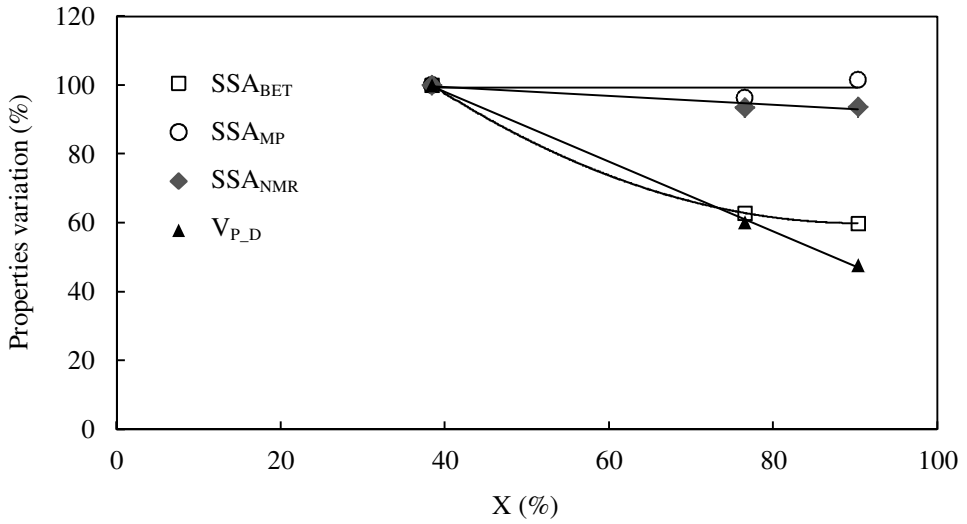

Figure 8.26. Variation of the textural properties of olivine nano-silica versus the conversion degree.

The SSA_{NMR} is an important parameter of the olivine nano-silica since it provides the specific surface area of a fully hydroxylated silica, being different that the SSA_{BET}. The SSA_{NMR} determinations can be used to estimate the amount of silanols in the ultramicropores and internal silanols. However, these surface areas are not accessible or difficult to access, which makes them not so useful from the point of view of some applications.

Considering all the results from the different analyses of this study and the literature data reviewed in Chapter 7 [4,118,131,141], the development of the nano-silica structure could be summarized with the following steps. 1) Initially, soluble silica nucleates and primary particles of 1 to 2 nm are formed. 2) The silica particles grow via a condensation route forming linear chains. 3) As the growth continues, the silica particles keep increasing in size, resulting in 3D networks. 4) With time, the aggregates become bigger and more compact. 5) The final result of the olivine nano-silica production process is agglomerates as large as 20 μm (see Figure 6.12). This texture development model of the olivine silica is described graphically in Figure 8.27, where the shown shape and morphology are only for illustrative purposes. Because the silica aggregates and agglomerates of silica consist of many more primary particles than are shown in this figure, this representation is not realistic but illustrative, and could be misleading regarding the PoSD and the pore volume between the particles.

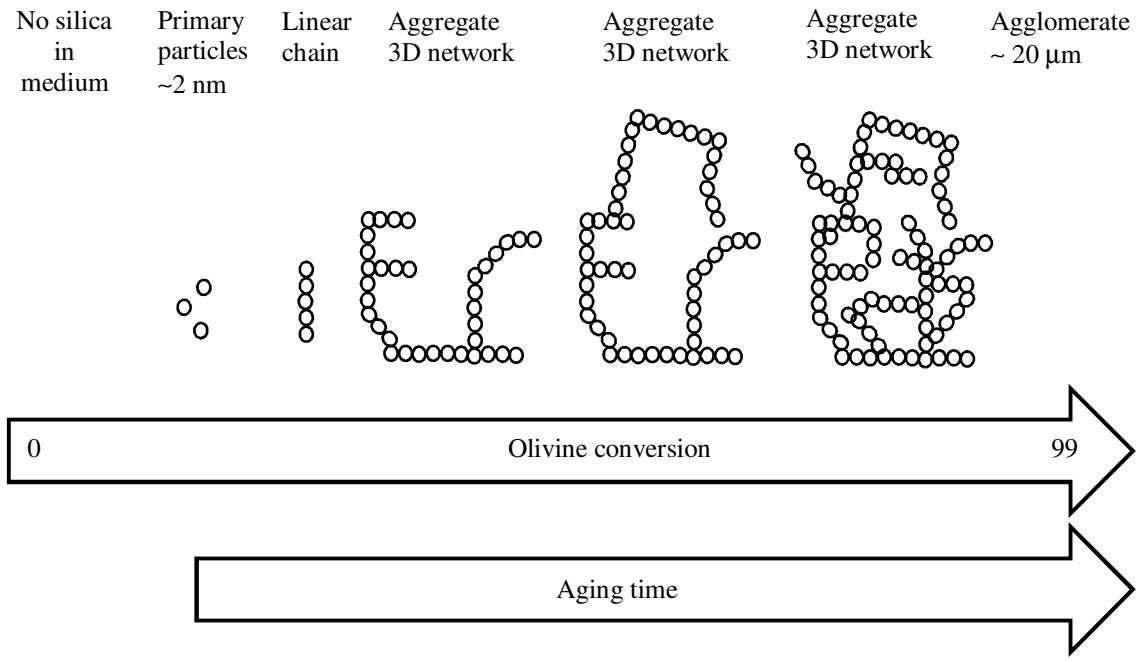

Figure 8.27. Texture development model of olivine nano-silica.

The silica agglomerates are not shown here since they are too big for the adopted scale.

Figure 8.28 represents the variation of the textural properties (SSA_{MP}, SSA_{NMR} and V_{P_D}) in percentage with the SSA_{BET} of the ripened olivine nano-silicas. The SSA_{BET} decreases with the ripening treatment (i.e., pH of ripening, see Figure 6.10). The SSA_{MP} decreases by 90% with the ripening. The V_{P_D} remains constant initially, decreasing drastically for samples after intensive ripening treatments (SSA_{BET} below 200 m^2/g). The SSA_{NMR} drops slightly with the ripening.

The pronounced decrease of SSA_{MP} is due to the reduction of pores of around 2 nm. That can be inferred from the results of the positron annihilation lifetime spectroscopy (PALS), where two types of pores were found. The intensity of pore 1 (~0.5 nm) did not change during the ripening treatment, but the intensity of pore 2 (~2.5 nm) decreased by 75%. Therefore, the microporosity was reduced significantly, but the ultramicropores remained unaffected. The BJH pore volume remained constant for non-intensive ripening treatments, decreasing for samples with a SSA_{BET} below 200 m^2/g. The pore range was also reduced during the ripening (see Figure 8.4), the pores below 9 nm being completely removed. This phenomenon is because dissolved silica condensates initially on the walls of accessible micropores, and when most of the micropores have been filled, the dissolved silica condensates on the smaller mesopores. A similar effect can be observed in Figure 6.11.

The SSA_{NMR} decreases gradually and slowly with the ripening treatment, resulting in a total reduction of 8% for the most intensive ripening. The most plausible explanation for the small reduction of SSA_{NMR} is that most of the silanols in olivine nano-silicas are

located on internal and ultramicropores surfaces. Therefore, they are not affected by the ripening treatment.

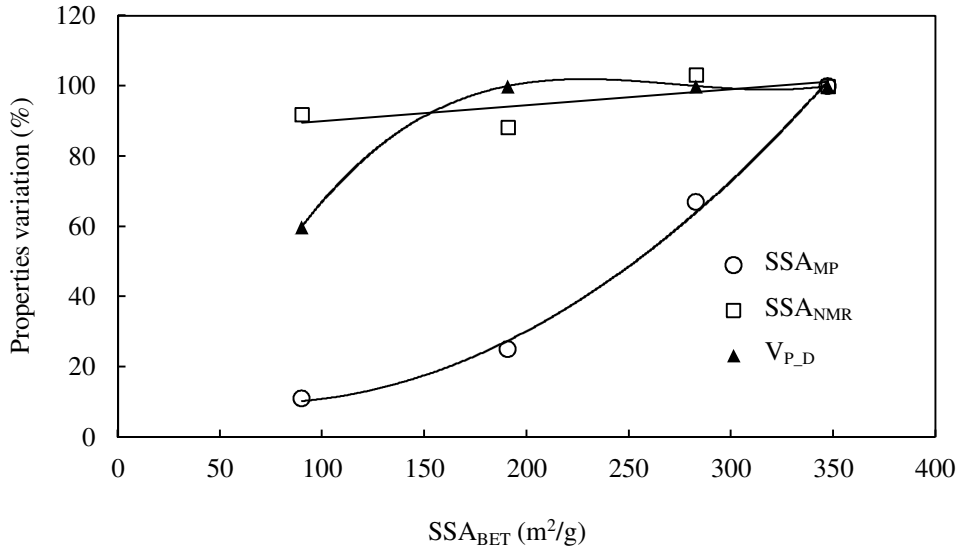

Figure 8.28. Variation of the textural properties of ripened olivine nano-silica versus the SSA_{BET}.

8.5 Conclusions

Olivine nano-silica exhibit a SSA_{BET} in the range of 100 to 500 m^2/g, with an average value of 350 m^2/g for silicas of high purity, X > 90% and filtered under vacuum. The BJH pore size distribution is in the range of 2 to 100 nm. The silanol number is in the range of 13 to 22 OH/nm^2 for olivine nano-silicas dried at 120 °C and 11 to 13 OH/nm^2 for silicas dried at 190 °C. These high silanol values are due to the presence of internal and ultramicropore silanols. In the PALS analyses two types of pores were found, one at around 6 Å (pore 1) and another one at around 25 Å (pore 2). Pore 1 was in the ultramicropore range, while pore 2 was in the low mesopore range. Pore 1 can be considered to be intrinsic to the amorphous matrix of olivine nano-silica, and pore 2 can be due to the voids between the primary particles. Therefore, olivine nano-silica is considered to be as microporous, mesoporous and macroporous.

The process conditions (i.e., the impurity content, conversion degree, pressure of filtration and ripening treatment) have an important influence on the textural properties of olivine nano-silica. The pore size distribution of olivine silica can be tailored to meet the requirements of different possible applications. This tailoring can be done by changing the filtration pressure, controlling the conversion degree and/or performing ripening treatments after the production process has been completed. Thus, the initial PoSD (2-100 nm) can be modified to a distribution of 9 to 30 nm.

The development of the nano-silica structure during the olivine process can be described by the following steps: 1) initially, soluble silica nucleates and primary particles of around 2 nm are formed; 2) the silica particles grow via a condensation route, forming linear chains; 3) as the growth continues, the silica particles keep increasing in size, resulting in 3D networks; and 4) with time, the aggregates become bigger and more compact. The final result of the olivine process is agglomerates as big as 20 μm. In addition, internal pores (also called closed pores) are developed with the conversion degree as the result of condensation of two blocks of silica particles.

In comparison with precipitated silica (Sipernat 310 and 50S), olivine nano-silica is characterized by: 1) a lower SSA_{BET} than Sipernat 310; 2) V_{P_D} is considerably lower, which means that precipitated silicas have a higher content of mesopores and macropores; 3) the V_{MP} is much higher which results in higher micropore surfaces areas; 4) the silanol content is higher; and 5) the SSA_{NMR} follows the order: Sipernat 310 > olivine nano-silica > Sipernat 50S, with an average value for olivine nano-silica of 780 m^2/g. On the other hand, pyrogenic silicas feature similar SSA_{BET} and V_{P_D}, but lower V_{MP} than olivine nano-silicas. In addition, all three types of silica form 3D network structures.

Chapter 9. Technical aspects of the production of olivine nano-silica

9.1 Introduction

As was mentioned previously, the olivine nano-silica process is not yet a commercialized product. This chapter addresses different practical points of the olivine nano-silica process, which will be useful in the case that this process is implemented industrially. The aspects presented here are:

1. conditions chosen of the olivine nano-silica process;
2. problems that can occur during the production;
3. experiments performed in pilot plants;
4. cost analysis of olivine nano-silica and precipitated silica;
5. generation of waste solutions and byproducts;
6. application of olivine nano-silica in concrete.

9.2 Conditions chosen

9.2.1 Type and concentration of acid

The acid used in the dissolution of olivine is sulfuric acid because of its relatively low cost and low corrosive behavior compared with HCl. In addition, experiments performed by Jonckbloedt [12] showed that the use of sulfuric acid produced nano-silica with higher specific surface area than using hydrochloric acid. He found that the dissolution of olivine in 3M sulfuric acid at 70 °C produced an amorphous silica with a specific surface area between 220 and 240 m^2/g, whereas using 6M hydrochloric acid at 70 °C produced a material of 97 m^2/g (no data about the chemical composition was reported) [12].

Initially, one may think that it could be convenient to work at the highest possible concentration of sulfuric acid in order to accelerate the dissolution rate; however, the maximum amount of sulfuric acid that can be used in the dissolution of olivine is limited by the solubility of $MgSO_4$. Table 9.1 lists the soluble concentration (mol/L) of $MgSO_4$ at different temperatures obtained from the solubility values [105].

As is shown in Table 9.1, the solubility at 20 °C is 2.67 mol/L. This value is the solubility of MgSO4 in water considering that no other compounds are in the solution, but the real solubility of $MgSO_4$ in the olivine slurry is influenced by the presence of other ions in the solution. No presence of crystals has been observed during the olivine reaction under the experimental conditions used (between 50 and 90 °C with 3M sulfuric acid). However, crystallization occurred when the slurry was filtered directly after decantation, as can be seen in Figure 9.1. This problem can be solved by diluting the slurry with water.

Table 9.1. Soluble concentration of $MgSO_4$ at different temperatures.

T (°C)	w_s (%)	ρ_s (g/cm^3)	m_s (g/L)	$[MgSO_4]_s$ (mol/L)
0	18.2	1.200	218.5	1.815
10	21.7	1.240	269.1	2.236
20	25.1	1.279	321.0	2.667
30	28.2	1.314	370.7	3.079
40	30.9	1.345	415.7	3.453
50	33.4	1.374	458.8	3.812
60	35.6	1.399	498.0	4.137
70	36.9	1.414	521.6	4.334
80	35.9	1.402	503.4	4.182
90	34.7	1.388	481.8	4.003

w_s is the saturation concentration, ρ_s density of the solution, m_s mass of the solute and $[MgSO_4]_s$ concentration at the saturation point.

Figure 9.1 Formation of $MgSO_4$ needle crystals during filtration.

9.2.2 Type of silicate mineral

The silicate mineral selected in this study to produce nano-silica is olivine due to the absence of Si-O bonds in its structure (see Figure 1.9), which makes the reaction faster than for other silicate minerals. In addition, dunite, which consists of 90% of olivine, is the most common rock in the upper mantle. Deposits of dunite rocks can also be found in the earth crust, which makes it a low price commodity (between 75 and 150 $ per ton [167]). Two types of dunite materials were used, one from Norway and another one from Greece. The Norwegian material is richer in olivine because the Greek material is a byproduct of a magnesite mine with a lower content of olivine (more details about the chemical composition of these materials are presented in Chapter 2).

9.2.3 Reactor design

The olivine silica setup consists of a stirred double-walled glass reactor, a thermostat bath and a cooling vessel that adjust the reactor temperature through the outer wall. Two reactors have been used, one of 1 liter and another one of 15 liters. The schematic diagram of the setup for the production of olivine nano-silica is shown in Figure 9.2. The reactors used are shown in Figures 9.3 and 9.4, respectively.

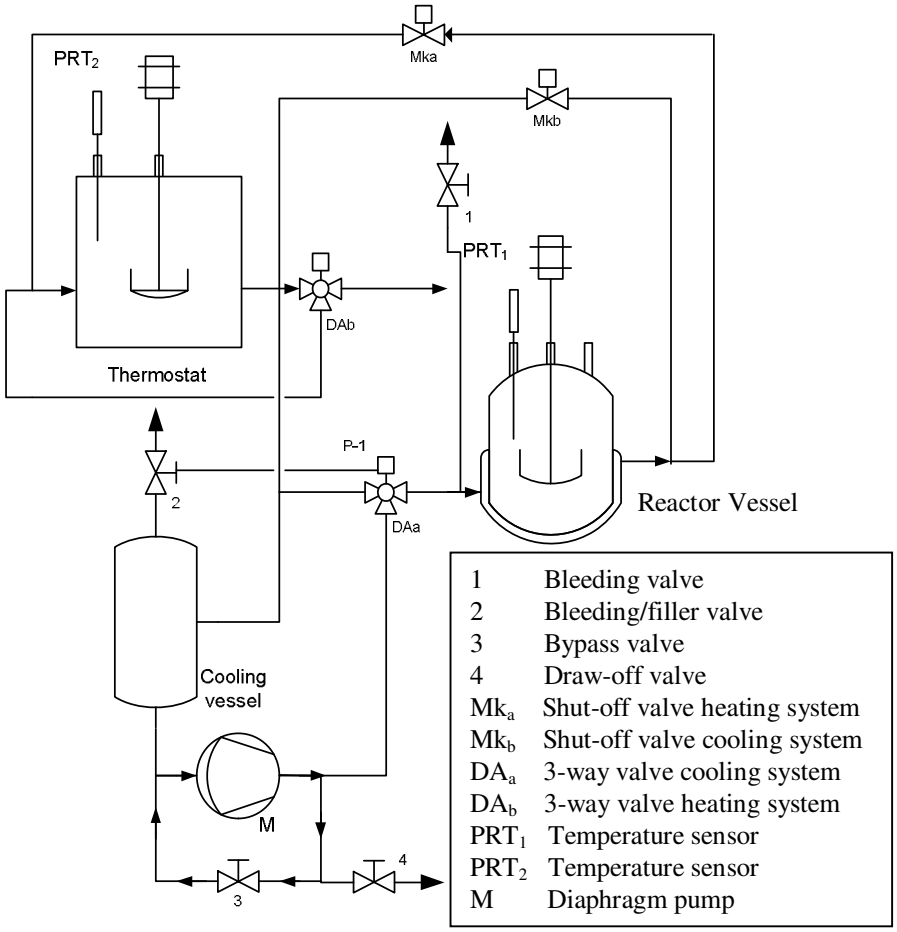

Figure 9.2. Diagram of the setup for the production of olivine nano-silica.

The reactors were designed following the recommendations of the Handbook of Industrial Mixing [103]. The main characteristics of the reactors are: 1) the reactors have baffles; 2) the reactor bottoms are rounded; 3) the stirrer type is a pitched blade turbine (PBT) with an angle of 45°. The stirrer engine is oversized in order to have enough power to keep all the particles in complete motion (known as Zwitering criterion) even at the most viscous state. When a slurry is under the Zwitering condition, the maximum surface area of the particles is exposed to the fluid for chemical reaction or mass transfer [103]. The minimum agitation speed (N_{js}) for the suspended state can be calculated with:

$$N_{js} = S\,\upsilon^{0.1}\left[\frac{g(\rho_s - \rho_l)}{\rho_l}\right]^{0.45} \cdot X^{0.13} \cdot d_{ol}^{0.2} \cdot d_I^{-0.85}, \qquad \textbf{(9.1)}$$

where S is a dimensionless number which is function of the type of impeller, ν the kinematic viscosity, g the gravitational acceleration, ρ_s the density of the solid particles, ρ_l the density of the solution, X the solid content, d_{ol} the olivine particle size and d_I the diameter of the impeller.

Figure 9.3. Reactor of 1 liter for the production of nano-silica.

Table 9.2 presents the values of N_{js} for the initial conditions and the maximum viscosity conditions found in Table 4.5 for olivine particles of 10, 100 and 500 μm. The parameters used in Eq. (9.1) for the 15 liter reactor are an impeller diameter of 0.0415 m, the Zwietering constant (S) of 3.4 and the mass ratio of suspended solids 0.22 kg solid/kg liquid. The agitation speed used in this study was around 8 rps. Therefore, the stirring speed is always above the minimum agitation speed for the suspended state except for olivine particles of 500 μm, where the agitation speed is slightly lower than N_{js}. It has not been considered in this calculation that the mass ratio of suspended solids decreases with time; thus, the real value of N_{js} should also decreases with time.

9.3 Production problems during the synthesis

As in many other production processes, while developing a new material or synthesis method, many problems appear related to the properties of the main product or to the production process such as material corrosion, control operation, inadequate mixing,

separation difficulties, etc. The problems encountered while performing the experiments are described below.

Table 9.2. Estimation of the minimum agitation speed.

	State 1	State 2
	Njs (rps)	**Njs (rps)**
d_{ol} = 10 μm	3.9	5.0
d_{ol} = 100 μm	6.1	8.0
d_{ol} = 500 μm	8.4	11.0

State 1 refers to the beginning of the reaction (ρ = 1180 kg/m^3 and $\mu = 1.70 \cdot 10^{-3}$ Pa·s), State 2 to the maximum viscosity conditions (ρ = 1364 kg/m^3 and μ = 0.0452 Pa·s) and d_{ol} is the diameter of the olivine grains.

Figure 9.4. Reactor of 15 liters for the production of nano-silica.

9.3.1 Iron oxidation in the slurry

Figure 9.5 plots the phase diagram (pSO_4/pH) of Fe (II) and Fe (III) when no other ions are in the medium [168]. The horizontal line describes the change of pH in a solution with a constant pSO_4 of -0.48 (equivalent to 3M without taking into account the activity coefficient). Thus, in a solution with only sulfates (3M), hydrogen ion and iron, the iron

species at the initial pH (around -0.77) would be in the form of $FeHSO_4^{2+}$. As the pH increases, the iron phase would change to $FeSO_4^{+}$, shortly after that to $Fe(SO_4)_2^{-}$, and finally around the pH value of 4 to $Fe(OH)_3$, which would precipitate.

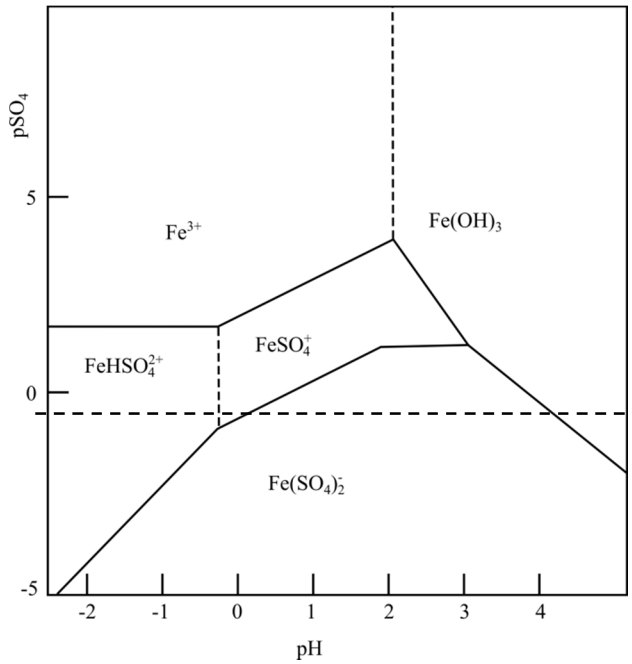

Figure 9.5. Phase diagram of $FeSO_4$ against the pH [168].

In the case of the dissolution of olivine in acid, the iron in the solution is susceptible to oxidation from Fe (II) to Fe (III) when the solution pH increases. When that happens the slurry changes its colour from green-grey to yellow-brown (see Figure 9.6) and the silica becomes contaminated. Besides iron and sulfates, there are more species in the slurry (i.e., magnesium, silica, silicate minerals) that modify the speciation of the iron. In order to determine the point of the precipitation of the iron, several experiments were performed under the olivine nano-silica production conditions. These experiments were conducted with slurries of different batches, masses of slurry and volume of distilled water, as can be seen in Table 9.3. The precipitation point, which is related to the change of colour, occurs in the pH range between 3.1 and 3.4 (excluding the experiment in batch 1 with a pH value of 4.2). Therefore, all the operations in the production of olivine nano-silica should be performed below this pH. That is the reason why in the previous chapters the washing and filtering of the nano-silica is carried out initially with an 0.1M sulfuric acid. Once most of the iron is removed, distilled water is used in order to further remove the sulfates from the silica (see Chapter 6). Using this procedure, the washing and filtering under nitrogen conditions (as was done by Jonckbloedt [12]) can be avoided.

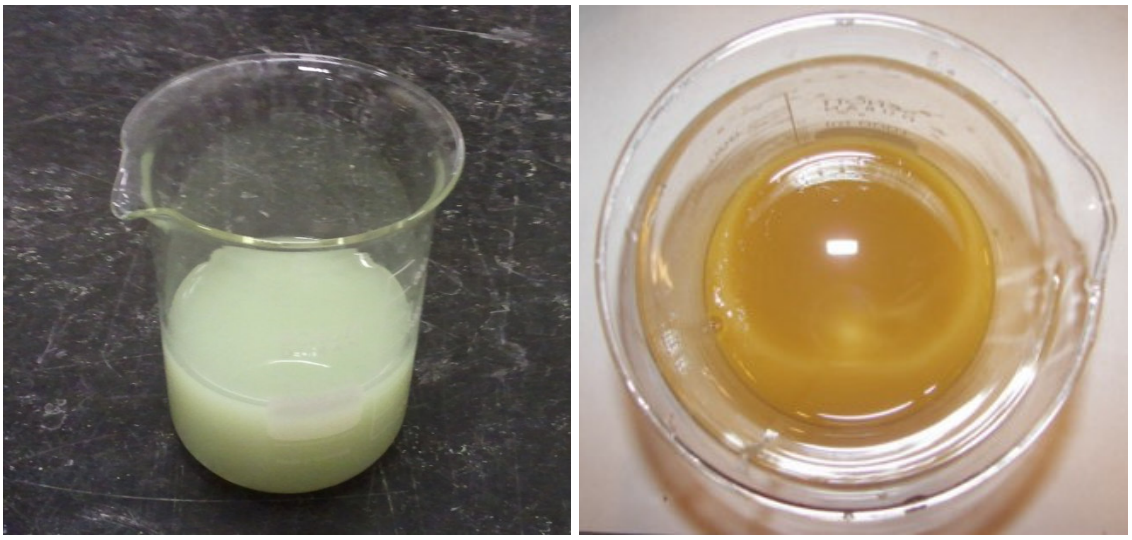

Figure 9.6. Change of color of the slurry with the pH.

Table 9.3. Precipitation point of the olivine nano-silica slurry.

Batch	m_{Sl} (g)	V_w (ml)	pH_i	pH_p
1	14.0	50	1.6	3.4
1	2.0	45	2.1	4.2
1	5.0	0	2.1	3.4
2	10.0	50	1.7	3.3
2	23.2	0	0.7	3.1

m_{Sl} refers to the slurry mass, V_w the water volume, pH_i to the initial pH and pH_p to the pH at the precipitation point.

9.3.2 Cleaning of the olivine nano-silica

One of the most problematic operations in the olivine nano-silica production process is the separation of nano-silica from the other components of the slurry. The first difficulties can occur during the decantation of the remaining silicate minerals. In a couple of experiments, some minerals went together with the silica/sulfate dispersion as can be seen in Figure 9.7. Besides the contamination, the presence of mineral grains allows the formation of preferential paths during the filtration, which considerably reduces the separation efficiency, letting some silica escape from the filter cake. This process should be optimized in order to completely separate the minerals from the slurry, and at the same time minimize the amount of silica loss. This could be done by using a decantation vessel designed specifically for this process and using more than one decantation step.

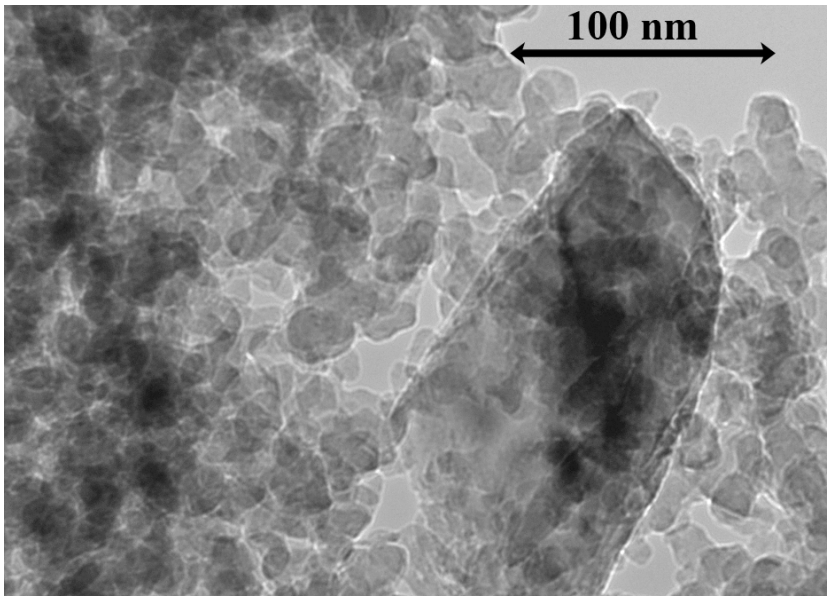

Figure 9.7. TEM picture of olivine nano-silica with mineral impurities.

Even when no minerals are present in the filter cake, some silica dispersion is passing through the filter at the beginning of the operation until the filter cake is formed. In Chapter 5, data about the separation efficiency is presented (see Figure 5.13), where it is mentioned that the separation efficiency increases with the specific surface area of nano-silica and aging time. A possibility to increase the separation efficiency beyond this value (80%) would be to add a recovery step to the process.

When using a laboratory filter press (Serfilco model 0.02 - 7PPMH) with a cake volume of 566 ml, clogging of the filter cloth and overpressure has been observed. However, when using a larger filter press (experiments performed by Eurosupport and Hellas Gold as is explained later in this chapter) this situation did not occur even though the filter cloth used was the same type. Probably, this was because with the lab filter was difficult to control the pressure in the initial stages. This initial high pressure could break down the pore structure of the nano-silica. Similar effects were described by Madeleine [114] for cakes consisting of nano-particles under the effects of high pressure resulting in a collapse of the structure.

When using Greek materials PROMGM-1 and PROMGM-3, additional problems related to the cleaning of the nano-silica were found. The separation of the silica from the slurry was impossible because a thick mud was formed, as can be seen in Figure 9.8. This thick mud was formed due to the presence of talc and precipitated gypsum ($CaSO_4 \cdot 2H_2O$); the latter as a result of the high content of CaO in the dunite.

Figure 9.8. Thick mud produced when dissolving PROMGM-1 in sulfuric acid 3M.

9.3.3 Overheating

Because the dissolution of olivine in acid is exothermic, heat is generated during the process. Table 1.2 shows that the temperature would rise up to 79 °C if 1.5 moles of olivine reacted with sulfuric acid in an adiabatic reactor. Actually, in the real case, systems are far away from adiabatic conditions since there are energy losses to the surrounding medium. However, for normal batch reactor shapes, the bigger the reactor the smaller the energy loss should be. The advantage when operating an industrial reactor is that the energy requirement to heat up the mixture can be neglected. However, whereas the temperature control is relatively simple in the laboratory reactors, a more careful approach should be considered when operating industrial reactors.

The heat generation rate depends on the kinetics of the olivine dissolution. Likewise, the kinetics depends on the hydrogen ion activity, olivine specific surface area and reaction temperature (as discussed in Chapter 4). The concentration of the hydrogen ion should be as high as possible to obtain the maximum amount of silica per batch, but should be below the saturation concentration of $MgSO_4$ to avoid its precipitation. That means the acid concentration is fixed at the highest possible value that ensures no crystallization of $MgSO_4$. The olivine specific surface area and the reaction temperature could be adjusted in order to slow down the reaction kinetics and, therefore, to avoid problems of overheating, and at the same time have short reaction times.

9.3.4 Cementation in the reactor

Another important problem is the cementation of the solid material when the whole reactor or part of it is not stirred vigorously enough. This happens as the result of the precipitation of silica on the olivine grains acting as a binder between the mineral grains. This phenomenon occurs when the mixing between the solid particles and the fluid is inadequate. Factors that make the mixing poor are the presence of dead zones, low stirring speed or a bad configuration of the stirrer.

9.3.5 Aggressive medium

The olivine nano-silica production is performed under aggressive conditions, which are 25% sulfuric acid, temperature between 50 and 90 °C and a solid content of 250 g/L. The main problems related to these aggressive conditions are the corrosion of some parts of the reactor and the difficulties in monitoring and controlling the pH. Resistant materials for these conditions are special stainless steel, special alloys and stainless steel covered with a protective layer (made of enamel, PTFE or special metals such as tantalum, zirconium and niobium). Steel 654 SMO is the stainless steel most resistant to elevated temperature at a concentration of sulfuric acid 25%, featuring a corrosion of 0.1 mm per year at 80 °C (see Figure 9.9) [169]. Hastelloy C and B-3 feature a corrosion of 0.13 mm per year in 25% sulfuric acid at 85 °C and 110 °C [170], respectively. The special metals tantalum, zirconium and niobium are very resistant to sulfuric acid, being corroded less than 0.13 mm per year [171]. The protective layers of enamel and PTFE are also resistant to corrosion under these conditions. However, the enamel layer could crack under impact, and the PTFE wears out more rapidly at this high solid content than the metallic materials.

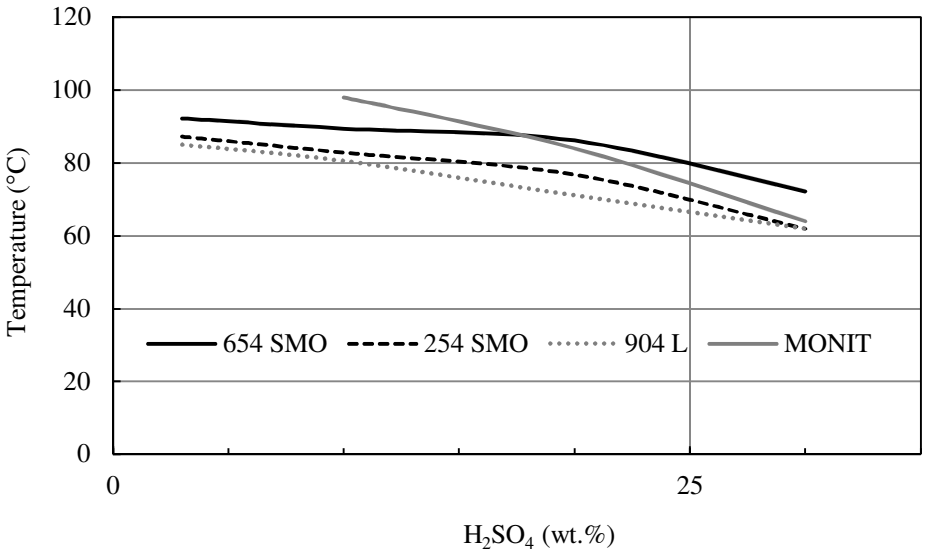

Figure 9.9. Isocorrosion curves (0.1 mm/year) of special stainless steels in H_2SO_4.
Where 654 SMO, 254 SMO and 904 L are austenitic stainless steels and MONIT is a ferritic stainless steel.

9.4 Experiments on pilot plants

In addition to the production of olivine nano-silica on laboratory scale at the Technical University of Eindhoven, other experiments were performed in larger reactors in collaboration with Eurosupport (The Netherlands) [172] and Hellas Gold (Greece) [173]. Figure 9.10 illustrates the schematic diagram of the pilot plant for the production of olivine nano-silica in Eurosupport [172], and Figure 9.11 shows the picture of the pilot

plant in Hellas Gold [173]. In the experiments performed by Eurosupport, Norwegian olivine GL50 (see Table 2.1) was employed in a batch reactor made up of stainless steel covered with enamel. In the experiments performed by Hellas Gold, the material PROMGM-10 (see Table 2.1) was used in a set of reactors made of stainless steel. In this case, no attention was paid to the corrosion of the steel because this system was used only for a limited number of experiments.

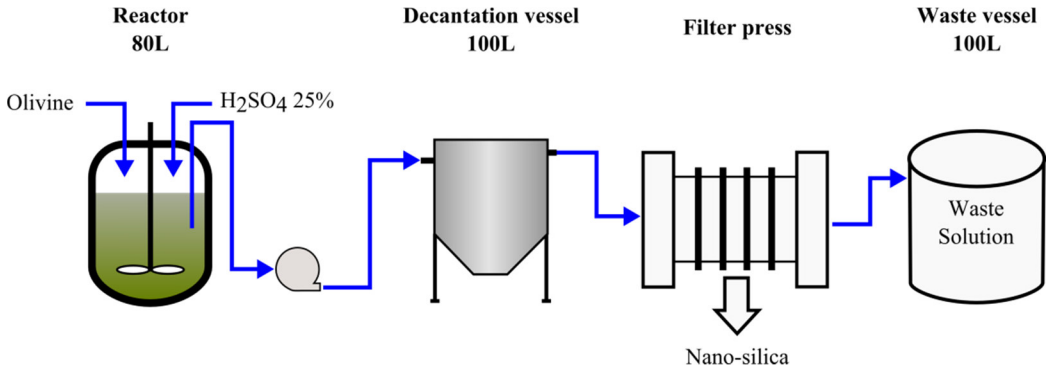

Figure 9.10. Schematic diagram of the pilot plant in Eurosupport (Netherlands).

Figure 9.11. Picture of the production pilot plant in Hellas Gold (Greece) [173].

Table 9.4 lists the reaction volumes, BET specific surface area (SSA_{BET}), sulfur content, purity of silica and the process yield of the olivine nano-silica produced. The scale up of the reaction from laboratory scale (1 and 15 liters) to pilot plant (60 and 80 liters) did not cause any problem. The cleaning of the nano-silica using a filter press gave excellent results in the case of Eurosupport. Olivine nano-silica produced by Eurosupport featured similar purities to the values presented in Chapter 6, and with an average process yield equal to the best values reported in Chapter 5. However, in the case of Hellas Gold, the

average purity obtained was 96.5% because some problems occurred during filtration. The filtration problems can be explained by the presence of minerals in the filter cake. The presence of minerals in the filter cake creates preferential paths and makes the cleaning of nano-silica inefficient. This means that with the set-up of Hellas Gold the decantation of the slurry was not performed properly.

Table 9.4. SSA_{BET}, sulfur content and purity of olivine nano-silica produced by Eurosupport [172] and Hellas Gold [173].

		SSA_{BET} (m^2/g)		Sulfur (%)		P_{Si} (%)		
	$Volume_R$ (L)	Range	Aver.	Range	Aver.	Range	Aver.	Y_{NS} (%)
Eurosupport	80	321-401	385	0.05-0.27	0.08	98.5-99.4	99.15	83
Hellas Gold	60	320-420	375	0.13-1.8	0.6	92.2-99.4	96.5	-

Where $Volume_R$ refers to the reaction volume.

9.5 Cost of the materials and energy requirements

In this section an estimation of the cost of the raw materials, the energy requirements and CO_2 emissions is presented for both production processes: the olivine nano-silica and precipitated nano-silica using water-glass. Table 9.5 presents the material properties (i.e., molecular weight and concentration) and the process yield of the olivine nano-silica process. The average prices of sulfuric acid, dunite and waterglass (WG) are listed in Table 9.6.

Table 9.7 shows the sulfuric acid and the dunite costs associated with the production of olivine nano-silica. The estimated total cost of the raw materials in the olivine nano-silica process is 1023 $ per ton of silica.

Table 9.5. Properties of the materials in the olivine nano-silica process.

M_{ol} (g/mol)	M_{SiO_2} (g/mol)	$M_{H_2SO_4}$ (g/mol)	H_2SO_4 (M)	H_2SO_4 (%)	m_{ol} (%)	$ratio_M$ H_2SO_4/Si	$ratio_M$ ol/si	Y_{NS} (%)
145.13	60.08	98.06	3	24.97	90	2	1	0.8

Table 9.6. Reagent prices of olivine nano-silica and precipitated silica processes.

	H_2SO_4 ($/tn)	Dunite ($/tn)	WG 27 wt.% ($/tn)
	152	113	555
Ref.	[174]	[167]	[1]

Where WG refers to waterglass. [1]Value obtained from the PQ corporation.

Table 9.7. Estimated costs of sulfuric acid and dunite for the production of 1 ton of olivine nano-silica

n_{NS} (kmol)	$n_{H_2SO_4}$ (kmol)	$m_{H_2SO_4}$ (kg)	$C_{H_2SO_4}$ ($)	n_{ol} (kmol)	m_{du} (kg)	C_{du} ($)	C_{RM} ($)
16.64	33.29	4250.48	645	16.64	3355.02	377	1023

Table 9.8 lists the estimated raw material (RM) cost of precipitated silica from the waterglass route, which results in a cost of 2266 $/ton. In addition, in the production of waterglass, 403 kg of CO_2/ton are released [2]. The required energy reported by several companies for the production of 2.0 sodium silicate liquor (SiO_2:Na_2O ratio of 2:1) with a 48% solid content (i.e., 32 wt.% of SiO_2) is between 420 and 1250 MJ/ton [2]. Taking the average of these two values and considering that 3900 kg of 27 wt.% waterglass is used per silica ton, results in an energy requirement of 2800 MJ/ton.

Table 9.8. Estimated raw material costs of precipitated silica using waterglass.

$m_{H_2SO_4}$ (kg)	$C_{H_2SO_4}$ ($)	m_{WG} (kg)	C_{WG} ($)	C_{RM} ($)
660	100	3900	2166	2266

The raw materials required for the production of olivine nano-silica are considerably cheaper than for the production of the precipitated silica using waterglass. The energy required during the synthesis of olivine nano-silica could be negligible since the reaction is exothermic (see Table 1.2), provided the reactor is sufficiently large and well insulated. The main energy consumption – not considering the energy in the drying step – is the electricity to crush the olivine. Thus, the energy requirement is lower for the olivine nano-silica process than for precipitated nano-silica. Likewise, the CO_2 emission is also lower for the olivine nano-silica than for the precipitated processes.

The estimated average price for precipitated silica, which is currently the silica most produced, in 2016 will be 2285 $/ton [3]. However, the prices of nano-silica can vary over in a wide range depending on the purity, physical state (dried powder, colloidal dispersion or gel), morphological properties (particle size, SSA_{BET}, pore size distribution), etc., being able to reach values of 15000 $/ton for special applications such as in the field of catalysis.

9.6 Waste solution management

The dissolution of olivine in acid produces a slurry that consists of a mixture of nano-silica, sulfates, metallic ions and unreacted minerals. This slurry is diluted by 50% with water for two reasons: 1) to decrease the viscosity of the mixture, and, thus, to allow the unreactive minerals to settle faster; and 2) to avoid precipitation of $MgSO_4$ in the filter

cake (see Figure 9.1). After removal of the unreacted minerals, the remaining slurry (here referred as mother slurry) is washed and filtered. Figure 9.12 depicts the filtrate conductivity of the mother slurry produced with 10 liters of 3M sulfuric acid against the rinsing volume during a continuos cleaning of the mother slurry and filtered using the lab filter press. The first 40 liters of rinsing fluid were 0.1 M H_2SO_4 to avoid the precipitation of iron, and after that water was used. The volume of rinsing fluid to reach a filtrate conductivity below 1 mS/cm was around 10 times the initial volume of the acid employed. The chemical composition of this sample (NS-HP) was presented in Table 6.2, resulting in a purity surprisingly high (i.e., 94.07%) due to the formation preferential paths (discussed in Chapter 6).

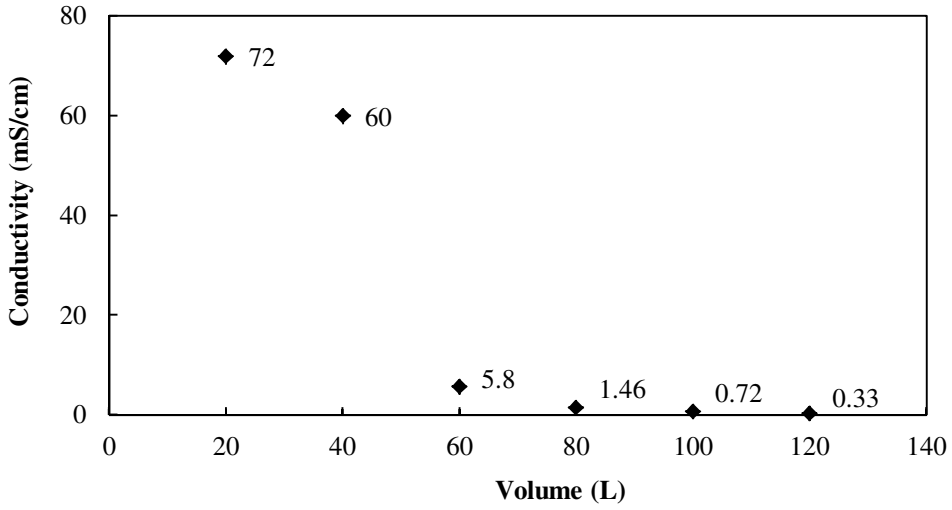

Figure 9.12. Conductivity of the filtrate versus the rinsing volume used during the cleaning of nano-silica produced with 10 L of 3M H_2SO_4.

Table 9.9 lists the volume of slurry produced for the synthesis of one ton of nano-silica using 3M (~25 wt.%) sulfuric acid. Table 9.10 presents the volume, concentrations and masses of the main components of the slurry after the dilution, without taking into account the minor components such as Al, Ca, Ni, etc. The total volume of waste solution after filtration is much larger than the value of 20 m^3 per ton of silica. Thus, after filtration, the waste volume should be around 228 m^3 with a sulfate concentration of 0.182 mol/L. The quantity of rinsing fluid can be further optimized using different approaches such as: 1) using a countercurrent flow for washing and cleaning; 2) adding a reverse osmosis step to concentrate to obtain two streams, one with high concentration of ion, and another one of clean water. Even after these optimization steps, the amount of waste solution will be considerably huge. Therefore, to make the whole olivine nano-silica process appealing, the waste solution should be cost efficiently treated to obtain byproducts that can be commercialized, or in the worst case, disposed with minor harmful effects for the environment and low economic costs.

Table 9.9. Stoichiometric calculations of the mother slurry for one ton of nano-silica.

n_{NS} (kmol)	$n_{H_2SO_4}$ (kmol)	$m_{H_2SO_4}$ (kg)	H_2SO_4 (%)	m_{Msl} (kg)	V_{Msl} (m^3)
16.64	33.29	4080	24.97	16341	13.87

m_{Msl} and V_{Msl} refers to the mass and volume of the mother slurry.

Table 9.10. Volume, concentration and mass after diluting the mother slurry with water for one ton of nano-silica.

V_{Msl+w} (m^3)	[Mg] (mol/L)	[Fe] (mol/L)	[SO_4] (mol/L)	m_{Mg} (kg)	m_{Fe} (kg)	m_{SO_4} (kg)
20.8	1.84	0.16	2	930.6	185.9	3997.6

V_{Msl+w} refers to the volume of the mother slurry plus 50% dilution water.

The main contaminants of the waste solution are sulfates, magnesium and iron ions. If iron could be removed from the solution, $MgSO_4$ hydrated salts, which are valuable products, could be produced; therefore, the problem would be reduced to efficiently concentrate the salts of magnesium. The salts of magnesium have different degrees of hydration (see Figure 9.13 [13]), but the most widely commercialized is epsonite ($MgSO_4 \cdot 7H_2O$).

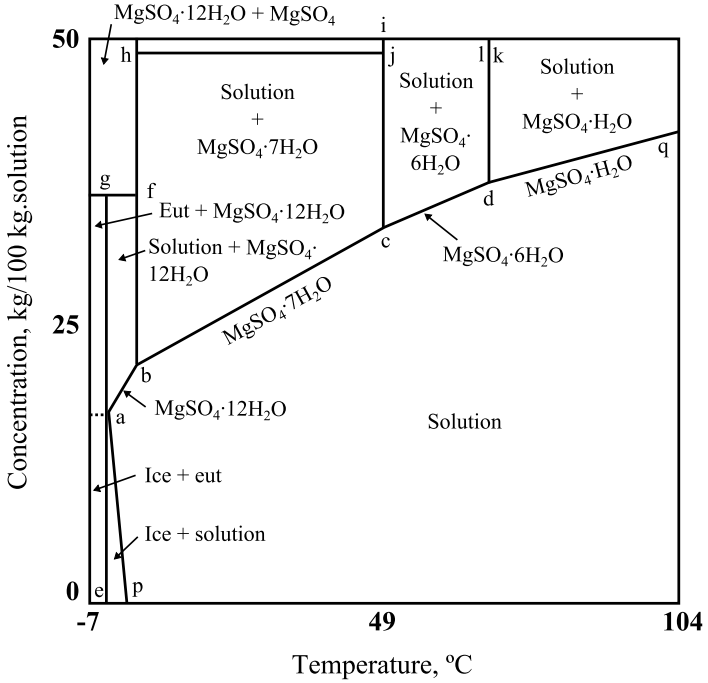

Figure 9.13. Phase diagram of $MgSO_4$, adapted from [13].

9.7 Possible applications

Olivine nano-silica could be used as a replacement of the commercial silicas (pyrogenic and precipitated silica) where its properties, i.e., chemical composition, SSA, aggregate size, pore size distribution and content of silanol groups, are desired. However, in this thesis only the use of olivine nano-silica in building materials was considered, leaving out for further research other possible applications. These experiments were performed in collaboration with MSc. G. Quercia (parallel PhD research project), who studied more deeply the application of nano-silica in concrete [175-177].

9.7.1 Application of olivine nano-silica in concrete

Nano-silica in concrete is not yet commonly applied, but silica fume, which is considered as a micro-silica, has already been used in concrete for several decades to produce high-performance concrete. The use of micro-silica in concrete continues to increase despite its relatively high cost because of its pozzolanic behavior and its content of fine particles. These two features of the micro-silica confer some benefits to the concrete. The pozzolanic behavior refers to the reaction between silica and portlandite, $Ca(OH)_2$, to produce C-S-H (calcium silicate hydrate) gel, which is the main phase contributing to the concrete's strength. Also, because of its small particle size, micro-silica fills the voids between the cement particles; this improves the packing and reduces the porosity. Besides the above mentioned features, nano-silica has the following effects on cement pastes and concrete mixes: acceleration of the setting, cement matrix densification and improvement of the interparticle transition zone (ITZ) of aggregates (filling effect).

One of the reasons to add micro-silica to concrete is to replace the cement content with micro-silica. Micro-silica can replace cement due to its pozzolanic reaction (1 part silica instead of 3 to 4 parts cement), while the strength is unaffected [178]. Therefore, the replacement of cement by micro-silica should considerably reduce the CO_2 footprint of the concrete. That is important because the cement industry is one of the industrial sectors that releases large amounts of CO_2 into the environment, accounting for 8% of global CO_2 emissions [179]. In addition to this interesting application, the largest use of micro-silica is for producing concrete with enhanced properties, such as high early strength, low permeability and enhanced durability [180]. Considering that the main difference between nano-silica and micro-silica is their respective particle sizes and assuming that the pozzolanic behaviors in both are similar, nano-silica will react faster with the cement due to its higher SSA.

9.7.2 Pozzolanic activity of olivine nano-silica

To determine the pozzolanic index of the olivine nano-silica, different cement mortars were prepared and tested following guideline CEN EN 196-1 [181]. A replacement of 7%,

based on the weight of binder (bwob), which is cement plus nano-silica, was selected using the procedure described by Justnes [182]. This silica was applied in concrete in dried form. In addition, two cement mortars, with and without the replacement of cement with micro-silica (PmS-4), were prepared. The superplasticizer (SP) content (see Table 9.11) of the mixes was adjusted to obtain a spread flow of 175 ± 15 mm ensuring the desired rheological properties of the mixture. The SP used was a polycarboxilic ether (PCE) type with a solid content of 35% and density of 1.095 g/ml. The mortar with olivine nano-silica needed more than four times the amount of SP than the mortar with micro-silica to exhibit a similar spread flow, and still, the result of this test was 20 mm smaller.

Table 9.11. Mix design of mortars used to determine the pozzolanic index.

Materials (g)	Reference	ONS	PMS-4
CEM I 52.5N	450	418.5	418.5
Olivine nano-silica	0	31.5	0
Micro-silica	0	0	31.5
Water	225	225	225
Standard sand	1350	1350	1350
SP	0	2.25	0.5
SP (% bwob)	0	0.5	0.11
w/c ratio	0.5	0.54	0.54
Spread flow (mm)	180 ± 3	167 ± 8	184 ± 7

Where ONS refers to a mixture with olivine nano-silica and PMS-4 to a mixture with micro-silica.

There are three reasons why the rheological properties of mortars with olivine nano-silica are more viscous than those with micro-silica. 1) Olivine nano-silica reduced the amount of free water in the mixture. This occurred because olivine nano-silica captured a high amount of water inside its structure as a result of its high specific surface area and mesoporosity. Therefore, less water was available to provide the desired rheological properties of the mix. 2) Also, nano-silica accelerated the hydration process of cement [183,184]. And 3) the last factor influencing the rheological properties of the mixture was the shape of nano-silica particles. The 3-D clusters of olivine nano-silica made the slurry more viscous than the spheres of micro-silica.

The flexural and compressive strengths of the mixtures were determined after 1, 7 and 28 days following the procedure of the guideline CEN EN 196-1. Finally, the pozzolanic activity index was calculated based on the results of the reference cement mortar. The strength development of the different mortars is shown in Figures 9.14 and 9.15. The flexural and compressive strengths after one day were lower for the nano-silica mortar than those of the reference and micro-silica mortars. This may be due to the higher dose of SP, which reduces the hydration kinetics of the cement, in the nano-silica mortar. The

flexural strength at 28 days of the nano-silica mortar was the lowest. The compressive strength of the nano-silica mortar at 28 days showed higher values than the reference mortar, but lower than the micro-silica mortar.

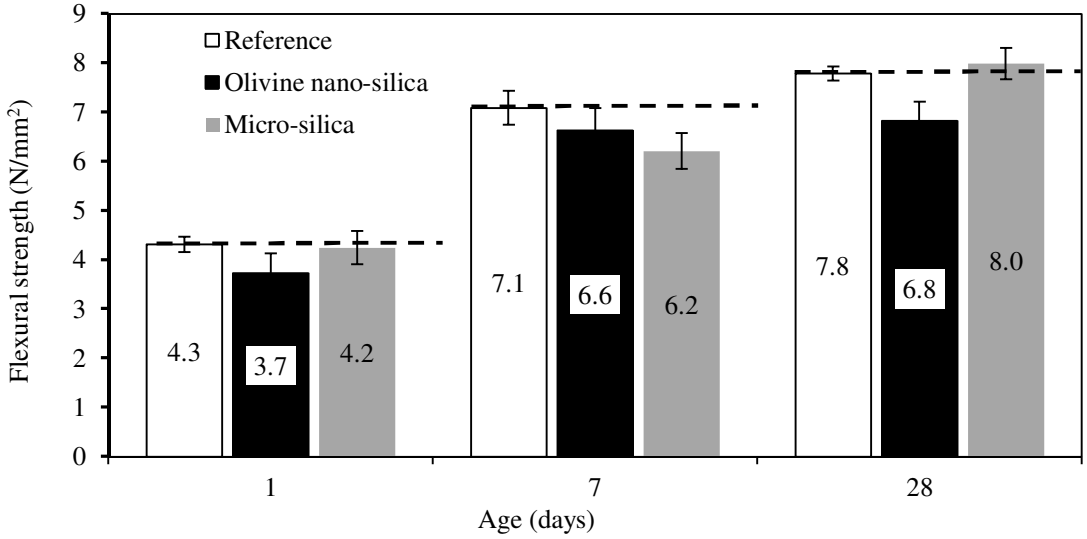

Figure 9.14. Flexural strength development of the tested mortars.

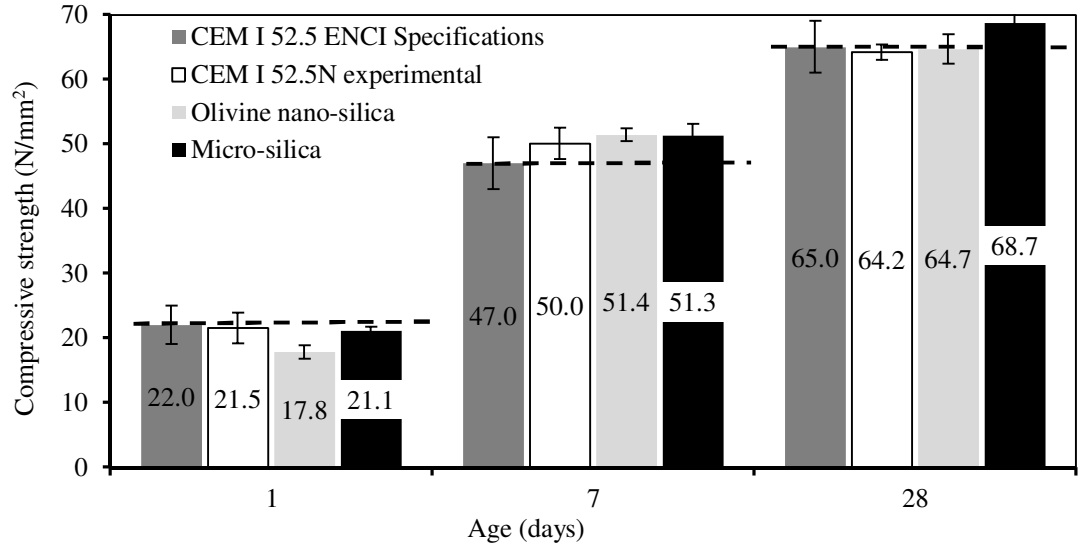

Figure 9.15. Compressive strength development of the tested mortars.

The 7-day and 28-day compressive strengths were used to estimate the relative pozzolanic activity index of the olivine nano-silica and micro-silica mortars. The pozzolanic index was calculated based on the compressive strength of the reference mortar (see Figure 9.16).

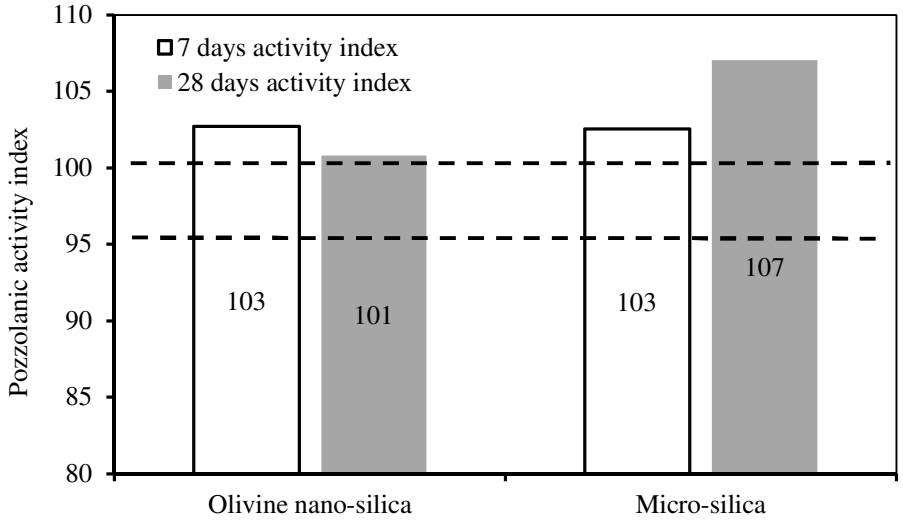

Figure 9.16. Pozzolanic activity index of nano-silica and micro-silica mortars.

The pozzolanic index shows that olivine nano-silica has a high pozzolanic reactivity (101%). Therefore, olivine nano-silica can be classified as a pozzolanic material [185]. Nevertheless, the 28-day activity index was lower than the activity index of micro-silica (107%). This was probably due to the higher specific surface area and the agglomerated state of the nano-silica regarding micro-silica, which means that the maximum wet packing was not achieved, resulting in a lower compressive strength. Despite the positive results that were obtained, further research is needed to understand the strength development of the mortars prepared with additions of olivine nano-silica.

9.7.3 Experiments about the application of nano-silica in concrete

The effect of olivine nano-silica in conventional vibrated concrete (CVC), which is the most commonly used concrete, was investigated by casting three mixtures with different replacement levels of CEM I 52.5N with olivine nano-silica (5, 7 and 10% by volume). The olivine nano-silica was applied in concrete in a water dispersion form. This dispersion was prepared using the high shear mixer (Silverson multifunctional L5M laboratory mixer with a shear screen) for around 10 minutes. The mix designs were based on a commercial recipe (see Table 9.12); eighteen cubes were cast using a vibrating table and were tested for their compressive strength after 1, 7 and 28 days. Additionally, the workability of the fresh concrete was investigated by analyzing the slump following 206-1 standard [186]. The SP used was Ha-BE 100 (polycarboxylate ether type). Table 9.12 also presents the results of the slump test. The only mix with similar slump values to the reference mix was the one with 5% replacement by volume. The SP requirement for this mix was more than double compared to the reference mix. In the cases of 7 and 10% replacement, even though the SP contents were higher than for concrete with 5% replacement, it was not possible to obtain the desired slump class (S2). Therefore, when

the specific surface area of the mix was increased by addition of nano-silica, more SP was required to maintain the same slump class. This is a clear disadvantage of the use of nano-silica, and it needs to be addressed in the future in order to find the type of SP that works more efficiently with olivine nano-silica. Another possible solution for this problem could be to tailor the properties of olivine nano-silica to get lower specific surface areas and more spherical particles.

Table 9.12. Mix designs of CVC with and without replacement of cement with olivine nano-silica.

Materials (kg/m^3)	Reference	5% vol.	7% vol.	10% vol.
Olivine nano-silica	0	6.9	10.3	13.7
CEM I 52.5 N	210	199.6	194.3	189.1
Fly-Ash	88.2	88.2	88.2	88.2
Sand 0-4	780.6	780.6	780.6	780.6
Gravel 4-16	1086.3	1086.3	1086.3	1086.3
Water	158.8	159.1	158.1	158.1
SP (% bwob)	0.5	1.12	1.33	1.75
w/f (%)	0.54	0.54	0.54	0.54
Slump class (mm)	S2 (60 mm)	S2 (60 mm)	S1 (40 mm)	S1 (40 mm)

Where w/f refers to the ratio between water and fines.

The compressive strengths of concrete after 1, 7 and 28 days are depicted in Figure 9.17. This figure shows that the strength after one day was not significantly affected by the increase of the SP content in these mixes. Only the mix with 10% replacement showed a lower strength than the reference. The 7-day compressive strength, on the other hand, displayed an increase for all the substitution levels. The 28-day compressive strength showed similar trends as the 1-day compressive strength; only the mix with 10% replacement showed a lower strength than the reference. The best result after 28 days was obtained for the mix with 5% replacement, where the compressive strength increase by 20% compared to the reference mix. This suggests that the optimum substitution of olivine nano-silica should be around this value.

Figure 9.18 presents the estimated CO_2 footprint per cubic meter of reference CVC and CVC with 5% replacement. These estimations were performed using the CO_2 footprint of each compound from a database of the Dutch precast concrete organization. The CO_2 footprint of olivine was estimated from a life cycle analysis performed by VTT (ProMine internal report, FP7). The reduction of CO_2 emissions for CVC with 5% replacement was 3% with respect to the reference concrete. This could be improved by tailoring the properties of olivine nano-silica so less SP would be necessary to maintain the same rheological properties or slump class. Since the compressive strength of CVC with 5% replacement was 20% higher than the reference concrete, there would be the possibility of

reducing the total amount of cement used while maintaining the same compressive strength as the reference material, therefore, minimizing CO_2 emissions.

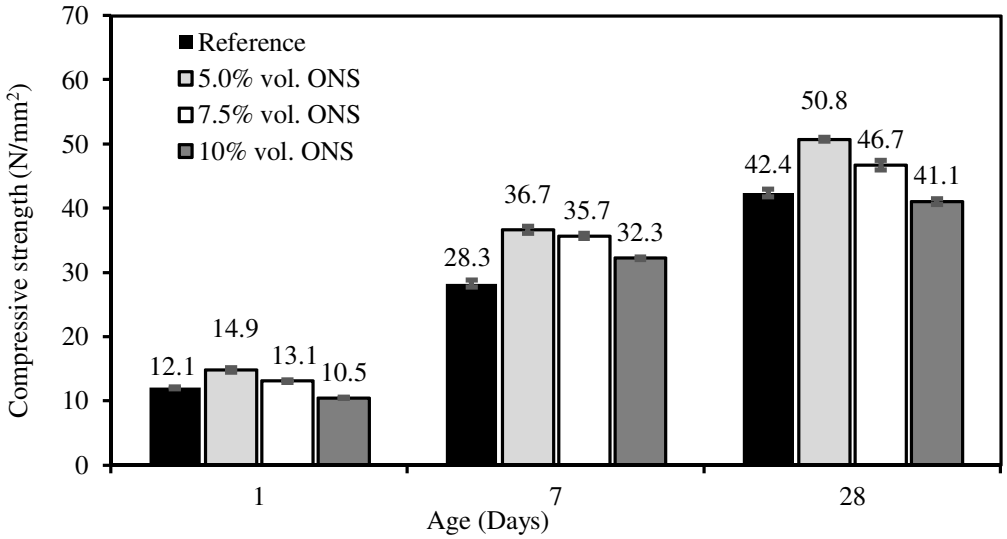

Figure 9.17. Compressive strength development of CVC at different replacement levels of cement with olivine nano-silica (ONS).

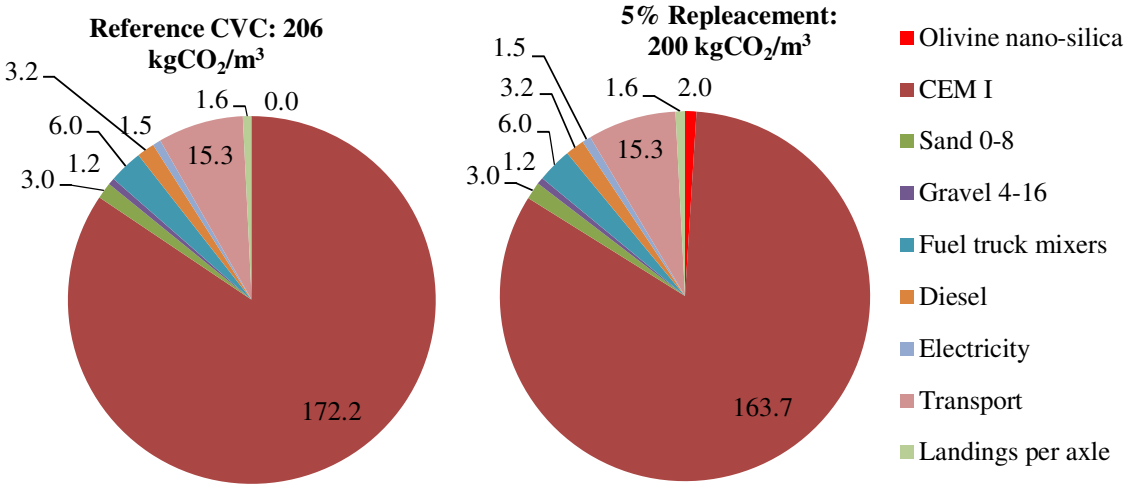

Figure 9.18. CO_2 footprint of CVC and of CVC with replacement of cement with ONS.

9.8 Conclusions

The results presented in this chapter can be summarized as follows:

1. The mother slurry changes its color between pH 3.1 and 3.4 due to the oxidation of iron. If that occurs, precipitation takes place, contaminating the silica.

2. The experiments performed in the pilot plants of Eurosupport and Hellas Gold show that the scale up can be performed straightforwardly, the most problematic point being the separation and purification of olivine nano-silica.
3. The estimated cost of raw materials is lower for olivine nano-silica than for precipitated silica using waterglass. In addition, the energy requirements and CO_2 emissions of olivine nano-silica are also much lower.
4. The volume of waste solution generated during the production of olivine nano-silica is around 11 times the initial volume of sulfuric acid. Further research is needed to reduce the waste volume during the washing and cleaning of the nano-silica, and to find a method to separate and reuse the different byproducts.
5. The compressive strength of the standard mortar is affected when cement is replaced with olivine nano-silica by 7% based on the weight of cement. Olivine nano-silica is a pozzolanic material with an activity index of 101%.
6. The optimal replacement of cement with olivine nano-silica in conventional vibrated concrete (CVC) is around 5%, resulting in an improvement in the compressive strength of 20%. The superplasticizer dosage is increased when cement is replaced with olivine nano-silica to maintain similar rheological properties. The CO_2 emissions are reduced by 3% for the CVC with 5% replacement compared to the reference concrete. Therefore, the use of the olivine nano-silica in CVC does not only improve its compressive strength but also reduces the CO_2 emissions.

Chapter 10. Conclusions and recommendations

10.1 Conclusions

Nanotechnology and nanomaterials have attracted great attention in the previous years as can be seen from the fact that the number of patents has increased by 600% from 1992 to 2002 [111] and the annual global turnover is estimated to increase up to € 1.5 trillion by 2015 [112]. Nano-silica is one of the compounds that is boosting the field of nanomaterials with an annual rise of 5.6% to reach a projected 2.8 million metric tons in 2016 [3]. Likewise, the market is estimated to grow by 7.5% to $6.4 billion [3].

Nowadays, the two most important commercial processes in the production of nano-silica are the thermal route (also known as flame hydrolysis) and the wet route (e.g., the neutralization of sodium silicate solutions). A high temperature process is involved in both production methods. The production of nano-silica by the dissolution of olivine is an interesting alternative to the existing commercial methods because of the good quality of the resulting silica and low energy requirements and CO_2 emissions.

The main objective of this research is to improve the technology of the olivine nano-silica production process to be able to tailor the properties of this nano-silica. A secondary objective is to optimize the olivine nano-silica process. In addition to these objectives, this research contributes to the understanding three topics: the dissolution of olivine at negative pH, the silica particle growth below the isoelectric point, and the development of the pore structure at negative pH.

In this thesis, three main topics of the olivine nano-silica process have been investigated: 1) the dissolution of olivine under the olivine nano-silica conditions; 2) the influence of the process conditions on the textural properties of olivine nano-silica; and 3) the technical aspects of the olivine nano-silica process. The conclusions concerning all these three parts are summarized in what follows.

10.1.1 Kinetic model of the dissolution of olivine in acid

A kinetic model for the dissolution of olivine is proposed based on the following assumptions: 1) the process is not controlled by the diffusion through a silica layer but by the surface reaction; 2) the olivine particles shrink over time as the shrinking particle model describes (Figure 4.1a); and 3) the specific surface area of olivine can be estimated using the roughness factor based on the Brantley equation. From the good correlation between the experimental data and the proposed model, it can be inferred that the assumptions made are reasonable. Thus, the dissolution of olivine at negative pH can be described by Eq. (4.19):

$$r = A \cdot \exp\left(\frac{-E_a}{R \cdot T}\right) \cdot a_{H^+}^{n} = 856 \cdot \exp\left(\frac{-78.5}{R \cdot T}\right) \cdot a_{H^+}^{0.5} ,$$

where r is the dissolution rate ($mol \cdot cm^{-2} \cdot s^{-1}$), A the pre-exponential factor ($mol \cdot cm^{-2} \cdot s^{-1}$), E_a the activation energy (kJ/mol), R the gas constant ($8.314 \cdot 10^{-3}$ $kJ \cdot mol^{-1} \cdot K^{-1}$), T the temperature (K), a_H^+ the hydrogen ion activity and n the reaction order.

The activation energy is slightly higher than that reported in most kinetics studies. The reaction order found here is the most common value reported in the literature. The dissolution rate and rate constant at pH of 2 and 25 °C are $1.5 \cdot 10^{-12}$ $mol \cdot cm^{-2} \cdot s^{-1}$ and $1.5 \cdot 10^{-11}$ $mol \cdot cm^{-2} \cdot s^{-1}$, respectively, which are comparable to the values found in the literature.

The average error between the reaction constants obtained from the fitting to the experimental data (k_{T_fit}) and from the estimation of Eq. (4.19) (k_{T_cal}) is 5%, which shows a good agreement between the present model and the olivine dissolution experiments for dunite CRS-US. The average error for dunite GL50 is slightly higher (7.6%). This kinetic model can be applied with good accuracy to predict the olivine dissolution under the nano-silica production conditions for other dunite materials than those used in this work, and for other reaction volumes.

10.1.2 Textural properties of olivine nano-silica

10.1.2.1 BET specific surface area

The process conditions (i.e., the impurity content, conversion degree, pressure of filtration and ripening treatment) of the olivine nano-silica production have a strong influence on the final SSA_{BET} of this material. Thus, modifying the process conditions, nano-silicas with different SSA_{BET} can be synthesized. The process conditions and the ripening treatment influence the properties of nano-silica in different ways:

1) The cleaner the nano-silica is, the higher its specific surface area is, reaching values between 300 and 400 m^2/g for olivine silicas with low content of salts or silica purities above 99%. The sulfate salts are located in the pores of the silica clusters, blocking them and drastically reducing the SSA_{MP}.
2) The higher the filtration pressure is, the higher the surface area will be. This is due to a reduction of the pore volume. However, if the applied pressure is too high, the pores of the material drastically collapse, reducing the SSA_{BET} drastically.
3) The smaller the conversion degree of the dissolution of olivine is, the higher the SSA_{BET} is. Silicas with surface areas above 500 m^2/g were produced at slow kinetics (50 °C) and conversions of 38% (see sample NS-50-S3).

4) The ripening process diminishes the specific surface area of nano-silica by 75%. In addition, this treatment removes the microporous surface area of the samples almost completely.

The SSA_{BET} of olivine silica can be tailored to meet the requirements of different possible applications. This tailoring can be done by changing the filtration pressure, controlling the conversion degree and/or performing ripening treatments after the production process has been completed. Thus, the typical SSA_{BET} for a clean nano-silica (~350 m^2/g) can be modified in the range 90 to 500 m^2/g.

10.1.2.2 Particle size

The particle size of olivine silica grows up to 420 nm after 4300 minutes (~72 h) of reaction at 20 °C in 2M H_2SO_4 solution. The particles will grow much faster under the synthesis conditions employed in this study for the olivine nano-silica process (i.e., 50-90 °C and 3M H_2SO_4). At these conditions olivine dissolves only in several hours (4 to 8 h). The particle growth shows a trend similar to the one found within Gorrepati's experiments using waterglass, which could mean that the mechanism of the particle growth of olivine silica is due to the nucleation of primary particles and subsequent aggregation of these primary particles.

At the production conditions of olivine nano-silica, this material does not exhibit gelling behaviour. This phenomenon could be due to three reasons: 1) silica polymerizes fast at 90 °C and in 3M H_2SO_4 solution, forming large particles above 100 nm in a short time; 2) the concentration of small silica colloids (i.e., below 100 nm) is low; and 3) the vigorous mixing in the reactor.

The combination of the high shear mixing and ripening treatment of olivine nano-silica is successful in tailoring the SSA; however, this treatment is not able to break the agglomerates into nano-particles. In fact, the agglomerates are likely to be even stronger since soluble particles condense on the junctions between particles, strengthening their union. On the other hand, the ultrasonic treatment can break apart the agglomerates, producing particles as small as 30 nm. Even though the deagglomeration process still has to be optimized, it is clear that the olivine nano-silica clusters can be deagglomerated using mechanical techniques. Therefore, these techniques make possible the preparation of stable colloidal dispersions using olivine nano-silica.

10.1.2.3 Pore size

Olivine nano-silica features a SSA_{BET} in the range of 100 to 500 m^2/g, with an average value of 350 m^2/g for silicas with high purity, conversion degree above 90% and filtered under vacuum. The BJH pore size distribution is in the range of 2 to 100 nm. The silanol number is in the range of 13 to 22 OH/nm^2 for olivine nano-silicas dried at 120 °C and 11

to 13 OH/nm^2 for silicas dried at 190 °C. These high silanol values are due to the presence of internal and ultramicropore silanols. The positron annihilation lifetime spectroscopy analysis found two types of pores, one at around 6 Å (pore 1) and another one at around 25 Å (pore 2). Pore 1 was in the ultramicropore range, whereas pore 2 was in the low mesopore range. Pore 1 can be considered to be intrinsic to the amorphous matrix of olivine nano-silica, and pore 2 can be due to the voids between the primary particles. Therefore, olivine nano-silica is considered as microporous, mesoporous and macroporous.

The pore size distribution of olivine silica can be tailored to meet the requirements of different possible applications. This tailoring can be done by changing the filtration pressure, controlling the conversion degree and/or performing ripening treatments after the production process has been completed. Thus, the initial PoSD (2-100 nm) can be modified to a distribution of 9 to 30 nm.

The development of the nano-silica structure during the olivine process could be summarized with the following steps (see Figure 8.27): 1) initially, soluble silica nucleates and primary particles of around 2 nm are formed; 2) the silica particles grow via a condensation route, forming linear chains; 3) as the growth continues, the silica particles keep increasing in size, resulting in 3D networks; and 4) with time, the aggregates become bigger and more compact. The final result of the olivine process is agglomerates as big as 20 µm. In addition, internal pores (also called closed porosity) are developed with the conversion degree as the result of condensation of two blocks of silica particles.

In comparison with precipitated silica (Sipernat 310 and 50S), olivine nano-silica is characterized by: 1) a lower SSA_{BET} than Sipernat 310; 2) V_{P_D} (pore volume from the desorption branch of the BJH pore size distribution) is considerably lower, which means that precipitated silicas have a higher content of mesopores and macropores; 3) the V_{MP} (micropore volume) is much higher, which results in higher micropore surface areas; 4) the silanol content is higher; and 5) the SSA_{NMR} follows the order: Sipernat 310 > olivine nano-silica > Sipernat 50S, with an average value for olivine nano-silica of 780 m^2/g. On the other hand, pyrogenic silicas feature similar SSA_{BET} and V_{P_D}, but lower V_{MP} than olivine nano-silicas. In addition, all three types of silica form 3D network structures.

10.1.3 Technical aspects

The technical aspects of the olivine nano-silica process can be summarized as follows:

1. The separation efficiency (E_{sep}) increases with the specific surface area of nano-silica and aging time. Process yields in the range of 66% to 83% were obtained for nano-silicas produced in the laboratory. An average process yield of 83% was obtained for nano-silicas produced in the pilot plant of Eurosupport [172].

2. The mother slurry (slurry obtained after the reaction of olivine with acid and with 50% water dilution) changes its color between pH 3.1 and 3.4 due to the oxidation of iron. If that occurs, precipitation takes place, contaminating the silica.
3. The experiments performed in the pilot plants of Eurosupport [172] and Hellas Gold [173] show that the scale up can be performed straightforwardly, being the most problematic point the separation and purification of olivine nano-silica.
4. The estimated cost of raw materials is lower for olivine nano-silica than for precipitated silica. In addition, the energy requirements and CO_2 emissions of olivine nano-silica are also much lower.
5. The volume of waste solution generated during the production of olivine nano-silica in the laboratory experiments was around 11 times the initial volume of sulfuric acid.
6. Olivine nano-silica is a pozzolanic material with an activity index of 101%.
7. The optimal replacement of cement with olivine nano-silica in conventional vibrated concrete (CVC) is around 5%, resulting in an improvement in the compressive strength of 20%. The superplasticizer dosage is increased when cement is replaced with olivine nano-silica to maintain similar rheological properties. The CO_2 emissions are reduced by 3% for the CVC with 5% replacement compared to the reference concrete. Therefore, the use of the olivine nano-silica in CVC does not only improve its compressive strength but also reduces the CO_2 emissions.

10.2 Recommendations for future research

This thesis studies the production process of olivine nano-silica in order to be able to tailor the properties of olivine nano-silica and to optimize the production process. The main recommendations for future investigations that have emerged during this study are summarized as follows:

1. Although the pore size distributions (PoSD) have been determined using the BJH method and the positron annihilation lifetime spectroscopy technique, it still would be convenient to determine the PoSD using gas physisorption at low relative pressures. With this analysis, density functional theories (DFT) models can be used; DFT models are particularly useful to estimate the pore size distribution in the range 0.5 to 10 nm.
2. A more extensive research about the particle growth of olivine nano-silica should be performed. The main aspects that should be further investigated are:
    a. The influence of the hydrogen ion concentration and olivine surface area on the rate of particle growth of olivine nano-silica.
    b. The growth of silica nanoparticles using waterglass (instead of olivine). The waterglass should be fed into the reactor at the same rate that the silica would be released from the olivine into the medium. This approach has two main advantages regarding the particle growth of silica using olivine:

1) olivine grains are not in the medium; and 2) the mechanism of the particle growth at similar conditions to the olivine nano-silica process can be studied.

3. A study of the viscosity of the slurry during the olivine dissolution is recommended to understand if and when an increase of the viscosity takes place. This study could clarify whether the increase of the viscosity depends on the concentration of silica in the medium or both the concentration of silica and pH.
4. The use of mechanical treatments (i.e., ultrasonic devices and colloidal mills) should be explored. The different aspects that can be studied employing these devices are:
    a. the possibility of breaking the agglomerates into nanoparticles;
    b. the preparations of stable colloidal dispersions;
    c. the influence of the combination of mechanical treatment and Ostwald ripening on the textural properties of olivine nano-silica.
5. A reduction and recycling method for the waste solution of the olivine nano-silica process should be investigated.

In addition to these recommendations, which are closely related to the research performed in the present study, the following other investigations are suggested: 1) the use of olivine nano-silica in different applications such as rubber, catalysis, etc.; and 2) the functionalization of the surface chemistry of this type of nano-silica.

Bibliography

[1] ECETOC, Synthetic Amorphous Silica (CAS No. 7631-86-9), Joint Assessment of Commodity Chemicals (JACC) report No. 51, Brussels, 2006.

[2] European Commission, Reference document on best available techniques for the manufacture of large volume inorganic chemicals - solids and others industry, 2007.

[3] Freedonia, World specialty silicas, 2012.

[4] R.K. Iler, The chemistry of silica: solubility, polymerization, colloid and surface properties, and biochemistry, John Wiley and Sons, 1979.

[5] O.W. Flörke, H.A. Graetsch, F. Brunk, L. Benda, S. Paschen, H.E. Bergna, W.O. Roberts, W.A. Welsh, C. Libanati, M. Ettlinger, D. Kerner, M. Maier, W. Meon, R. Schmoll, H. Gies, and D. Shiffmann, Silica. Ullmann's Encyclopedia of Industrial Chemistry, Wiley Online Library, 2008.

[6] H.E. Bergna and W.O. Roberts, Colloidal silica: fundamentals and applications, CRC, 2006.

[7] A.M. Neville, Properties of concrete, Pearson Education Limited, 1995.

[8] R. Siddique and M.I. Khan, Supplementary cementing materials, Springer, 2011.

[9] O.S. Pokrovsky and J. Schott, Kinetics and mechanism of forsterite dissolution at 25 °C and pH from 1 to 12, Geochim. Cosmochim. Acta 64 (2000) 3313-3325.

[10] J.J. Rosso and J.D. Rimstidt, A high resolution study of forsterite dissolution rates, Geochim. Cosmochim. Acta 64 (2000) 797-811.

[11] E.H. Oelkers, An experimental study of forsterite dissolution rates as a function of temperature and aqueous Mg and Si concentrations, Chem. Geol. 175 (2001) 485-494.

[12] R.C.L. Jonckbloedt, The dissolution of olivine in acid, a cost effective process for the elimination of waste acids. PhD Thesis, Utrecht University, 1997.

[13] R.H. Perry and D.W. Green, Perry's chemical engineers' handbook, McGraw-Hill, 2008.

[14] R.A. Robie, B.S. Hemingway, and H. Takei, Heat capacities and entropies of Mg2SiO4, Mn2SiO4, and Co2SiO4 between 5 and 380 K, American Mineralogist 67 (1982) 470-482.

[15] R.D. Schuiling, A method for neutralizing waste sulphuric acid by adding a silicate [US 1987/4707348] 1986.

[16] S. Olerud, Method for manufacturing spherical silica from olivine [US 1998/5780005] 1998.

[17] G. Gunnarsson, O. Wallevik, L.Ø. Ekornød, and P.B. Engseth, Process for production of precipitated silica from olivine [US 2012/8114371] 2012.

[18] D.E. Grandstaff, The dissolution rate of forsteritic olivine from Hawaiian beach sand, in: S.M. Colman and D.P. Dethier (Eds.), Rates of chemical weathering of rocks and minerals, Academic press, inc., Orlando, 1986, pp. 41-59.

[19] M. Hänchen, V. Prigiobbe, G. Storti, T.M. Seward, and M. Mazzotti, Dissolution kinetics of fosteritic olivine at 90–150 °C including effects of the presence of CO_2, Geochim. Cosmochim. Acta 70 (2006) 4403-4416.

[20] A.A. Olsen and J. Donald Rimstidt, Oxalate-promoted forsterite dissolution at low pH, Geochim. Cosmochim. Acta 72 (2008) 1758-1766.

[21] R.A. Wogelius and J.V. Walther, Olivine dissolution kinetics at near-surface conditions, Chem. Geol. 97 (1992) 101-112.

[22] A. Awad, A.F. Koster van Groos, and S. Guggenheim, Forsteritic olivine: effect of crystallographic direction on dissolution kinetics, Geochim. Cosmochim. Acta 64 (2000) 1765-1772.

[23] A. Blum and A. Lasaga, Role of surface speciation in the low-temperature dissolution of minerals, Nature 331 (1988) 431-433.

[24] Y. Chen and S.L. Brantley, Dissolution of forsteritic olivine at 65°C and 2<pH<5, Chem. Geol. 165 (2000) 267-281.

[25] R.C.L. Jonckbloedt, Olivine dissolution in sulphuric acid at elevated temperatures-implications for the olivine process, an alternative waste acid neutralizing process, J. Geochem. Explor 62 (1998) 337-346.

[26] C. Okkerse, Submicroporous and macroporous silica. PhD Thesis, Hoogland en Waltman, 1961.

[27] B.A. Fleming, Kinetics of reaction between silicic acid and amorphous silica surfaces in NaCl solutions, Journal of Colloid and Interface Science 110 (1986) 40-64.

[28] L.W. Kelts, N.J. Effinger, and S.M. Melpolder, Sol-gel chemistry studied by ^{1}H and ^{29}Si nuclear magnetic resonance, Journal of Non-Crystalline Solids 83 (1986) 353-374.

[29] M.K. Titulaer, M.J. den Exter, H. Talsma, J.B.H. Jansen, and J.W. Geus, Control of the porous structure of silica gel by the preparation pH and drying, Journal of Non-Crystalline Solids 170 (1994) 113-127.

[30] D.J. Lieftink, The preparation and characterization of silica from acid treatment of olivine. PhD Thesis, Utrecht University, 1997.

[31] C. Okkerse, Porous silica, in: B.G. Linsen (Eds.), Physical and chemical aspects of adsorbents and catalysts, Academic Press, 1970, pp. 213-264.

[32] D.J. Lieftink and J.W. Geus, The preparation of silica from the olivine process and its possible use as a catalyst support, Journal of Geochemical Exploration 62 (1998) 347-350.

[33] A. Meidani, ProMine internal report: Dunite samples characterization - Gerakini mine, 2010.

[34] Glycerine Producers' Association, Physical Properties of Glycerine and Its Solutions, Glycerine Producers' Association, 1963.

[35] A.N. op de Hoek, Master Thesis: Experiments on the behaviour of dense-phase neutrally bouyante particle-liquid suspensions. PhD Thesis, University of Twente, 2011.

[36] M. Cyr and A. Tagnit-Hamou, Particle size distribution of fine powders by LASER diffraction spectrometry. Case of cementitious materials, Mater. Struct. 34 (2001) 342-350.

[37] Malvern Instruments, Mastersizer 2000 User Manual, 2004.

[38] International Organization for Standardization, ISO 13320:2009. Particle size analysis - Laser diffraction methods, 2009.

[39] Malvern Instruments, Zetasizer Nano User Manual MAN0317, 2009.

[40] International Organization for Standardization, ISO 13321: Particle size analysis - Photon correlation spectroscopy, 1996.

[41] A.D. McNaught and A. Wilkinson, IUPAC Compendium of chemical terminology: the Gold Book, Blackwell Science Oxford, 1997.

[42] A.V. Delgado, F. González-Caballero, R.J. Hunter, L.K. Koopal, and J. Lyklema, Measurement and interpretation of electrokinetic phenomena (IUPAC technical report), International Union of Pure and Applied Chemistry, 2005.

[43] K.S.W. Sing, D.H. Everett, R.A. Haul, L. Moscous, R.A. Pierotti, J. Rouquerol, and T. Siemieniewska, Reporting physisorption data for gas/solid systems with special reference to the determination of surface area and porosity, Pure Appl. Chem. (1985) 603-619.

[44] S. Lowell, J.E. Shields, M.A. Thomas, and M. Thommes, Characterization of porous solids and powders: surface area, pore size and density, Springer, 2006.

[45] Micromeritics, Tristar II 3020 - Operator's manual V1.03., 2009.

[46] S. Brunauer, P.H. Emmett, and E. Teller, Adsorption of Gases in Multimolecular Layers, J. Am. Chem. Soc. (1938) 309-319.

[47] S. Brunauer, Further discussion of micropore analysis, J. Colloid Interface Sci. 41 (1972) 612-614.

[48] M.C. Duke, S.J. Pas, A.J. Hill, Y.S. Lin, and J.C.D. da Costa, Exposing the molecular sieving architecture of amorphous silica using positron annihilation spectroscopy, Adv. Funct. Mater. 18 (2008) 3818-3826.

[49] ISO 9277:2010, Determination of the specific surface area of solids by gas adsorption - BET method, 2010.

[50] B.C. Lippens and J.H. de Boer, Studies on pore systems in catalysts: V. The t method, J. Catal. 4 (1965) 319-323.

[51] J.H. de Boer, B.C. Lippens, B.G. Linsen, J.C.P. Broekhoff, A. van den Heuvel, and T. Osinga, Thet-curve of multimolecular N2-adsorption, J. Colloid Interface Sci. 21 (1966) 405-414.

[52] W.H. Harkins and G. Jura, Surfaces of Solids. XIII. A Vapor Adsorption Method for the Determination of the Area of a Solid without the Assumption of a Molecular Area, and the Areas Occupied by Nitrogen and Other Molecules on the Surface of a Solid, J. Am. Chem. Soc. (1944) 1366-1373.

[53] E.P. Barrett, L.G. Joyner, and P.P. Halenda, The Determination of Pore Volume and Area Distributions in Porous Substances. I. Computations from Nitrogen Isotherms, J. Am. Chem. Soc. (1951) 373-380.

[54] W. Thomson, On the equilibrium of vapour at a curved surface of liquid, The London, Edinburgh, and Dublin Philosophical Magazine and Journal of Science 42 (1871) 448-452.

[55] J.C. Groen, L.A.A. Peffer, and J. Perez-Ramirez, Pore size determination in modified micro- and mesoporous materials. Pitfalls and limitations in gas adsorption data analysis, Microporous Mesoporous Mater. 60 (2003) 1-17.

[56] A.V. Neimark, P.I. Ravikovitch, M. Grün, F. Schüth, and K.K. Unger, Pore size analysis of MCM-41 type adsorbents by means of nitrogen and argon adsorption, J. Colloid Interface Sci. 207 (1998) 159-169.

[57] S.J. Tao, Positronium annihilation in molecular substances, The Journal of Chemical Physics 56 (1972) 5499.

[58] M. Eldrup, D. Lightbody, and J.N. Sherwood, The temperature dependence of positron lifetimes in solid pivalic acid, Chem. Phys. 63 (1981) 51-58.

[59] K. Sato, K. Fujimoto, M. Nakata, and T. Hatta, Diffusion-Reaction of Water Molecules in Angstrom Pores as Basic Mechanism of Biogenic Quartz Formation, The Journal of Physical Chemistry C 115 (2011) 18131-18135.

[60] D.W. Gidley, H. Peng, R. Vallery, C.L. Soles, H. Lee, B.D. Vogt, E.K. Lin, W. Wu, and M.R. Baklanov, Porosity of Low Dielectric Constant Materials, Dielectric Films for Advanced Microelectronics (2007) 85-136.

[61] K. Ito, H. Nakanishi, and Y. Ujihira, Extension of the equation for the annihilation lifetime of ortho-positronium at a cavity larger than 1 nm in radius, The Journal of Physical Chemistry B 103 (1999) 4555-4558.

[62] E. Kondoh, M.R. Baklanov, E. Lin, D. Gidley, and A. Nakashima, Comparative Study of Pore Size of Low-Dielectric-Constant Porous Spin-on-Glass Films Using Different Methods of Non-destructive Instrumentation, Jpn. J. Appl. Phys. , Part 2 40 (2001) L323-L326.

[63] T.L. Dull, W.E. Frieze, D.W. Gidley, J.N. Sun, and A.F. Yee, Determination of pore size in mesoporous thin films from the annihilation lifetime of positronium, The Journal of Physical Chemistry B 105 (2001) 4657-4662.

[64] J.N. Sun, Y.F. Hu, W.E. Frieze, and D.W. Gidley, Characterizing porosity in nanoporous thin films using positronium annihilation lifetime spectroscopy, Radiat. Phys. Chem. 68 (2003) 345-349.

[65] G. Engelhardt and D. Michel, High-resolution solid-state NMR of silicates and zeolites, John Wiley and Sons, 1987.

[66] A.R. Grimmer and R. Radeglia, Correlation between the isotropic ^{29}Si chemical shifts and the mean silicon-oxygen bond lengths in silicates, Chem. Phys. Lett. 106 (1984) 262-265.

[67] S. Leonardelli, L. Facchini, C. Fretigny, P. Tougne, and A.P. Legrand, Silicon-29 NMR study of silica, J. Am. Chem. Soc. 114 (1992) 6412-6418.

[68] S.L. Brantley and N.P. Mellott, Surface area and porosity of primary silicate minerals, Am. Mineral. 85 (2000) 1767-1783.

[69] C. Anbeek, Surface roughness of minerals and implications for dissolution studies, Geochim. Cosmochim. Acta 56 (1992) 1461-1469.

[70] A.F. White and M.L. Peterson, Role of reactive-surface-area characterization in geochemical kinetic models, in: D.C. Melchoir and R.L. Bassett (Eds.), Chemical Modeling of Aqueous Systems II, ACS Publications, 1990, pp. 461-475.

[71] A.F. White, Chemical weathering rates of silicate minerals in soils, Rev. Mineral. Geochem 31 (1995) 407-461.

[72] D.E. Grandstaff, Changes in surface area and morphology and the mechanism of forsterite dissolution, Geochim. Cosmochim. Acta 42 (1978) 1899-1901.

[73] J. Van Herk, H.S. Pietersen, and R.D. Schuiling, Neutralization of industrial waste acids with olivine — The dissolution of forsteritic olivine at 40–70°C, Chem. Geol. 76 (1989) 341-352.

[74] T.A. Haug, R.A. Kleiv, and I.A. Munz, Investigating dissolution of mechanically activated olivine for carbonation purposes, Appl. Geochem. 25 (2010) 1547-1563.

[75] P.A. Webb and C. Orr, Analytical methods in fine particle technology, Norcross, GA: Micromeritics, 1997.

[76] R. Osland, Modelling of variation is Norwegian olivine deposits (Causes of variation and estimation of key quality factors). PhD Thesis, Norwegian University of Science and Technology, 1997.

[77] H.S. Yoder and T.G. Sahama, Olivine X-ray determinative curve, Amer. Min 42 (1957) 475-491.

[78] R.A. Kleiv and M. Thornhill, Dry magnetic separation of olivine sand, Physicochem. Probl. Miner. Process 47 (2011) 213-228.

[79] W.A. Deer, R.A. Howie, and J. Zussman, Rock-forming minerals. 2B. Double-chain silicates, Geological Society, 1997.

[80] W. Vedder and R.W.T. Wilkins, Dehydroxylation and rehydroxylation, oxidation and reduction of micas, Am. Mineral. 54 (1969) 482-509.

[81] C. Viti, Serpentine minerals discrimination by thermal analysis, Am. Mineral. 95 (2010) 631-638.

[82] H.J. Hurst, The thermal decomposition of magnesite in nitrogen, Thermochim. Acta 189 (1991) 91-96.

[83] M. Wesolowski, Thermal decomposition of talc: a review, Thermochim. Acta 78 (1984) 395-421.

[84] F. Villieras, J. Yvon, J.M. Cases, P. De Donato, F. Lhote, and R. Baeza, Development of microporosity in clinochlore upon heating, Clays Clay Miner. 42 (1994) 679-688.

[85] E. Nickel, Experimental dissolution of light and heavy minerals in comparison with weathering and intrastratal solution, Contributions to Sedimentology 1 (1973) 1-68.

[86] F.C. Lin and C.V. Clemency, The dissolution kinetics of brucite, antigorite, talc, and phlogopite at room temperature and pressure, Am. Mineral. 66 (1981) 801-806.

[87] R.C. Bales and J.J. Morgan, Dissolution kinetics of chrysotile at pH 7 to 10, Geochim. Cosmochim. Acta 49 (1985) 2281-2288.

[88] H.M. May, D.G. Klnniburgh, P.A. Helmke, and M.L. Jackson, Aqueous dissolution, solubilities and thermodynamic stabilities of common aluminosilicate clay minerals: Kaolinite and smectites, Geochim. Cosmochim. Acta 50 (1986) 1667-1677.

[89] G.G. Ferruzzi, The character and rates of dissolution of pyroxenes and pyroxenoids (MS Thesis), University of California, 1993.

[90] J. Drever, The Geochemistry of Natural Waters, Prentice-Hall, 1988.

[91] J.D. Rimstidt, S.L. Brantley, and A.A. Olsen, Systematic review of forsterite dissolution rate data, Geochim. Cosmochim. Acta 99 (2012) 159-178.

[92] G.B. Alexander, W.M. Heston, and R.K. Iler, The solubility of amorphous silica in water, The Journal of Physical Chemistry 58 (1954) 453-455.

[93] E.A. Gorrepati, P. Wongthahan, S. Raha, and H.S. Fogler, Silica Precipitation in Acidic Solutions: Mechanism, pH Effect, and Salt Effect, Langmuir 26 (2010) 10467-10474.

[94] O. Levenspiel, Chemical reaction engineering, John Wiley & Sons, 1999.

[95] K.C. Liddell, Shrinking core models in hydrometallurgy: What students are not being told about the pseudo-steady approximation, Hydrometallurgy 79 (2005) 62-68.

[96] V. Safari, G. Arzpeyma, F. Rashchi, and N. Mostoufi, A shrinking particle - shrinking core model for leaching of a zinc ore containing silica, Int. J. Miner. Process. 93 (2009) 79-83.

[97] A.H.A. Park and L.S. Fan, mineral sequestration: physically activated dissolution of serpentine and pH swing process, Chem. Eng. Sci. 59 (2004) 5241-5247.

[98] J. Schott and R.A. Berner, X-ray photoelectron studies of the mechanism of iron silicate dissolution during weathering, Geochim. Cosmochim. Acta 47 (1983) 2233-2240.

[99] O.S. Pokrovsky and J. Schott, Forsterite surface composition in aqueous solutions: a combined potentiometric, electrokinetic, and spectroscopic approach, Geochim. Cosmochim. Acta 64 (2000) 3299-3312.

[100] H. Bearat, M.J. McKelvy, A.V.G. Chizmeshya, D. Gormley, R. Nunez, R.W. Carpenter, K. Squires, and G.H. Wolf, Carbon Sequestration via Aqueous Olivine Mineral Carbonation: Role of Passivating Layer Formation, Environ. Sci. Technol. 40 (2006) 4802-4808.

[101] D.E. Giammar, J. Bruant, and C.A. Peters, Forsterite dissolution and magnesite precipitation at conditions relevant for deep saline aquifer storage and sequestration of carbon dioxide, Chem. Geol. 217 (2005) 257-276.

[102] D. Daval, O. Sissmann, N. Menguy, G.D. Saldi, F. Guyot, I. Martinez, J. Corvisier, B. Garcia, I. Machouk, K.G. Knauss, and R. Hellmann, Influence of amorphous silica layer formation on the dissolution rate of olivine at 90 °C and elevated pCO_2, Chem. Geol. 284 (2011) 193-209.

[103] E.L. Paul, V. Atiemo-Obeng, and S.M. Kresta, Handbook of industrial mixing: science and practice, Wiley. com, 2004.

[104] D.M. Levins and J.R. Glastonbury, Particle-liquid hydrodynamics and mass transfer in a stirred vessel. Part II:mass transfer, t. i. chem. eng-lond 50 (1972) 132-146.

[105] D.R. Lide, CRC Handbook of Chemistry and Physics, CRC Press/Taylor and Francis, Boca Raton, FL, 2009.

[106] D.L. Parkhurst and C.A.J. Appelo, User's guide to PHREEQC (Version 2): A computer program for speciation, batch-reaction, one-dimensional transport, and inverse geochemical calculations, US Geological Survey Denver, 1999.

[107] B.A. Fleming, Kinetics of reaction between silicic acid and amorphous silica surfaces in NaCl solutions, Journal of Colloid and Interface Science 110 (1986) 40-64.

[108] H. Tagawa, Thermal decomposition temperatures of metal sulfates, Thermochim. Acta 80 (1984) 23-33.

[109] M.J. Neil, P.E. Heckelman, C.B. Koch, and K.J. Roman, The Merck Index, Merck Whitehouse Station, 2006.

[110] S.J. Gregg and K.S.W. Sing, Adsorption, Surface Area and Porosity, 1991.

[111] M.J. Pitkethly, Nanomaterials - the driving force, Mater. Today 7 (2004) 20-29.

[112] Cientifica, Half Way to Trillion Dollar Market? A critical Review of the Diffusion of Nanotechnologies, 2007.

[113] G. Cao, Nanostructures & nanomaterials: synthesis, properties & applications, Imperial College Pr, 2004.

[114] J.B. Madeline, M. Meireles, C. Bourgerette, R. Botet, R. Schweins, and B. Cabane, Restructuring of colloidal cakes during dewatering, Langmuir 23 (2007) 1645-1658.

[115] M. Mindick and P.H. Vossos, Large particle silica sols and method of production [US3538015] 1970.

[116] D.L. MacDonald, Method of producing silica sols with controllable broad size distribution and minimum particle size [US2009/0018219A1] 2009.

[117] E.C. Angcoy Jr, An experiment on monomeric and polymeric silica precipitation rates from supersaturated solutions, United Nations University, 2006.

[118] T.W. Zerda, I. Artaki, and J. Jonas, Study of polymerization processes in acid and base catalyzed silica sol-gels, Journal of non-crystalline solids 81 (1986) 365-379.

[119] A. Karami, Study on modification of colloidal silica surface with magnesium ions, Journal of Colloid and Interface Science 331 (2009) 379-383.

[120] S.H. Chan, A review on solubility and polymerization of silica, Geothermics 18 (1989) 49-56.

[121] O. Weres, A. Yee, and L. Tsao, Kinetics of silica polymerization, Journal of Colloid and Interface Science 84 (1981) 379-402.

[122] G.A. Icopini, S.L. Brantley, and P.J. Heaney, Kinetics of silica oligomerization and nanocolloid formation as a function of pH and ionic strength at 25 C, Geochimica et Cosmochimica Acta 69 (2005) 293-303.

[123] R.J. Hunter, Foundations of colloid science (POD), Oxford university press, 2000.

[124] B.V. Derjaguin, Theory of the stability of strongly charged lyophobic sols and the adhesion of strongly charged particles in solutions of electrolytes, Acta Physicochim. USSR 14 (1941) 633-662.

[125] E.J.W. Verwey and J.T.G. Overbeek, Theory of the stability of lyophobic colloids, Courier Dover Publications, 1999.

[126] R.G. Larson, The structure and rheology of complex fluids, Oxford university press New York, 1999.

[127] M. Larsson, A. Hill, and J. Duffy, Suspension Stability; Why Particle Size, Zeta Potential and Rheology are Important, Annual transactions of the nordic rheology society 20 (2012) 209-214.

[128] G.A. Parks, The isoelectric points of solid oxides, solid hydroxides, and aqueous hydroxo complex systems, Chemical Reviews 65 (1965) 177-198.

[129] G.V. Franks, Zeta potentials and yield stresses of silica suspensions in concentrated monovalent electrolytes: isoelectric point shift and additional attraction, Journal of Colloid and Interface Science 249 (2002) 44-51.

[130] K. Goto, States of silica in aqueous solution. I. Polymerization and depolymerization, J. Chern. Soc. Japan 76 (1955) 1364-1366.

[131] E.A. Gorrepati, Silica Precipitation from Analcime Dissolution. PhD Thesis, University of Michigan, 2009.

[132] ASTM, Standard Test Method for Silica in Water - D859-10, 2010.

[133] E.W. Rice, R.B. Baird, A.D. Eaton, and L.S. Clesceri, Standard methods for the examination of water and wastewater, American Public Health Association, 2012.

[134] A.R. Marsh III, G. Klein, and T. Vermeulen, Polymerization kinetics and equilibria of silicic acid in aqueous systems. PhD Thesis, California Univ., Davis (USA). Dept. of Engineering, 1975.

[135] A.C. Makrides, M. Turner, and J. Slaughter, Condensation of silica from supersaturated silicic acid solutions, Journal of Colloid and Interface Science 73 (1980) 345-367.

[136] K. Goto, Effect of pH on polymerization of silicic acid, The Journal of Physical Chemistry 60 (1956) 1007-1008.

[137] A.G. Walton, Nucleation of crystals from solution, Science 148 (1965) 601-607.

[138] I. Shapiro and I.M. Kolthoff, Studies on aging of precipitates and coprecipitation. XLIII. Thermal aging of precipitated silica (silica gel), Journal of the American Chemical Society 72 (1950) 776-782.

[139] J.R. Baylis, S.T. Powell, and A.P. Black, Silicates as aids to coagulation, Journal American Water Works Association 29 (1937) 1355-1396.

[140] M. Donald, Silica aquasols and powders [US 1971/3591518] 1971.

[141] C. Okkerse, J.H. de Beor, and M. Cyrot, La Texture de La Silice En Tant Que Resultat de SA Formation par Effet Catalytique, J. chim. phys 57 (1960) 534.

[142] B. Himmel, T. Gerber, and H. Bürger, WAXS-and SAXS-investigations of structure formation in alcoholic SiO_2 solutions, Journal of non-crystalline solids 119 (1990) 1-13.

[143] F. Ordway, Condensation Model Producing Crystalline or Amorphous Tetrahedral Networks, Science 143 (1964) 800-801.

[144] L.H. Allen and E. Matijevíc, Stability of colloidal silica: I. Effect of simple electrolytes, Journal of Colloid and Interface Science 31 (1969) 287-296.

[145] J. Depasse and A. Watillon, The stability of amorphous colloidal silica, Journal of Colloid and Interface Science 33 (1970) 430-438.

[146] P.G. Hartley, I. Larson, and P.J. Scales, Electrokinetic and direct force measurements between silica and mica surfaces in dilute electrolyte solutions, Langmuir 13 (1997) 2207-2214.

[147] M. Colic, M.L. Fisher, and G.V. Franks, Influence of ion size on short-range repulsive forces between silica surfaces, Langmuir 14 (1998) 6107-6112.

[148] M. Kobayashi, F. Juillerat, P. Galletto, P. Bowen, and M. Borkovec, Aggregation and charging of colloidal silica particles: effect of particle size, Langmuir 21 (2005) 5761-5769.

[149] A.C.J. Johnson, P. Greenwood, M. Hagström, Z. Abbas, and S. Wall, Aggregation of nanosized colloidal silica in the presence of various alkali cations investigated by the electrospray technique, Langmuir 24 (2008) 12798-12806.

[150] A. Amiri, G. Oye, and J. Sjöblom, Influence of pH, high salinity and particle concentration on stability and rheological properties of aqueous suspensions of fumed silica, Colloids and Surfaces A: Physicochemical and Engineering Aspects 349 (2009) 43-54.

[151] D.E. Yates and T.W. Healy, The structure of the silica/electrolyte interface, Journal of Colloid and Interface Science 55 (1976) 9-19.

[152] G. Vigil, Z. Xu, S. Steinberg, and J. Israelachvili, Interactions of silica surfaces, Journal of Colloid and Interface Science 165 (1994) 367-385.

[153] R.K. Iler and R.L. Dalton, Degree of hydration of particles of colloidal silica in aqueous solution, The Journal of Physical Chemistry 60 (1956) 955-957.

[154] D.W. Lambert, P.H. Greenwood, and M.C. Reed, Advances in gelled-electrolyte technology for valve-regulated lead-acid batteries, Journal of power sources 107 (2002) 173-179.

[155] P.C. Yates, Kinetics of gel formation of colloidal silica sols, Abstracs of papers of the american chemical society,1990., American Chemical Society

[156] R.G. Avery and J.D.F. Ramsay, The sorption of nitrogen in porous compacts of silica and zirconia powders, Journal of Colloid and Interface Science 42 (1973) 597-606.

[157] S.J. Gregg and J.F. Langford, Study of the effect of compaction on the surface area and porosity of six powders by measurement of nitrogen sorption isotherms, J. Chem. Soc. , Faraday Trans. 1 73 (1977) 747-759.

[158] C.J. Plank and L.C. Drake, Differences between silica and silica-alumina gels I. Factors affecting the porous structure of these gels, Journal of Colloid Science 2 (1947) 399-412.

[159] K.S.W. Sing and J.D. Madeley, The surface properties of silica gels. I. Importance of pH in the preparation from sodium silicate and sulphuric acid, Journal of Applied Chemistry 3 (1953) 549-556.

[160] M.M. Dubinin and L.V. Radushkevich, Equation of the characteristic curve of activated charcoal, Chem. Zentr 1 (1947) 875.

[161] A. Saito and H.C. Foley, Curvature and parametric sensitivity in models for adsorption in micropores, AlChE J. 37 (1991) 429-436.

[162] L.T. Zhuravlev, The surface chemistry of amorphous silica. Zhuravlev model, Colloids and Surfaces A: Physicochemical and Engineering Aspects 173 (2000) 1-38.

[163] J.P. Gallas, J.M. Goupil, A. Vimont, J.C. Lavalley, B. Gil, J.P. Gilson, and O. Miserque, Quantification of water and silanol species on various silicas by coupling ir spectroscopy and in-situ thermogravimetry, Langmuir 25 (2009) 5825-5834.

[164] K.S. Sing, Characterization of porous materials: past, present and future, Colloids and Surfaces A: Physicochemical and Engineering Aspects 241 (2004) 3-7.

[165] P.J.M. Carrott and K.S.W. Sing, The adsorption of nitrogen on precipitated and pyrogenic silicas, Adsorption science & technology 1 (1984) 31-39.

[166] D. Barby, G.D. Parfitt, and K.S.W. Sing, Characterization of powder surfaces, Academic Press, London, 1976.

[167] Industrial Minerals, Industrial Minerals Prices May 2012, 2012.

[168] A.F. Gil, L. Salgado, L. Galicia, and I. González, Predominance-zone diagrams of Fe (III) and Fe (II) sulfate complexes in acidic media. Voltammetric and spectrophotometric studies, Talanta 42 (1995) 407-414.

[169] C.W. Kovach, High performance stainless steels, Nickel Development Institute, 2000.

[170] J.R. Davis, Nickel, cobalt, and their alloys, ASM International, 2000.

[171] M. Schütze, R. Bender, and K.G. Schütze, Corrosion resistance of high-performance materials: titanium, tantalum, zirconium, Wiley, 2012.

[172] E. Romër and A. Knuth, Personal communication: Production of olivine nano-silica by Eurosupport, 2012.

[173] Hellas Gold, Personal communication (Internal report - ProMine Deliverable 3.5): Technical and operational characteristic of the proces - Nano-silica production by the dissolution of olivine, 2013.

[174] P.P. Indexes, PPI Detailed Report Data for June 2013, 2013.

[175] G. Quercia, P. Spiesz, G. Hüsken, and H.J.H. Brouwers, SCC modification by use of amorphous nano-silica, Cement and Concrete Composites (2013) 69-81.

[176] G. Quercia, J.J.G. van der Putten, G. Hüsken, and H.J.H. Brouwers, Photovoltaic's silica-rich waste sludge as supplementary cementitious material (SCM), Cement and Concrete Research 54 (2013) 161-179.

[177] G. Quercia, G. Hüsken, and H.J.H. Brouwers, Water demand of amorphous nano silica and its impact on the workability of cement paste, Cement and Concrete Research (2011) 344-357.

[178] N. Vijayarethinam, Silica fume applications, World Cement (2009) 97-100.

[179] PBL Netherlands Environmental Assessment Agency, Trends in global CO2 emissions, 2012.

[180] P. Spiesz, Durability of concrete with emphasis on chloride migration. PhD Thesis, Eindhoven University of Technology, 2013.

[181] European Commission for Standardization (CEN), CEN EN 196-1. Methods of testing cement Part 1: Determination of strength, 2005.

[182] H. Justnes and T. Ostnor, Pozzolanic, Amorphous Silica Produced from the Mineral Olivine, Special Publication ACI 199 (2001) 769-782.

[183] J. Björnström, A. Martinelli, A. Matic, L. Börjesson, and I. Panas, Accelerating effects of colloidal nano-silica for beneficial calcium-silicate-hydrate formation in cement, Chemical Physics Letters 392 (2004) 242-248.

[184] G. Land and D. Stephan, The influence of nano-silica on the hydration of ordinary Portland cement, Journal of Materials Science 47 (2012) 1011-1017.

[185] CEN European Committee for Standardization and Nederlands Normalisatie-instituut, NEN-EN 13263-1+A1. Silica fume for concrete - Part 1: Definitions, requirements and conformity criteria, 2009.

[186] E.N. DIN, 206-1: Beton - Teil 1: Festlegung, Eigenschaften, Herstellung und Konformität, 2000.

[187] IUPAC, Manual of Symbols and Terminology for Physico-chemical Quantities and Units, Appendix II, Part I, Definitions, Terminology and Symbols in Colloid and Surface Chemistry, Pure Appl. Chem. 31 (1972) 579.

[188] M. Vert, K.H. Hellwich, M. Hess, P. Hodge, P. Kubisa, M. Rinaudo, and F. Schue, Terminology for biorelated polymers and applications (IUPAC Recommendations 2012), Pure Appl. Chem. 84 (2012) 377-410.

[189] P. Moriarty, Nanostructured materials, Rep. Prog. Phys. 64 (2001) 297.

[190] DIN 53206-1:1972-08: Prüfung von Pigmenten; Teilchengrößenanalyse, Grundbegriffe (Testing of pigments; particle size analysis, basic terms), Deutsches Institut für Normung, Berlin, Germany, 1972.

List of abbreviations and symbols

Abbreviations

BET	Referring to the Brunaer, Emmett and Teller method
BJH	Referring to the Barrett, Joyner and Halenda method
bwob	Based on the weight of binder
CVC	Conventional vibrated concrete
DLS	Dynamic light scattering
DLVO	Theory named after Derjaguin and Landau, Verwey and Overbeek.
DS	Dry sieving
DU	Dimensionless units
F	Filtration steps
Fo	Forsterite content
HM	High energy mixer
ICP-MS	Inductively couple plasma - mass spectrometry
ITZ	Interparticle transition zone
LLS	Light laser scattering
LOI	Loss on ignition
Me/Si	Molar ratio of Metal (Mg+Fe) to silicon (Si)
NMR	Nuclear magnetic resonance
NS	Nano-silica
ol	Olivine
ol_unr	Olivine unreacted
PALS	Positronium annihilation lifetime spectroscopy
PCE	Polycarboxilic ether
PSD	Particle size distributionb
PoSD	Pore size distribution
RM	Raw material
RP	Ripening
RT	Room temperature
RSD	Relative standard deviation
SAS	Synthetic amorphous silica
STD	Standard deviation
SP	Superplasticizer

TG	Thermogravimetry
TSE	Tensile strength effect
US	Ultrasounds
w/c	Water cement ratio
w/f	Water fine ratio
WS	Wet sieving
XRD	X-ray diffraction
XRF	X-ray fluorescence
Du	Dunite

Symbols

Roman

a	Activity	(-)
A	Pre-exponential factor	($mol \cdot cm^{-2} \cdot s^{-1}$)
C_D	Drag coefficient	(-)
d	Diameter, usually referring to particle size	(µm) or (nm)
d_A	Average size	(µm) or (nm)
d_1	Primary particle size	(nm)
d_2	Aggregate size	(µm)
d_3	Agglomerate size	(µm)
d_{p_A}	Average pore diameter calculated with the BJH method for the adsorption branch	(nm)
d_{p_D}	Average pore diameter calculated with the BJH method for the desorption branch	(nm)
d_{p1}	Average pore diameter calculated with PALS for pore 1	(Å)
d_{p2}	Average pore diameter calculated with PALS for pore 2	(Å)
D	Diffusion coefficient	(m^2/s)
D_H	Hydrodynamic diameter	(nm)
E	Efficiency	(%)
E_a	Activation energy	(kJ/mol)
E_{sep}	Separation efficiency	(%)
I	Intensity	(%)
k_T	Rate constant	($mol \cdot cm^{-2} \cdot s^{-1}$)
k	Boltzmann constant	$1.38065 \cdot 10^{-23}$ ($J \cdot K^{-1}$)

k_L	Liquid-phase mass-transfer coefficient	(m/s)
L	Length	(mm)
m	Mass	(g)
M	Molar mass	(g/mol)
n	Number of moles	(moles)
N	Molar flux per unit of area	($mol \cdot cm^{-2} \cdot s^{-1}$)
P_{Si}	Purity	(%)
r	Reaction/dissolution rate	($mol \cdot cm^{-2} \cdot s^{-1}$)
R	Gas constant or radius	8.3144 ($J \cdot mol^{-1} \cdot K^{-1}$) or (µm)
R_a	Radius of the outer cylinder of the Haake viscometer	(mm)
Re	Reynolds number	(-)
R_i	Radius of the inner cylinder of the Haake viscometer	(mm)
Sc	Schmidt number	(-)
Sh	Sherwood number	(-)
SSA_{BET}	BET specific surface area	(m^2/g)
SSA_{Br}	Brantley specific surface area	(m^2/g)
SSA_E	External specific surface area	(m^2/g)
SSA_G	Geometric specific surface area	(m^2/g)
SSA_{MP}	Microporous specific surface area	(m^2/g)
SSA_{NMR}	Specific surface area calculated from the NMR analysis	(m^2/g)
SSA_T	Total specific surface area calculated from the t-plot	(m^2/g)
t	Time or layer thickness	(h) or (Å) or (nm)
t_{ag}	Aging time	(h)
t_r	Reaction time	(h)
T	Temperature	(°C)
T_r	Temperature in the reactor	(°C)
V	Volume	(mL) or (L)
v_s	Slip velocity	(m/s)
v_t	Free settling velocity	(m/s)
V_{MP}	Micropore volume	(cm^3/g)
V_{P_D}	Volume of pores calculated with the BJH method for the desorption branch	(cm^3/g)
w	Mass fraction or mass content	(%)

X	Conversion degree	(%)
Y_{NS}	Production Yield	(%)

Greek

α	Contact angle between the solid and condensed phase	(°)
α_{OH}	Silanol number	(OH groups/nm^2)
γ	Shear rate	(s^{-1})
Δ	Increment	(-)
ε	Dielectric constant	(-)
ϕ	Volume fraction	(%)
θ_{Si}	Layer thickness of silica	(µm) or (nm)
$(\theta_0)_m$	Fraction of surface not covered by any molecule	(-)
λ	Roughness factor	(-)
μ	Viscosity (dynamic)	(Pa·s) or (mPa·s)
ν	Kinematic viscosity	(m^2/s)
ρ	Density	(g/cm^3)
τ	Shear stress	(Pa)
$\tau_{o\text{-}Ps}$	Lifetime of ortho-Ps	(ns)

Subscripts

A	Average
Br	Brantley
cal	Calculated
du	Dunite
exp	Experimental
G	Geometric
i	Initial
neu	Neutralized
ol	Olivine
pu	Pure
r	Reaction
re	Real
Si	Silica
t	Time
T	Temperature

B	Bulk
Br	Brantley
con	Consumed
e	Effective
L	Liquid
G	Geometric
i	Initial
ol	Olivine
p	Particle
r	Reaction
so	Solid
t	Time
T	Temperature
th	Theoretical

Appendix I: Definitions

Colloidal dispersion:

A colloidal dispersion is defined by the IUPAC [187] as a system in which colloidal particles (i.e., 1 to 1000 nm) of any nature (solid, liquid or gas) are dispersed in continuous phase of a different composition or state.

Nano-material:

Particle of any shape with dimensions in the range of 1 to 100 nm [188]. The basis of the 100-nm limit is the fact that novel properties that differentiate particles from the bulk material typically develop at a critical length scale of under 100 nm [188].

Nanostructured material:

Nanostructured materials may be defined as those materials whose structural elements — clusters, crystallites or molecules — have dimensions in the 1 to 100 nm range [189]. Also, it can be defined from the point of view of the specific surface area as a material with an equivalent specific surface area to the one of a nanomaterial.

Aggregate:

Regarding the definitions of aggregate and agglomerate there is some controversy because these terms have been used indistinctively referring to the same concept or because the terms are switching. An example of the last one is the difference between the German standard DIN and the British Standards Institution, which define these terms the other way around. In this PhD thesis we follow the nomenclature of the German Standard DIN [190], which is also adopted in the JACC report about synthetic amorphous silica [1].

Aggregates can be defined as the assembly of primary particles which are grown together face-to-face in the form of chains or clusters [190]. The aggregates are formed by the collision of primary particles during particle growth and/or by the further deposition of silica onto these aggregates. Synthetic amorphous silica (SAS) aggregates represent the smallest, stable, non-dispersible particle units of three-dimensional structure, with a size ranging from 100 to 1000 nm for pyrogenic and precipitated SASs.

Agglomerate:

Agglomerates are assemblies of aggregates, held together by strong physical adhesion forces [190].

Cluster:

According to the IUPAC [41] a cluster is a number of metal centers grouped close together which can have direct metal bonding interactions or interactions through a bridging ligand, but are not necessarily held together by these interactions.

The encyclopedia Britannica provides a more general definition, which is: clusters are aggregates of atoms, molecules, or ions that adhere together under forces like those that bind the atoms, ions, or molecules of bulk matter.

Olivine:

Olivine is a solid solution between the minerals forsterite (Mg_2SiO_4) and fayalite (Fe_2SiO_4).

Forsterite:

Forsterite is the mineral (Mg_2SiO_4)

Fayalite:

Fayalite is the mineral (Fe_2SiO_4)

Dunite:

Dunite is a rock where 90% of the volume is made up of olivine.

Appendix II: Dissolution curves with the best fitting parameters

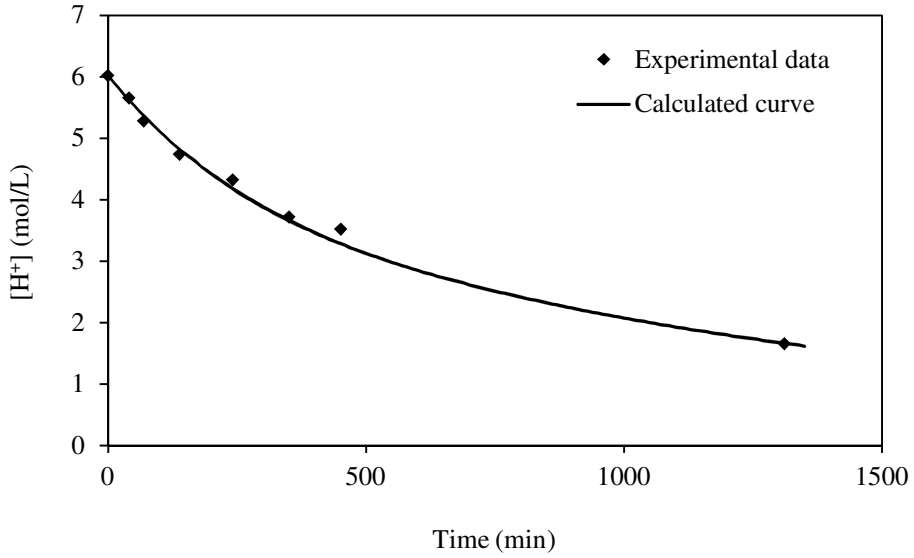

Figure A.II-1. Experimental data of experiment NS-1 and calculated curve using $k_T = 1.45 \cdot 10^{-10}$ and n = 0.5.

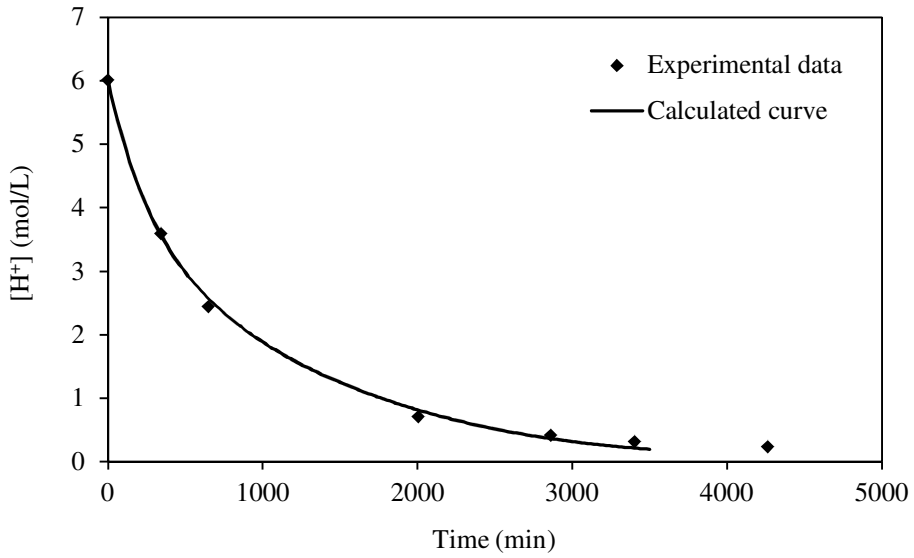

Figure A.II-2. Experimental data of experiment NS-2 and calculated curve using $k_T = 2.1 \cdot 10^{-10}$ and n = 0.5.

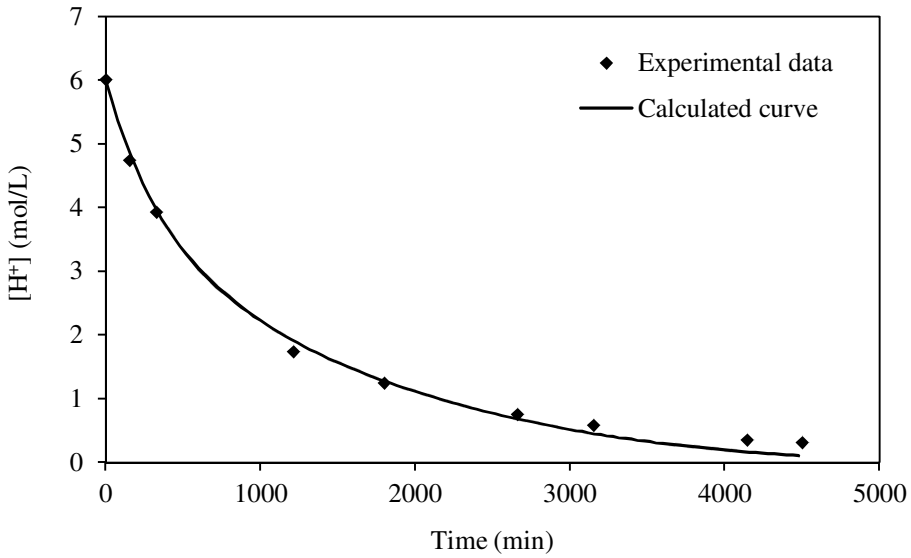

Figure A.II-3. Experimental data of experiment NS-3 and calculated curve using $k_T = 3 \cdot 10^{-10}$ and n = 0.5.

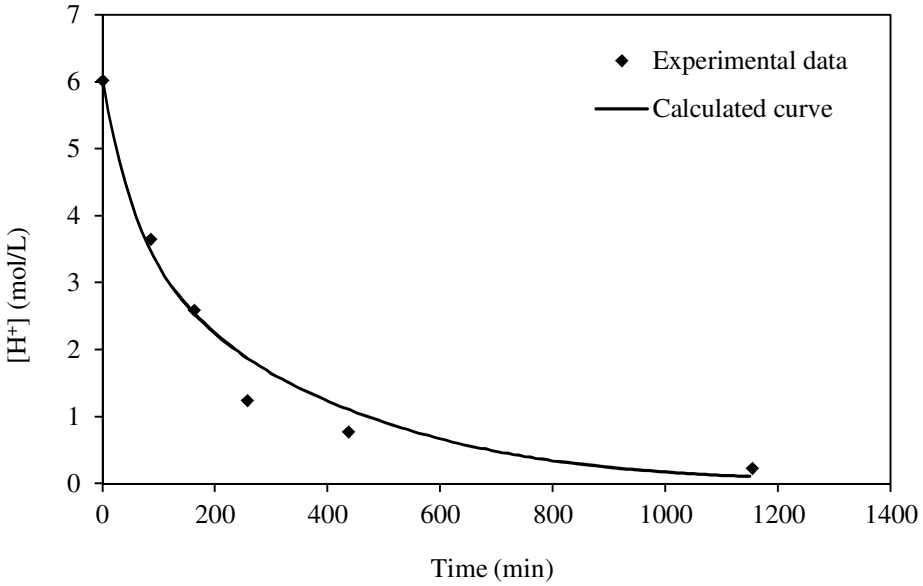

Figure A.II-4. Experimental data of experiment NS-4 and calculated curve using $k_T = 9.3 \cdot 10^{-10}$ and n = 0.5.

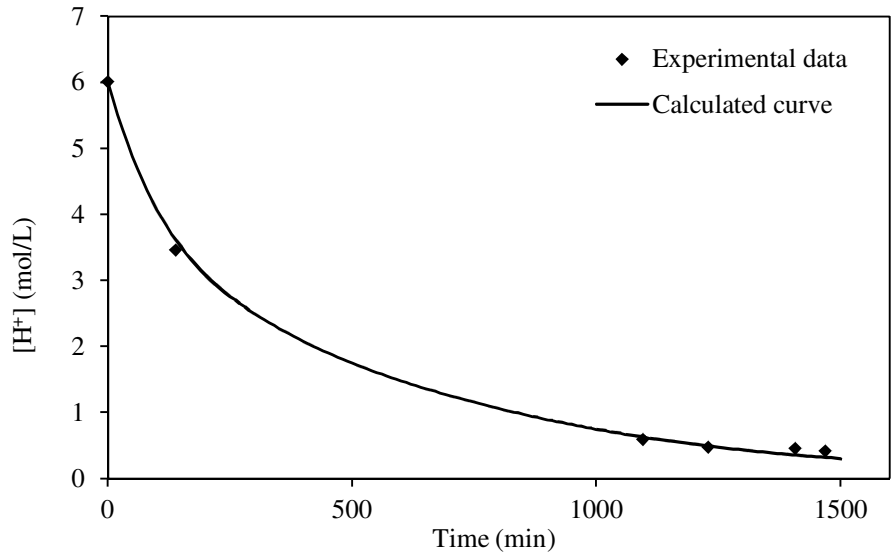

Figure A.II-5. Experimental data of experiment NS-5 and calculated curve using $k_T = 10.4 \cdot 10^{-10}$ and n = 0.5.

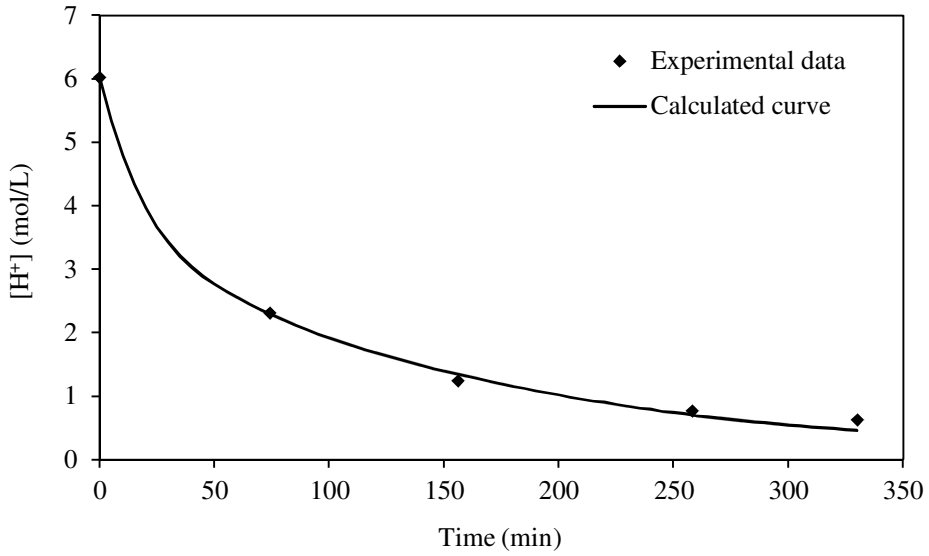

Figure A.II-6. Experimental data of experiment NS-7 and calculated curve using $k_T = 41 \cdot 10^{-10}$ and n = 0.5.

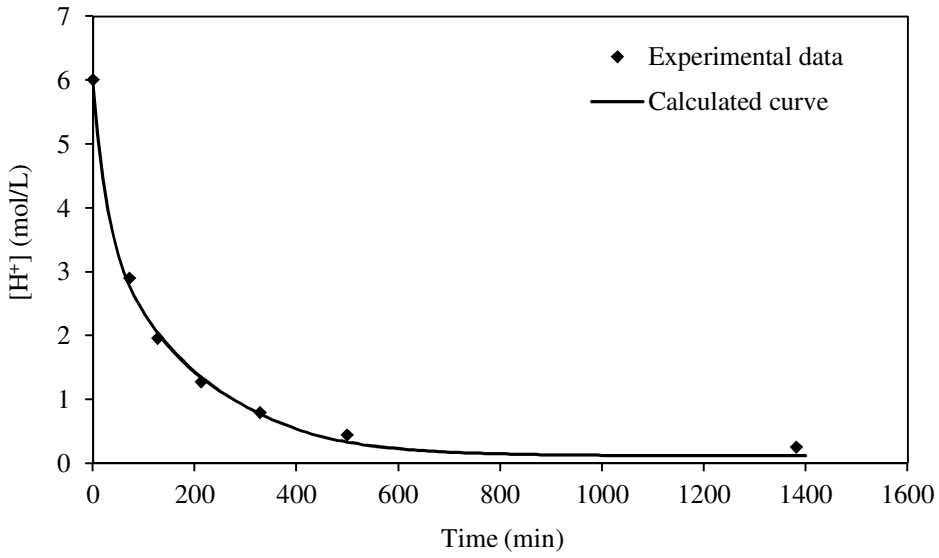

Figure A.II-7. Experimental data of experiment NS-8 and calculated curve using $k_T = 34.5 \cdot 10^{-10}$ and n = 0.5.

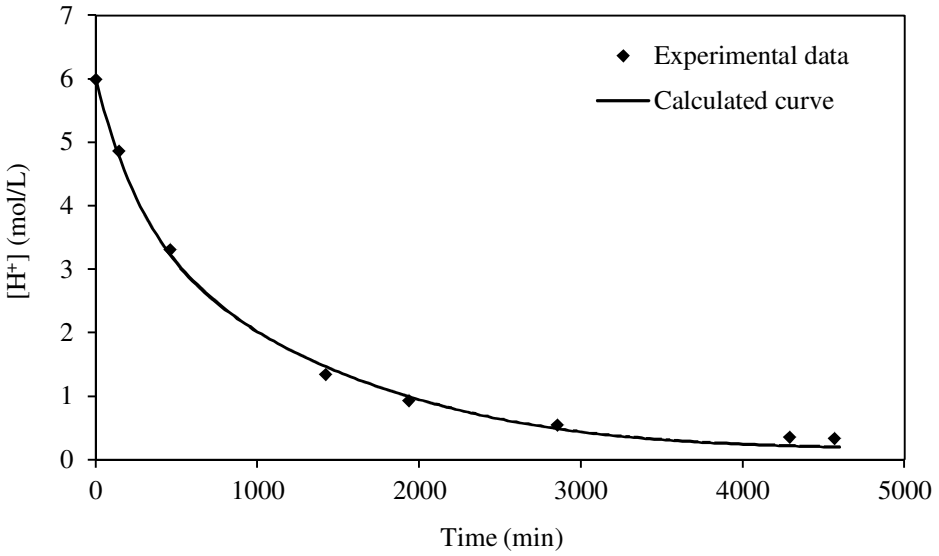

Figure A.II-8. Experimental data of experiment NS-9 and calculated curve using $k_T = 1.95 \cdot 10^{-10}$ and n = 0.5.

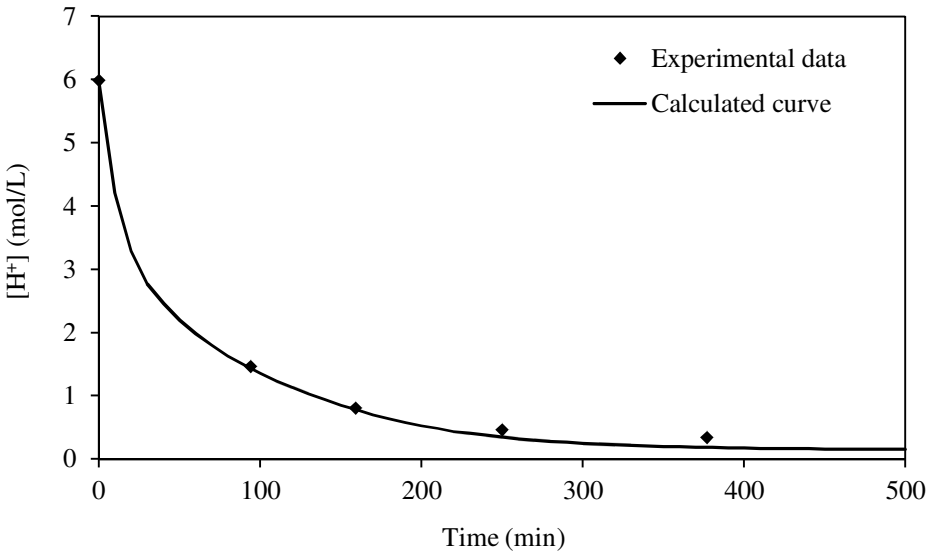

Figure A.II-9. Experimental data of experiment NS-10 and calculated curve using $k_T = 39 \cdot 10^{-10}$ and n = 0.5.

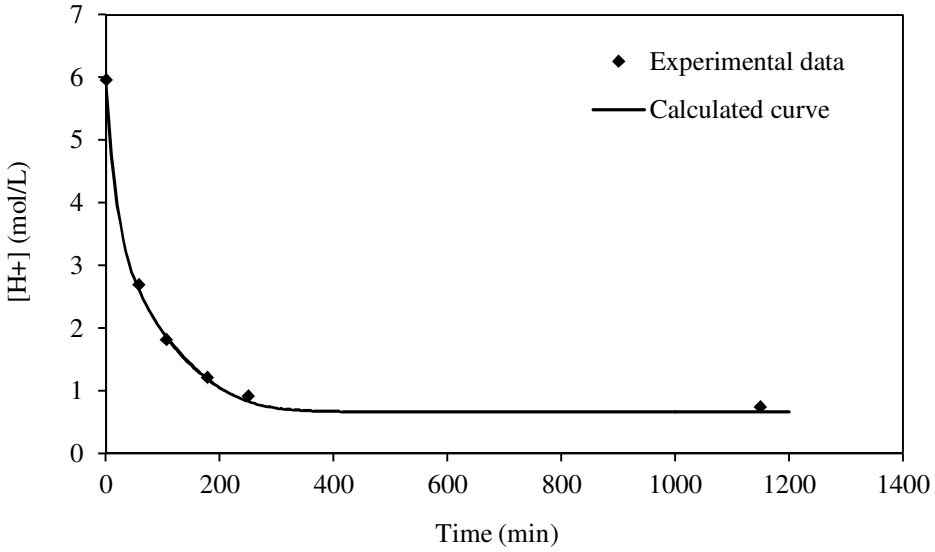

Figure A.II-10. Experimental data of experiment NS-11 and calculated curve using $k_T = 39.5 \cdot 10^{-10}$ and n = 0.5.

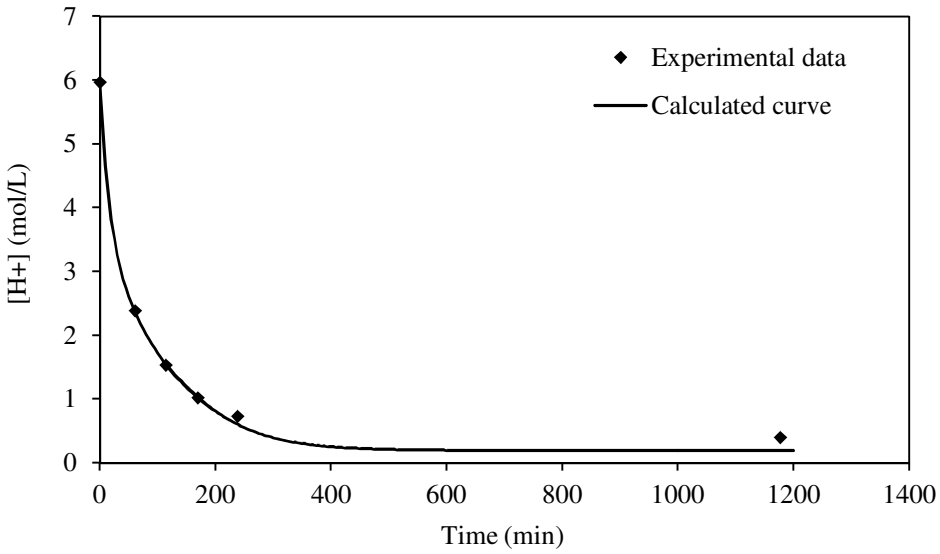

Figure A.II-11. Experimental data of experiment NS-12 and calculated curve using $k_T = 40 \cdot 10^{-10}$ and n = 0.5.

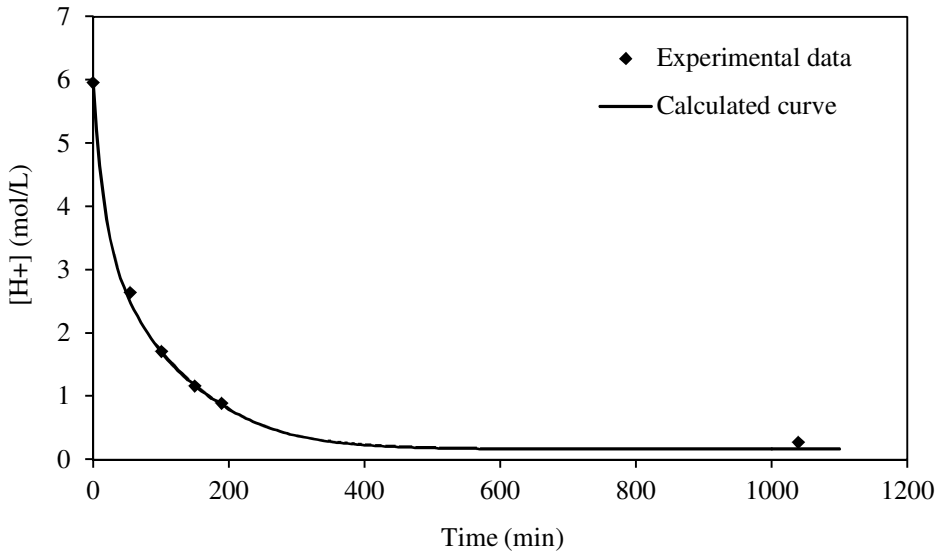

Figure A.II-12. Experimental data of experiment NS-13 and calculated curve using $k_T = 40.2 \cdot 10^{-10}$ and n = 0.5.

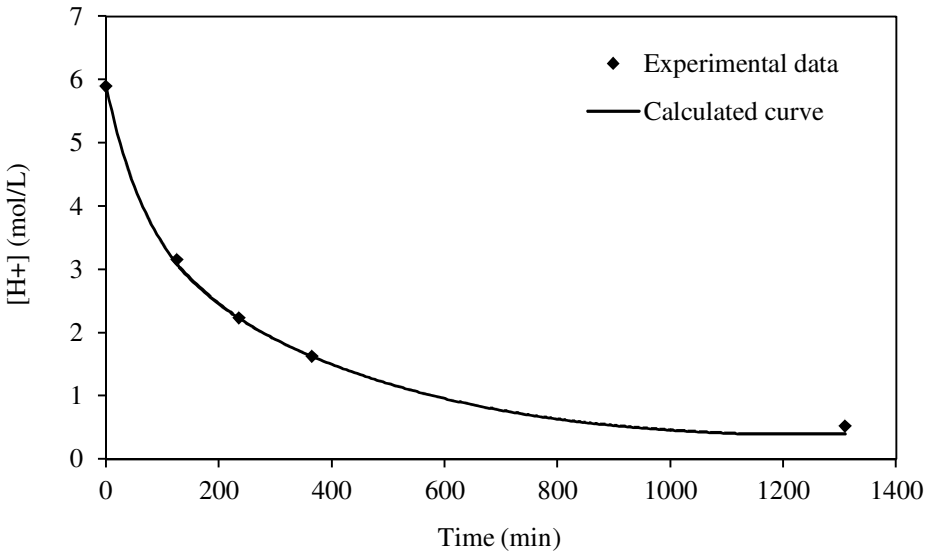

Figure A.II-13. Experimental data of experiment NS-14 and calculated curve using $k_T = 10.4 \cdot 10^{-10}$ and n = 0.5.

Summary

Nano-silica is one of the most used nano-materials, and its use is rising 5.6 per cent per year to reach a projected 2.8 million metric tons in 2016. Likewise, the market for specialty silicas is estimated to grow 7.5% per year reaching a total value of $6.4 billion in 2016. The current production methods involve steps with high temperatures. To reach these temperatures, vast amounts of fuel are consumed making these processes: a) unsustainable because of the scarcity of fuels; b) environmentally unfriendly because of the high amount of CO_2 emitted; and c) expensive because of the fuel price. The production of nano-silica by the dissolution of olivine is an interesting alternative to the existing commercial methods because of the good quality of the resulting silica and low energy requirements and CO_2 emissions.

The main purpose of this research is to improve the technology of the olivine nano-silica production process to be able to tailor the properties of this nano-silica. A secondary objective is to optimize the olivine nano-silica process. In addition to these objectives, this research contributes to the understanding of three topics: the dissolution of olivine at negative pH; the silica particle growth below the isoelectric point; and the development of the pore structure at negative pH.

The content of this PhD thesis can be divided up into the following parts: 1) the dissolution of olivine under the olivine nano-silica conditions; 2) the influence of the process conditions on the textural properties of olivine nano-silica; and 3) the technical aspects of the olivine nano-silica process.

The main conclusions of this work are:

1. The kinetic model proposed here can be applied with good accuracy to predict the olivine dissolution under the nano-silica production conditions.
2. Olivine nano-silica features an average SSA_{BET} of 350 m^2/g and a BJH pore size distribution in the range of 2 to 100 nm for silicas with purities above 99%, extent of conversion above 90% and filtered under vacuum.
3. The process conditions of the olivine nano-silica production have a strong influence on the final SSA_{BET} of this material. Thus, modifying the process conditions, nano-silicas with different textural properties can be synthesized.
4. After the tailoring, olivine silicas with a SSA_{BET} between 100 and 500 m^2/g and a pore size distribution of 9 to 30 nm can be obtained.
5. The growth model for the olivine silica particles proposed here explains the rapid growth of particles above 1 μm and the porous structure of the material.
6. Mechanical techniques such as ultrasonification can be employed to break apart the agglomerate into nano-particles.

List of publications

Journals

[1] A. Lazaro, M.C. Van de Griend, H.J.H. Brouwers, and J.W. Geus, The influence of process conditions and Ostwald ripening on the specific surface area of olivine nano-silica, Microporous Mesoporous Mater. 181 (2013) 254-261.

[2] A. Lazaro, G. Quercia, H.J.H. Brouwers, and J.W. Geus, Synthesis of a green nano-silica material using beneficiated waste dunites and its application in concrete, World Journal of Nano Science and Engineering 3 (2013) 41-51.

[3] G. Quercia, A. Lazaro, J.W. Geus, and H.J.H. Brouwers, Characterization of morphology and texture of several amorphous nano-silica particles used in concrete, Cement Concrete Comp. 44 (2013) 77-92.

[4] A. Lazaro, H.J.H. Brouwers, G. Quercia, and J.W. Geus, The properties of amorphous nano-silica synthesized by the dissolution of olivine, Chem. Eng. J. 211-212 (2012) 112-121.

[5] A. Lazaro, C. García Portilo, J. De la Torre, and J. Bastida, Caracteristicas fisicas y composicionales de pastas de gres porcelaínico con arcillas de teruel, Boletin de la Sociedad Española de Ceramica y Vidrio 51 (2012) 201-210.

[6] A. Lazaro, L. Benac-Vegas, H.J.H. Brouwers, J.W. Geus, and J. Bastida, The kinetics of the olivine dissolution for nano-silica production (submitted 2014).

[7] A. Lazaro, J.W. Geus and H.J.H. Brouwers, Polymerization and particle growth of nano-silica synthesized at negative pH (in preparation).

[8] A. Lazaro, J.W. Geus and H.J.H. Brouwers, Development of the pore structure of nano-silica synthesized at negative pH (in preparation).

Conference Proceedings

[9] A. Lazaro, G. Quercia Bianchi, and H.J.H. Brouwers, Tailoring the properties of olivine nano-silica and its application in concrete., Proceedings of the 1st International Conference on the Chemistry of Construction Materials, 7-9 October 2013, Berlin, Germany,2013.

[10] A. Lazaro, H.J.H. Brouwers, and J.W. Geus, The influence of process conditions on the properties of olivine nano-silica, 125th BASF International Summer Course,2013.

[11] A. Lazaro, G. Quercia, and H.J.H. Brouwers, Production and application of a new type of nano-silica in concrete, International conference on building materials, Ibausil,2012.

[12] A. Lazaro, J.W. Geus, and H.J.H. Brouwers, Influence of the production process conditions on the specific surface area of olivine nano-silicas, Nanomaterials: Application and properties,2012.

[13] M.C. van de Griend, A. Lazaro, and H.J.H. Brouwers, The Effect of Hydrothermal Treatment on Olivine Nano-Silica, Proceedings of the international conference Nanomaterials: Application and properties,2012.

[14] A. Lazaro and H.J.H. Brouwers, Nano-silica production by a sustainable process; application in building materials, 8th fib International - PhD Symposium in Civil Engineering,2010.

Other types

[15] A. Lazaro, G. Quercia Bianchi, and H.J.H. Brouwers, Production of a new type of nanosilica — olivine nano-silica — and its application in concrete. Cement and its Applications (in Russian) 3, 56-60. 2013.

[16] J.W. Geus, G. Quercia Bianchi, and A. Lazaro, Silica particles and method of preparation thereof [P97844NL00] 2013.

Curriculum vitae

Alberto Lázaro García was born in 1981 in Valencia, Spain. Currently he is a research assistant at Eindhoven University of Technology (TU/e) in the Building Materials Group, chaired by Prof. Dr. ir. H.J.H. (Jos) Brouwers. He graduated with a Master of Science degree in Chemical Engineering from the University of Valencia, Spain in 2005. He carried out his Master thesis in the academic year 2004/05 in the Hogeschool Gent (Belgium) in the field of waste water treatment. In 2005 and 2006, he worked in the chemical company Tecnidex (Spain), where his main functions were: 1) planning and controlling the production of waxes; 2) costumer-oriented product development for waxes and fungicides; and 3) development of an industrial treatment plant for the wastewater of the postharvest industry. In 2006, he started working as a part-time researcher at the Department of Geology in the University of Valencia for the national project Habitat 2030. His tasks in Habitat 2030 consisted of: 1) studying the hydration of calcium oxide and mortar samples by means of X-Ray diffraction; and 2) investigating the impact of replacing foreign with national clays on the properties of porcelanic stoneware. In 2006, he received a scholarship for the Master of Environmental Engineering in the Polytechnic University of Valencia, obtaining his diploma in 2008. In 2008, he undertook a traineeship in the waste water treatment plant of La Pobla de Farnals (Spain). After finishing his Master studies, he moved to the Netherlands to work on his PhD in the field of synthesis of nano-materials with Prof. Brouwers and Prof. Geus. His research interests include synthesis of nano-materials, inorganic materials, colloidal materials and mesoporous materials. During his PhD project he daily supervised two master theses. From the results of his PhD thesis, 4 peer reviewed articles and 1 professional article have been published, and 1 peer reviewed article and 1 patent are under review.

Bouwstenen is een publikatiereeks van de Faculteit Bouwkunde, Technische Universiteit Eindhoven. Zij presenteert resultaten van onderzoek en andere aktiviteiten op het vakgebied der Bouwkunde, uitgevoerd in het kader van deze Faculteit.

Bouwstenen zijn telefonisch te bestellen op nummer
040 - 2472383

Kernredaktie
MTOZ

Reeds verschenen in de serie
Bouwstenen

nr 1
Elan: A Computer Model for Building Energy Design: Theory and Validation
Martin H. de Wit
H.H. Driessen
R.M.M. van der Velden

nr 2
Kwaliteit, Keuzevrijheid en Kosten: Evaluatie van Experiment Klarendal, Arnhem
J. Smeets
C. le Nobel
M. Broos
J. Frenken
A. v.d. Sanden

nr 3
Crooswijk: Van 'Bijzonder' naar 'Gewoon'
Vincent Smit
Kees Noort

nr 4
Staal in de Woningbouw
Edwin J.F. Delsing

nr 5
Mathematical Theory of Stressed Skin Action in Profiled Sheeting with Various Edge Conditions
Andre W.A.M.J. van den Bogaard

nr 6
Hoe Berekenbaar en Betrouwbaar is de Coëfficiënt k in x-ksigma en x-ks?
K.B. Lub
A.J. Bosch

nr 7
Het Typologisch Gereedschap: Een Verkennende Studie Omtrent Typologie en Omtrent de Aanpak van Typologisch Onderzoek
J.H. Luiten

nr 8
Informatievoorziening en Beheerprocessen
A. Nauta
Jos Smeets (red.)
Helga Fassbinder (projectleider)
Adrie Proveniers
J. v.d. Moosdijk

nr 9
Strukturering en Verwerking van Tijdgegevens voor de Uitvoering van Bouwwerken
ir. W.F. Schaefer
P.A. Erkelens

nr 10
Stedebouw en de Vorming van een Speciale Wetenschap
K. Doevendans

nr 11
Informatica en Ondersteuning van Ruimtelijke Besluitvorming
G.G. van der Meulen

nr 12
Staal in de Woningbouw, Korrosie-Bescherming van de Begane Grondvloer
Edwin J.F. Delsing

nr 13
Een Thermisch Model voor de Berekening van Staalplaatbetonvloeren onder Brandomstandigheden
A.F. Hamerlinck

nr 14
De Wijkgedachte in Nederland: Gemeenschapsstreven in een Stedebouwkundige Context
K. Doevendans
R. Stolzenburg

nr 15
Diaphragm Effect of Trapezoidally Profiled Steel Sheets: Experimental Research into the Influence of Force Application
Andre W.A.M.J. van den Bogaard

nr 16
Versterken met Spuit-Ferrocement: Het Mechanische Gedrag van met Spuit-Ferrocement Versterkte Gewapend Betonbalken
K.B. Lubir
M.C.G. van Wanroy

nr 17
De Tractaten van Jean Nicolas Louis Durand
G. van Zeyl

nr 18
Wonen onder een Plat Dak: Drie Opstellen over Enkele Vooronderstellingen van de Stedebouw
K. Doevendans

nr 19
Supporting Decision Making Processes: A Graphical and Interactive Analysis of Multivariate Data
W. Adams

nr 20
Self-Help Building Productivity: A Method for Improving House Building by Low-Income Groups Applied to Kenya 1990-2000
P. A. Erkelens

nr 21
De Verdeling van Woningen: Een Kwestie van Onderhandelen
Vincent Smit

nr 22
Flexibiliteit en Kosten in het Ontwerpproces: Een Besluitvormingondersteunend Model
M. Prins

nr 23
Spontane Nederzettingen Begeleid: Voorwaarden en Criteria in Sri Lanka
Po Hin Thung

nr 24
Fundamentals of the Design of Bamboo Structures
Oscar Arce-Villalobos

nr 25
Concepten van de Bouwkunde
M.F.Th. Bax (red.)
H.M.G.J. Trum (red.)

nr 26
Meaning of the Site
Xiaodong Li

nr 27
Het Woonmilieu op Begrip Gebracht: Een Speurtocht naar de Betekenis van het Begrip 'Woonmilieu'
Jaap Ketelaar

nr 28
Urban Environment in Developing Countries
editors: Peter A. Erkelens
George G. van der Meulen (red.)

nr 29
Stategische Plannen voor de Stad: Onderzoek en Planning in Drie Steden
prof.dr. H. Fassbinder (red.)
H. Rikhof (red.)

nr 30
Stedebouwkunde en Stadsbestuur
Piet Beekman

nr 31
De Architectuur van Djenné: Een Onderzoek naar de Historische Stad
P.C.M. Maas

nr 32
Conjoint Experiments and Retail Planning
Harmen Oppewal

nr 33
Strukturformen Indonesischer Bautechnik: Entwicklung Methodischer Grundlagen für eine 'Konstruktive Pattern Language' in Indonesien
Heinz Frick arch. SIA

nr 34
Styles of Architectural Designing: Empirical Research on Working Styles and Personality Dispositions
Anton P.M. van Bakel

nr 35
Conjoint Choice Models for Urban Tourism Planning and Marketing
Benedict Dellaert

nr 36
Stedelijke Planvorming als Co-Produktie
Helga Fassbinder (red.)

nr 37
Design Research in the Netherlands
editors: R.M. Oxman
M.F.Th. Bax
H.H. Achten

nr 38
Communication in the Building Industry
Bauke de Vries

nr 39
Optimaal Dimensioneren van Gelaste Plaatliggers
J.B.W. Stark
F. van Pelt
L.F.M. van Gorp
B.W.E.M. van Hove

nr 40
Huisvesting en Overwinning van Armoede
P.H. Thung
P. Beekman (red.)

nr 41
Urban Habitat: The Environment of Tomorrow
George G. van der Meulen
Peter A. Erkelens

nr 42
A Typology of Joints
John C.M. Olie

nr 43
Modeling Constraints-Based Choices for Leisure Mobility Planning
Marcus P. Stemerding

nr 44
Activity-Based Travel Demand Modeling
Dick Ettema

nr 45
Wind-Induced Pressure Fluctuations on Building Facades
Chris Geurts

nr 46
Generic Representations
Henri Achten

nr 47
Johann Santini Aichel: Architectuur en Ambiguiteit
Dirk De Meyer

nr 48
Concrete Behaviour in Multiaxial Compression
Erik van Geel

nr 49
Modelling Site Selection
Frank Witlox

nr 50
Ecolemma Model
Ferdinand Beetstra

nr 51
Conjoint Approaches to Developing Activity-Based Models
Donggen Wang

nr 52
On the Effectiveness of Ventilation
Ad Roos

nr 53
Conjoint Modeling Approaches for Residential Group preferences
Eric Molin

nr 54
Modelling Architectural Design Information by Features
Jos van Leeuwen

nr 55
A Spatial Decision Support System for the Planning of Retail and Service Facilities
Theo Arentze

nr 56
Integrated Lighting System Assistant
Ellie de Groot

nr 57
Ontwerpend Leren, Leren Ontwerpen
J.T. Boekholt

nr 58
Temporal Aspects of Theme Park Choice Behavior
Astrid Kemperman

nr 59
Ontwerp van een Geïndustrialiseerde Funderingswijze
Faas Moonen

nr 60
Merlin: A Decision Support System for Outdoor Leisure Planning
Manon van Middelkoop

nr 61
The Aura of Modernity
Jos Bosman

nr 62
Urban Form and Activity-Travel Patterns
Daniëlle Snellen

nr 63
Design Research in the Netherlands 2000
Henri Achten

nr 64
Computer Aided Dimensional Control in Building Construction
Rui Wu

nr 65
Beyond Sustainable Building
editors: Peter A. Erkelens
Sander de Jonge
August A.M. van Vliet
co-editor: Ruth J.G. Verhagen

nr 66
Das Globalrecyclingfähige Haus
Hans Löfflad

nr 67
Cool Schools for Hot Suburbs
René J. Dierkx

nr 68
A Bamboo Building Design Decision Support Tool
Fitri Mardjono

nr 69
Driving Rain on Building Envelopes
Fabien van Mook

nr 70
Heating Monumental Churches
Henk Schellen

nr 71
Van Woningverhuurder naar Aanbieder van Woongenot
Patrick Dogge

nr 72
Moisture Transfer Properties of Coated Gypsum
Emile Goossens

nr 73
Plybamboo Wall-Panels for Housing
Guillermo E. González-Beltrán

nr 74
The Future Site-Proceedings
Ger Maas
Frans van Gassel

nr 75
Radon transport in Autoclaved Aerated Concrete
Michel van der Pal

nr 76
The Reliability and Validity of Interactive Virtual Reality Computer Experiments
Amy Tan

nr 77
Measuring Housing Preferences Using Virtual Reality and Belief Networks
Maciej A. Orzechowski

nr 78
Computational Representations of Words and Associations in Architectural Design
Nicole Segers

nr 79
Measuring and Predicting Adaptation in Multidimensional Activity-Travel Patterns
Chang-Hyeon Joh

nr 80
Strategic Briefing
Fayez Al Hassan

nr 81
Well Being in Hospitals
Simona Di Cicco

nr 82
Solares Bauen: Implementierungs- und Umsetzungs-Aspekte in der Hochschulausbildung in Österreich
Gerhard Schuster

nr 83
Supporting Strategic Design of Workplace Environments with Case-Based Reasoning
Shauna Mallory-Hill

nr 84
ACCEL: A Tool for Supporting Concept Generation in the Early Design Phase
Maxim Ivashkov

nr 85
Brick-Mortar Interaction in Masonry under Compression
Ad Vermeltfoort

nr 86
Zelfredzaam Wonen
Guus van Vliet

nr 87
Een Ensemble met Grootstedelijke Allure
Jos Bosman
Hans Schippers

nr 88
On the Computation of Well-Structured Graphic Representations in Architectural Design
Henri Achten

nr 89
De Evolutie van een West-Afrikaanse Vernaculaire Architectuur
Wolf Schijns

nr 90
ROMBO Tactiek
Christoph Maria Ravesloot

nr 91
External Coupling between Building Energy Simulation and Computational Fluid Dynamics
Ery Djunaedy

nr 92
Design Research in the Netherlands 2005
editors: Henri Achten
Kees Dorst
Pieter Jan Stappers
Bauke de Vries

nr 93
Ein Modell zur Baulichen Transformation
Jalil H. Saber Zaimian

nr 94
Human Lighting Demands: Healthy Lighting in an Office Environment
Myriam Aries

nr 95
A Spatial Decision Support System for the Provision and Monitoring of Urban Greenspace
Claudia Pelizaro

nr 96
Leren Creëren
Adri Proveniers

nr 97
Simlandscape
Rob de Waard

nr 98
Design Team Communication
Ad den Otter

nr 99
Humaan-Ecologisch Georiënteerde Woningbouw
Juri Czabanowski

nr 100
Hambase
Martin de Wit

nr 101
Sound Transmission through Pipe Systems and into Building Structures
Susanne Bron-van der Jagt

nr 102
Het Bouwkundig Contrapunt
Jan Francis Boelen

nr 103
A Framework for a Multi-Agent Planning Support System
Dick Saarloos

nr 104
Bracing Steel Frames with Calcium Silicate Element Walls
Bright Mweene Ng'andu

nr 105
Naar een Nieuwe Houtskeletbouw
F.N.G. De Medts

nr 108
Geborgenheid
T.E.L. van Pinxteren

nr 109
Modelling Strategic Behaviour in Anticipation of Congestion
Qi Han

nr 110
Reflecties op het Woondomein
Fred Sanders

nr 111
On Assessment of Wind Comfort by Sand Erosion
Gábor Dezsö

nr 112
Bench Heating in Monumental Churches
Dionne Limpens-Neilen

nr 113
RE. Architecture
Ana Pereira Roders

nr 114
Toward Applicable Green Architecture
Usama El Fiky

nr 115
Knowledge Representation under Inherent Uncertainty in a Multi-Agent System for Land Use Planning
Liying Ma

nr 116
Integrated Heat Air and Moisture Modeling and Simulation
Jos van Schijndel

nr 117
Concrete Behaviour in Multiaxial Compression
J.P.W. Bongers

nr 118
The Image of the Urban Landscape
Ana Moya Pellitero

nr 119
The Self-Organizing City in Vietnam
Stephanie Geertman

nr 120
A Multi-Agent Planning Support System for Assessing Externalities of Urban Form Scenarios
Rachel Katoshevski-Cavari

nr 121
Den Schulbau Neu Denken, Fühlen und Wollen
Urs Christian Maurer-Dietrich

nr 122
Peter Eisenman Theories and Practices
Bernhard Kormoss

nr 123
User Simulation of Space Utilisation
Vincent Tabak

nr 125
In Search of a Complex System Model
Oswald Devisch

nr 126
Lighting at Work: Environmental Study of Direct Effects of Lighting Level and Spectrum on Psycho-Physiological Variables
Grazyna Górnicka

nr 127
Flanking Sound Transmission through Lightweight Framed Double Leaf Walls
Stefan Schoenwald

nr 128
Bounded Rationality and Spatio-Temporal Pedestrian Shopping Behavior
Wei Zhu

nr 129
Travel Information: Impact on Activity Travel Pattern
Zhongwei Sun

nr 130
Co-Simulation for Performance Prediction of Innovative Integrated Mechanical Energy Systems in Buildings
Marija Trčka

nr 131
Allemaal Winnen
M.J. Bakker

nr 132
Architectural Cue Model in Evacuation Simulation for Underground Space Design
Chengyu Sun

nr 133
Uncertainty and Sensitivity Analysis in Building Performance Simulation for Decision Support and Design Optimization
Christina Hopfe

nr 134
Facilitating Distributed Collaboration in the AEC/FM Sector Using Semantic Web Technologies
Jacob Beetz

nr 135
Circumferentially Adhesive Bonded Glass Panes for Bracing Steel Frame in Façades
Edwin Huveners

nr 136
Influence of Temperature on Concrete Beams Strengthened in Flexure with CFRP
Ernst-Lucas Klamer

nr 137
Sturen op Klantwaarde
Jos Smeets

nr 139
Lateral Behavior of Steel Frames with Discretely Connected Precast Concrete Infill Panels
Paul Teewen

nr 140
Integral Design Method in the Context of Sustainable Building Design
Perica Savanović

nr 141
Household Activity-Travel Behavior: Implementation of Within-Household Interactions
Renni Anggraini

nr 142
Design Research in the Netherlands 2010
Henri Achten

nr 143
Modelling Life Trajectories and Transport Mode Choice Using Bayesian Belief Networks
Marloes Verhoeven

nr 144
Assessing Construction Project Performance in Ghana
William Gyadu-Asiedu

nr 145
Empowering Seniors through Domotic Homes
Masi Mohammadi

nr 146
An Integral Design Concept for Ecological Self-Compacting Concrete
Martin Hunger

nr 147
Governing Multi-Actor Decision Processes in Dutch Industrial Area Redevelopment
Erik Blokhuis

nr 148
A Multifunctional Design Approach for Sustainable Concrete
Götz Hüsken

nr 149
Quality Monitoring in Infrastructural Design-Build Projects
Ruben Favié

nr 150
Assessment Matrix for Conservation of Valuable Timber Structures
Michael Abels

nr 151
Co-simulation of Building Energy Simulation and Computational Fluid Dynamics for Whole-Building Heat, Air and Moisture Engineering
Mohammad Mirsadeghi

nr 152
External Coupling of Building Energy Simulation and Building Element Heat, Air and Moisture Simulation
Daniel Cóstola

nr 153
Adaptive Decision Making In Multi-Stakeholder Retail Planning
Ingrid Janssen

nr 154
Landscape Generator
Kymo Slager

nr 155
Constraint Specification in Architecture
Remco Niemeijer

nr 156
A Need-Based Approach to Dynamic Activity Generation
Linda Nijland

nr 157
Modeling Office Firm Dynamics in an Agent-Based Micro Simulation Framework
Gustavo Garcia Manzato

nr 158
Lightweight Floor System for Vibration Comfort
Sander Zegers

nr 159
Aanpasbaarheid van de Draagstructuur
Roel Gijsbers

nr 160
'Village in the City' in Guangzhou, China
Yanliu Lin

nr 161
Climate Risk Assessment in Museums
Marco Martens

nr 162
Social Activity-Travel Patterns
Pauline van den Berg

nr 163
Sound Concentration Caused by Curved Surfaces
Martijn Vercammen

nr 164
Design of Environmentally Friendly Calcium Sulfate-Based Building Materials: Towards an Improved Indoor Air Quality
Qingliang Yu

nr 165
Beyond Uniform Thermal Comfort on the Effects of Non-Uniformity and Individual Physiology
Lisje Schellen

nr 166
Sustainable Residential Districts
Gaby Abdalla

nr 167
Towards a Performance Assessment Methodology using Computational Simulation for Air Distribution System Designs in Operating Rooms
Mônica do Amaral Melhado

nr 168
Strategic Decision Modeling in Brownfield Redevelopment
Brano Glumac

nr 169
Pamela: A Parking Analysis Model for Predicting Effects in Local Areas
Peter van der Waerden

nr 170
A Vision Driven Wayfinding Simulation-System Based on the Architectural Features Perceived in the Office Environment
Qunli Chen

nr 171
Measuring Mental Representations Underlying Activity-Travel Choices
Oliver Horeni

nr 172
Modelling the Effects of Social Networks on Activity and Travel Behaviour
Nicole Ronald

nr 173
Uncertainty Propagation and Sensitivity Analysis Techniques in Building Performance Simulation to Support Conceptual Building and System Design
Christian Struck

nr 174
Numerical Modeling of Micro-Scale Wind-Induced Pollutant Dispersion in the Built Environment
Pierre Gousseau

nr 175
Modeling Recreation Choices over the Family Lifecycle
Anna Beatriz Grigolon

nr 176
Experimental and Numerical Analysis of Mixing Ventilation at Laminar, Transitional and Turbulent Slot Reynolds Numbers
Twan van Hooff

nr 177
Collaborative Design Support: Workshops to Stimulate Interaction and Knowledge Exchange Between Practitioners
Emile M.C.J. Quanjel

nr 178
Future-Proof Platforms for Aging-in-Place
Michiel Brink

nr 179
Motivate: A Context-Aware Mobile Application for Physical Activity Promotion
Yuzhong Lin

nr 180
Experience the City: Analysis of Space-Time Behaviour and Spatial Learning
Anastasia Moiseeva

nr 181
Unbonded Post-Tensioned Shear Walls of Calcium Silicate Element Masonry
Lex van der Meer

nr 182
Construction and Demolition Waste Recycling into Innovative Building Materials for Sustainable Construction in Tanzania
Mwita M. Sabai

nr 183
Durability of Concrete with Emphasis on Chloride Migration
Przemysław Spiesz

nr 184
Computational Modeling of Urban Wind Flow and Natural Ventilation Potential of Buildings
Rubina Ramponi

nr 185
A Distributed Dynamic Simulation Mechanism for Buildings Automation and Control Systems
Azzedine Yahiaoui

nr 186
Modeling Cognitive Learning of Urban Networks in Daily Activity-Travel Behavior
Şehnaz Cenani Durmazoğlu

nr 187
Functionality and Adaptability of Design Solutions for Public Apartment Buildings in Ghana
Stephen Agyefi-Mensah

nr 188
A Construction Waste Generation Model for Developing Countries
Lilliana Abarca-Guerrero

nr 189
Synchronizing Networks: The Modeling of Supernetworks for Activity-Travel Behavior
Feixiong Liao

nr 190
Time and Money Allocation Decisions in Out-of-Home Leisure Activity Choices
Gamze Zeynep Dane

nr 191
How to Measure Added Value of CRE and Building Design
Rianne Appel-Meulenbroek

nr 192
Secondary Materials in Cement-Based Products: Treatment, Modeling and Environmental Interaction
Miruna Florea

nr 193
Concepts for the Robustness Improvement of Self-Compacting Concrete: Effects of Admixtures and Mixture Components on the Rheology and Early Hydration at Varying Temperatures
Wolfram Schmidt

nr 194
Modelling and Simulation of Virtual Natural Lighting Solutions in Buildings
Rizki A. Mangkuto

The production of nano-silica by the dissolution of olivine is an interesting alternative to the existing commercial methods because of the good quality of the resulting silica and low energy requirements and CO_2 emissions.

The main purpose of this research is to improve the technology of the olivine nano-silica production process to be able to tailor the properties of this nano-silica. A secondary objective is to optimize the olivine nano-silica process. In addition to these objectives, this research contributes to the understanding of three topics: the dissolution of olivine at negative pH; the silica particle growth below the isoelectric point; and the development of the pore structure at negative pH.

The content of this PhD thesis can be divided up into the following parts: 1) the dissolution of olivine under the olivine nano-silica conditions; 2) the influence of the process conditions on the textural properties of olivine nano-silica; and 3) the technical aspects of the olivine nano-silica process.

F A C

B W K

E H T

/ Department of the Built Environment

TU/e Technische Universiteit Eindhoven University of Technology